DIF

1+26

(NASA-CR-164542) THE TELECOMMUNICATIONS AND DATA ACQUISITION REPORT Progress Report, Mar. - Apr. 1981 (Jet Propulsion Lab.) 232 p HC A11/MF A01 CSCL 22D
G3/12

N81-27123
THRU
N81-27149
Unclas
26799

The Telecommunications and Data Acquisition Progress Report 42-63

March and April 1981

N. A. Renzetti
Editor

June 15, 1981

National Aeronautics and
Space Administration

Jet Propulsion Laboratory
California Institute of Technology
Pasadena, California

The Telecommunications and Data Acquisition Progress Report 42-63

March and April 1981

N. A. Renzetti
Editor

June 15, 1981

National Aeronautics and
Space Administration

Jet Propulsion Laboratory
California Institute of Technology
Pasadena, California

The research described in this publication was carried out by the Jet Propulsion Laboratory, California Institute of Technology, under contract with the National Aeronautics and Space Administration.

Preface

This publication was formerly entitled *The Deep Space Network Progress Report*. Although the practice of reporting progress in the development and operations of the Deep Space Network continues, the report has been expanded to include developments in Earth-based radio technology as applied to other research programs. These programs are:

(1) Geodynamics: For several years, the laboratory has been developing radio interferometry at microwave frequencies for application to geodetic measurements. This branch of telecommunications technology is now being applied to the study of geodynamics.

(2) Astrophysics: The deep space stations, individually and in pairs as an interferometer, have been used by radio astronomers for astrophysics research by direct observations of radio sources.

(3) An activity closely related to radio astronomy's use of the deep space stations is NASA's continuing program of radio search for extraterrestrial intelligence in the microwave region of the electromagnetic spectrum.

Each succeeding issue of this report will present material in some, but not all, of the following categories:

Radio Astronomy
Search for Extraterrestrial Intelligence
Radio Interferometry at Microwave Frequencies

    Geodetic Techniques Development
    Spacecraft Navigation
    Orbiting Very Long Baseline Interferometry

Deep Space Network

    Description
    Program Planning
    Planetary and Interplanetary Mission Support
    Advanced Systems
    Network and Facility Engineering and Implementation
    Operations
    Spacecraft Radio Science
    Planetary Radar
    Energy

In each issue, there will be a report on the current configuration of one of the seven DSN systems (Tracking, Telemetry, Command, Monitor and Control, Test Support, Radio Science, and Very Long Baseline Interferometry).

The work described in this report series is either performed or managed by the Telecommunications and Data Acquisition organization of JPL.

Contents

RADIO ASTRONOMY

THE DEEP SPACE NETWORK
DESCRIPTION

PLANETARY AND INTERPLANETARY MISSION SUPPORT
Planetary Flight Projects

Interplanetary Flight Projects

ADVANCED SYSTEMS
Tracking and Ground-Based Navigation

Communications

PRECEDING PAGE BLANK NOT FILMED

Station Control and System Technology

Network Data Processing and Productivity

NETWORK AND FACILITY ENGINEERING AND IMPLEMENTATION

Network

OPERATIONS

Network Operations

Deep Space Stations

PLANETARY RADAR

N81-27124 D/

Radio Astronomy

R. D. Shaffer and P. R. Wolken
Control Center Operations Section

S. Gulkis
Planetary Atmospheres Section

This article reports on the activities of the Deep Space Network in support of Radio Astronomy operations during the first quarter of 1981. Preliminary results of the use of a low-noise maser on loan from NRAO are presented, as well as updates in DSN support of experiments sanctioned by the Radio Astronomy Experiment Selection Panel.

I. Introduction

Deep Space Network (DSN) 26-, 34-, and 64-meter-antenna stations are utilized in support of three categories: NASA Office of Space Science (OSS), Radio Astronomy Experiment Selection (RAES), and Host Country.

II. Radio Astronomy Operations

A. NASA OSS Category

During this period, support was given for 95 hours of station time for Planetary Radio Astronomy (OSS 196-41-73) and Interstellar Microwave Spectroscopy (OSS 188-41-55-12-55) at DSS 43 utilizing the Tidbinbilla Interferometer (OSS 188-41-55-16). This support includes the installation of a K-band (20-25 GHz) maser on loan from the National Radio Astronomy Observatory (NRAO). A particular observational objective of this configuration is the search for spectroscopic lines of molecules. Of special interest is the search for interstellar molecular water at 22.235 GHz.

Preliminary results of work in progress reveal startling technological as well as scientific advances. A reflection-type maser is used as the first RF amplifier, providing an instantaneous bandwidth of about 150 MHz. A feature of this system, which is unique to low noise systems is the beam switching allowed by a cryogenic switch in front of the maser. Two avenues of spectral analysis are available: a 256-channel digital FFT (Fast Fourier Transform) spectrometer (10-MHz bandwidth) and a wideband 36-channel filter bank system. To date, this configuration has measured a system temperature of about 65 K at zenith and aperture efficiency of about 20% at 45° elevation. Observationally, three new water-line masers, as well as six ammonia-line sources, have been detected thus far.

B. RAES Category

1. **RA 175 (SS433).** During the first quarter of 1981, the Goldstone 26-meter station supported VLBI observations of the source SS433 (1909 + 04) for a total of 55.5 hours. These observations represent continuing efforts in support of the experimental objective of resolving this bizarre galactic object

to determine its angular radio structure and possibly its origin. Preliminary results are reported in *TDA Progress Report 42-62, January – February 1981*

2. **RA 176 (Twin Quasi-Stellar Object (QSO) VLBI).** 51.5 hours of 64-meter antenna time (DSS 14 and DSS 63) was devoted to observing two apparent twin QSOs: 0957 + 561 A, B and 1038 + 528 A, B. The first twin is postulated to be a single QSO, whose image has been optically split by an intervening galaxy, the mass of which is thought to be acting as a gravitational lens. This is supported by the identical red shifts and other structural similarities between the A and B components of 0957 + 561, as well as independent optical resolution of the intervening galaxy. 1038 + 528 A, B is considered to be a coincidental twin or double QSO, analogous to optical or apparent binary stars. Of approximately 1500 known QSOs, these two sources are unique as the only known apparent twins. Proof of the gravitational lens effect has ramifications in terms of determining mass distribution in the cluster of galaxies of which the lens is a member as well as the location and distance to the QSO. The double QSO displays apparent morphological changes with time, the explanation of which could be useful in resolving questions concerning structure, origin, and evolution of QSOs in general.

The DSN's participation in this experiment was as an integral component of a VLBI network encompassing radio observatories across the North American and European Continents.

3. **RA 177 (Milliarcsecond VLBI).** In the ongoing statistical investigation into milliarcsecond quasar and galactic nuclei to determine the frequency of their occurrence, the DSN supported 34 hours and 50 minutes of observations with 64-meter antennas (DSS 14 and DSS 63) utilizing VLBI techniques.

C. Host Country

Pulsar observations conducted for the Commonwealth Scientific and Industrial Research Organization (CSIRO) in Australia, as described in *TDA Progress Report 42-60, September-October 1980*, are the only Host Country activities to report for this period. This continuing research is supported by the 26-meter antenna at Honeysuckle Creek (DSS 44) for six hours per week, allocated as two distinct periods of three hours each.

D2

N81-27125

Mark IV-A DSCC Telemetry System Description

R. Burt
TDA Engineering Office

This article provides a description of the Deep Space Communications Complex (DSCC) portion of the Mark IV A Telemetry System. This system is currently being designed as a replacement for the Mark III. The Ground Communications Facility (GCF) and Network Operations Control Center (NOCC) portions of the DSN Telemetry System will be changed less extensively. These changes, which are presently not well understood, will be described in later articles.

I. Introduction

The present DSN Telemetry System, the Mark III, is described in Ref. 1. The DSN is undertaking a major modification of the Mark III. The modified Network, described elsewhere in this volume, will be called the Mark IV-A, and will be implemented between 1983 and 1985. The DSCC portion of the DSN Telemetry System will be changed in two major ways as a result of the Mark IV-A DSN implementation:

(1) Two 34-meter antennas will be added to each Deep Space Communications Complex (DSCC). The arraying of those antennas with the existing 64- and 34-meter antennas will provide the equivalent of two separate 64-meter antennas or two 64-meter antennas arrayed together. To accomplish this, the DSCC will be modified to provide carrier arraying and baseband combining of three 34-meter antennas and one 64-meter antenna.

(2) The Telemetry System will be configured to support either two deep space missions and one highly elliptical orbiter, or two highly elliptical orbiters and one deep space mission. Highly elliptical orbiter (HEO) missions will have data rates up to 1.2 Msps modulated directly on the carrier. Since the maximum Ground Communications Facility (GCF) rate will be limited, data rates higher than 115 kbps will be recorded at the Signal Processing Center (SPC) and played back in non-real time.

Implementation of these changes, when combined with the existing capabilities, will prepare the network to support both DSN and HEO missions.

The DSN missions will be the following:

Pioneer 6 through 9
Pioneer 10 and 11
Pioneer Venus
Viking
Voyager
Galileo
International Solar Polar

The Highly Elliptical Orbiter (HEO) missions will be the following:

- ISEE-C (International Sun Earth Explorer)
- AMPTE (Active Magnetospheric Particle Tracer Experiment)
  - – CCE (Charge Composition Explorer)
  - – IRM (Ion Release Module)
- OPEN (Origin of Plasmas in the Earth's Neighborhood)
  - – IPL (Interplanetary Physics Laboratory)
  - – GTL (Geomagnetic Tail Laboratory)
  - – PPL (Polar Plasma Laboratory)
  - – EML (Equatorial Magnetosphere Laboratory)

Note that there are two AMPTE and four OPEN spacecraft.

II. Key Characteristics

The key characteristics of the DSCC portion of the Mark IV-A Telemetry System are:

(1) Standard DSN data rate capability: up to 250 kilosymbols per sec (ksps).

(2) Highly Elliptical Orbiter Mission data rates up to 1.2 megasymbols per sec (Msps).

(3) Carrier arraying and baseband combining for up to 6 antennas.

(4) Deletion of analog recording.

(5) Four complete groups of telemetry equipment at each complex, each with the capacity to support one of the above missions.

(6) Demodulation of Manchester coded (Biφ-L) or NRZ-L data modulated directly on the carrier.

(7) Maximum likelihood decoding of short-constraint-length convolutional codes and sequential decoding of long-constraint-length convolutional codes.

(8) Precise measurement of received signal level and system noise temperature.

(9) Centralized control by (and real-time reporting to) the Monitor and Control Subsystem.

(10) Production of a digital Telemetry Original Data Record (ODR) at each telemetry group with playback via local manual control or in automatic response to GCF inputs; reduced playback rates for data rates above 115 kbps.

The characteristics that reflect new or modified capabilities due to Mark IV-A design requirements, are underlined. The handling of increased data rates and demodulation of NRZ or bi-phase data modulated directly on carrier directly respond to a requirement for telemetry support of Highly Elliptical Orbiter (HEO) spacecraft. Baseband combining and carrier arraying provides for improved sensitivity to high data rate X-band signals in support of deep space telemetry and is driven by the Voyager project requirement for support of 19.2 kbps at Uranus encounter. The provision for four groups of telemetry equipment at each SPC responds to the requirement to provide telemetry support to three projects concurrently. The absence of project requirements for analog recording allows that function to be removed. The characteristics which are non-underlined exist presently in the Mark III and are discused in Ref. 1.

III. HEO Mission Data Rate and Coding Requirements

HEO missions are for the most part compatible with the existing DSN capabilities. This is illustrated in Table 1, which defines the single link data handling requirements for the HEO projects included in the Mark IV-A mission set. A telemetry single link can be defined as all of the functional elements, from the antenna(s) through an SPC telemetry group, that have been selected for support of a project. The data rate and coding requirements not supportable by the existing DSN capabilities are:

(1) Biφ-L (Manchester coding) directly on the carrier.

(2) 600 kbps.

The combination of Manchester coding and 600 kbps data rate produces a symbol rate of 1.2 Msps. The next section describes the way these HEO requirements will be met by the Mark IV-A DSN Telemetry System.

IV. DSCC Conceptual Description

The DSCC block diagram in Fig. 1 provides a conceptual description of the portion of the Mark IV-A Telemetry System to be located at the DSCC. At each complex there will be one 64-meter antenna, three 34-meter antennas, and a 9-meter antenna. The 64-meter and 34-meter transmit/receive antennas will be able to receive an S-band plus an X-band carrier simultaneously while the 34-meter Listen Only antennas will receive either one S-band or one X-band carrier. The receivers recover the baseband signals which are routed to the Telemetry Subsystem.

The Telemetry Subsystem is arranged to provide four telemetry groups. All groups will include existing strings of equipment (Symbol Synchronizer Assembly, Maximum Likelihood Convolutional Decoder and Telemetry Processor Assembly, TPA). Groups 3 and 4 will also be equipped with the capability needed to support HEO missions. This will be accomplished by incorporating a Spaceflight Tracking and Data Network (STDN) bit synchronizer as well as a newly designed coupler for interface with the TPA. The other two Telemetry Groups (Groups 1 and 2) will be equipped with a new Baseband Assembly (BBA) which will include the functions of baseband combining, subcarrier demodulation and symbol synchronization. The BBA will be designed to accommodate either deep space or highly elliptical orbiters. HEO missions will have data rates up to 1.2 Msps (600 kbps Biφ-L) modulated directly on the carrier. Since the maximum GCF rate will be limited, data rates higher than 115 kbps will be recorded at the SPC and played back in non-real time.

The 64- and 34-meter antennas can be arrayed by combining the carriers within the receiver subsystem. Then the detected baseband signals are combined in the BBA in either Telemetry Group 1 or Telemetry Group 2. The combined signal is then decoded in the Maximum Likelihood Convolutional Decoder and formatted for transmission to JPL in the Telemetry Processor Assembly. When combining is not required, outputs from any antenna may also be routed by any Subcarrier Demodulator Assembly, or directly to the GSTDN symbol synchronizer.

Any of the telemetry equipment groups can accept two data streams. In Groups 1 and 2, one data stream is processed by Channel A and one by Channel C. Similarly, in Groups 3 and 4, one data stream is also processed by Channel A while the other is processed by Channel B. The performance parameters for Channels A, B and C are listed in Table 2. Comparing Table 1 with Table 2, it may be noted that Data Stream 1 in Table 1 is processed by Channel A, while Data Stream 2 is processed in Channel B or C. Similarly, deep space missions require dual data stream support, which is provided by Channels A and B or C. Channel B is used to support higher rates for deep space missions unless combining is required and then Channel C is used. Channel B or C may be used to support HEO missions except for the data rates above 250 ksps, which can be supported by Channel C only.

Reference

1. Gatz, E. C., "DSN Telemetry System Mark III-77," in *DSN Progress Report 42-49*, Jet Propulsion Laboratory, Pasadena, Calif., Feb. 15, 1979.

Table 1. Single link requirements for Earth Orbiter Missions

Mission	Data stream 1	Data stream 2
OPEN-PPL	Uncoded; NRZ-L; 25 kbps	Uncoded; Biφ-L; 600 kbps
OPEN-EML	Uncoded; 6 kbps NRZ-L; or 14 kbps	Uncoded Biφ-L; 600 kbps early in mission, then 94 kbps
OPEN-IPL	Uncoded; NRZ-L; 2 kbps	Uncoded; Biφ-L; 94 kbps
OPEN-GTL	Uncoded; NRZ-L; 6 kbps	Uncoded Biφ-L; 94 kbps
ISEE-C	Convolutionally coded, K = 24, R = 1/2, NRZ-L; 64 bps	Uncoded; Biφ-L, 256 bps. or Convolutionally coded; K = 24, R = 1/2; 512-2048 bps; Biφ-L
AMPTE-CCE	Uncoded; NRZ-L; 1500 bps	Biφ-L; convolutionally coded; K = 7, R = 1/2; 60,000 bps
AMPTE-IRM	Uncoded; NRZ-L; 1000 bps	

Table 2. Telemetry Subsystems 1 and 2, performance parameters

Channel A
Process one NRZ-L coded or uncoded data stream needing
Subcarrier demodulation 512 Hz to 1 MHz
Symbol synchronizing 6 to 25 ksps
Sequential decoding 6 to 10 kbps – K = 24, 32; R = 1/2, frame length variable
Block decoding; Reed Muller 32/6; up to 2 kbps
Channel B
Process one NRZ-L biphase data stream needing
Subcarrier demodulation; 512 Hz to 1 MHz or Manchester decoding. 10 sps to 1.2 Msps
Symbol synchronizing; 6 sps to 1.2 Msps
Sequential decoding 6 to 10 kbps; K = 32; R = 1/2, frame length variable
Maximum likelihood Viterbi decoding – 10 bps to 125 kbps (K = 7, R = 1/2 or 1/3)
Real-time data rates up to 115 kbps
On-site recording and non-real-time playback for data rates above 115 kbps
Channel C
Process one NRZ-L or biphase data stream needing
Baseband combining of up to 6 antenna receiver signals
Subcarrier demodulation: 10 kHz to 2 MHz
Symbol synchronizing and Manchester decoding: 4 sps to 1.2 Msps
Sequential decoding 6 to 10 kbps; K = 32, 24; R = 1/2, frame length variable
Maximum likelihood Viterbi decoding – 10 bps to 125 kbps (K = 7, R = 1/2 or 1/3)
Real-time data rates up to 115 kbps
On-site recording and non-real-time playback for data rates above 115 kbps

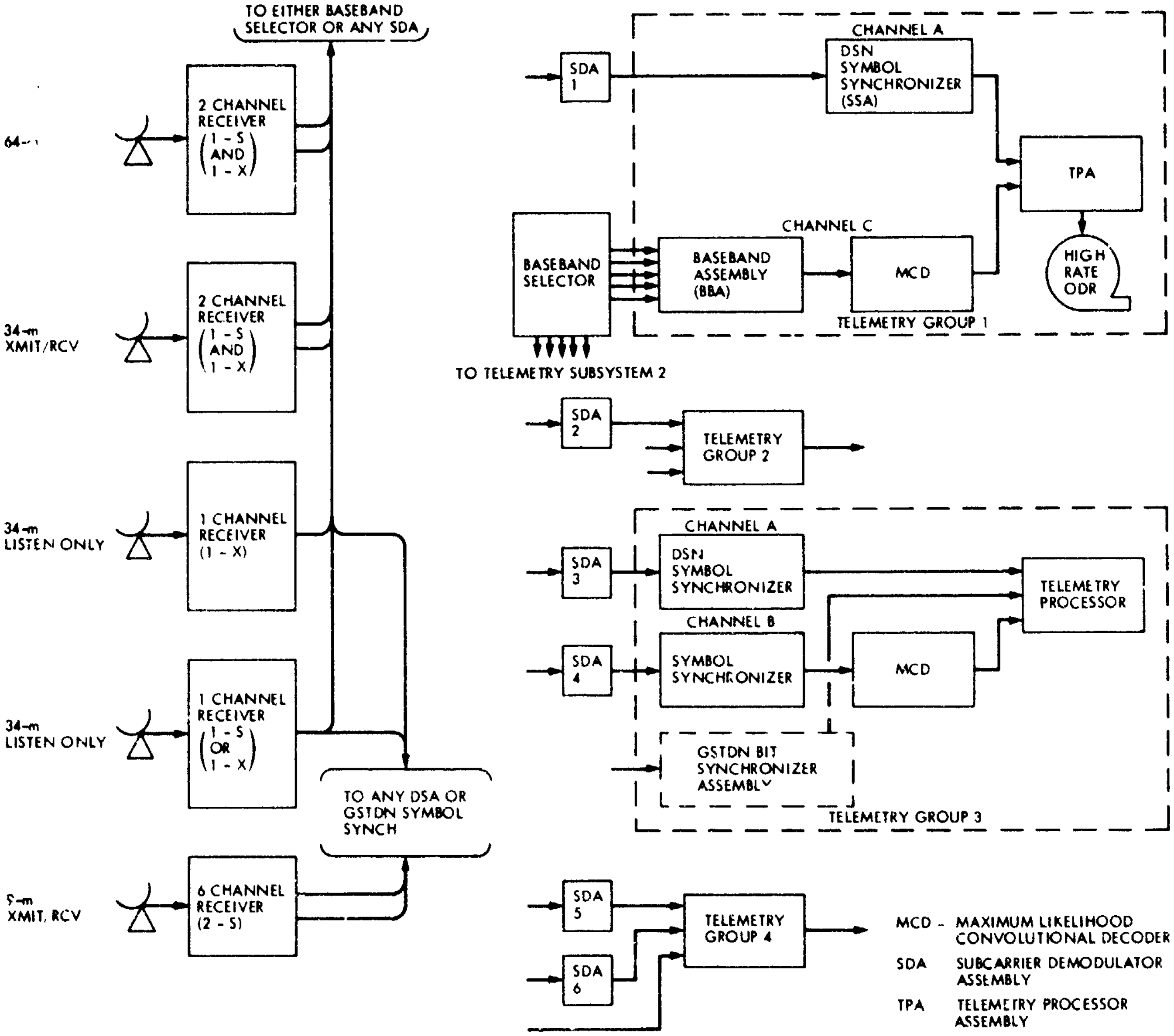

Fig. 1. Telemetry System: DSCC level block diagram

D3

N81-27126

TDA Progress Report 42-63 March and April 1981

The DSN Tracking System

J. A. Wackley
TDA Engineering Office

The DSN Tracking System, one of the eight generic systems of the DSN, has recently undergone a period of extensive software and hardware changes. This article presents a description of the functions of the Tracking System and details the recent changes.

I. Introduction

The Deep Space Network (DSN) Tracking System consists of the hardware, software, personnel and procedures required to perform four primary functions:

(1) Acquire and maintain a communication link (uplink and/or downlink) with a spacecraft

(2) Generate radio metric data

(3) Transmit radio metric data to the data users

(4) Perform radio metric data validation to assure that performance requirements are satisfied

The radio metric data are defined as range, range rate and angle data. These data are used by flight project navigation teams for spacecraft orbit determination, platform parameter determination and ephemeris development. Additionally, as described in Ref. 1, the data have numerous radio science applications for celestial mechanics experiments, planetary atmosphere studies, interplanetary media studies and relativity experiments. Within the DSN, the data are used to monitor the operation of the Tracking System and to validate its performance.

The following sections of this article will present a functional description of the DSN Tracking System and explanations of the many modifications to the system that have been made since the last report (Ref. 2).

II. Functional Description

Figure 1 illustrates the various subsystems and intersubsystem data flow of the Tracking System. The Receiver-Exciter subsystem provides a range modulated uplink carrier to the Antenna Microwave Subsystem where it is amplified and channeled to the antenna. The antenna is precisely pointed by the instructions given to the Antenna Mechanical Subsystem by the Antenna Pointing Subsystem. This allows the uplink carrier to be radiated toward and eventually received by the spacecraft.

At the spacecraft, the carrier is coherently multiplied to provide a downlink carrier, modulated with range data and retransmitted to earth.

The downlink carrier is received and focussed by the antenna and provided to the Antenna Microwave Subsystem.

Here it is amplified and channeled to the Receiver Assembly of the Receiver-Exciter Subsystem. The receiver phase tracks the received signal via a phase-locked loop. The output of the phase-locked loop is provided to the Doppler Extractor Assembly where it is compared to the transmitted frequency. The frequency difference (doppler) is counted by the Metric Data Assembly of the DSS Tracking Subsystem (DTK).

Simultaneously, the receiver provides a range modulated intermediate frequency to the Range Demodulator Assembly of the DTK. Here the ranging signal is demodulated and cross correlated with a model of the transmitted range code. The Planetary Ranging Assembly of the DTK uses the correlation measurement to make a precise determination of the range to the spacecraft.

The range measurement is provided to the MDA where it, as well as the counted doppler and various status and configuration indicators, is formatted for transmission. The MDA provides the formatted data to the Communications Monitor and Formatter Assembly of the Ground Communications Facility (GCF).

The GCF transmits the data to the Network Operations Control Center. The GCF additionally provides an Intermediate Data Record of all data to the end user of the data, typically a project navigation team.

At the NOCC, the radio metric data are received by the NOCC Tracking Subsystem, which generates data displays and alarms used for real-time validation of the data.

The data received by the navigation team are eventually returned to the DSN in the form of ephemeris data for use in generating tracking predictions. These predictions are used for acquisition of the downlink and uplink of the spacecraft as well as radio metric data validation.

Details of the required performance parameters of the elements of the system may be found in Ref. 2.

III. System Modifications

Since the last report concerning the Tracking System, modifications have been made to the software and hardware in the Receiver-Exciter Subsystem, the DSS Tracking Subsystem and the NOCC Tracking subsystem.

A. Receiver-Exciter Subsystem

In July, 1980, implementation of the new microprocessor based exciter frequency controller was begun. The controller, or DCO (digitally controlled oscillator) as it has been dubbed, has the following characteristics:

(1) Control via the Metric Data Assembly or a computer terminal

(2) Capability of storing up to 100 ramps

(3) Minimum ramp duration of 0.1 second

(4) Maximum ramp rate of 100 kHz/second

(5) Maximum phase error (over 8 hours) of 0.0001 cycle

The initial installation of the DCO was hampered by hardware, software and operational problems. The DCO hardware was modified in early 1981 to resolve a problem of sudden large exciter frequency changes. The MDA control interface originally was not compatible for frequency rate reporting and required modification. The operational procedures were, at first, incomplete and resulted in a significant number of errors.

At the completion of implementation in February 1981, the DCO's were installed in the 64 meter and 34 meter subnets. The POCA's remained in the 26 meter subnets.

B. DSS Tracking Subsystem

The Metric Data Assembly (MDA) and the Planetary Ranging Assembly (PRA) of the DSS Tracking Subsystem have had extensive hardware and software modifications during the past year.

1. Metric Data Assembly. The MDA software has been modified to provide, among other items:

(1) A real-time interface with the Meteorological Monitor Assembly. This interface allows the real-time validation of data by NOCC and transference of data to the Occultation Data Assembly (ODA) during VLBI observation sessions.

(2) An interface with the ODA for support of VLBI observation sessions. Besides the previously mentioned MMA data, this interface allows for the transference of the source schedule which is used for data recorder control, source identification, and angle residual calculation.

(3) Automatic control of the DCO and POCA and manual control of the DCO

In the automatic mode of operation, the MDA supplies the control parameters necessary to accomplish the special uplink tuning required to support the Voyager 2 spacecraft and standard uplink tuning required to support the other spacecraft. A complete description of this capability may be found in Ref. 3.

Upon receipt of uplink control predictions (consisting of frequency and time pairs), the MDA computes the parameters (such as rate and time) necessary to tune the uplink to compensate for doppler and allow coherent tracking of the Voyager 2 spacecraft.

Additionally, the MDA can generate the control statements to allow the performance of the "seven point best lock frequency check." This special procedure is performed during Voyager 2 tracks to determine an estimate of the spacecraft's receiver frequency. In order to perform the "seven point best lock frequency check," the MDA constructs a special set of uplink control predicts. These predicts cause the DCO (or POCA) to tune through a series of predetermined changes in frequency as shown in Fig. 2.

Tuning starts at the estimate of the spacecraft receiver best lock frequency. Five minutes prior to the transmitter being turned on, the MDA-generated predicts cause the DCO (or POCA) to snap +1.5 Hz and then continue the tuning necessary to compensate for doppler. Five minutes after the transmitter is turned on, and every five minutes thereafter, the frequency is snapped -0.5 Hz until the lower limit of 1.5 Hz below the estimated best lock frequency is reached. Between snaps the uplink frequency is tuned to compensate for doppler.

Five minutes after reaching the lower limit, the predicts cause the DCO (or POCA) to return to the original estimate of the best lock frequency and to continue tuning through the remainder of the pass. One round trip light time after performing this procedure, the spacecraft signal levels are analyzed to determine the actual best lock frequency. Previously, this procedure required constant operator intervention in order to be accomplished.

For other spacecraft, the MDA computes the control statements for a wide spectrum of sweeps. The type of sweep performed is dependent on both the activity and the relationship between appropriate frequencies. If an uplink acquisition sweep is desired in order to achieve a two-way link with the spacecraft, the operator enters the expected Tracking Synthesizer Frequency (TSF), spacecraft best lock frequency (XA), sweep range and tuning rate. The MDA determines the appropriate direction to tune (by differencing TSF with XA) and the frequencies which encompass the desired sweep range. Possible sweep profiles as determined by the MDA are illustrated in Figs. 3(a) through 3(d). To accomplish these sweeps the MDA generates special uplink control predicts and loads them into the DCO (or POCA).

If an uplink transfer is desired, the operator enters the same information as previously described. In this case, however, the sweep range must be equal to zero hertz. The MDA will generate a predicts set that causes the DCO (or POCA) to tune to the XA and, after the specified time interval, return to the TSF. This type of sweep is illustrated in Figs. 3(e) and 3(f).

Prior to the addition of this capability, a Hewlett-Packard calculator was used to determine the sweep parameters. The parameters were then manually entered into the DCO.

The MDA also provides the control point for manual operation of the DCO. In this mode, DCO control statements are transferred to the DCO. The MDA also provides a display of DCO status.

In order to provide a precise report of tuning activities at the DSS, a new data type, Programmed Frequency data, was developed for inclusion in the radio metric data stream. These data, consisting of precise frequency and frequency rate information, are required to allow for correct processing of the radio metric data by the project navigation teams and to allow remote monitoring of the tuning activities.

Because of the addition of these capabilities the MDA became seriously overloaded causing numerous processing errors. In an attempt to alleviate this problem, floating point hardware was retrofit to the MDA. As of this writing, it had not been determined if this change was completely successful.

2. **Planetary Ranging Assembly**. The quality of ranging data generated by the DSN has been improved by several major modifications to the Planetary Ranging Assembly (PRA). These modification include:

(1) Doubling of the highest frequency component to the 1 MHz

(2) Addition of selectable high frequency components

(3) A new harmonic filter to decrease wave form distortion

All of these changes combine to decrease noise levels on ranging data and to improve ranging capabilities under conditions encountered as the angular separation between the spacecraft and the sun decreases. Figure 4 illustrates the improvement obtained using the new PRA hardware and software. Ranging data acquired by DSS 12 when in its original hardware and software configuration are given in Fig. 4(a). As can be seen, the noise level for these two passes is quite high; more than eight meters during each pass. Figure 4(b) presents data taken after the configuration was modified.

In both of these passes data noise is well less than four meters, an improvement of at least 100 percent. (The absolute differences between the passes are due to orbit and other errors independent of PRA performance.)

C. NOCC Tracking Subsystem

The Prediction Assembly software of the NOCC Tracking Subsystem was replaced by new software. The original software was developed in the mid-1970's to meet existing Tracking System requirements and to provide the NOCC with a replacement for capabilities then residing in the Mission Control and Computing Center (MCCC) 360/75 computer. Because of recent requirements to generate Radio Science predictions and uplink frequency control predictions, the software had been extensively modified to the point where it was difficult to operate and contained many anomalies.

The redevelopment of the software consisted of: making ample use of Network Support Controller (NSC) operating system functions not available when the original software was developed; revising data generation algorithms; updating output formats to correspond to current desires and print capabilities; and most importantly, integrating the functions in a coherent manner.

The result was an improved software package with more easily understood input, and improved running characteristics (run time was decreased well over 50 percent).

IV. Conclusion

Over the past year, various elements of the Tracking System have undergone extensive modifications to both hardware and software. These modifications have, in general, resulted in improved data and increased operational support capabilities. Because of the upcoming Mark IV-A implementations, the Tracking System should remain unchanged over the next few years.

References

1. Renzetti, N. A., and Berman, A. L., *The Deep Space Network – An Instrument for Radio Science Research*, JPL Publication 80-93, Jet Propulsion Laboratory, Pasadena, CA, February 15, 1981.
2. Spradlin, G. L., "DSN Tracking System, Mark III-1979," in *Deep Space Network Progress Report 42-56*, pp. 7-25, Jet Propulsion Laboratory, Pasadena, CA, April 15, 1980.
3. Spradlin, G. L., "DSN Tracking System Uplink Frequency Control" in *Deep Space Network Progress Report 42-53*, pp. 108-112, Jet Propulsion Laboratory, Pasadena, CA, October 15, 1979.

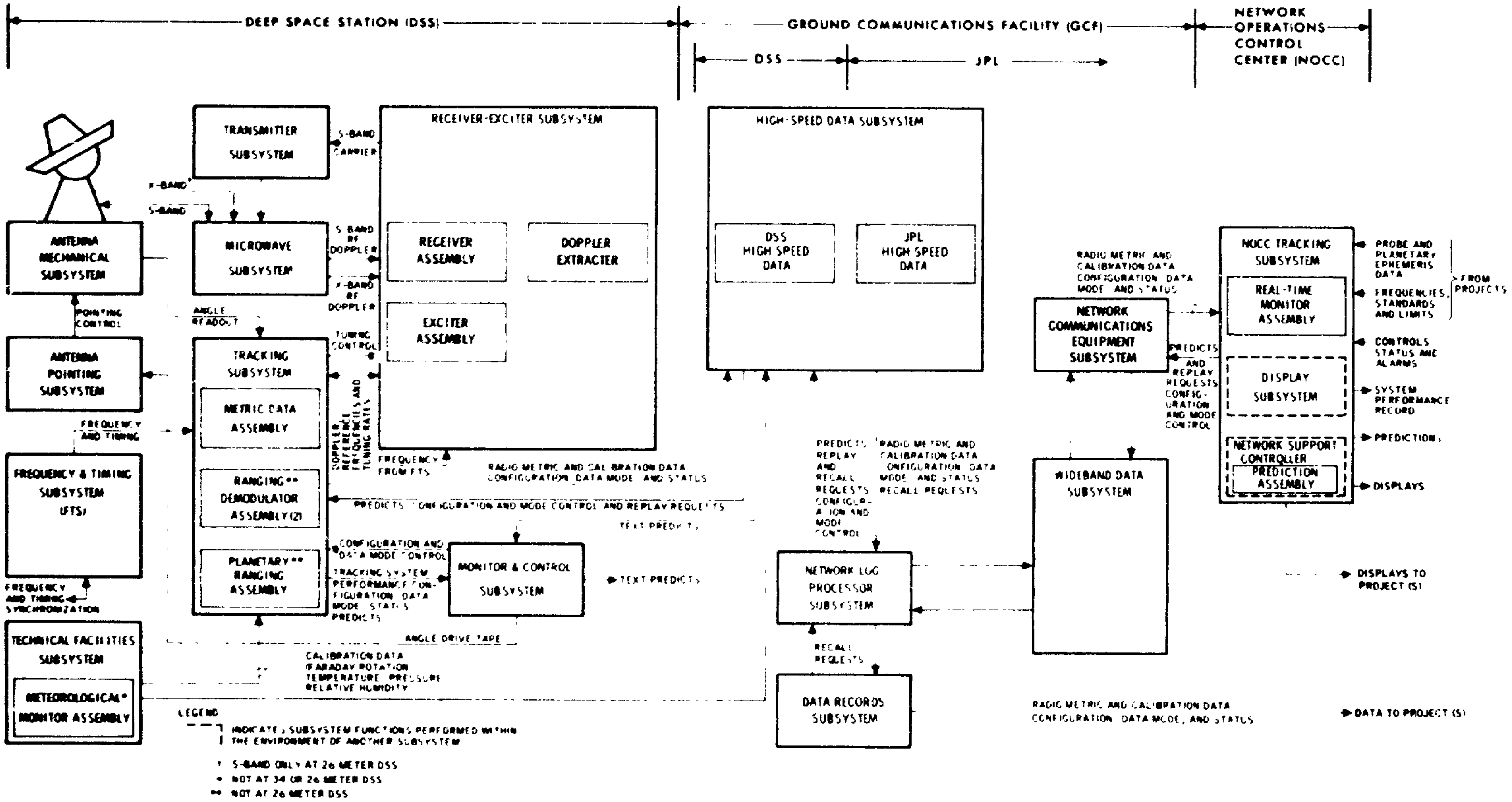

Fig. 1. DSN tracking system

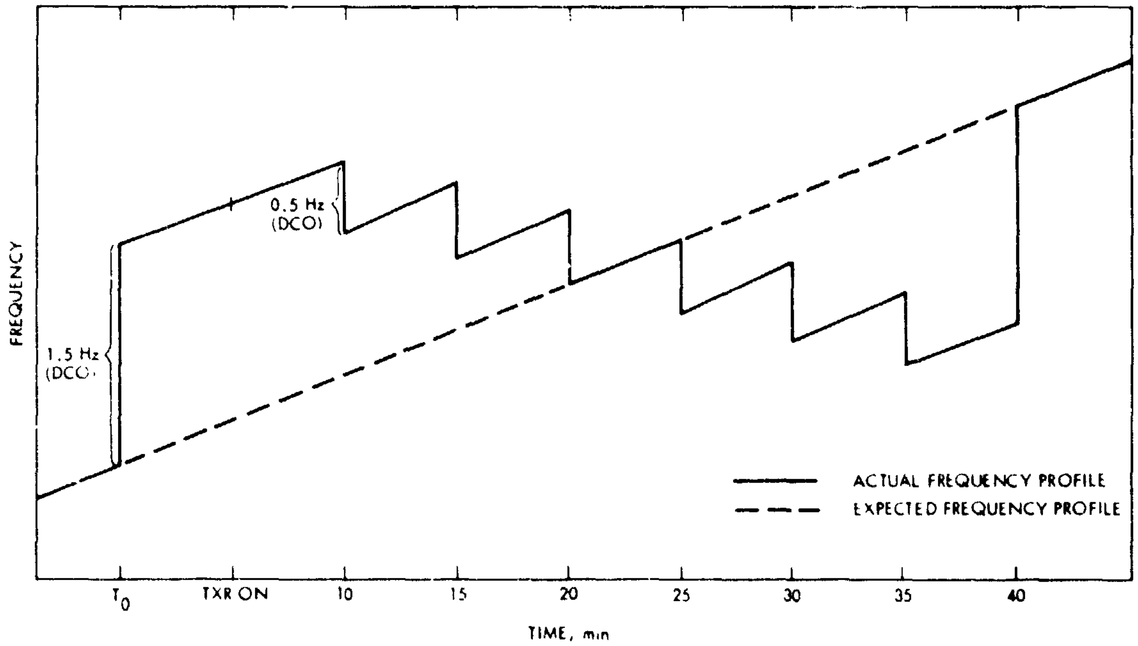

Fig. 2. Voyager 2 best lock frequency check

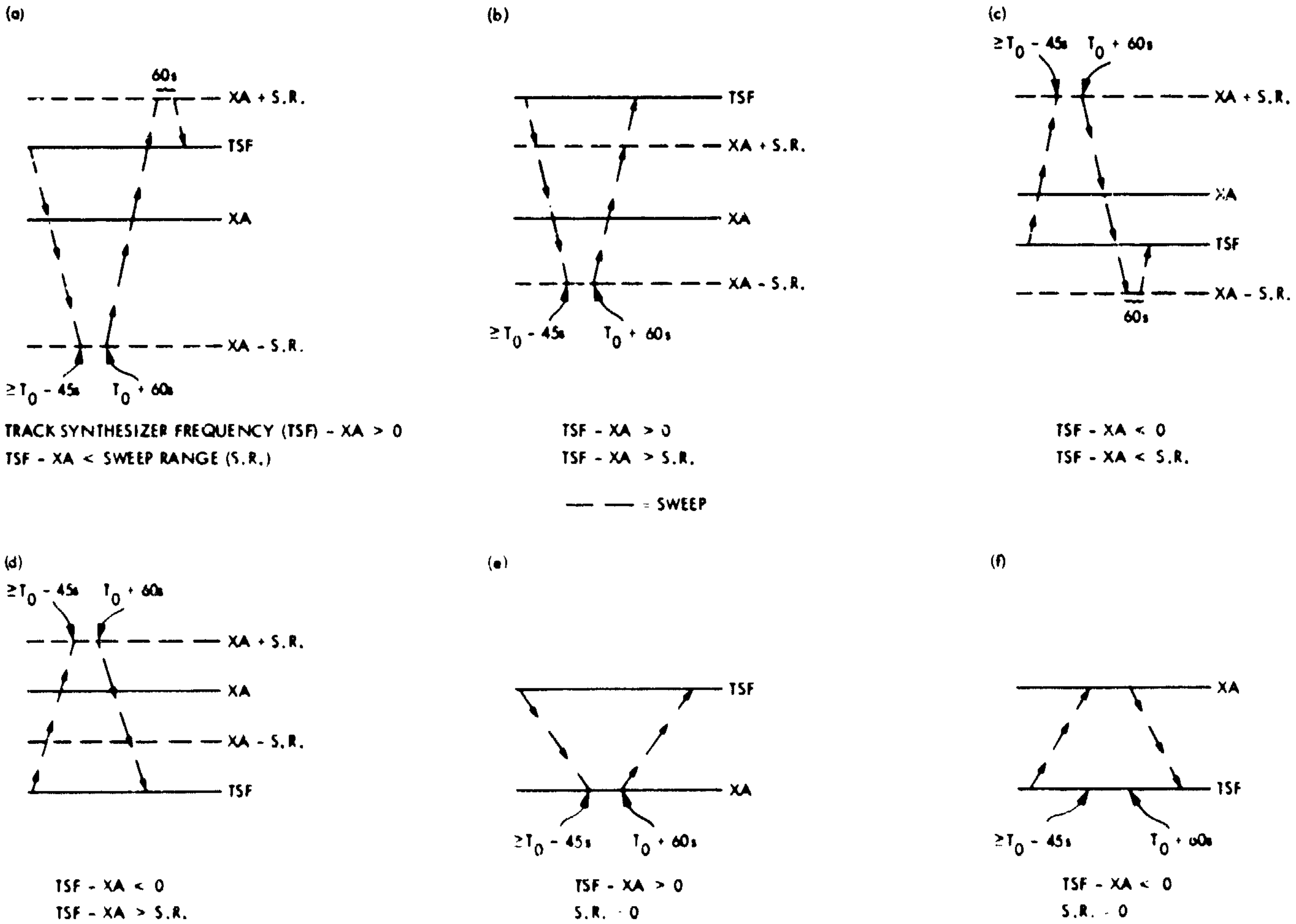

(a) TRACK SYNTHESIZER FREQUENCY (TSF) - XA > 0
TSF - XA < SWEEP RANGE (S.R.)

(b) TSF - XA > 0
TSF - XA > S.R.

— — = SWEEP

(c) TSF - XA < 0
TSF - XA < S.R.

(d) TSF - XA < 0
TSF - XA > S.R.

(e) TSF - XA > 0
S.R. = 0

(f) TSF - XA < 0
S.R. = 0

Fig. 3. MDA generated uplink sweeps

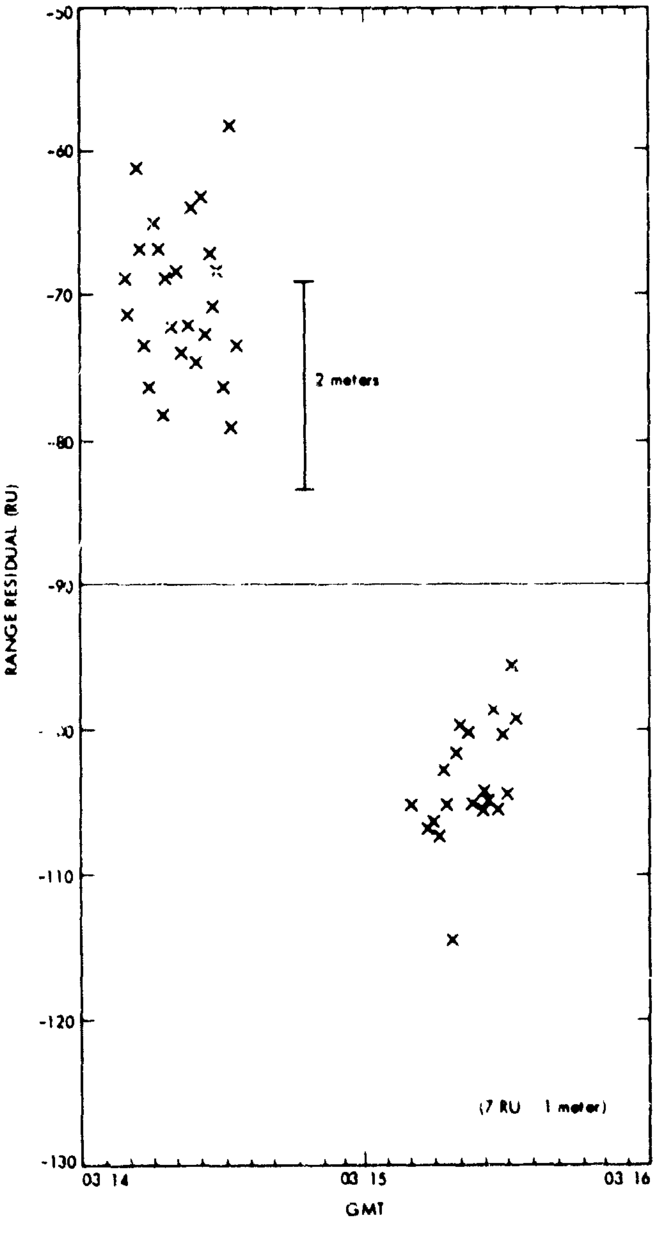

Fig. 4(a). DSS 12 ranging data before modifications

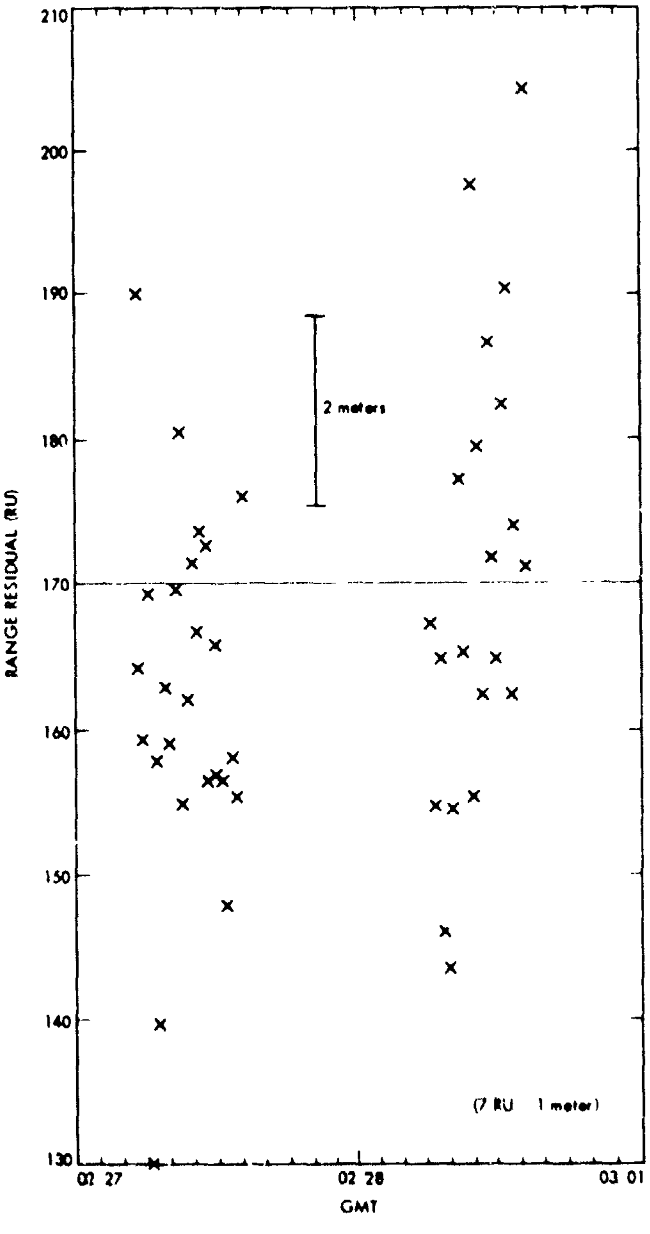

Fig. 4(b). DSS 12 ranging data after modifications

D4

N81-27127

Pioneers 6 Through 12 Mission Support

R. Nevarez
Control Center Operations Section

This article discusses the activities of DSN Operations in support of the Pioneers 6 through 9, Pioneer 10, Pioneer 11, and Pioneer Venus Orbiter (Pioneer 12) Missions from June 1980 through March 1981.

I. Introduction

The information contained in this report covers the continuing efforts of the Deep Space Network in support of Pioneer Mission Operations during the cruise phases of Pioneers 6 through 9, Pioneer 10, Pioneer 11, and the orbital operations of Pioneer 12 spacecrafts.

II. Mission Operations and Status

A. Pioneer 6

In June of 1980, Pioneer 6 went through superior conjunction. The first track after superior conjunction found the spacecraft on-board systems in good health and functioning nominally. In December of 1980, Pioneer 6 celebrated its fifteenth year in operation with signs of continuing for another fifteen years.

B. Pioneer 7

During this reporting period, tracking support increased due to tracking availability of the Network. The spacecraft has been and is left in the engineering format to provide an early means of establishing the spacecraft's health in the event of a problem. The on-board science experiments, which continue to function nominally, are turned on only when the spacecraft is tracked.

C. Pioneer 8

In August of 1980 as the spacecraft approached perihelion, the Sun sensor and plasma analyzer on board the spacecraft functioned for the first time in several years and produced valid data. During perihelion, tracking support was limited. Additional tracking support is scheduled for the next perihelion.

D. Pioneer 9

The spacecraft continues to function nominally. An analysis indicates that the spacecraft on-board systems continue in good health.

E. Pioneer 10

A special procedure using the imaging photopolarimeter (IPP) instrument to determine the roll pulse was developed. When the spacecraft loses its Sun pulse, which is estimated to reach threshold in approximately two years, there will be a means of determining the spacecraft roll reference for experimenter use plus the capability of determining precession maneuvers and conscans will be maintained. A signal strength test was performed to determine the spacecraft receiver threshold at low to high transmitter powers. The results are not known at this reporting period, however; further testing will be performed in the future. The spacecraft continues to perform nominally and all on-board systems are healthy.

F. Pioneer 11

The spacecraft went through superior conjunction in October 1980 successfully. The spacecraft continues performing nominally and based on data analysis all systems on board the spacecraft are in good health.

G. Pioneer 12

The spacecraft went through a long eclipse season in August 1980 with no problems experienced. The decision to cease controlling periapsis altitude was made; thus the spacecraft will continue to rise until 1986. As a result of this decision, requirements for the radar altimeter (ORAD) instrument were completed, thus eliminating the need of daily ORAD instrument command loads. Occasional ORAD calibrations and various other procedures are still planned. Imaging will continue for some time, with radio science experiments to be performed upon request. The spacecraft started a superior conjunction phase in mid-March 1981 and will continue through April 1981. The spacecraft continues performing nominally with all on-board systems in good health.

III. Special Activities

Pioneer Project continues to utilize the Deep Space Network Compatibility Test Area (CTA-21) in concurrence with the Project's command software development and operations training.

IV. Summary

As of this reporting period, all Pioneer spacecraft appear in good health and are operating nominally. Pioneers 6, 7, 8, 9, 10, and 11 are in the cruise mode. Pioneer 12 operations continue in orbit about Venus. Tracking coverage from June 1980 through March 1981 is shown in Table 1.

Table 1. Tracking coverage, June 1980 through March 1981

Month, year	Pioneer spacecraft	Station type	Number of tracks	Tracking time, h:min
June 1980	6	64-m	10	51:15
	7	64-m	3	19 20
	9	64-m	7	49:00
	10	64-m	58	466 10
	11	26-m	47	356:35
		64-m	22	180:15
	12	26-m	100	918.30
		34-m	5	44:39
		64-m	1	10:30
July 1980	6	64-m	5	19:50
	7	64-m	1	10:45
	9	64-m	6	44:45
	10	64-m	47	379:20
	11	26-m	46	386.45
		34-m	3	25·35
		64-m	14	110.30
	12	26-m	82	754·50
		34-m	2	17:05
		64-m	2	10 55
Aug 1980	6	64-m	6	24:10
	7	64-m	1	5:05
	8	64-m	1	8:10
	9	64-m	3	16.20
	10	64-m	44	382 15
	11	26-m	30	211 20
		34-m	8	50.30
		64-m	30	227.00
	12	26-m	77	703 30
		34-m	6	26 50
		64-m	8	56 15
Sept 1980	6	64-m	3	12 55
	8	64-m	5	20.40
	9	64-m	5	28 30
	10	64-m	62	476 20
	11	26-m	46	314.10
		34-m	16	79.35
		64-m	15	116.00
	12	26-m	80	763.55
		34-m	15	139 20
		64-m	14	117.25
Oct 1980	6	64-m	1	3 50
	7	64-m	1	4:55
	9	64-m	4	15.35
	10	34-m	6	28.55
		64-m	53	353 20
	11	26-m	23	162.55
		34-m	11	56 40
		64-m	6	52 05
	12	26-m	56	508:20
		34-m	8	83.45
		64-m	11	118 20
Nov 1980	6	64-m	4	19.30
	9	64-m	4	20:30
	10	34-m	10	57:35
		64-m	38	243:00
	11	26-m	24	219.55
		64-m	7	79:15
	12	26-m	35	352:40
		34-m	2	16:00
Dec 1980	6	64-m	2	13:00
	8	64-m	2	13:30
	9	64-m	1	4:50
	10	34-m	5	29.25
		64-m	45	353:45
	11	26-m	24	222·30
		34-m	3	33·25
		64-m	18	170:20
	12	26-m	40	394:05
		34-m	3	27:45
		64-m	23	220 40
Jan 1981	6	64-m	2	15 00
	7	64-m	3	14:50
	8	64-m	2	15.25
	9	64-m	3	14:20
	10	26-m	8	28·45
		64-m	52	556 35
	11	26-m	41	280.20
		34-m	2	19 00
	12	64-m	30	235.35
		26-m	78	646 50
		34-m	3	27 35
		64-m	28	335.30
Feb 1981	6	64-m	3	18.00
	8	64-m	2	12 10
	9	64-m	3	20 15
	10	26-m	6	20.35
		34-m	4	16 15
		64-m	39	327 10
	11	26-m	32	286 05
		34-m	23	198 05
		64-m	17	146·05
	12	26-m	26	173:20
		34-m	37	302 20
		64-m	49	372 50
March 1981	6	64-m	2	11.50
	9	64 m	3	20·20
	10	26-m	3	9:00
		34-m	4	12 45
		64-m	50	378.30
	11	26-m	33	333 30
		34-m	17	186·35
		64-m	16	129 30
	12	26-m	21	134·15
		34-m	16	262.10
		64-m	82	576 00

Ds

N81-27128

Voyager Mission Support

N. Fanelli and H. Nance
Control Center Operations

This is a continuation of the Deep Space Network Report on Tracking and Data Acquisition for Project Voyager. This article covers the period of December 1980 through March 1981.

I. Introduction

Voyager 1 completed the Saturn Post Encounter Phase of its prime mission operation and started the extended mission phase of operations.

Voyager 2 continued in the Jupiter-Saturn Cruise Phase with increased tracking in anticipation of the Saturn Encounter.

II. DSN Support

A. Voyager 1

The Post Encounter period was scheduled to end on 15 December 1980, but due to the unusual observations of the rings during the near encounter, the post encounter period was extended to 19 December 1980 so that another movie could be made.

1. **Long time-base observation and system scans.** The post encounter support consisted primarily of the observations of Saturn's atmosphere at high phase angles over a long-time base and periodic imaging of Saturn and system scans at phase angles and at latitudes different from those in the pre-encounter phases. Imaging data was returned at the higher data rates (29.8 and 44.8 kpbs) in the imaging formats. The system scan data was returned at the lower data rate (7.2 kpbs) in the general science format. Deep Space Stations (DSS) 14/12 and DSS 43/42 in the arrayed configuration were scheduled to receive the imaging data, with DSS 61 or 63 scheduled to receive the general science data consistent with station view period.

2. **Saturn ring movie.** The Saturn Rings movie activity was conducted on 18 December between Day of Year (DOY) 353 1012Z and DOY 354 0523Z. DSS 14/42/43/61/63 supported the activity with the DSS 61/63 and the DSS 42/43 complexes being in the array configuration to enhance the image data reception. This activity completed the Voyager 1 Saturn Encounter phase and the spacecraft entered the extended mission phase of activity.

B. Voyager 2

During the Post Encounter phase of the Voyager 1 mission operation, the activity of Voyager 2 was relatively quiet, with the majority of the tracking support being provided by the 26-meter network (DSS/11/44/62).

1. **Navigation cycle.** On 3-4 December 1980 a navigation cycle was conducted with Voyager 2. The Navigation cycle was supported by DSS 42/63/12. Software problems with the

Metric Data Assembly-Digitally Controlled Oscillator (MDA-DCO) interface required that the VGR-2 Navigation cycle support be conducted with a Programmed Oscillator Control Assembly (POCA) configuration. DSS 42 and 12 were, therefore, required to reconfigure with the POCA, vice the DCO, before their supporting passes. DSS 63 was configured with the POCA, so was not required to reconfigure for support. Near simultaneous ranging was conducted during the DSS 63/12 and DSS 12/42 overlap periods in addition to normal ranging. The Navigation cycle was completed successfully, with required data being delivered to the Project.

2. **Mini cruise science maneuver.** On 16 December (DOY 351 2213Z to DOY 352 0321Z) a mini cruise science maneuver was completed. The maneuver consisted of four yaw turns and four roll turns being accomplished, during which the spacecraft antenna was off earth point, therefore, no data were received. DSS 42 supported the activity that immediately preceded the maneuver with DSS 63 supporting the reacquisition activity. Playback reception of the data recorded by the spacecraft during the maneuver was supported by DSS 43 on 17 December (DOY 352).

3. **Trajectory correction maneuver.** On 26 February 1981 (DOY 057 2059-2246Z) a Trajectory Correction Maneuver (TCM-B7) was completed successfully. The objective of the maneuver was to place Voyager 2 on a more accurate trajectory to rendezvous with Saturn. The spacecraft was programmed to execute a negative roll turn followed by a negative yaw turn to align itself on a required burn vector. The TCM thrusters imparted a 0.574 meter/sec delta velocity after a burn duration of 215 seconds. The spacecraft returned to earth point by accomplishing complementary yaw and roll turns. The activity was supported by DSS 43 during the preparation phase and by DSS 63 during the actual maneuver. During the burn, the spacecraft was off earth point, no telemetry data were being received in real-time, but were being recorded aboard the spacecraft. The playback of the recorded data was accomplished during DSS 43's viewperiod the next day.

C. General

1. **Doubly differenced range.** In continuing effort to further refine tracking techniques to provide more precise spacecraft position information, the DSN is supporting doubly differenced range activity. The first activity supported occurred on DOY 355. This technique required that both DSS 61 and 12 track and range on Voyager 2, then, after a quick turn-around, track and range on Voyager 1. The turn-around from Voyager 2 to Voyager 1 was accomplished in 20 minutes. The stations were required to perform pre- and post-track calibrations on the ranging equipment for both spacecraft (S/C). This was a new requirement, as a station normally tracks only one S/C and performs the necessary pre- and post-track calibrations to support that one S/C. Although there were some problems in preparing for and executing the activity events, the results look promising. Another test was supported on DOY 031 (1981) by DSS 61 and 12. Fewer problems were experienced during this test and the results are being evaluated.

2. **Metric data assembly software.** Metric Data Assembly Software, DMK-5106-OP-F, which provides the capability to automatically control the Digitally Controlled Oscillator (DCO) and the uplink frequency required for tracking Voyager 2 started engineering testing at Goldstone on 6 January 1981. DCO implementation at the 34/64 meter stations was completed on 26 February 1981. After a series of Voyager demonstration tracks, during which problems were identified and corrected, a preliminary operational disk was provided. The Goldstone stations began Probationary Testing on 5 February 1981 with this disk supporting all projects. The software was also sent to the overseas stations where they began Probationary Testing on 16 February 1981. The software was transferred to operations on 2 March 1981 for an Operational Certification period by the stations prior to the official replacement of the previous operational support software. The software became the prime support software on 28 March 1981.

III. DSN Capabilities

A. Radio Science

The Saturn Near Encounter Radio Science activities for Voyager 2 will occur during the viewperiod of DSS 43. Since DSS 63 was the prime supporting station for the Voyager 1 Saturn Encounter Occultation Experiment, it was necessary to relocate the DSS 63 Radio Science equipment from DSS 63 to DSS 43. This equipment included the four channel narrow/medium band multi-mission receiver plus the backup wideband four channel multi-mission receiver and its associated digital recording assemblies. DSS 43 sent its two channel open loop receiver to DSS 63. This equipment relocation was accomplished during the month of January 1981. DSS 14 has the narrow/medium equipment comparable to DSS 43. Following successful installation of the equipment and subsequent system performance tests, a series of operational verification tests were conducted with the new equipment and an updated version of the Occultation Data Assembly (ODA) software. The checkout of the new software (DMO-5123-OP-C) was started over DSS 14 on 4 February, since their equipment was installed and operational at the time. Pioneer and Voyager X-band signals were used during this testing. The ODA OP-C testing started at DSS 43 on 19 February and at DSS 63 on 27 February. Only minor problems have been encountered;

the operational procedures are being refined and crew training accomplished during the testing. The software was transferred to operations on 16 March and tests will continue through August 1981 to ensure and maintain facility readiness. These tests will continue to use live spacecraft data and accomplish the functions of recording open loop data, playback of recorded data and on-site validation of recording quality, as will be required during the encounter.

B. Adaptive Tracking

The problems caused by the failure of the receivers on Voyager 2 (DSN Progress Report 42-49, Nov-Dec 1978) with the resultant 200 Hz bandpass in the operating receiver are complicated by spacecraft internal temperature changes. It has been determined that after various spacecraft activities, compartment temperatures rise and change the center frequency of the receiver bandpass and the rate of drift as the temperatures return to normal. Therefore, after these spacecraft activities, the Best Lock Frequency (BLF) is unknown and normally a command moratorium is declared, due to the uncertainty of establishing a proper uplink. During the Saturn Near Encounter, after the spacecraft comes out of occultation, this condition will exist, but it will be necessary to command the spacecraft sooner than a moratorium would allow. To provide background data on the frequency offset and to allow better estimates of the BLF after these activities, the DSN has been supporting special tracking procedures called "adaptive tracking and BLF determination". Essentially, after a spacecraft temperature change, the 34/64 meter station will accomplish the BLF determination sequence. This is a sequence of five predetermined ramps by the DCO through the estimated BLF. The data are analyzed in near-real-time to refine the BLF. The adaptive tracking sequence is exercised, during which the DSN is provided a frequency offset to "snap to", then to automatically ramp with the appropriate predicts. The frequency drift from the predicted is used to determine the new frequency offset, and used to keep the uplink centered in the receiver bandpass. This procedure is continued as long as necessary to ensure a proper uplink for commanding activities. This procedure relies on the DCO and the capabilities of the MDA S/W DMK-5106-OP-F automatic uplink feature.

C. DSS 12 Antenna Efficiency Improvement

DSS 12 was decommitted from support operations on 6 March 1981 and scheduled to become operational again on 24 April 1981. The purpose of the DSS 12 downtime is to improve the overall antenna efficiency.

The two outer rows of the primary antenna dish panels will be replaced and all panels reset. The subreflector surface tolerance will also be improved. This additional antenna work should improve overall antenna gain by at least 0.75 dB.

During the downtime, the subreflector controller will be modified and upgraded. New circuit boards and internal adjustments will provide improved antenna pointing accuracy, which will also improve overall antenna performance.

After the antenna work is completed, and prior to returning the station to operational support status, a series of star tracks will be performed to evaluate actual antenna gain improvement.

D6

N81-27129

TDA Progress Report 42-63 March and April 1981

Navigation Using X-Ray Pulsars

T. J. Chester and S. A. Butman
Communications Systems Research Section

Approximately one-dozen X-ray pulsars are presently known which emit strong stable pulses with periods of 0.7 to ~1000 s. By comparing the arrival times of these pulses at a spacecraft and at the Earth (via an Earth-orbiting satellite), a three-dimensional position of the spacecraft can be determined. One day of data from a small (~0.1 m^2) on-board X-ray detector yields a three-dimensional position accurate to ~150 km. This accuracy is independent of spacecraft distance from the Earth. Present techniques for determining the two spacecraft coordinates other than range measure angles and thus degrade with increasing spacecraft range. Thus navigation using X-ray pulsars will always be superior to present techniques in measuring these two coordinates for sufficiently distant spacecraft. At present, the break-even point occurs near the orbit of Jupiter. The Crab pulsar can also be used to obtain one transverse coordinate with an accuracy of ~20 km.

I. Introduction

At present, as spacecraft are targeted farther from Earth, it becomes increasingly difficult to measure the transverse spacecraft coordinates (the two other than range). Fundamentally, present techniques measure the angular coordinates of a spacecraft and hence the positional uncertainty of the spacecraft grows linearly with distance. Thus navigation to the outer planets and beyond will be limited by these large uncertainties unless a better measurement tool is used.

We present in this article a promising new technique that involves comparing the arrival times of pulses from X-ray pulsars at a spacecraft and at the Earth. The positional accuracy given by this technique is independent of distance from the Earth. Only a small (~0.1 m^2) X-ray detector need be carried by the satellite. This is in sharp contrast to navigation using radio pulsars, which give more precise times but require impractically large antennas on the spacecraft.

II. Details

Several relevant parameters of the known X-ray pulsars are given in Table 1, as well as the parameters of the Crab pulsar, which is a radio pulsar (an entirely different beast) that is also detectable in X-rays. There are two major classes of X-ray pulsars -- "steady" and transient sources. The transient sources are detectable only at (usually) irregular intervals -- for example, perhaps for only 30 days – and then are below detection limits for a year or more. Thus only the "steady" sources can be relied upon for navigation. Unfortunately, even the "steady" sources sometimes turn off for about a month. This can occur at regular intervals, as for Her X-1 which is detectable for 10 days and then undetectable (except briefly) for 25 days, or the off period can be irregular, as for Cen X-3 and SMC X-1. Nonetheless, this should cause little problem, both because it is unlikely that all usable sources would be off simultaneously, and also because the long transit times necessary on deep space voyages allow some short gaps in the measurements of some coordinates.

The pulses from X-ray pulsars are largely sinusoidal, with only a little power in the lower harmonics and no power in the higher harmonics. This is quite unlike radio pulsars, which pulse for only ~10% of their periods. Thus the time of arrival accuracy is given by how well the phase of a sinusoidal pulse can be measured, and not by the arrival of any sharp feature in the pulse.

Taking Her X-1 as an example, 20 seconds of data taken by the UHURU satellite, with a detector area of 0.1 m^2, determined arrival times accurate to 0.03 s (Ref. 1), which gives a positional measurement good to 10,000 km in the direction toward the X-ray pulsar. One full day of measurements would beat the error down to $10{,}000 \text{ km} \sqrt{20 \text{ s}/86{,}400 \text{ s}} = 150 \text{ km}$. Both SMC X-1 and Cen X-3 are similar to Her X-1, and would give comparable positional accuracies. Thus these three pulsars would suffice to give a three-dimensional spacecraft position. Figure 1 shows the geometry of these three pulsars, referenced to the ecliptic plane.

Of course, with ranging, only two pulsars are needed for a good three-dimensional position. The other short-period pulsars can provide more information when they are pulsing. Even the long-period pulsars give positional measurements which are only slightly worse because they tend to have more harmonic content in their pulses, and thus timing accuracies do not degrade as badly as linearly with pulse period.

The Crab pulsar, with its period of only 0.033 s and its low duty cycle pulse, gives much more precise arrival times, and is always detectable. However, a larger detector would be required to take full advantage of this resolution. With a small detector, again 0.1 m^2, the time resolution should be ~10 times better than for Her X-1. Unfortunately, the Crab pulsar is in the ecliptic plane and thus cannot give any information about the spacecraft coordinate perpendicular to the ecliptic plane. Of course, except when the spacecraft lies along the direction to the Crab, such timing observations will measure one transverse spacecraft coordinate in the ecliptic plane.

Because the pulse periods of X-ray pulsars (and radio pulsars) are derived from the rotation of a neutron star, the period is very stable. Typically, $\dot{P}/P \sim 10^{-11}$, except for some of the long-period X-ray pulsars, which can have $\dot{P}/P \sim 10^{-4}$. The most important source of timing error on the spacecraft will therefore come from the spacecraft clock itself. Fortunately, any drift of the spacecraft clock can be treated as an additional unknown, if it is important enough, and can be found by using an additional pulsar. In that case, with ranging, three pulsars are needed for a good three-dimensional position and the determination of the spacecraft clock offset. The spacecraft clock need only be stable over the chosen integration time for an individual arrival time determination.

Finally, the positional uncertainty of the X-ray pulsars themselves can be neglected. An angular uncertainty of θ in the coordinates of a pulsar gives rise to an error of $\theta^2/2$ times the distance between the Earth and the spacecraft projected along the pulsar direction. Thus if $\theta = 5 \times 10^{-7}$ (0.1 arc sec), then the error at Saturn is less than 10 cm.

III. Discussion

Navigation using X-ray pulsars is a practical method that yields three-dimensional positions accurate to ~150 km with one day of data. It is the best practical method for sufficiently distant spacecraft, requiring only a small X-ray detector on board the spacecraft coupled with an Earth-orbiting satellite that provides the arrival of X-ray pulses at Earth. (In the last decade, there has been an average of several such satellites in orbit at any given time.)

Present positional accuracies for the transverse coordinates of a spacecraft are ~300-400 km at Saturn (Ref. 2) with ~1 day of data. Thus X-ray navigation is comparable to present techniques at roughly the orbit of Jupiter and is clearly superior at Saturn and beyond.

References

1. Fechner, W. B., and Joss, P. C., "Evidence for a 35 Day Precession in the Orbit of Hercules X-1," *Astrophys. J. Letters*, 1977, Vol. 213, p. L57.

2. Melbourne, W. G., "Navigation Between the Planets," *Scientific American*, June 1976, Vol. 234, No. 6.

Table 1. The known X-ray pulsars

Name[a]	Period, s	Peak counts/s[b]	Class[c]
3U0531 + 21 Crab pulsar	0.03	100	R
3U0115 −37 SMC X-1	0.7	28	S
3U1653 + 35 Her X-1	1.2	100	S
4U0115 + 63	3.6	70	T
3U1118 −60 Cen X-3	4.8	160	S
3U1626 − 67	7.7	10	S
OA01653 − 40	38	600	T
A0535 + 26	104	1900	T
3U1728 − 24	122	60	S
A1239 − 59	191	12	S
3U1258 − 61	272	47	S
3U0900 − 40	283	100	S
4U1145 − 61	297	72	S
A1118 − 61	405		T
3U1538 − 52	529	11	S
3U1223 − 62	696	32	S
3U0352 + 30	835	20	S

[a] The name begins with a 1- or 2-character catalogue designation, followed by the right ascension (HHMM) and the declination

[b] 2-6 keV counts per second for a 0.1 m^2 detector

[c] R – radio pulsar, S – steady, T – transient

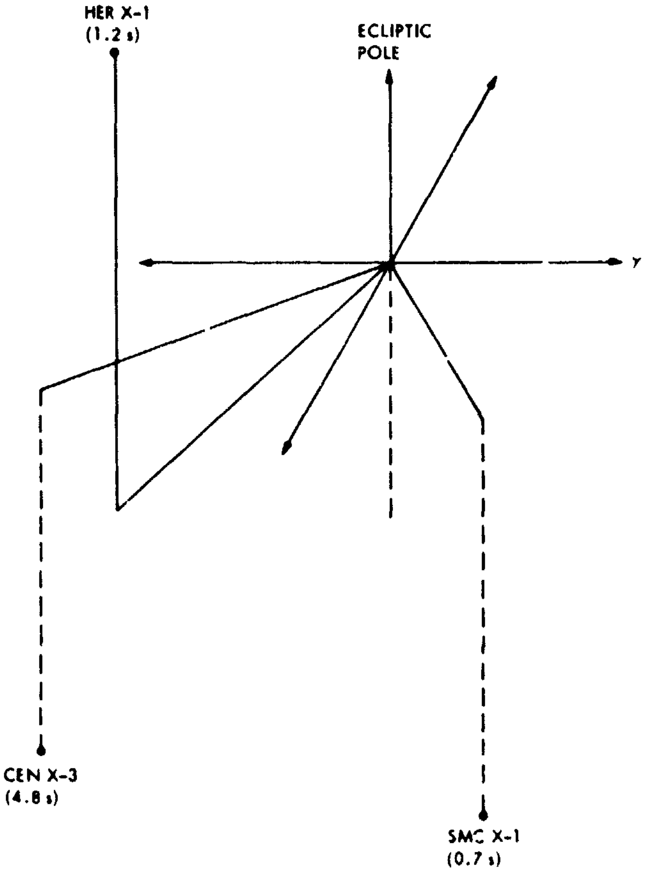

Fig. 1. Location of several X-ray pulsars relative to the ecliptic plane

97

N81-27130

Propagation Path Length Variations Due to Bending of Optical Fibers

K. Y. Lau
Communications Systems Research Section

The propagation path length variation due to bending of optical fibers is analyzed in this article. Both the geometric effect and material stress effects are included in the analysis. These calculations put an upper limit on the expected phase shift in single mode fibers. The fractional change in propagation constant is given by

$$\frac{\delta\beta}{\beta} = (0.15)\left(\frac{a}{R}\right)^2,$$

where a is the core radius of the fiber (either single or multimode), and R is the bending radius of curvature. Moding effects in multimode fibers cause extraneous phase shifts of unusually high magnitude. This does not occur in single mode fibers, rendering them very insensitive to bending with a theoretical limit given by the above relation.

I. Introduction

To transmit a time and frequency standard with accuracies required for such applications as VLBI (very long baseline interferometry), both a stable transmission path *and* a sophisticated electronic compensation system are required. The choice of a relatively stable transmission medium can greatly alleviate the stringent requirements for the electronic compensation system. Contenders for the transmission path include coaxial system, microwave, and optic-fiber system. Preliminary phase noise measurements on a 3-km multimode fiber-optics link indicate that its performance surpasses all of the other available systems (Ref. 1). It was also observed that bending the optical fiber introduces noticeable phase shift in the transmitted RF signal. The purpose of this article is to analyze this phenomenon and to establish a limit on the amount of RF phase shift introduced due to bending of single-mode fibers. This same calculation procedure cannot be applied to multimode fibers. It has been observed experimentally that bending a multimode fiber introduces unusually high phase shift in the carried RF signal which cannot be accounted for by changes in propagation constants alone. The reason, we believe, is due to moding effects. Multimode fibers carry a large number (several hundred) of transverse modes, some tightly held, some loosely held, and some are even cladding modes. These different modes have different propagation constants (which, in fact, is the origin of dispersion in multimode fibers). Bending the fiber causes a redistribution of the power contained in each mode, with some tightly held modes converted into loosely held or cladding modes. If these loose modes were allowed to enter the receiver, a very large phase shift will be observed, because the effective propagation constant between the receiver and the point when the bend occurs is changed. However, if the loosely held or the cladding modes were lost before they enter the receiver, no effect should be seen on the RF phase shift. This proposition is supported by the experimental observation that, while bending the fiber within several hundred meters of the receiver produces several degrees of phase changes in a 100-MHz RF signal, bending the fiber more than 1 km away from the receiver does not produce any significant effect on the phase.

The above phenomenon does not occur in single-mode fibers because they carry only one mode. Experimentally, bending a single-mode fiber anywhere along the link does not produce any noticeable phase shifts on the signal (as observed with a 100-MHz RF signal on a vector voltmeter with a phase resolution of 0.1 degree). The analysis below gives an upper limit on the amount of phase shift expected in single-mode fibers.

II. Field Solutions of a Straight Optical Fiber

Figure 1 shows a step-index fiber cross section and the refractive index variation. Typical core dimension for a multimode fiber is 50 μm diameter, for a single-mode fiber it is about 5 to 10 μm diameter. The refractive index difference ($n_{core} - n_{clad}$) between the core and cladding material is typically of the order of 10^{-3}. A multimode fiber supports hundreds of transverse modes, in a single-mode fiber all but one of these modes are beyond cutoff. The fundamental mode (HE_{11} mode) that propagates in a single-mode fiber theoretically does *not* have a cutoff frequency (in contrast to a hollow metallic waveguide), but for sufficiently low optical frequency the power contained in the core is so small that for all practical purposes it can be regarded as beyond cutoff.

Electromagnetic wave propagation inside a dielectric fiber is governed by the wave equation

$$\nabla^2 \mathbf{E} + k^2 n^2(x, y, z)\, \mathbf{E} = 0 \qquad (1)$$

where $\mathbf{E}$ is the electric field vector, n is the refractive index and k is the free space propagation constant $= 2\pi/\lambda$. For weakly guiding fibers (small difference between cladding and core index) the fields are very nearly uniformly and linearly polarized (Ref. 2) so that a scalar wave equation, obtained by replacing the $\mathbf{E}$ vector by a scalar quantity ψ, suffices to describe the modal behavior. As illustrated in Fig. 1, propagation is in the y direction, giving rise to a factor $e^{-i\beta y}$ in the field ψ, and the transverse mode pattern can be solved from Eq. (1) subjected to pertinent boundary conditions. They can be represented in cylindrical coordinates by the Bessel functions

$$\psi_l(r,\phi) = \begin{cases} J_l(ur/a)/J_l(u) & r < a \\ K_l(ur/a)/K_l(u) & r > a \end{cases} \cos l\phi \qquad (2)$$

where r and ϕ are the radial and azimuthed coordinates on a cross section of the fiber. J_l and K_l are respectively the Bessel and modified Bessel functions of order l, l is a positive integer describing the mode order, and u and w are a pair of parameters related to the propagation constant β through a set of transcendental characteristic equations. These field solutions have been extensively computed and well documented (Refs. 3, 4).

The problem of solving the field inside a bent fiber is considerably more complicated. The circular symmetry, which enables closed form solutions to be written down as in the case of a straight fiber, no longer exists when the fiber is bent. Previous analyses on bending effects concentrate on radiation loss (Refs. 5, 6). It was shown that such bending loss is negligible if the bend radius is larger than a few centimeters (Ref. 3). This would be assumed in the following analysis.

III. Analysis of a Bent Optical Fiber by Conformal Transformation

Figure 2 shows a sketch of the top view of a bent fiber. With the help of conformal transformation (Ref. 7), a bent section of fiber can be transformed into a straight section with a modified index of refraction profile. For large radius of bend curvature, this modified index profile differs only slightly from the unmodified (straight fiber) one, so that a perturbation technique can be used to evaluate the change in propagation constant due to bending.

The bent fiber, as illustrated in Fig. 2a, lies on the x-y plane. Define a complex number $Z = x + iy$, and a complex function

$$w = u + iv = R\, ln\left(\frac{Z}{R}\right) \qquad (3)$$

which maps every point on the x-y plane onto a point in the u-v plane. Under this transformation, a circular annulus as shown in Fig. 2a will be transformed into a straight section as shown in Fig. 2b. The equation which describes wave propagation in the u-v plane is obtained by applying a similar coordinate transformation, Eq. (2), on the wave Eq. (1), and results in

$$\frac{\partial^2 \psi}{\partial u^2} + \frac{\partial^2 \psi}{\partial v^2} + \left(\frac{\partial^2 \psi}{\partial z^2} + k^2 n^2 \psi\right) \left|\frac{dZ}{dw}\right|^2 = 0 \qquad (4)$$

On the original x-y plane, the wave propagates along the circular arc of the bent fiber governed by the wave equation (1). On the transformed u-v plane, the wave propagates along the v direction of the transformed straight fiber, governed by the transformed wave equation (4). The factor $|dZ/dw|^2$ can be easily evaluated from Eq. (2):

$$\left|\frac{dZ}{dw}\right| = \exp(u/\bar{R}) \tag{5}$$

Not unexpectedly, as the bend radius $\bar{R}$ goes to ∞, $|dZ/dw|$ goes to 1 and Eq. (4) is the same as that for a straight fiber, resulting in mode solutions given in Eq. (2).

IV. Modification of Index Profile Due to Bending Stress

The conformal transformation technique illustrated above takes care of the geometric factor due to bending. However, there is a material factor due to the stress and strain induced in the bent fiber. Obviously, when a fiber is bent, the inner part is compressed and the outer part rarefied. We can assume that at the mean radius of bending $\bar{R}$ (along the axis of the bent fiber) the density of the fiber material is unchanged, and that the local density of the fiber material is inversely proportional to R, the local radius of bending.

To calculate the variation of the refractive index due to a variation in fiber material density, we use the Clausius-Mosotti relation (Ref. 8) for the refractive index of dense material:

$$n^2 = 1 + \frac{N\alpha}{1 - \left(\frac{N\alpha}{3}\right)} \tag{6}$$

where n = refractive index, N is the number of atoms/unit volume of the medium, and α is the atomic polarizability. N is inversely proportional to the local radius of curvature R:

$$N = \frac{\bar{R}}{R} N_0 \tag{7}$$

where N_0 is the material density of the fiber without bending, which corresponds to a refractive index n_0 of about 1.5:

$$n_0^2 = 1 + \frac{N_0\alpha}{1 - \frac{N_0\alpha}{3}} \simeq (1.5)^2 \tag{8}$$

The refractive index at a point in the fiber where the radius of bending is $R = \bar{R} + \rho$ is given by substituting Eq. (7) into (6), expanding in a Taylor series, and assuming $\rho \ll \bar{R}$:

$$\begin{aligned}
n^2 &= 1 + \frac{\left(1 - \frac{\rho}{\bar{R}} + \left(\frac{\rho}{\bar{R}}\right)^2 + \cdots\right)\alpha N_0}{1 - \frac{N_0\alpha}{3}\left(1 - \frac{\rho}{\bar{R}} + \left(\frac{\rho}{\bar{R}}\right)^2 + \cdots\right)} \\
&= 1 + \left(\frac{\alpha N_0}{1 - \frac{N_0\alpha}{3}}\right)\left(1 - \frac{\rho}{\bar{R}} + \left(\frac{\rho}{\bar{R}}\right)^2 + \cdots\right) \\
&\quad \cdot \Bigg(1 - \frac{N_0\alpha}{3}\left(\frac{\rho}{\bar{R}} - \left(\frac{\rho}{\bar{R}}\right)^2 + \cdots\right) \\
&\quad + \frac{\left(\frac{N_0\alpha}{3}\right)^2\left(\frac{\rho}{\bar{R}}\right)^2}{\left(1 - \frac{N_0\alpha}{3}\right)^2} + \cdots\Bigg) \\
&= n_0^2\Bigg(1 - \frac{\rho}{\bar{R}}\left(1 + \frac{\frac{N_0\alpha}{3}}{1 - \frac{N_0\alpha}{3}}\right) + \left(\frac{\rho}{\bar{R}}\right)^2\left(1 + \frac{\frac{N_0\alpha}{3}}{1 - \frac{N_0\alpha}{3}}\right)^2 \\
&\quad + \cdots\Bigg)
\end{aligned} \tag{9}$$

Using the actual numerical values,

$$n^2(\rho) = n_0^2\left(1 - \frac{\rho}{\bar{R}}(1.4167) + \left(\frac{\rho}{\bar{R}}\right)^2(2.0069) + \cdots\right) \tag{10}$$

where it is understood that $n_0 = n_{core}$ inside the core and $n_0 = n_{clad}$ inside the cladding.

Since the conformal transformation Eq. (3) transforms the radius ρ into the u-coordinate, Eq. (10) can be substituted directly into the wave equation (4) in the transformed u-v plane:

$$\frac{\partial^2\psi}{\partial u^2} + \frac{\partial^2\psi}{\partial v^2} + \left(\frac{\partial^2\psi}{\partial z^2} + k^2 n^2(u)\psi\right)\left|\frac{dZ}{dw}\right|^2 = 0 \tag{11}$$

V. Perturbation Calculation of the Propagation Constant

As mentioned at the end of Section III, when the bending radius $\bar{R}$ is large, $|dZ/dw|$ will be very close to 1, and we can assume that the transverse mode profiles themselves are not significantly modified. We can, however, calculate the change in propagation constant of each mode due to bending. Perturbation theory gives the following first order corrections $\delta\beta_l$ to the propagation constant β_l of the lth mode (Appendix):

$$\delta\left(\beta_l^2\right) = k^2 \int_A |\psi_l|^2 \left(\left|\frac{dZ}{dw}\right|^2 n^2(u) - n_0^2\right) dA \qquad (12)$$

where ψ_l is the lth transverse mode profile as given in Eq. (2), $|dZ/dw|$ is given in Eq. (5), and $n^2(u)$ in Eq. (10). The area integral of Eq. (12) is evaluated over the cross section A of the fiber, namely the uz plane. Substitution for the various quantities in Eq. (12) yields

$$\delta\left(\beta_l^2\right) = k^2 \iint_A |\psi_l(u,z)|^2\, n_0^2 \left[e^{2u/\bar{R}} \left(1 - 1.4167\frac{u}{\bar{R}} + 2.0069\left(\frac{u}{\bar{R}}\right)^2 + \cdots\right)^{-1}\right] dudz$$

$$\simeq k^2 n_0^2 \iint_A |\psi_l(u,z)|^2 \left(\frac{u}{\bar{R}}(0.5833) + \left(\frac{u}{\bar{R}}\right)^2 (1.1736) + \cdots\right) dudz \qquad (13)$$

In the following, we shall compute the change in propagation constant in single-mode fibers, using the above Eq. (13).

Only one mode propagates in a single-mode fiber: the HE_{11} mode. This mode is circularly symmetric, and is given by Eq. (2) with $l = 0$. Moreover, it can be very closely approximated by a single Gaussian function (Ref. 9) to within 1% error:

$$\psi_0(r,\phi) = \frac{1}{b}\sqrt{\frac{2}{\pi}}\, e^{-r^2/b^2} \qquad (14)$$

where the mode width b is given by

$$\frac{b}{a} = 0.65 + \frac{1.619}{V^{3/2}} + \frac{2.879}{V^6} \qquad (15)$$

a is the radius of the fiber core, V is the normalized frequency

$$V = \left(n_{core}^2 - n_{clad}^2\right)^{1/2} a^2 \left(\frac{2\pi}{\lambda}\right)^2 \qquad (16)$$

and λ is the free space wavelength. Substituting Eq. (14) into Eq. (13) gives

$$\delta\left(\beta_0^2\right) = k^2 n_0^2 \iint_A \frac{1}{w^2}\frac{2}{\pi} e^{-2r^2/b^2} \left(\frac{u}{\bar{R}}(0.5833) + \left(\frac{u}{\bar{R}}\right)^2 (1.1736) + \cdots\right) dA \qquad (17)$$

$$= k^2 n_0^2 \int_0^{2\pi}\int_0^{\infty} \frac{1}{b^2}\frac{2}{\pi} e^{-2r^2/b^2} \left(\frac{r\cos\phi}{\bar{R}}(0.5833) + \frac{r^2\cos^2\phi}{\bar{R}^2}(1.1736) + \cdots\right) rdrd\phi \qquad (18)$$

$$= 1.1736\frac{k^2 n_0^2}{b^2}\int_0^{\infty} e^{-2r^2/b^2}\frac{r^3}{\bar{R}^2}\, dr + \text{higher order terms in } \frac{1}{\bar{R}} \qquad (19)$$

$$\delta(\beta^2) = 0.293\, k^2 n_0^2 \left(\frac{b}{\bar{R}}\right)^2 \qquad (20)$$

$$\frac{\delta\beta}{\beta} = 0.147\left(\frac{b}{\bar{R}}\right)^2 \qquad (21)$$

The fractional change in the propagation constant is thus proportional to the square of the ratio of mode width b to bending radius R. According to Eq. (15), the width b of the fundamental mode is approximately equal to the core radius, which is about 5 μm for single-mode fiber. Eq. (21) can thus be rewritten as

$$\frac{\delta\beta}{\beta} \simeq 4 \times 10^{-8}\left(\frac{1}{\bar{R}\text{ (in cm)}}\right)^2 \qquad (22)$$

A bending radius of, say, 4 cm will thus cause a change in the propagation constant of 1 part in 10^8 in single-mode fibers.

VI. Conclusion

Measurements on an experimental multimode fiber link indicate that fiber-optics is the most appropriate means for transmitting time and frequency standards. The above calculations indicate that single-mode fibers can be very insensitive to bending perturbations. However, the problem still remains as to how to efficiently couple the laser source to a single-mode fiber in a convenient, compact and noncritical way. With very tight focusing and critical alignments, a coupling coefficient of over 50% has been achieved (Ref. 10). However, typical coupling loss in actual single-mode fiber systems amounts to 10 dB or more (Ref. 11), compared to an easily achieved 3-dB coupling loss in multimode fiber systems. The type of lasers used is also crucial in determining the coupling coefficient. Since the mode in single-mode fibers is symmetric, a laser with a symmetric output field would facilitate coupling. Means of achieving noncritical coupling into a single-mode fiber (such as tapers) are currently under investigation. Also under investigation are means to reduce moding effects in multimode fibers.

References

1. Lutes, G., "Experimental Optical Fiber Communication Link," in *Telecommunications and Data Acquisition Progress Report 42-59*, Jet Propulsion Laboratory, Pasadena, Calif., Oct. 15, 1980.
2. Gloge, D., "Weakly Guiding Fibers," *Appl. Opt.*, Vol. 10, p. 2252, 1971.
3. Gloge, D., "Propagation Effects in Optical Fibers," *IEEE Trans. Microwave Theory*, Vol. MTT-23, p. 154, 1975.
4. Marcuse, D., *Theory of Dielectric Optical Waveguides*, Academic Press, 1974.
5. Marcatili, E. A. J., and Miller, S. E., "Improved Relations Describing Directional Control in Electromagnetic Wave Guidance," *Bell Syst. Tech. J.*, Vol. 48, p. 2161, 1969.
6. Neumann, E. G., and Rudolph, H. D., "Radiation from Bends in Dielectric Rod Transmission Line," *IEEE J. Microwave Theory*, Vol. MTT-23, p. 142, 1975.
7. Heiblum, M., and Harris, J. H., "Analysis of Curved Optical Waveguides by Conformal Transformation," *IEEE Jour. Quant. Electron.*, Vol. QE-11, p. 75, 1975.
8. Feymann, R. P., and Sands, M., *Lectures on Physics*, p. 32-7, Addison-Wesley, 1966.
9. Marcuse, D., "Loss Analysis of Single Mode Fiber Splices," *Bell Syst. Tech. Jour.*, Vol. 56, p. 703, 1977.
10. Saruwatari, M., and Nawata, K., "Semiconductor Laser to Single Mode Fiber Coupler," *Appl. Opt.*, Vol. 18, p. 1847, 1979.
11. Yamada, J. I., et al., "High-Speed Optical Pulse Transmission at 1.29 μm Wavelength Using Low-loss Single-Mode Fibers," *IEEE Jour. Quant. Electron.*, Vol. QE-14, p. 791, 1978.
12. Mathews, J., and Walker, R. L., *Mathematical Physics*, Second Edition, W. A. Benjamin, Inc., 1973.

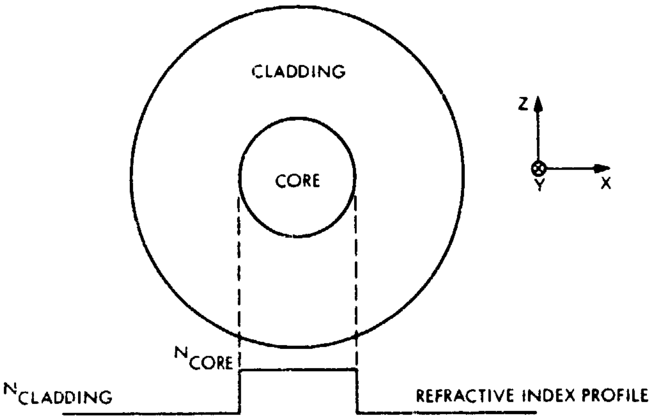

Fig. 1. Cross section of a step index optical fiber

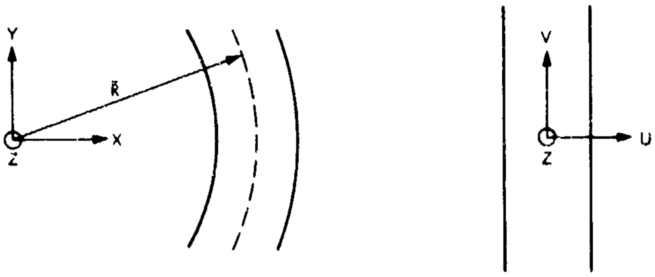

(a)

(b)

Fig. 2 Top view of a bent (2a) and a transformed straight (2b) fiber section

Appendix

Perturbation Analysis of a Bent Optical Fiber

The perturbation formula Eq. (12) is derived here. The equation that describes wave propagation in straight fiber is Eq. (4)

$$\frac{\partial^2\psi}{\partial u^2} + \frac{\partial^2\psi}{\partial v^2} + \left(\frac{\partial^2\psi}{\partial z^2} + k^2 n_0^2 \psi\right) = 0 \qquad \text{(A-1)}$$

Propagation is in the v direction (Fig. 2b); hence the factor is $e^{i\beta v}$, where β is the propagation constant. With this, A-1 becomes

$$\left(\frac{\partial^2}{\partial u^2} + \frac{\partial^2}{\partial z^2} + k^2 n_0^2\right)\psi = \beta^2\psi \qquad \text{(A-2)}$$

or

$$H\psi = \beta^2\psi \qquad \text{(A-3)}$$

where the operator H is as defined from (A-2) and (A-3).

For a bent fiber, the wave equation becomes (Eq. 11)

$$\frac{\partial^2\psi}{\partial u^2} + \frac{\partial^2\psi}{\partial v^2} + \left(\frac{\partial^2\psi}{\partial z^2} + k^2 n^2(u)\psi\right)\left|\frac{dZ}{dw}\right|^2 = 0 \qquad \text{(A-4)}$$

Assuming a propagation constant is β', in this case we can write

$$\frac{\partial^2\psi}{\partial u^2} + \left(\frac{\partial^2\psi}{\partial z^2} + k^2 n^2(u)\psi\right)\left|\frac{dZ}{dw}\right| \doteq \beta'^2\psi \qquad \text{(A-5)}$$

or

$$H'\psi = \beta'\psi \qquad \text{(A-6)}$$

where

$$H' = \frac{\partial^2}{\partial u^2} + \left(\frac{\partial^2}{\partial z^2} + k^2 n^2(u)\right)\left|\frac{dZ}{dw}\right| \qquad \text{(A-7)}$$

If the bending radius is large, H' is not very different from H, and we can write

$$H' = H + H_1 \qquad \text{(A-8)}$$

where H_1 is "small" compared to H, and $\beta'^2 = \beta^2 + \delta(\beta^2)$, where $\delta(\beta^2)$ represents a small correction to the original β^2. The problem now is in the standard form of the perturbation theory (Ref. 12), and the correction to β^2 is given by

$$\delta(\beta^2) = \int_A H_1 |\psi|^2 \, dA \qquad \text{(A-9)}$$

where the area integral is evaluated over the cross section of the mode ψ. From Eqs. (A-8), (A-7) and (A-2) we have

$$\begin{aligned} H_1 &= H' - H \\ &= \frac{\partial^2}{\partial z^2}\left(\left|\frac{dZ}{dw}\right|^2 - 1\right) + k^2\left(n^2(u)\left|\frac{dZ}{dw}\right|^2 - n_0^2\right) \end{aligned} \qquad \text{(A-10)}$$

Now, since a mode can be interpreted as plane waves bouncing along the waveguide walls at grazing angles, the field variation in the transverse direction is much smaller than a wavelength, and thus

$$\frac{\partial^2\psi}{\partial z^2} << k^2\psi \qquad \text{(A-11)}$$

H_1 can thus be approximated to

$$H_1 = k^2\left(n^2(u)\left|\frac{dZ}{dw}\right|^2 - n_0^2\right) \qquad \text{(A-12)}$$

Substituting this into Eq. (A-9) gives Eq. (12).

N81-27131

DB

TDA Progress Report 42-63

March and April 1981

Performance of Concatenated Codes for Deep Space Missions

S. A. Butman, L. J. Deutsch, and R. L. Miller
Communications Systems Research Section

Computer simulation results are presented on the performance of convolutional codes of constraint lengths 7 and 10 concatenated with the (255, 223) Reed-Solomon code (a proposed NASA standard). These results indicate that as much as 0.8 dB can be gained by concatenating this Reed-Solomon code with a (10, 1/3) convolutional code, instead of the (7, 1/2) code currently used by the DSN.

I. Introduction

The purpose of this article is to present new results on the combined performance of short constraint length Viterbi-decoded convolutional codes and Reed-Solomon codes. When one coding scheme is superimposed upon another the resulting combination is called a concatenated code. Those interested in learning about these coding schemes can find elementary presentations in Ref. 1. Our interest is in their performance.

The DSN currently has both (7, 1/2) and (7, 1/3) Viterbi decoders. The performance of several convolutional codes of rates 1/2 and 1/3 with constraint lengths between 7 and 10 have been known for some time (Refs. 2, 3). At the time that the DSN Viterbi decoders were built, hardware speeds were not fast enough to build Viterbi decoders of constraint lengths beyond 7 that were sufficiently reliable and inexpensive. However, with current and expected technological advancements in mind, we have given another look at the possible performance of Viterbi decoders of constraint length 10 and rates 1/2 and 1/3.

This article not only extends previous Viterbi performance results, but also contains new performance results for convolutional codes concatenated with a (255, 223) Reed-Solomon code. (The performance of the DSN (7, 1/2) code concatenated with this Reed-Solomon code appears in Ref. 4.) The Reed-Solomon bit-error probability depends not only on the (average) Viterbi bit error rate, but also on the lengths of the Viterbi error bursts and the density of the errors within the bursts. Consequently, additional simulations are required to gather these statistics

The Galileo Project and the International Solar Polar Mission are planning to employ a concatenated Reed-Solomon/Viterbi coding scheme for telemetering science and engineering data over the space communications channel. Even the Voyager mission has this capability on board. The reason for using a concatenated coding scheme over convolutional coding alone is due to its more efficient use of signal power to achieve bit error probabilities in the 10^{-5} range. Such low error rates are necessary to make data compression schemes workable. Data compression algorithms, while promising to remove substantial information redundancy, are very sensitive to transmission errors.

The quest for good codes is more than just an academic pursuit. A 1 dB or 26 percent improvement from coding is equivalent to enhancing the utilization of the current DSN by arraying a 34-m and a 64-m antenna. With current DSN antenna costs estimated near $100 million, such a gain represents $26 million. Similar tradeoffs can be made on board a spacecraft.

A block diagram of a concatenated coding system is shown in Fig. 1. Binary data generated on board the spacecraft are first encoded by the Reed-Solomon encoder. This encoder also interleaves the Reed-Solomon symbols so as to minimize the effect of error bursts on individual Reed-Solomon codewords. After this first level of coding the data pass to the convolutional encoder. The modulator converts these binary data to a phase modulated radio frequency signal which is amplified and sent out towards the Earth. Two modulation stages are actually performed in the transmitter. The binary data are first multiplied by a square wave subcarrier, and then the resulting waveform is used to phase-modulate a high frequency sinusoidal carrier.

On the ground, the analog signal is detected and tracked by the receiver. A carrier reference is derived and is used to heterodyne the signal to subcarrier frequency. The subcarrier demodulator assembly (SDA) removes the square wave subcarrier, and the symbol synchronizer assembly (SSA) attempts to recover the original coded bit stream. Due to channel noise (and other degradations caused within the receiver system) the SSA does not output the original binary sequence. Instead, it outputs a stream of quantized estimates of these bits. The Viterbi decoder takes these estimates as inputs and decodes the convolutional level of the coding. The Reed-Solomon decoder then deinterleaves the symbols and does the final decoding.

The simulations discussed in this article assumed that there are no losses from carrier and subcarrier tracking and demodulation, and that the Viterbi decoder retains node synchronization at all times. Studies of these degradations are being undertaken, and the results will appear in future publications. For the purpose of this article, only signal degradation caused by the Gaussian noise of the space channel is assumed. The comparisons made in this article should remain valid when degradations are added.

II. Summary of Simulation Results

Figure 2 indicates the performances of several decoding schemes as a function of bit-energy to noise ratio. In particular it shows the relative performances of several Viterbi decoded convolutional codes including the (7, 1/2) code, which is the present standard for deep space applications. Also shown in Fig. 2 are Shannon's theoretical performance limits for rate 1/2 and rate 1/3 binary codes and the performance of uncoded transmission. The Shannon limits represent the best possible error performance for binary codes of these rates (Ref. 5). It is easily seen that the (7, 1/2) code is 2.3 dB away from the theoretical limit at an error probability of 5×10^{-3}. Also, the (10, 1/3) code is less than 2 dB from Shannon's limit for rate 1/3 binary codes.

Also shown in Fig. 2 are the results of concatenating these convolutional codes with an outer Reed-Solomon (255, 223) code. Ideal interleaving is assumed as well as no system losses other than Gaussian channel noise. The performance of the concatenated scheme is very sensitive to SNR; a 1 dB change can result in a bit-error probability jump of several orders magnitude. Consequently, the use of such a concatenated scheme should be accompanied by tight control of the signal to noise ratio of the communications link. Otherwise, the additional operating margin may negate the advantages derived from coding.

III. Simulated Performance of Several Coding Schemes

The key to computing the performance of the concatenated coding system is determining the Reed-Solomon symbol-error statistics. This information cannot be deduced from Viterbi bit-error performance curves. Consequently, extensive simulations were performed on the Xerox Data Systems Sigma 5 computer to calculate both the Viterbi bit-error and Reed-Solomon symbol-error statistics. Each data point was generated by processing 900,000 bits through a modification of the software Viterbi decoder developed by J. W. Layland. The simulations assumed that there were no system losses due to receiver noise or lack of synchronization. The only degradation present in the simulation was that of the random number generator simulating additive white Gaussian noise to reflect the channel SNR. Also, sufficient Reed-Solomon symbol interleaving was assumed so that the symbol error events were independent. This is referred to as ideal interleaving. It is worth noting that interleaving to a depth of 5 is nearly ideal for the DSN (7, 1/2) inner convolutional code at SNRs above 2.0 dB.

Figure 3 shows the results of these simulations. In addition to the plots of Viterbi bit-error probability, p, as a function of channel SNR (E_b/N_o), each graph displays the Reed-Solomon symbol-error probability, π. The Reed-Solomon bit- and word-error probabilities are calculated from π and other burst statistic information derived from these simulations. These Reed-Solomon performance curves are plotted against concatenated channel SNR which is 0.58 dB greater than that of the Viterbi channel due to the overhead of the Reed-Solomon parity symbols.

IV. Conclusion and Discussion

The Viterbi decoders currently used by the DSN suffer loss of node synchronization at low SNRs. This means that if the signal is too weak, the decoder cannot decide which of the two code symbols associated with each data bit should be first. The concatenated coding system allows transmission of data at SNRs lower than those required for a convolutional-only scheme. This means that node synchronization losses will be higher in the concatenated scheme.

There are also synchronization problems associated with the Reed-Solomon code. A method for determining Reed-Solomon symbol and word boundaries is needed. If a packet telemetry system such as the one proposed by the EEIS (Ref. 6) is to be implemented, then a frame synchronization device is also required

For this article, only the error correcting capability of the Reed-Solomon code was considered. However, this code is also capable of correcting a number of erasures, i.e., Reed-Solomon symbols that are previously known to be in error. The (255, 233) code can correct E errors and e erasures in each codeword as long as $2E + e < 33$. If erasures can be detected, then the performance of the Reed-Solomon decoder may improve by as much as 0.3 dB.

It should be noted that the loss of node synchronization and subsequent recovery by the Viterbi decoder may cause a deletion or insertion of a bit into the data stream entering the Reed-Solomon decoder. When this occurs, Reed-Solomon symbol and word synch will be lost. In the proposed EEIS packet telemetry scheme a node synch failure could result in a loss of over 8000 information bits. Consequently, the sensitivity of the concatenated coding to node synchronization losses is potentially greater than that of convolutional coding alone.

The effects of carrier, subcarrier, symbol, and bit tracking in the system are also important to the overall performance of the coded channel since poor tracking increases the number of Viterbi decoder bit errors.

The strict error rate requirements of data compression are a major reason for investigation concatenated coding schemes. These requirements stem from the removal of redundant information, hence compression. As an example, one of the data compression schemes under consideration (Ref. 7) reduces the number of bits per picture by over one half without loss of information. The reconstructed compressed data, however, are more sensitive to transmission errors than the original data. Hence error correcting coding schemes must be used. Notice that the concatenated schemes described in this article more than double the number of bits that are transmitted per information bit. This seems to neutralize the useful effects of data compression. Actually, this is not the case since an SNR of 9.5 dB would be required if no coding were employed to achieve an error rate of 10^{-5} (see Fig. 2), whereas the concatenated scheme with the (7, 1/2) inner code requires only 2.3 dB, and only 1.6 dB is required when the (10, 1/3) inner code is used. It might be beneficial to consolidate data compression and channel coding into a one-step process.

References

1. McEliece, R. J., The Theory of Information and Coding, Addison-Wesley, London, 1977.

2. Layland, J. W., "Information Systems: Performance of Short Constraint Length Convolutional Codes and a Heuristic Code-Construction Algorithm," *JPL Space Program Summary 37-64*, Vol. II, August, 1970.

3. Heller, J. A., and Jacobs, I. M., "Viterbi Decoding for Satellite and Space Communications," *IEEE Trans. Comm. Tech.*, Vol. COM-19, part II, pp. 835-848, October, 1971.

4. Odenwalder, J. P., "Concatenated Reed-Solomon/Viterbi Channel Coding for Advanced Planetary Missions: Analysis, Simulations, and Tests," Submitted to the Jet Propulsion Laboratory by Linkabit Corp., San Diego, California, Contract No. 953866, December, 1974.

5 Butman, S. A., and McEliece, R. J., "The Ultimate Limits of Binary Coding for a Wideband Gaussian Channel," in *The Deep Space Network Progress Report 42-22*, pp. 78-80, May and June, 1974.

6. Hooke, A. J., "Multimission Packet Telemetry Guidelines and Standards for Deep Space Missions," JPL document 663-9, November 1979 (internal document).

7. Rice, R. F., and Plaunt, J. R., "Adaptive Variable Length Coding of Spacecraft Television Data," *IEEE Trans. Commun. Tech.*, Vol COM-19, part I, pp. 889-897, December, 1971.

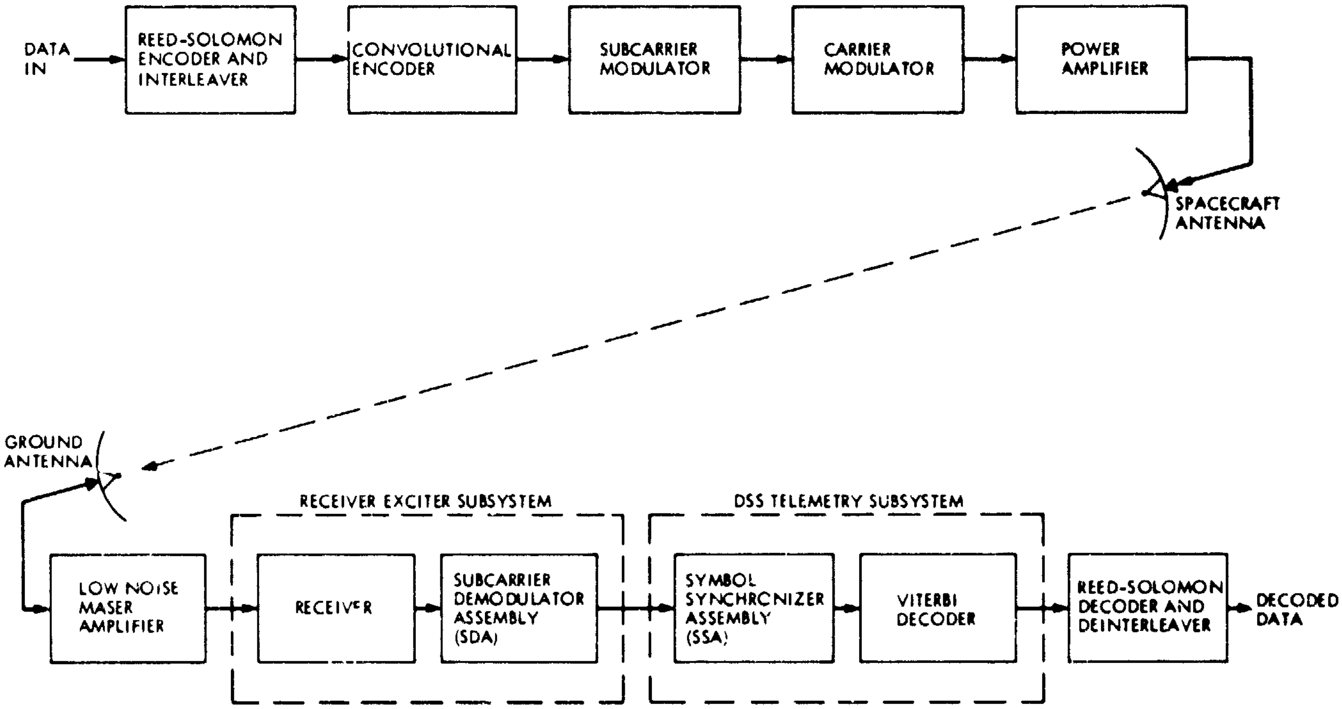

Fig. 1. The concatenated coding system

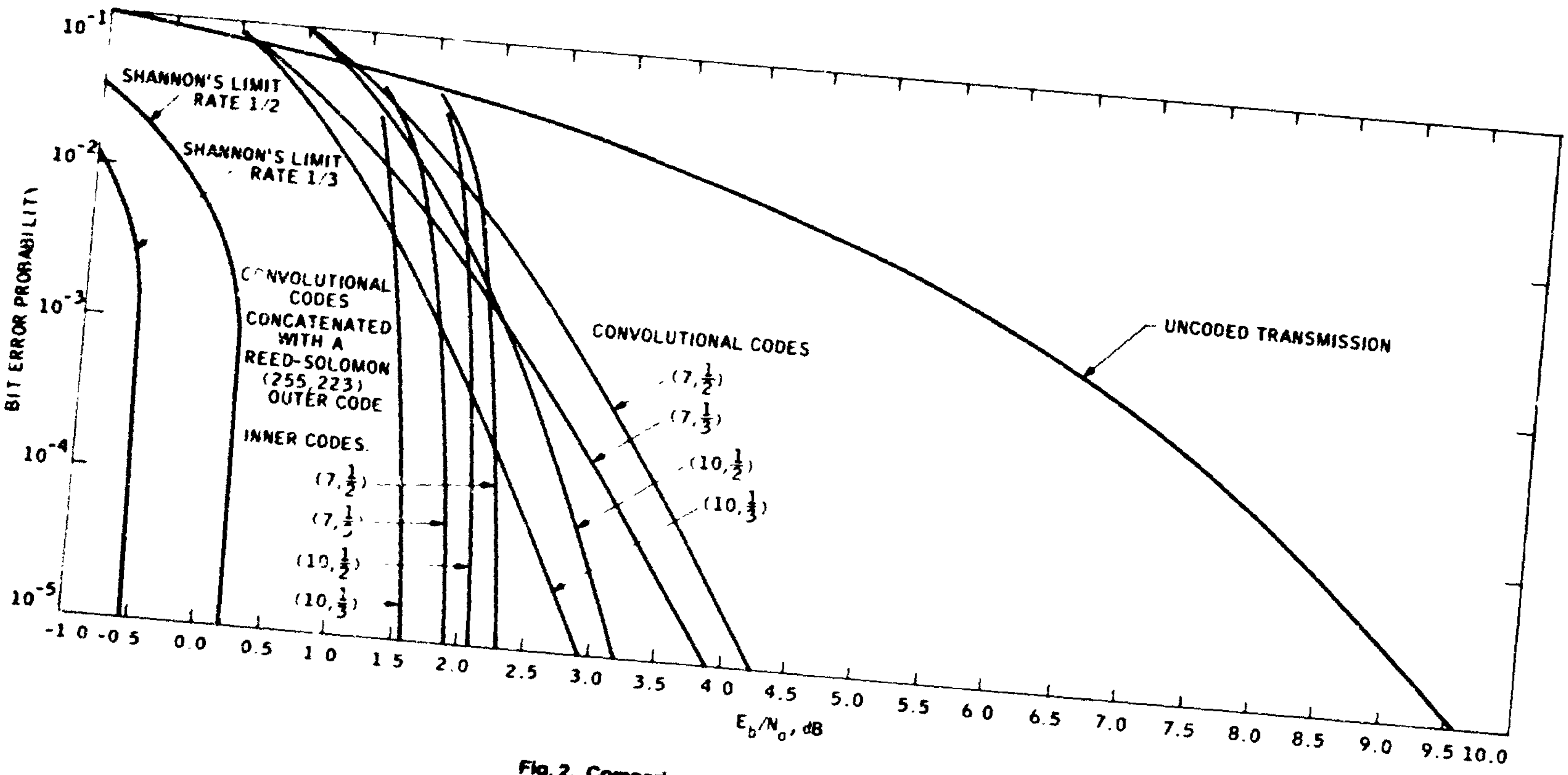

Fig. 2. Comparison of several coding schemes

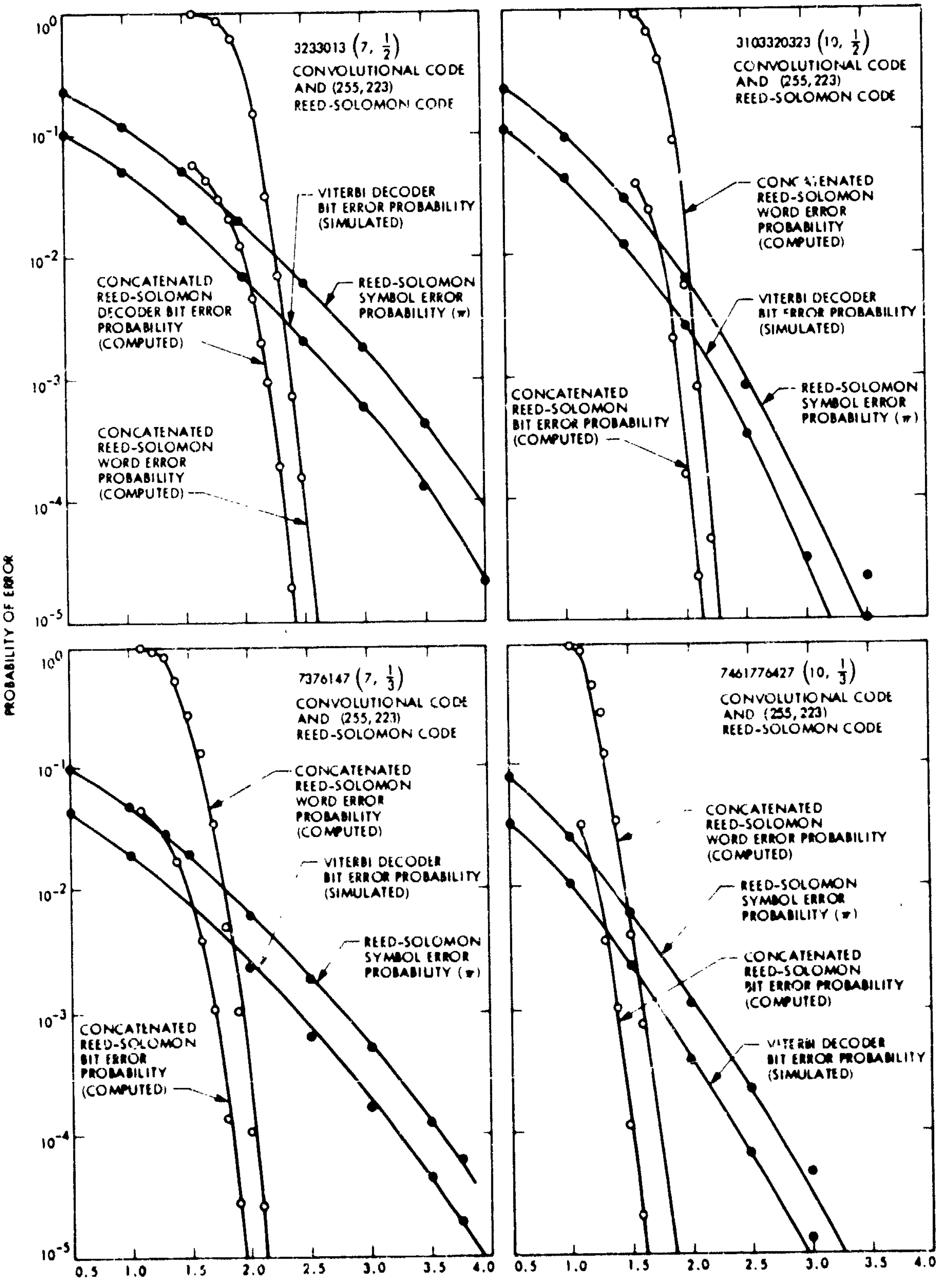

Fig. 3. Performance statistics for ideally interleaved concatenated coding scheme, assuming no system losses

D9

N81-27132

TDA Progress Report 42-63

March and April 1981

High Power Semiconductor Lasers for Deep Space Communications

J. Katz
Communications Systems Research Section

The parameters of semiconductor lasers pertaining to their application as optical emitters for deep space communications are discussed. Several methods to overcome their basic disadvantage, which is the low level of powers they emit, are reviewed. Most of these methods are based on a coherent power combining of several lasers.

I. Introduction

The DSN is currently considering optical frequencies for far deep space communications. In (Ref. 1) it was shown that optical wavelengths in the 0.85 μm region appear to be the most desirable, primarily due to the facts that quantum detectors exist for such wavelengths and the optical signals can be generated by AlGaAs semiconductor injection lasers. It is the purpose of this report to present the basic operational characteristics of semiconductor injection lasers, discuss their basic limitation, namely, the low power levels that they emit, and finally, to outline various possible methods to mitigate this problem. For reference purposes, three tables are given in the Appendix which list the semiconductor laser devices that are commercially available today. Further details on semiconductor lasers can be found in one of the following textbooks (Refs. 2-4).

II. Advantages and Disadvantages of Semiconductor Laser Devices

Semiconductor injection lasers have many inherent advantages, which loom significantly in our application. First, they have a high overall efficiency. An efficiency of 35 percent was demonstrated for a particular device at room temperature (Ref. 5), and efficiencies of over 20 percent can be expected for most device structures. Furthermore, an additional improvement can be expected at lower temperatures (see next section).

Semiconductor lasers are also small in size, rugged and reliable solid state devices. Projected room temperature operation lifetimes exceeding 10^5 hours have been demonstrated (Refs. 6 and 7). Finally, semiconductor lasers can be easily and directly modulated at high rates up to the GHz region (Ref. 8).

The primary drawback of these types of lasers is that a single laser cannot supply the amount of optical power needed for far deep space communication. For this reason, combined operation of several lasers must be accomplished. This topic will be discussed in Section IV of this article.

Semiconductor laser operation has been demonstrated in many atomic systems. Among these, lasers based on the (Al,Ga)As system are an attractive choice because the technology of this system is the most mature, compared to other candidates. These lasers emit their radiation in the 0.8-0.9 μm (near IR) region.

Other current research is conducted mainly in systems which produce lasers with longer wavelengths (1.3-1.5 μm). Such wavelengths are optimum for fiber-optic communication, but not for space applications, where shorter wavelengths are desirable because of their smaller beam divergence.

III. Operational Parameters of Semiconductor Injection Lasers

A semiconductor injection laser is basically a p-n diode where the dominant recombination process is radiative, thus enabling under the conditions of high injection (necessary for sufficient population inversion) and optical feedback a laser operation. The population inversion is established directly via the current passing through the device, and the optical feedback is usually supplied by the mirrors formed naturally by the cleavage planes of the semiconductor crystal itself. A schematic view of an injection laser is shown in Fig. 1

The most important characteristic of the injection laser is the light vs current (L-I) curve. A typical curve for a good laser is shown in Fig. 2. The important parameters shown in this figure are:

(1) I_{th} threshold current. Below this current the light output consists of multimode, incoherent and weak spontaneous emission. For currents above I_{th}, lasing occurs

(2) I_{max} Maximum amount of light that can be extracted from the laser before a failure occurs.

(3) $\eta_d = (e\lambda/hc)(\Delta L/\Delta I)$ differential quantum efficiency (e is the electron charge, λ is the emission wavelength, h is Planck's constant and c is the velocity of light). Values exceeding 30 percent per facet have been achieved (Refs. 9-13)

The overall operational efficiency of the laser at an operating point (I,L) is

$$\eta = \frac{\eta_d}{2}\left(1 - \frac{I_{th}}{I}\right) \qquad (1)$$

The factor of 1/2 is due to the fact that in most applications, light from only one of the two laser facets is utilized. Ohmic losses in the contacts of the diodes have not been included in Eq. (1).

In the following paragraphs, some of the laser parameters will be described in more detail.

A. Threshold Current (I_{th})

For commonly used heterojunction lasers (see below), the threshold current density (J_{th}) ranges from about 1-3 KA/cm^2 at room temperature (depending on the laser type), leading to threshold currents of few tens to a few hundreds of milliamperes for typical device dimensions. The formula for calculating J_{th} can be found in (Ref. 3). An important feature of I_{th} is its rather strong dependence on temperature. As the laser temperature is decreased (by ΔT) the threshold current is reduced, according to (approximately) exp [$-\Delta T/T_0$](T_0 ~120° K), thus increasing the overall device efficiency. (It is worth mentioning that there is also a ten-fold improvement in reliability for every 30° K cooling). This property of semiconductor lasers is an added advantage, since in deep space missions it is possible to cool the optical emitter passively (i.e., without investing power) down to temperatures of about 120° K.

B. Limitations on the Power Output

The maximum power that can be reliably extracted from a laser diode depends both on the type of laser (with cleaved mirrors or distributed feedback) and on the mode of operation (pulsed or CW).

For lasers with cleaved mirrors (which are the most commonly used), the ultimate limit in pulsed operation is reached when the light intensity at the laser facet exceeds a certain limit. This failure mechanism, known as catastrophic degradation, is somewhat analogous to dielectric breakdown. The light intensity at the failure is about 10 MW/cm^2 although this value depends inversely on the square root of the pulse width (Ref. 2). Special laser structures (Ref. 14), (Ref. 15), or special laser coating (Ref. 16), have been demonstrated where the catastrophic damage occurs at much higher intensities. The catastrophic degradation limit may be a function of the operating temperature, but this dependence is as yet unknown. As an example, assume that the safe working limit of a specific device is 5 MW/cm^2. Then, an emitting area of 200 (μm)^2 is needed to achieve a peak power of 10 watts.

When the laser is operated in a CW fashion, which is not likely to be the case in our application, the limiting factor is usually due to thermal effects. This limit is lower than the catastrophic damage limit (e.g., 10 mW for CW operation vs ~100 mW for pulsed operation).

As a final remark, we should mention that for lasers without mirror feedback (e.g., Distributed Feedback (DFB) and Distributed Bragg Reflector (DBR) lasers), the limiting mechanism is not known. The ultimate limit—the dielectric breakdown of the material—occurs above 1 W/$(\mu m)^2$, which is about one to two orders of magnitude higher than the catastrophic facet damage. It is possible, however, that other mechanisms will prevent one from achieving this limit. Although mirrorless lasers are more amenable to integration, they usually have a higher threshold current and a lower differential quantum efficiency than the ones with cleaved mirrors. Thus lasers without mirror feedback are less attractive for our application, although their possible application must not be completely ruled out.

C. Radiation Pattern of a Laser

Due to the small dimensions of the laser active region cross-section, the light output is emitted into a large solid angle: up to 50° in a direction perpendicular to the junction plane and about 10° in the direction of the junction plane. This large angle can interfere with subsequent efficient light processing (collimating, etc.).

D. Single Spatial Mode Operation

For deep space applications one needs more power than a single laser diode can supply. We have seen before that the limiting device parameter is the light intensity at the laser facet. One could ask why is it not possible to get higher power levels simply by increasing the cross-section area of the device active region. The answer is that this is not a good solution since by doing so, the active region cross-section dimensions become much larger than the radiation wavelength ($\sim 0.9\ \mu$), and such a structure cannot support a stable radiation pattern. Thus, the use of a single large emitting area would cause the transmitted beam to vary spatially in an unpredictable fashion, a situation which is unacceptable for deep space applications. Possible methods to overcome this problem are discussed in the next section.

IV. Possible Approaches for Obtaining High Power Semiconductor Laser Emitters

It has been noted that a single commercially available semiconductor injection laser, operating in the fundamental transverse mode, can deliver a few milliwatts in a CW operation, and at the most, a few hundred milliwatts in pulsed operation. This amount of power is far below that needed for space communications, which is about 1 W average power and with peak powers as large as possible.

There are several approaches to partly or totally overcome this problem, as outlined in the following.

A. Optimization of the Parameters of Single Laser Diodes

This is done by modifying the cross-section shape of the active region, which results in a better mode selection (Refs. 17 and 18). By using this approach, it seems feasible to obtain devices that maintain a single mode behavior up to power levels of 100 mW.

B. Phase Locking of Several Lasers by Placing Them in a Common External Cavity

The cavity includes optical elements which cross-couple the radiation fields of the individual lasers. Under certain conditions, the amount of coupling is sufficient to obtain phase-locking (Refs. 19 and 20). An example of such a device is shown in Fig. 3.

The disadvantages of this method are that it relies heavily on mechanical structures, which makes it inherently less stable, and it is larger in size. The advantage of such a structure, however, is that the powers of individual diodes can be combined coherently, thus providing a more finely defined radiation beam. This is similar to the fine pointing characteristics of phased arrays.

C. Monolithic Phase Locking: One Dimensional Array

In this method the power of several lasers is also combined coherently. However, unlike the last method, in this scheme all the lasers are grown monolithically on a common substrate, and all the lasers in this array are electrically operated in parallel (Refs. 21–24). In this case, the coupling mechanism leading to phase locking is achieved via overlapping the electromagnetic fields of adjacent lasers. To achieve this, the lasers must be in close proximity ($\leqslant 10\ \mu$) to one another. With such a device, there is no need for an external cavity. This method has been used to produce devices consisting of 10 phase locked diodes and which are capable of delivering up to 900 mW of peak power in 100 ns 1 percent duty cycle pulses.

D. Monolithic Phase Locking: Two Dimensional Array

In this method, each laser diode in the parallel monolithic array described above is replaced by either a vertical combination of several diode lasers (Fig. 5), or by a laser diode that can emit higher power levels (for example, diodes of the types described in paragraph A. of this section). Operation of a device with a vertical combination of several active regions has already been demonstrated (Ref. 25). Basic potential problems expected in the fabrication and operation of a two-dimensional array are maintaining the uniformity of the emitted radiation patterns and the coupling required for locking, as well as the removal of heat generated within the device structure.

E. Hybrid Device

Hybrid combinations of the above approaches have also been recently suggested (Ref. 26). The proposed device would consist of many injection lasers put on a common substrate in a common DBR resonator which supplies the cross-coupling between the lasers (see Fig. 6). The proposed device is expected to emit 0.1 - 1 W average power from an emitting area of about 10 mm^2.

V. Conclusion

The basic properties of semiconductor injection lasers were described and their advantages discussed. The primary disadvantage of these devices (i.e., low single spatial mode output power) was then identified and several methods for overcoming this limitation were discussed. The technologies for solving the power limited emitter problem are just now emerging, but with so many independent approaches in progress, one can be quite confident that commercial devices capable of delivering the requisite power will soon be available.

References

1. Katz, J., and Lesh, J. "Optical Communication for Deep Space Missions Using Integrated Semiconductor Injection Lasers," Technical Report (in preparation), Jet Propulsion Laboratory, Pasadena, Calif.
2. Kressel, H., and Butler, J. K., *Semiconductor Lasers and Heterostructure Leds*, Academic Press, 1977.
3. Casey, Jr., H. C., and Panish, M. B., *Heterostructure Lasers*, Academic Press, New York, 1978.
4. Thompson, G. H. B., *Physics of Semiconductor Laser Devices*, Wiley Interscience, Chichester, 1980.
5. Chinone, N., et al, "Highly Efficient (GaAl)As Buried Heterostructure Lasers with Buried Optical Guide," *Appl Phys. Lett.* 35, pp. 513-516, Oct. 1, 1979.
6. Hartman, R. L., Schumaker, N. E., and Dixon, R. W., "Continuously Operated (Al,Ga)As Double-Heterostructure Lasers with 70°C Lifetimes as Long as Two Years," *Appl. Phys. Lett.* 31, pp. 756-759, Dec. 1, 1977.
7. Nita, S., Namizaki, H., Takamiya, S., and Sugaki, W., "Single Mode Junction-Up TJS Lasers with Estimated Lifetime of 10^6 Hours," *IEEE J. Quant. Electron.* QE-15, pp. 1208-1209, 1979.
8. Arnold G., and Russer, P., "Modulation Behavior of Semiconductor Injection Lasers," *Appl. Phys.* 14, pp. 255-268, 1977.
9. Tsang, W. T., and Logan, R. A., "GaAs-Al$_x$Ga$_{1-x}$As Strip Buried Heterostructure Lasers," *IEEE J. Quant. Electron.* QE-15, pp. 451-469, June 1979.
10. Aiki, K., et al, "Transverse Mode Stabilized Al$_x$Ga$_{1-x}$As Injection Laser with Channeled-Substrate-Planar Structure," *IEEE J. Quant. Electron.* QE-14, pp. 89-94, Feb. 1978.

11. Burnham, R. D., and Scifres, R., "Etched Buried Heterostructure GaAs/GaAlAs Injection Lasers," *Appl. Phys. Lett.* 27, pp. 510-511, Nov. 1, 1975.

12. Wittke, J. P., and Laddany, I., "Lateral Mode Selection in Semiconductor Injection Lasers," *J. Appl. Phys.* 48, pp. 3122-3124, July 1977.

13. Tsang, W. T., and Logan, R. A., "Lateral Current Confinement by Reverse-Biased Junctions in GaAs-$Al_xGa_{1-x}As$ DH Lasers," *Appl Phys. Lett.* 30, pp. 538-540, May 15, 1977.

14. Yonezu, H. O., Veno, M., Kamejima, T., and Hayashi, I., "An AlGaAs Window Structure Laser," *IEEE J. Quant. Electron.* QE-15, pp. 775-781, 1979.

15. Takamiya, S., et al, "One Order Power Improvement of Single Mode TJS Laser Diodes by Crank Structure," in the *7th IEEE Intl. Semicond. Laser Conf.*, (Paper P8).

16. Namizaki, H., Takamiya, S., Ishii, M., and Susaki, W., "High-Power-Density Single Mode Operation of GaAs-GaAlAs TJS Lasers Utilizing Si_3N_4 Plasma Deposition for Facet Coating," *J Appl. Phys* 50, pp. 3743-3745, 1979.

17. Botez, D., "CW High Power Single Mode Operation of Constricted Double Heterojunction AlGaAs Laser with a Large Optical Cavity," *Appl Phys Lett.* 36, pp 190-192, 1980; Botez, D, Butler, J K., and Connolly, J. C., "Mode Control in High-Power CDH-LOC Diode Lasers the W-Shaped Lateral Waveguide," in the *3rd Intl. Conf. Integrated Optics and Optical Fiber Commun.*, (Paper MB-5), 1981

18. Streifer, W., Scifres, D. R., and Burnham, R D., "Above Threshold Analysis of Double-Heterostructure Diode Lasers with Laterally Tapered Active Regions," *Appl Phys Lett* 37, pp 877-879, 1980

19 Crowe, J W, "External Cavity Coupling and Phase Locking of Gallium Arsenide Injection Lasers," *IEEE J. Quant Electron.* QE-4, pp. 169-174, Apr. 1968.

20 Philipp-Rutz, E. M., "Single Laser Beam of Spatial Coherence from an Array of GaAs Lasers Free Running Mode," *J Appl. Phys 46*, pp. 4552-4556, Oct. 1975

21. Scifres, D. R., Streifer, W., and Burnham, R D, "High-Power Coupled-Multiple-Stripe Phase-Locked Injection Laser," *Appl. Phys Lett 34*, pp. 259-261, Feb. 15, 1979.

22. Ripper, J. E, and Paoli, T. L., "Optical Coupling of Adjacent Stripe-Geometry Junction Lasers," *Appl. Phys Lett 17*, pp. 371-373, Nov 1, 1970.

23. Scifres, D. R., Burnham, R. D., and Streifer, W., "Phase-Locked Semiconductor Laser Array," *Appl. Phys. Lett 33*, pp 1015-1017, Dec. 15, 1978.

24. Tsang, W. T., Logan, R. A., and Salathe, R P., "A Densely Packed Monolithic Linear Array of GaAs-$Al_xGa_{1-x}As$ Strip Buried Heterostructure Laser," *Appl Phys. Lett. 34*, pp. 162-165, Jan. 15, 1979

25. Katz, J., Bar-Chaim, N., Margalit, S., and Yariv, A., "Large Optical Cavity AlGaAs Injection Lasers with Multiple Active Regions," *J. Appl Phys* 51, pp 4038-4041, 1980.

26. Evans, G A., et al, "Progress Toward a Monolithically integrated Coherent Diode Laser Array," (Interim report prepared by the Aerospace Corporation under Contract F04701-79-C-0080).

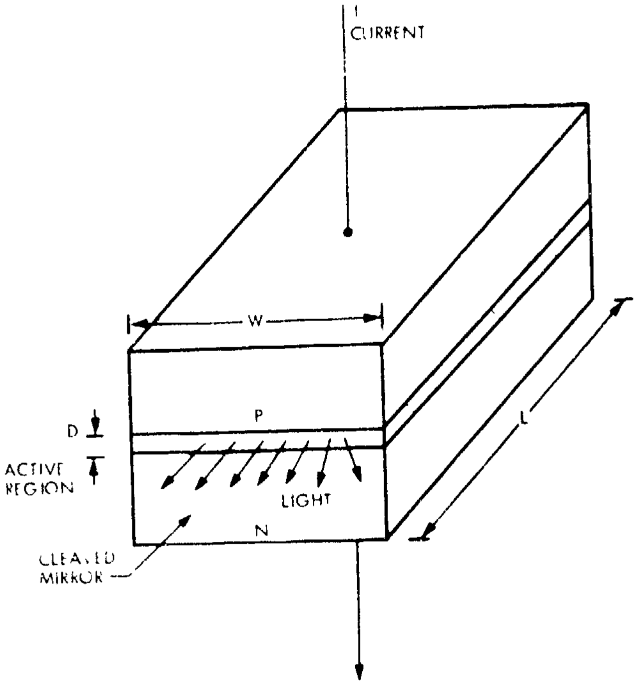

Fig. 1. Schematic view of an injection laser

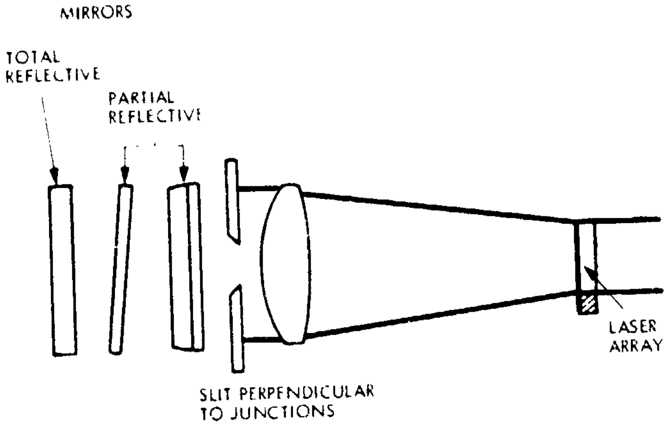

Fig. 3. Locking of discrete devices with external optical cavity (Adapted from Fig. 4 in Ref. 19)

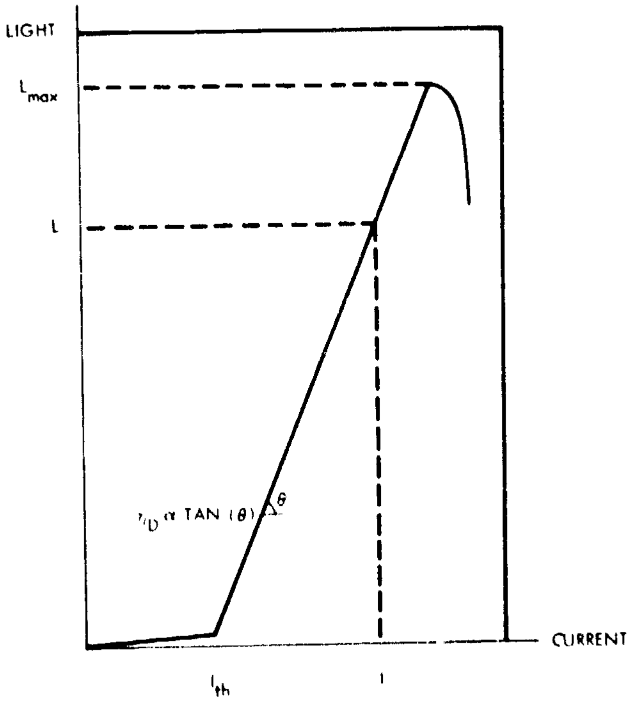

Fig. 2. Light-current curve of an injection laser

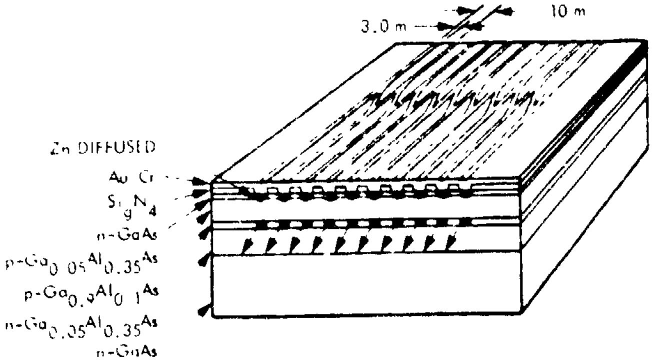

Fig. 4. High-power phase locked injection laser array (Fig. 1 in Ref. 21)

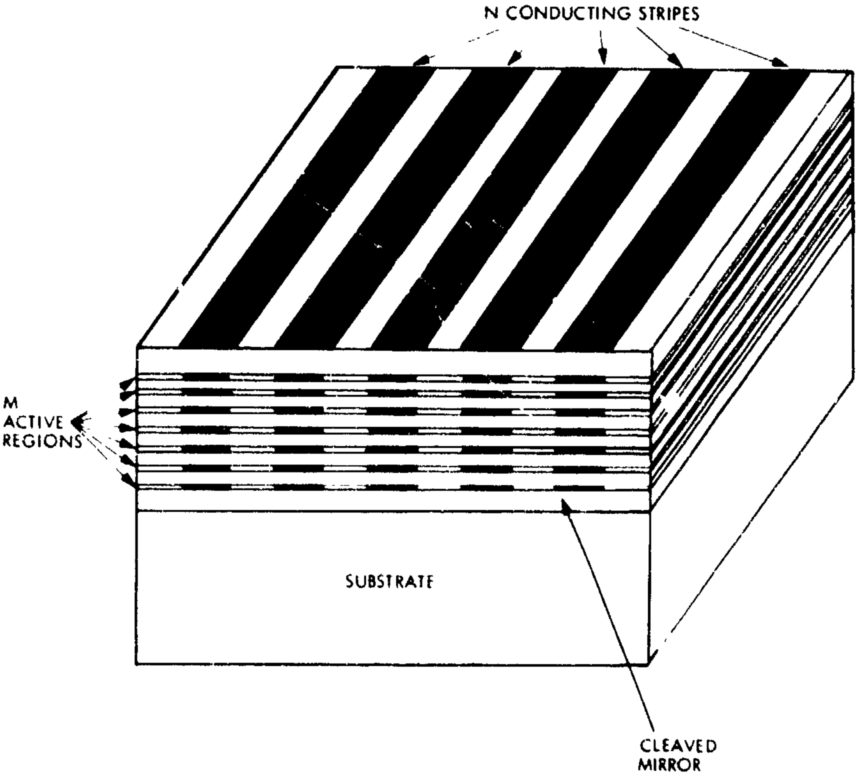

Fig. 5. Schematic view of proposed two-dimensional phase-locked laser array

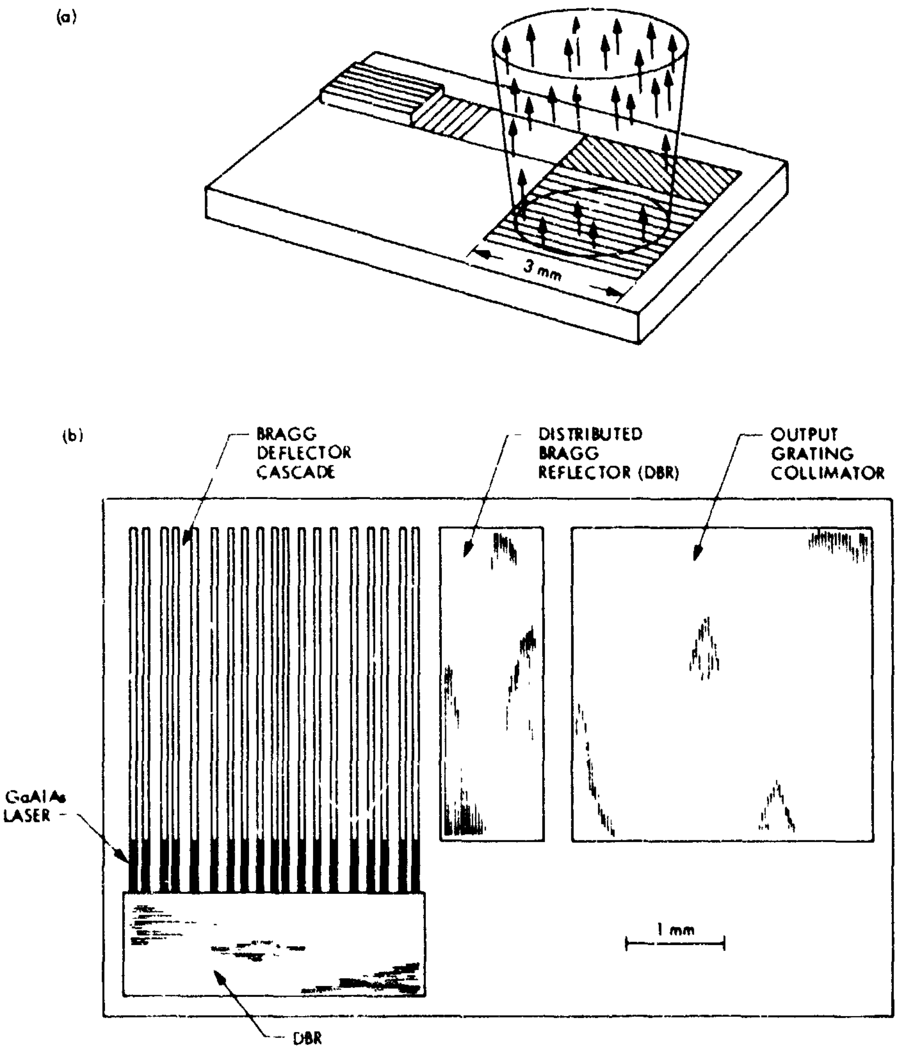

Fig. 6. High brightness GaAs laser array: (a) Schematic view, (b) Top view and details of the structure from Ref. 26

Appendix

Devices Available on the Market

The next three tables summarize the parameters of GaAlAs lasers and laser arrays that are available on the market. Table A-1 lists double heterostructure diodes, which have high reliability and operate at low power levels. Table A-2 lists diodes intended for high peak power pulsed operation. These diodes have lower reliability and less controlled beam pattern. Table A-3 lists laser arrays, made of diodes of the type listed in Table A-2. In each table, only the best device in each category of each manufacturer is listed.

Table A-1. AlGaAs injection lasers: CW low power double heterostructure diodes (available on the market, March 1981)

Company	Country	Model	Type	Nominal Output Power [mW]	Operating Electrical Power [mW]	Power Efficiency %	Single Transverse Mode	Source Size [μ^2]	Beam Divergence [deg^2]
Hitachi	Japan	HLP3000	Buried Optical Guide	6	81	7.4	Yes		20 × 35
LDI	U.S.	SCW-20	CSP	7.5	170	4.4	Yes	0.2 × 7	10 × 35
Mitsubishi	Japan	ML-2200	TJS	3	72	4.1	Yes	0.4 × 2	10 × 40
RCA	U.S.	C86014E	Double Dovetail	7	200	3.5	Yes	2 × 6	
General Optronics	U.S.	GOLS	Proton Bombardment	5	200	2.5	Yes		10 × 45
Exxon/OIS	U.S.	OL3150Z		5	220	2.3	Yes	1 × 12	20 × 45
ITT	U.K.	LS7737		7	320	2.2	Yes		
		LS7735	Broad Area-DH	20	360	5.5	No		

Table A-2. AlGaAs injection lasers: pulsed, high peak power diodes (available on the market, March 1981)

Company	Country	Model	Type	Nominal Peak Output Power [W]	Duty Cycle (max) %	Power Efficiency %	Source Size [μm²]
LDI	U.S.	LD 68	Single Hetero-Structure	20	0.1	3.3	2 × 400
RCA	U.S.	SG 2012	Single Hetero-Structure	20	0.1	1.7	2 × 600
ITT	U.K.	LA 15	Single Hetero-Structure	15	0.2	1.9	2 × 230
		LB 1	Double Hetero-Structure	0.2	15	4.4	0.5 × 100

Table A-3. AlGaAs injection laser arrays (available on the market, March 1981)

Company	Country	Model	No. of Diodes	Nominal Peak Output Power [W]	Duty Cycle (max) %	Power Efficiency %	Source Size [μm²]	Remarks
LDI	U.S.	LA 410	120	1000	0.01	3	3900 × 4600	
		MH 167	5	80	0.03	5	400 × 400	
		LDI 167	5	80	0.04	4	500 × 500	Array with fiber integrator
RCA	U.S.	C 30042	6	100	0.01		500 × 500	
		C 30009	60	300	0.02	3	1500 × 4000	
ITT	U.K.	LS 7728	40	300		3	500 × 3800	

D10

N81-27133

TDA Progress Report 42-63

March and April 1981

Capacity of a Multimode Direct Detection Optical Communication Channel

H. H. Tan
(Consultant from University of California at Irvine)
Communications Systems Research Section

The capacity of a free-space optical channel with received background noise using a multimode direct detection receiver is derived under both peak and average signal power constraints and without a signal bandwidth constraint. A random telegraph wave type signalling scheme of Kabanov is shown to achieve capacity provided enough signalling bandwidth is available. In the absence of received background noise, an optimally coded PPM system is shown to achieve capacity with greatly reduced bandwidth as compared to Kabanov signals.

I. Introduction

There has been considerable research on optical communication systems in recent years. In particular there is considerable interest (Refs. 1-6) in determining the channel capacity or the maximum theoretically attainable information rate at which reliable communication is possible over optical channels. This article is concerned with the channel capacity of a free-space optical communication system. The reliability of such channels is affected by the quantum mechanical limitations on the measurement of the received optical field as well as the presence of noise in the received field. In addition the channel capacity depends on the particular type of receiver employed — for example, coherent linear amplifier receivers, heterodyne receivers, homodyne receivers and direct detection receivers. Furthermore, constraints imposed on the allowable transmitted signal power also affect the available channel capacity.

In order to put the results of this paper in proper perspective, we briefly review related work. Gordon's benchmark work (Ref. 1) gave the ultimate capacity of any free-space optical communication system under an average signal power constraint. This value of channel capacity determined by Gordon (Ref. 1) places no limitation on the receiver employed other than the quantum mechanical limitation on the accuracy of measurement of the received optical field and the presence of additive noise in the received field. Hence it represents the maximum reliable information rate that can be attained by any system. The importance of this result notwithstanding, the channel capacity with specified receiver structures is also of interest. Gordon (Ref. 1) has obtained the channel capacity using coherent amplification, heterodyne and homodyne receivers respectively. These channel capacities are substantially less than the ultimate channel capacity

We are concerned here with determining the channel capacity using a direct detection or photon counting receiver. In direct detection systems, the photon counter output can be modeled by a Poisson process with a stochastic intensity rate function (Refs. 8 10, 17). The stochastic intensity rate process describes the average rate at which photoelectrons are generated by the detector. It contains stochastic signal and stochastic noise components. The noise component in the stochastic intensity rate process arises because of the background noise observed in the receiver's field of view and can be modeled by a Gaussian white noise process (Refs. 8, 17). However, for the purpose of determining channel capacity, this Poisson model does not appear to be tractable without further simplifying assumptions. This is because of the difficulty in dealing with the Gaussian white noise component in the stochastic intensity rate process of the Poisson process. This problem is of course not present in situations of negligible background noise, thus removing the Gaussian white noise component from the stochastic intensity rate process model. This is the situation considered for example in Refs. 3-5, where the channel capacity is obtained under various signal power constraints and signal modulation constraints.

We are concerned here with the situation when the background noise cannot be neglected. Suppose also that the receiver either observes many spatial modes (i.e., a large field of view) and/or many temporal modes exist (i.e., the signal bandwidth is much smaller than the receiver's optical bandwidth) (Ref. 17). Then the stochastic photon arrival rate due to the background noise can be replaced by its expected value (Ref. 17). This is the situation considered here. Kabanov (Ref. 6) has previously derived the channel capacity in this situation under a peak signal power constraint. We shall extend his results by considering simultaneously a peak and an average signal power constraint. Finally, consider the other situation of a small number of spatial and temporal modes. This is the situation of a small field of view at the receiver and signal bandwidths approaching the optical bandwidth of the receiver. In this case Pierce et al. (Ref. 18) have determined the channel capacity.

Summarizing, this article is concerned with a free-space optical communication system using a direct detection receiver. It is assumed that the receiver either observes a large number of spatial modes and/or a large number of temporal modes. This is generally called a multimode direct detection system. The main result of this article (Theorem 1, Section II) gives the average and peak power constrained channel capacity in this situation. The derivation of this theorem is given in Section III. A random telegraph wave type signalling scheme due to Kabanov (Ref. 6) is shown to achieve capacity provided that sufficient signalling bandwidth is available. Finally, in the case of no background noise, it is shown in Section IV that the channel capacity can be achieved using *M*-ary pulse position modulation (PPM) along with coding, provided that sufficient signalling bandwidth is available. It is also shown that the coded PPM signalling scheme achieves capacity with a greatly reduced bandwidth as compared to the Kabanov signalling scheme.

II. Channel Capacity

Consider an optical channel using an intensity modulated light source transmitter and a multimode direct detection receiver with an ideal photodetector. The transmission medium is assumed to be free space so that no degradation other than a geometric power loss is imparted on the transmitted light beam. The receiver light power at the photodetector is assumed to be weak (Ref. 7) so that the photodetector current output can be characterized by the sequence of time instants of the photon absorption photoelectron emission process of the photodetector. We can then model the photodetector output in terms of a counting process $\{N(t),\ t \geq 0\}$ where $N(t)$ = number of photoelectron emission events in $(0, t)$. Hence this type of receiver is often called a "photon counter." It has been shown (Refs. 8, 17) that $N(t)$ can be modeled as a conditionally Poisson counting process given the intensity of the received light process at the photodetector. Let $\lambda(t)$ be the instantaneous average rate at which photoelectrons are generated at time t in units of photons per second. We shall assume that $\lambda(t)$ is given by

$$\lambda(t) = \lambda_s(t) + \bar{n} \tag{1}$$

where $\lambda_s(t)$ is the instantaneous average rate at which photoelectrons are generated as a result of the received signal field and $\bar{n}$ is the average rate of photoelectron generation due to the received background noise field and detector dark current. We shall assume that $\bar{n}$ is constant since the receiver is assumed to be multimodal (Ref. 17). Let $\{S(t)\}$ be the information bearing message stochastic process that is transmitted. Since $\lambda_s(t)$ depends on this process $\{S(t)\}$, it is also a stochastic process. In the case where there is instantaneous feedback from the photodetector output to the transmitter, $\lambda_s(t)$ can in addition also depend on $\{N(\tau): 0 \leq \tau < t\}$. In this case $\{N(t)\}$ is referred to as a compound regular point process by Rubin (Ref. 9), who first studied detection problems involving these processes. In the case where there is no feedback link of any kind present, $\lambda_s(t)$ depends only on the external message signal process $\{S(t)\}$. In this case $\{N(t)\}$ is often called a doubly stochastic Poisson process (Ref. 10). In either case, the stochastic process $\{\lambda(t)\}$ given by Eq. (1) is usually called the intensity rate process of the point process $\{N(t)\}$. We shall call $\{\lambda_s(t)\}$ the signal intensity rate process.

The goal of this article is to determine the channel capacity with constraints on the average and the peak received light signal power. Since $\lambda_s(t)$ is directly proportional to the instantaneous received signal power, we shall impose peak and average value constraints on the admissible $\lambda_s(t)$ processes in calculating the channel capacity. In order to define the channel capacity, denote

$$S_T = \{S(t) : 0 \leqslant t \leqslant T\}, \tag{2}$$

$$N_T = \{N(t) : 0 \leqslant t \leqslant T\}, \tag{3}$$

$$\lambda_{sT} = \{\lambda_s(t) : 0 \leqslant t \leqslant T\}, \tag{4}$$

for each $T > 0$. Also let $I(S_T; N_T)$ = average mutual information between S_T and N_T (in units of nats)

For each $0 < \bar{s} \leqslant \bar{p}$, let $\mathscr{C}(\bar{s},\bar{p})$ denote the class of all message processes $\{S(t)\}$ and signal intensity rate processes $\{\lambda_s(t)\}$ satisfying the following conditions.

(a) λ_{sT} is a deterministic function of S_T for each $T > 0$.

(b) $0 \leqslant \lambda_s(t) \leqslant \bar{p}$ (5)

(c) For every $T > 0$,

$$G_T(\lambda_s) \overset{\Delta}{=} \frac{1}{T}\int_0^T E[\lambda_s(t)]\, dt \leqslant \bar{s}. \tag{6}$$

We shall use $\mathscr{C}(\bar{s},\bar{p})$ as the admissible class of message processes and signal intensity rate processes for calculating the channel capacity without feedback. In particular, for each $T > 0$ define

$$C_T(\bar{s},\bar{p}) = \sup_{\{(S(t),\,\lambda_s(t))\} \in \mathscr{C}(\bar{s},\bar{p})} \frac{1}{T} I(S_T; N_T). \tag{7}$$

By definition (Ref. 11),

$$C(\bar{s},\bar{p}) = \lim_{T\to\infty} C_T(\bar{s},\bar{p}) \tag{8}$$

is the channel capacity (in units of nats per second) without feedback under peak power constraint Eq. (5) and average power constraint Eq. (6). It is clear that the maximization in Eq. (7) is over all possible message processes $\{S(t)\}$ and over all possible modulation formats by varying $\lambda_s(t)$. Moreover Eq. (5) limits the received peak signal power and Eq. (6) limits the received average signal power.

Next let $\mathscr{C}_F(\bar{s},\bar{p})$ denote the class of all message processes $\{S(t)\}$ and signal intensity rate processes $\{\lambda_s(t)\}$ satisfying the conditions (b) and (c) above along with the following condition (a′) in place of (a) above:

(a′) λ_{sT} is a deterministic function of S_T and N_T for each $T > 0$

Then $\mathscr{C}_F(\bar{s},\bar{p})$ will be the admissible class of message and signal intensity rate processes used to calculate the channel capacity with feedback. That is, define

$$C_{FT}(\bar{s},\bar{p}) = \sup_{\{(S(t),\,\lambda_s(t))\} \in \mathscr{C}_F(\bar{s},\bar{p})} \frac{1}{T} I(S_T; N_T), \tag{9}$$

for each $T > 0$ and let

$$C_F(\bar{s},\bar{p}) = \lim_{T\to\infty} C_{FT}(\bar{s},\bar{p}). \tag{10}$$

$C_F(\bar{s},\bar{p})$ is the channel capacity (in units of nats per second) with feedback under peak power constraint Eq. (5) and average power constraint Eq. (6). The presence of instantaneous feedback arises through the possible dependence of the modulation format $\lambda_s(t)$ on the photodetector output as given by condition (a′) defining $\mathscr{C}_F(\bar{s},\bar{p})$. The following theorem gives an expression for $C(\bar{s},\bar{p})$ and also shows that $C(\bar{s},\bar{p}) = C_F(\bar{s},\bar{p})$. That is, the use of instantaneous noiseless feedback does not increase channel capacity. This feedback result is really just a special case of a similar result (Ref. 19) that is valid for all memoryless channels. The Poisson optical channel considered here is also a memoryless channel.

Theorem 1

Let

$$\sigma = \min\left\{\bar{s}, (\bar{p} + \bar{n}) \exp\left[\frac{\bar{n}}{\bar{p}} \log\left(1 + \frac{\bar{p}}{\bar{n}}\right) - 1\right] - \bar{n}\right\} \text{ photons/sec.} \tag{11}$$

Then

$$C_F(\bar{s},\bar{p}) = C(\bar{s},\bar{p})$$

where

$$C(\bar{s},\bar{p}) = \left(1 - \frac{\sigma}{\bar{p}}\right)\bar{n} \log \bar{n} + \left(\frac{\sigma}{\bar{p}}\right)(\bar{p} + \bar{n}) \log(\bar{p} + \bar{n})$$

$$- (\sigma + \bar{n}) \log(\sigma + \bar{n}) \text{ nats/second.} \tag{12}$$

Moreover, in order to achieve channel capacity with or without feedback, the received average signal power must be σ photons/second.

The case when $\bar{n} = 0$ corresponds to the situation where there are no received photons due to extraneous background radiation and when the detector dark current is zero. This situation has received considerable recent attention

(Refs. 3-5). Setting $\bar{n}=0$ in the above theorem yields the following expression for channel capacity in the no background noise case.

Corollary 1

When

$$\bar{n} = 0, C_F(\bar{s},\bar{p}) = C(\bar{s},\bar{p}),$$

where

$$C(s,p) = \sigma \log \frac{\bar{p}}{\sigma} \text{ nats/sec.} \tag{13}$$

and

$$\sigma = \min(\bar{s}, e^{-1}\bar{p}) \text{ photons/sec.} \tag{14}$$

is the received average signal power required to achieve channel capacity.

Since the average received signal power $\bar{s}$ is always less than or equal to the peak received signal power $\bar{p}$, then by setting $\bar{s}=\bar{p}$ we effectively remove the constraint on the average received signal power. That is, $C_F(\bar{p},\bar{p})$ and $C(\bar{p},\bar{p})$ are respectively the peak power constrained channel capacity with feedback and the peak power constrained channel capacity without feedback. Hence we obtain the following corollary.

Corollary 2

Under only a peak received signal power constraint of $\bar{p}$, the channel capacity with feedback is $C_F(\bar{p},\bar{p})$ and the channel capacity without feedback is $C(\bar{p},\bar{p})$. Then $C_F(\bar{p},\bar{p}) = C(\bar{p},\bar{p})$ is given by Eq. (12) with

$$\sigma = (\bar{p}+\bar{n})\exp\left[\frac{\bar{n}}{\bar{p}}\log\left(1+\frac{\bar{p}}{\bar{n}}\right)-1\right]-\bar{n}. \tag{15}$$

Proof

We need only show that $\bar{p} \geqslant \sigma$ given by Eq. (11). This is true because it is clear that

$$\left(\frac{\bar{n}}{\bar{p}}\right)\log\left(1+\frac{\bar{p}}{\bar{n}}\right)-1 \leqslant 0 \tag{16}$$

by using the inequality $\log(1+x) \leqslant x$. Q.E.D.

We note that Kabanov's expression (Ref. 6) for the peak received signal power constrained channel capacity when $\bar{n}=1$ is a special case of Corollary 2.

In most laser communication systems, the available peak signal power is usually substantially greater than the available average signal power. The usual case is that $\bar{p} >> \bar{s}$. It is interesting to note that in contrast to additive Gaussian noise channels (Ref. 13), the primary constraint on the available channel capacity is the available peak signal power, rather than the available average signal power. This can be easily seen from Eqs. (11) and (12) where for a fixed background noise level $\bar{n}$ and fixed available average signal power $\bar{s}$, the channel capacity $C(\bar{s},\bar{p})$ can be made arbitrarily large by making the available peak signal power $\bar{p}$ arbitrarily large. We also note in this regard that constraining only the available peak signal power results in an unrealistically large estimate of the maximum achievable reliable information rate of the channel. This can be seen more readily in the no background noise case ($\bar{n}=0$), where the peak signal power constrained channel capacity is

$$C(\bar{p},\bar{p}) = e^{-1}\bar{p} \text{ nats/sec} \tag{17}$$

and the average and peak signal power constrained capacity is

$$C(\bar{s},\bar{p}) = \bar{s}\log\left(\frac{\bar{p}}{\bar{s}}\right) \text{nats/sec} \tag{18}$$

when $\bar{p} \geqslant e\bar{s}$. So in the usual case when $\bar{p} >> \bar{s} >> 1$, $C(\bar{s},\bar{p})$ is substantially smaller than $C(\bar{p},\bar{p})$. For example, in a deep space optical channel, present technology (Ref. 5) can achieve a system with negligible background noise, $\bar{s} = 10^4$ photons/sec and $\bar{p} = 10^7$ photons/sec. Then $C(\bar{s},\bar{p}) = 6.9 \times 10^4$ nats/sec and $C(\bar{p},\bar{p}) = 3.7 \times 10^6$ nats/sec. We also note from Eq. (13) that in order to achieve $C(\bar{p},\bar{p})$, $\bar{s}$ must be at least $e^{-1}\bar{p}$. In a laser communication system, the available peak signal power must be reduced considerably to attain such a high average to peak signal power ratio. Similar conclusions can be reached in the case where there is background noise present.

The derivation of Eq. (11) and (12) follows Kabanov's approach (Ref. 6) and involves the following two steps:

(1) The first step establishes the formula Eq. (12) as an upper bound on $C_f(\bar{s},\bar{p})$ and so also an upper bound on $C(\bar{s},\bar{p})$.

(2) The second step gives a sequence of message processes

$$\{S_m(t) . 0 \leqslant t \leqslant T\}$$

and signal intensity rate processes

$$\{\lambda_s^{(m)}(t) : 0 \leqslant t \leqslant T\}$$

belonging to $\mathcal{C}'(\bar{s},\bar{p})$ (see Eqs. (48) and (51) in Section III) with average mutual information $I(S_{mT};N_T)$ and demonstrates that $I(S_{mT}, N_T)/T$ converges to Eq. (12) as m tends to infinity. This then proves that the upper bound in Step (1) can be achieved and is equal to $\mathcal{C}(\bar{s},\bar{p})$ and $C_F(\bar{s},\bar{p})$.

The technical details involved in these two steps are discussed in the next section of this article.

The optical signalling bandwidth of this photon counting optical communication system can be taken to be the bandwidth of the signal intensity rate process. Section IV of this article investigates the optical signalling bandwidth required to achieve channel capacity. The bandwidth of the signal intensity rate process $\{\lambda_s^{(m)}(t)\}$ used in Step (2) above to achieve channel capacity is determined and is shown to be unbounded as m tends to infinity. Thus the formula Eq. (12) is the channel capacity without bandwidth constraint. The rate at which the bandwidth of $\{\lambda_s^{(m)}(t)\}$ increases as capacity is approached is also derived. In the case where there is no background noise, an optimally coded pulse-position modulation (PPM) system is shown to be capable of achieving channel capacity at a reduced bandwidth as compared to the signalling scheme used in Step (2). The reader who is more interested in these results than the involved technical details in Section III can skip that section and go directly to Section IV without essential loss of continuity. Section V relates the results of this article to previous work.

III. Derivation of Channel Capacity

We first carry out Step (1) to establish that Eq. (12) is an upper bound on $C_F(\bar{s},\bar{p})$ and hence also an upper bound on $\mathcal{C}(\bar{s},\bar{p})$ since $\mathcal{C}(\bar{s},\bar{p}) \leqslant C_F(\bar{s},\bar{p})$. In order to examine Eqs. (6) and (7) we must use the following formula for the average mutual information, which is valid for all $\{(S(t), \lambda_s(t))\}$ in $\mathcal{C}'_F(\bar{s},\bar{p})$:

$$I(S_T;N_T) = \int_0^T \{E[(\lambda_s(t)+\bar{n})\log(\lambda_s(t)+\bar{n})] - E[(\hat{\lambda}_s(t)+\bar{n})\log(\hat{\lambda}_s(t)+\bar{n})]\}\,dt \tag{19}$$

where

$$\hat{\lambda}_s(t) = E[\lambda_s(t)|N_t] \tag{20}$$

is the conditional mean estimator of $\lambda_s(t)$ given observations $N_t = \{N(\tau) : 0 \leqslant \tau \leqslant t\}$. The formula Eq. (19) is given in Ref. 12. We provide a formal derivation of Eq. (19) in Appendix A for completeness. Note from Eq. (20) that $I(S_T; N_T)$ depends on S_T only through λ_{sT}. So denote

$$I(S_T;N_T) \overset{\Delta}{=} I(\lambda_{sT}). \tag{21}$$

Note that since the function $f(x) = x \log x$ is convex, Jensen's inequality gives

$$\begin{aligned} & E[(\hat{\lambda}_s(t)+\bar{n})\log(\hat{\lambda}_s(t)+\bar{n})] \\ \geqslant\ & [E(\hat{\lambda}_s(t)+\bar{n})]\log[E(\hat{\lambda}_s(t)+\bar{n})] \\ =\ & [E(\lambda_s(t)+\bar{n})]\log[E(\lambda_s(t)+\bar{n})], \end{aligned} \tag{22}$$

the last equality following since $E[\hat{\lambda}_s(t)] = E\{E[\lambda_s(t)|N_t]\} = E[\lambda_s(t)]$. Hence Eqs. (19) and (22) yield

$$\begin{aligned} I(\lambda_{sT}) \leqslant & \int_0^T \{E[(\lambda_s(t)+\bar{n})\log(\lambda_s(t)+\bar{n})] \\ & - [E(\lambda_s(t)+\bar{n})]\log[E(\lambda_s(t)+\bar{n})]\}\,dt \\ \overset{\Delta}{=}\ & J(\lambda_{sT}). \end{aligned} \tag{23}$$

From Eqs. (9), (21) and (23) we have the following upper bound on $C_{FT}(\bar{s},\bar{p})$:

$$T\,C_{FT}(\bar{s},\bar{p}) \leqslant \sup_{\{(S(t),\,\lambda_s(t))\}\,\in\,\mathcal{C}'_F(\bar{s},\bar{p})} J(\lambda_{sT}) \overset{\Delta}{=} J_T(\bar{s},\bar{p}). \tag{24}$$

We shall solve the optimization problem Eq. (24) to determine $J_T(\bar{s},\bar{p})$. Let us first introduce a slack variable for this optimization problem to change the inequality constraint Eq. (6) to an equality constraint. In particular, define $\mathcal{S}_F(\bar{s},\bar{p})$ to be the set of all message processes $\{S(t)\}$, signal intensity rate processes $\{\lambda_s(t)\}$ and nonnegative numbers x such that conditions (a') and (b) in the definition of $\mathcal{C}'_F(\bar{s},\bar{p})$ hold and such that

$$0 \leqslant x \leqslant \bar{s}, \tag{25}$$

$$G_T(\lambda_{sT}) + x = \bar{s}. \tag{26}$$

Then it is clear from the definitions of $\mathcal{C}'_F(\bar{s},\bar{p})$ and $\mathcal{S}_F(\bar{s},\bar{p})$, and Eqs. (24) through (26) that

$$J_T(\bar{s},\bar{p}) = \sup_{(x,\{(S(t),\lambda_s(t))\})\in\mathcal{F}_F(\bar{s},\bar{p})} J(\lambda_{sT}). \tag{27}$$

Let us next introduce the Lagrange multiplier for the equality constraint Eq. (26) in the optimization problem Eq (27) In particular define $\hat{\mathcal{F}}_F(\bar{p})$ to be the set of all message processes $\{S(t)\}$ and signal intensity rate processes $\{\lambda_s(t)\}$ such that conditions (a′) and (b) in the definition of $\mathcal{C}'_F(\bar{s},\bar{p})$ hold.

Now for each real number $\mu \geqslant 0$, consider the following optimization problem:

$$\sup_{\substack{0\leqslant x\leqslant\bar{s}\\ \{(S(t),\lambda_s(t))\}\in\hat{\mathcal{F}}_F(\bar{p})}} J(\lambda_{sT}) - \mu[G_T(\lambda_{sT}) + x]. \tag{28}$$

The following proposition then relates (28) to (27).

Proposition 1

Suppose there exists a $x^*\epsilon\ [0,\bar{s}]$ and $\{(S^*(t),\lambda_s^*(t))\}\epsilon\ \hat{\mathcal{F}}_F(\bar{p})$ which achieves the supremum in Eq. (28) for some $\mu \geqslant 0$ so that $(x^*, \{(S^*(t),\lambda_s^*(t))\})\ \epsilon\ \mathcal{F}_F(\bar{s},\bar{p})$. Then this $(x^*, \{(S^*(t),\lambda_s^*(t))\})$ achieves the supremum in Eq. (27).

Comment

This proposition essentially says that if we find a Lagrange multiplier $\mu \geqslant 0$ so that the solution of the optimization problem Eq. (28) is also feasible for the optimization problem Eq. (27), then this solution of Eq. (28) also solves Eq. (27). Note that since $J(\lambda_{sT})$ is not concave in λ_{sT}, generalized Kuhn-Tucker theorems valid in function space could not be invoked here to obtain this proposition.

Proof

By hypothesis,

$$(x^*, \{(S^*(t),\lambda_s^*(t))\})\ \epsilon\ \mathcal{F}_F(\bar{s},\bar{p}).$$

So from Eq. (27),

$$J(\lambda_{sT}^*) \leqslant J_T(\bar{s},\bar{p}), \tag{29}$$

where

$$\lambda_{sT}^* = \{\lambda_s^*(t) : 0 \leqslant t \leqslant T\}.$$

But for this $\mu \geqslant 0$, it follows from Eqs. (26) and (27) that

$$\begin{aligned} J_T(\bar{s},\bar{p}) &= \sup_{(x,\{(S(t),\lambda_s(t))\})\in\mathcal{F}_F(\bar{s},\bar{p})} J(\lambda_{sT}) \\ &= \sup_{(x,\{(S(t),\lambda_s(t))\})\in\mathcal{F}_F(\bar{s},\bar{p})} J(\lambda_{sT}) \\ &\qquad - \mu[G_T(\lambda_{sT}) + x - \bar{s}] \\ &\overset{①}{\leqslant} \sup_{\substack{0\leqslant x\leqslant\bar{s}\\ \{(S(t),\lambda_s(t))\}\in\hat{\mathcal{F}}_F(\bar{p})}} J(\lambda_{sT}) \\ &\qquad - \mu[G_T(\lambda_{sT}) + x - \bar{s}] \\ &\overset{②}{=} J(\lambda_{sT}^*) - \mu[G_T(\lambda_{sT}^*) + x^* - \bar{s}] \\ &\overset{③}{=} J(\lambda_{sT}^*), \end{aligned} \tag{30}$$

where ① is because $(x, \{(S(t),\lambda_s(t))\})\ \epsilon\ \mathcal{F}_F(\bar{s},\bar{p})$ implies that $0 \leqslant x \leqslant \bar{s}$ and $\{(S(t),\lambda_s(t))\}\ \epsilon\ \hat{\mathcal{F}}_F(\bar{p})$; ② is because $(x^*, \{(S^*(t),\lambda_s^*(t))\})$ achieves the supremum in Eq. (28); and ③ is because by hypothesis $G_T(\lambda_{sT}^*) + x^* = \bar{s}$ since $(x^*, \{(S^*(t),\lambda_s^*(t))\})\ \epsilon\ \mathcal{F}_F(\bar{s},\bar{p})$. Then Eqs. (29) and (30) establish the proposition.

Q.E.D.

We shall solve the optimization problem Eq. (27) by finding a solution of Eq. (28) which satisfies the hypothesis of Proposition 1. Let $\mu \geqslant 0$ be arbitrary for the time being. We shall restrict μ later. The optimization problem Eq. (28) may be written as

$$\sup_{0\leqslant x\leqslant\bar{s}} \left\{ \sup_{\{(S(t),\lambda_s(t))\}\in\hat{\mathcal{F}}_F(\bar{p})} [J(\lambda_{sT}) - \mu G_T(\lambda_{sT})] - \mu x \right\}. \tag{31}$$

Then from Eqs. (6) and (23) we have

$$\sup_{\{(S(t),\lambda_s(t))\}\in\hat{\mathcal{F}}_F(\bar{p})} J(\lambda_{sT}) - \mu G_T(\lambda_{sT})$$

$$= \sup_{\{(S(t),\, \lambda_s(t))\} \in \hat{\mathscr{S}}_F(\bar{p})} \int_0^T \Big\{ E[(\lambda_s(t) + \bar{n}) \log (\lambda_s(t) + \bar{n})]$$

$$- [E(\lambda_s(t) + \bar{n})] \log [E(\lambda_s(t) + \bar{n})]$$

$$- \left(\frac{\mu}{T}\right) E[\lambda_s(t)] \Big\} \, dt$$

$$\overset{①}{=} T \sup_{\Lambda \in \mathscr{R}(\bar{p})} \Big\{ E[(\Lambda + \bar{n}) \log (\Lambda + \bar{n})]$$

$$- [E(\Lambda + \bar{n})] \log [E(\Lambda + \bar{n})] - \left(\frac{\mu}{T}\right) E[\Lambda] \Big\}, \qquad (32)$$

where $\mathscr{R}(\bar{p})$ is the set of all random variables Λ such that $0 \leqslant \Lambda \leqslant \bar{p}$. To establish ① in Eq. (32), note that for each $t \in [0, T]$, the integrand in the preceding line cannot be larger than $[1/T \times$ last line of Eq. (32)$]$. Hence the last line of Eq. (32) is an upper bound. This upper bound can be achieved if we restrict $\{(S(t),\, \lambda_s(t))\}$ to be such that for every t, $\lambda_s(t) = \Lambda \in \mathscr{R}(\bar{p})$ in the supremum in the preceding line.

In Appendix B we prove the following proposition, which gives the solution of the optimization problem in the right-hand side of Eq. (32).

Proposition 2

Suppose $\mu \geqslant 0$ is such that $k \geqslant 0$, where

$$k = (\bar{p} + \bar{n}) \exp \left[-\left(\frac{\mu}{T} + 1\right) + \frac{\bar{n}}{\bar{p}} \log \left(1 + \frac{\bar{p}}{\bar{n}}\right)\right] - \bar{n}. \qquad (33)$$

Then

$$T \sup_{\Lambda \in \mathscr{R}(\bar{p})} \Big\{ E[(\Lambda + \bar{n}) \log (\Lambda + \bar{n})] - [E(\Lambda + \bar{n})] \log [E(\Lambda + \bar{n})]$$

$$- \left(\frac{\mu}{T}\right) E[\Lambda] \Big\}$$

$$= T \left[\left(\frac{k}{\bar{p}}\right) (\bar{p} + \bar{n}) \log (\bar{p} + \bar{n}) + \left(1 - \frac{k}{\bar{p}}\right) \bar{n} \log \bar{n} \right.$$

$$\left. - (k + \bar{n}) \log (k + \bar{n}) - \left(\frac{\mu}{T}\right) k \right]. \qquad (34)$$

where the $\Lambda^* \in \mathscr{R}(\bar{p})$ which achieves the supremum in Eq. (34) has distribution

$$P(\Lambda^* = \bar{p}) = 1 - P(\Lambda^* = 0) = \frac{k}{\bar{p}}. \qquad (35)$$

In particular $E[\Lambda^*] = k$.

From Eqs. (31), (32) and (34) of Proposition 2, the value of this optimization problem Eq. (28) for $\mu \geqslant 0$ such that $k \geqslant 0$ is given by

$$\sup_{\substack{0 \leqslant x \leqslant \bar{s} \\ \{(S(t),\, \lambda_s(t))\} \in \hat{\mathscr{S}}_F(\bar{p})}} J(\lambda_{sT}) - \mu [G_T(\lambda_{sT}) + x]$$

$$= \sup_{0 \leqslant x \leqslant \bar{s}} \Big\{ T \left[\left(\frac{k}{\bar{p}}\right) (\bar{p} + \bar{n}) \log (\bar{p} + \bar{n}) + \left(1 - \frac{k}{\bar{p}}\right) \bar{n} \log \bar{n} \right.$$

$$\left. - (k + \bar{n}) \log (k + \bar{n}) - \left(\frac{\mu}{T}\right) k \right] - \mu x \Big\}$$

$$= T \left[\left(\frac{k}{\bar{p}}\right) (\bar{p} + \bar{n}) \log (\bar{p} + \bar{n}) + \left(1 - \frac{k}{\bar{p}}\right) \bar{n} \log \bar{n} \right.$$

$$\left. - (k + \bar{n}) \log (k + \bar{n}) - \left(\frac{\mu}{T}\right) k \right]. \qquad (36)$$

Moreover, the solution $x^* \in [0, \bar{s}]$ and $\{(S^*(t),\, \lambda_s^*(t))\} \in \hat{\mathscr{S}}_F(\bar{p})$ of this optimization problem is given as follows for the two cases $\mu > 0$ and $\mu = 0$.

Case 1: $\mu > 0$ such that $k \geqslant 0$

(i) $x^* = 0$ (37)

(ii) $\lambda_s^*(t) = \Lambda^* = \begin{cases} \bar{p}, \text{ with probability } \dfrac{k}{\bar{p}} \\ 0, \text{ with probability } \left(1 - \dfrac{k}{\bar{p}}\right) \end{cases}$ (38)

Case 2. $\mu = 0$ (in which case $k \geqslant 0$) (see Appendix B).

(i) x^* arbitrary in $[0, \bar{s}]$. (39)

(ii) $\lambda_s^*(t)$ given by Eq. (38).

Also, in either Case 1 or Case 2, Eq. (38) gives

$$G_T(\lambda_{sT}^*) = k \qquad (40)$$

In order to solve the optimization problem Eq. (27) we now appeal to Proposition 1. From Proposition 1, we need to find $\mu \geqslant 0$ so that the above solution $x^* \in [0, \bar{s}]$, $\{(S^*(t),\, \lambda_s^*(t))\} \in \hat{\mathscr{S}}_F(\bar{p})$ of the optimization problem Eq. (28) is also feasible for the optimization problem Eq. (27). That is, we need to find $\mu \geqslant 0$ so that $(x^*, \{(S^*(t),\, \lambda_s^*(t))\}) \in \mathscr{S}_F(\bar{s}, \bar{p})$. In examining the definition of $\hat{\mathscr{S}}_F(\bar{p})$ and $\mathscr{S}_F(\bar{s}, \bar{p})$, it is clear that we need only find $\mu \geqslant 0$ so that

$$G_T(\lambda_{sT}^*) + x^* = \bar{s}. \qquad (41)$$

To do this we consider two separate cases below:

Case I. $\bar{s} < (\bar{p} + \bar{n}) \exp\left[\frac{\bar{n}}{\bar{p}} \log\left(1 + \frac{\bar{p}}{\bar{n}}\right) - 1\right] - \bar{n}$

In this case it follows from Eq. (33) that there is a $\mu > 0$ so that

$$k = (\bar{p} + \bar{n}) \exp\left[-\frac{\mu}{T} + \frac{\bar{n}}{\bar{p}} \log\left(1 + \frac{\bar{p}}{\bar{n}}\right) - 1\right] - \bar{n} = \bar{s}. \quad (42)$$

So here, Case I above applies for this $\mu > 0$. Then from Eqs. (37), (40) and (42) it is clear that Eq. (41) is true. So the hypothesis of Proposition 1 is satisfied. Moreover, Eqs. (23), (27), (38), (42) and Proposition 1 then give the following expression for $J_T(\bar{s}, \bar{p})$:

$$J_T(\bar{s}, \bar{p}) = T\left[\left(1 - \frac{\sigma}{\bar{p}}\right)\bar{n} \log \bar{n} + \left(\frac{\sigma}{\bar{p}}\right)(\bar{p} + \bar{n}) \log (\bar{p} + \bar{n}) - (\sigma + \bar{n}) \log (\sigma + \bar{n})\right] \quad (43)$$

with

$$\sigma = \bar{s} \quad (44)$$

Case II: $\bar{s} \geqslant (\bar{p} + \bar{n}) \exp\left[\frac{\bar{n}}{\bar{p}} \log\left(1 + \frac{\bar{p}}{\bar{n}}\right) - 1\right] - \bar{n}$

Let $\mu = 0$. It then follows from Eq. (33) with $\mu = 0$ that

$$k = (\bar{p} + \bar{n}) \exp\left[\frac{\bar{n}}{\bar{p}} \log\left(1 + \frac{\bar{p}}{\bar{n}}\right) - 1\right] - \bar{n} \leqslant \bar{s}. \quad (45)$$

Since $\mu = 0$, Case II above applies. Now $x^* = \bar{s} - k$ satisfies Eq. (39) since $0 \leqslant k \leqslant \bar{s}$. Also it follows from Eq. (40) that Eq. (41) is true for this choice of x^*. Hence the hypothesis of Proposition 1 is satisfied. Finally Eqs. (23), (27), (38), (45), and Proposition 1 show that $J_T(\bar{s}, \bar{p})$ is given by Eq. (43) with

$$\sigma = (\bar{p} + \bar{n}) \exp\left(\frac{\bar{n}}{\bar{p}} \log\left(1 + \frac{\bar{p}}{\bar{n}}\right) - 1\right) - \bar{n}. \quad (46)$$

We can now conclude from Eqs. (10), (24), (43), (44) and (46) the following upper bound on $C_F(\bar{s}, \bar{p})$:

$$C_F(\bar{s}, \bar{p}) \leqslant \left(1 - \frac{\sigma}{\bar{p}}\right)\bar{n} \log \bar{n} + \left(\frac{\sigma}{\bar{p}}\right)(\bar{p} + \bar{n}) \log (\bar{p} + \bar{n}) - (\sigma + \bar{n}) \log (\sigma + \bar{n}), \quad (47)$$

where σ is given by Eq. (11). That is, we have established that the expression Eq. (12) in the theorem is an upper bound on $C_F(\bar{s}, \bar{p})$ and hence, also an upper bound on $C(\bar{s}, \bar{p})$. This completes Step (1).

Let us now carry out Step (2). In his derivation (Ref. 6) of the peak power constrained channel capacity, Kabanov constructed a sequence of signal processes $\{S_m(t)\}$ and associated signal intensity rate process $\{\lambda_s^{(m)}(t)\}$ satisfying the peak power constraint, so that for each T, $(1/T)\, I(S_{mT}; N_T)$ converges to the upper bound on channel capacity as $m \to \infty$. Our derivation above in Step (1) of the upper bound on the peak and average power constrained capacity differs considerably from Kabanov's work (Ref. 6). In the sequel, however, we shall show that Kabanov's construction can still be used to attain our upper bound.

Kabanov's construction applied here is as follows. Denote $1_A(\ )$ as the indicator function of the set A. For each integer $m \geqslant 1$, define a $\{0, 1\}$- valued left-continuous stochastic process $\{S_m(t) : t \geqslant 0\}$ by

$$S_m(t) = \left(\frac{1}{2}\right) - \left(\frac{1}{2}\right) [1 - 2 \times 1_{\{1\}}(S_m(0))] (-1)^{M(t)}$$
$$= \begin{cases} \left(\frac{1}{2}\right) + \left(\frac{1}{2}\right)(-1)^{M(t)}, & \text{if } S_m(0) = 1 \\ \left(\frac{1}{2}\right) - \left(\frac{1}{2}\right)(-1)^{M(t)}, & \text{if } S_m(0) = 0 \end{cases} \quad (48)$$

for $t > 0$ where $S_m(0) = S_{m0}$ has distribution

$$\alpha \triangleq P(S_{m0} = 1) = 1 - P(S_{m0} = 0) = \frac{\sigma}{\bar{p}} \quad (49)$$

and where σ is given by Eq. (11). Here $\{M(t)\}$ is a regular point process (Ref. 9) with intensity rate process

$$\nu(t) = m\, 1_{\{0\}}(S_m(t^-)) + m\left(\frac{1 - \alpha}{\alpha}\right) 1_{\{1\}}(S_m(t^-))$$
$$= \begin{cases} m & , \text{if } S_m(t^-) = 0 \\ m\left(\frac{1 - \alpha}{\alpha}\right) & , \text{if } S_m(t^-) = 1. \end{cases} \quad (50)$$

In other words, $\{S_m(t)\}$ takes on values 0 or 1 and switches between 0 and 1 at random times according to the occurrence times of the point process $\{M(t)\}$. The instantaneous average rate at which these point occurrences arrive at a given time t depends on the immediate past value of $S_m(t)$, being of rate m

when $S_m(t^-) = 0$ and rate $m(1 - \alpha/\alpha)$ when $S_m(t^-) = 1$. Finally, set

$$\lambda_s^{(m)}(t) = \bar{p}|S_m(t)| = \bar{p}\,S_m(t). \tag{51}$$

It can be seen from Eqs. (48) and (51) that in the Kabanov signalling scheme $\lambda_s^{(m)}(t)$ is a random telegraph wave type process. A typical sample path of this process is shown in Fig. 2 in the case when $\alpha = \sigma/\bar{p} << 1$ (for high peak-to-average signal power ratios). When $\alpha << 1$ it can be seen from the rate process $\nu(t)$ given by Eq. (50) that $S_m(t)$ stays in the 0-state a larger percentage of time than in the 1-state. This results in a typical $\lambda_s^{(m)}(t)$ as shown in Fig. 2.

It is clear that $0 \leqslant \lambda_s^{(m)}(t) \leqslant \bar{p}$. Kabanov (Ref. 6) has shown that $E[S_m(t)] = \alpha$. An elaboration of his derivation is given in Appendix C for completeness. Since $E[S_m(t)] = \alpha$, then from Eqs. (49) and (51) we have

$$E[\lambda_s^{(m)}(t)] = \sigma, \tag{52}$$

so from Eqs. (11) and (52) we can conclude that

$$\frac{1}{T}\int_0^T E[\lambda_s^{(m)}(t)]\,dt = \sigma \leqslant \bar{s}. \tag{53}$$

Finally, it is clear from Eq. (51) that $\lambda_{sT}^{(m)} = \{\lambda_s^{(m)}(t) : 0 \leqslant t \leqslant T\}$ is a deterministic function of $S_{mT} = \{S_m(t) : 0 \leqslant t \leqslant T\}$ for each $T > 0$. So $(\{S_m(t)\}, \{\lambda_s^{(m)}(t)\}) \in \mathscr{C}(\bar{s}, \bar{p})$ for each integer $m \geqslant 1$. Thus we conclude from Eq. (7) that for each $T > 0$ and each $m \geqslant 1$,

$$C_T(\bar{s}, \bar{p}) \geqslant \frac{1}{T}\, I(S_{mT}; N_T). \tag{54}$$

Next, a minor modification of Kabanov's proof (Ref. 6) is given in Appendix D to show that for each $T > 0$,

$$\lim_{m\to\infty} \frac{1}{T}\, I(S_{mT}; N_T) = \left(1 - \frac{\sigma}{\bar{p}}\right)\bar{n}\log\bar{n} + \left(\frac{\sigma}{\bar{p}}\right)(\bar{p} + \bar{n})$$

$$\log(\bar{p} + \bar{n}) - (\sigma + \bar{n})\log(\sigma + \bar{n}). \tag{55}$$

Since $C(\bar{s}, \bar{p}) \leqslant C_F(\bar{s}, \bar{p})$, Eqs. (8), (47) and (55) show that $C(\bar{s}, \bar{p}) = C_F(\bar{s}, \bar{p})$ is given by Eq. (12), thus completing Step (2) and establishing the theorem.

IV. Signal Bandwidth and Coded PPM

Consider the sequence of signal intensity rate processes $\{\lambda_s^{(m)}(t)\}$ given by Eq. (51) used in the previous section to attain channel capacity. The bandwidth of this process can be taken to represent the optical signalling bandwidth of the channel. In order to examine the bandwidth of the $\{\lambda_s^{(m)}(t)\}$ process, consider

$$K_\lambda(t, \tau) = \mathrm{Cov}(\lambda_s^{(m)}(t), \lambda_s^{(m)}(\tau)). \tag{56}$$

Appendix E shows that

$$K_\lambda(t, \tau) = K_\lambda(t - \tau) = \bar{p}\sigma\left(1 - \frac{\sigma}{\bar{p}}\right)e^{-m\bar{p}(\sigma^{-1})|t-\tau|}. \tag{57}$$

Thus the power spectral density of this process is

$$S_\lambda(\omega) = \frac{\left(\frac{2\sigma^2}{m}\right)\left(1 - \frac{\sigma}{\bar{p}}\right)}{1 + \left(\frac{\omega\sigma}{m\bar{p}}\right)^2}. \tag{58}$$

So the bandwidth B of the $\{\lambda_s^{(m)}(t)\}$ process and hence also the optical signalling bandwidth can be taken to be

$$B = \frac{m\bar{p}}{\sigma}. \tag{59}$$

We see from Eqs. (55) and (59) that in order to approach capacity with this sequence of signal processes $\{\lambda_s^{(m)}(t)\}$ given by Eqs. (48) and (51), the optical signalling bandwidth B has to tend to infinity. Hence $C(\bar{s}, \bar{p})$ given by Eq. (12) is the channel capacity without bandwidth constraint.

Let us examine the amount of bandwidth of $\{\lambda_s^{(m)}(t)\}$ required for the average mutual information $(1/T)I(S_{mT}; N_T)$ to approach channel capacity $C(\bar{s}, \bar{p})$. It follows from Eqs. (12), (D-2), (D-7) and (D-13) that for $0 < \epsilon < 1$ and any $T > 0$,

$$C(\bar{s}, \bar{p}) - (1/T)\,I(S_{mT}; N_T) = \epsilon\, C(\bar{s}, \bar{p}) \tag{60}$$

implies that the bandwidth B of $\{\lambda_s^{(m)}(t)\}$ satisfies

$$B \geqslant \frac{1}{\epsilon^2}\left[\frac{A^2\bar{p}^2\sigma}{2\,C^2(\bar{s}, \bar{p})}\right] \tag{61}$$

where A is given by Eq. (D-6). Consider a case where $\bar{n} = 0$, $\bar{p} = 10^7$ photons per second, $\bar{s} = 10^4$ photons per second so that $C(\bar{s}, \bar{p}) = 6.9 \times 10^4$ nats per second. Then Eq. (61) becomes

$$B \geqslant \frac{2 \times 10^{10}}{\epsilon^2} \text{ Hz} \tag{62}$$

For $\epsilon = 0.1$, we require $B \geqslant 2 \times 10^{12}$ Hz and for $\epsilon = 0.01$, we require $B \geqslant 2 \times 10^{14}$ Hz.

We now show that for the no background noise case ($\bar{n} = 0$), using coded PPM to achieve capacity is much more bandwidth-efficient than the signalling given by Eqs. (48) and (51). Consider a M-ary PPM modulation scheme shown in Fig. 1 with signal duration T, pulse duration T/M and peak power $\bar{p}$. The M possible signal intensity rate functions $\lambda_{s1}(t), \ldots, \lambda_{sM}(t)$ are given as in Fig. 1. The average power of this signal set is

$$\bar{s} = \frac{\bar{p}}{M}. \tag{63}$$

We shall assume that $M \geqslant 3$. For peak power constraint $\bar{p}$ and average power constraint $\bar{s}$ given by Eq. (63), Corollary 1 gives the channel capacity as

$$C = \bar{s} \log M \text{ nats/sec.} \tag{64}$$

Let us determine the capacity of a system that uses the PPM modulation described in Fig. 1 along with the coding. Since $\bar{n} = 0$, the demodulator then decides that the mth signal was transmitted if a photoelectron is emitted in the mth time slot in $[0, T]$, and declares an error E if no photoelectrons are emitted in the entire interval $[0, T]$. Since the Poisson process has independent increments, one use of the optical direct-detection channel with modulator and demodulator is equivalent to one use of the DMC with input alphabet $\{1, 2, \ldots, M\}$, output alphabet $\{1, 2, \ldots, M, E\}$ and transition probabilities

$$P(j|k) = \begin{cases} 1 - \eta \;, j = k \\ \eta \;\;\;\;\;\;\, , j = E, 1 \leqslant k \leqslant M \\ 0 \;\;\;\;\;\;\; \text{, otherwise} \end{cases} \tag{65}$$

where

$$\eta = e^{-\bar{s}T} \tag{66}$$

is the probability of having no photoelectrons emitted in the time interval $[0, T]$. If we optimally code this DMC, then the capacity of the above coded PPM channel is just the capacity of the DMC given by Eq. (65). Let C_{PPM} denote the capacity of the optimally coded PPM channel. Then it is easy to show (Ref. 11) that

$$\begin{aligned} C_{PPM} &= \frac{(1 - \eta) \log M}{T} \text{ nats/sec} \\ &= \left(\frac{1 - e^{-\bar{s}T}}{T}\right) \log M \text{ nats/sec.} \end{aligned} \tag{67}$$

From Eqs. (64) and (67) we see that

$$\frac{C_{PPM}}{C} = \frac{1 - e^{-\bar{s}T}}{\bar{s}T} \leqslant 1 \tag{68}$$

and that

$$\lim_{T \to 0} \frac{C_{PPM}}{C} = 1.$$

Hence this optimally coded PPM system is capable of achieving channel capacity C in the limit as $T \to 0$. This also entails increasing the signalling bandwidth to infinity because the bandwidth B_{PPM} of the PPM signal set can be taken to be

$$B_{PPM} = \frac{M}{T} = \left(\frac{\bar{p}}{\bar{s}}\right) \frac{1}{T}. \tag{69}$$

Note from Eqs. (68) and (69) that for any $0 < \epsilon < 1$,

$$C - C_{PPM} = \epsilon C \tag{70}$$

implies that the bandwidth B_{PPM} satisfies

$$1 - \frac{1 - \exp(-\bar{p}/B_{PPM})}{(\bar{p}/B_{PPM})} = \epsilon. \tag{71}$$

For small $(\bar{p}/B_{PPM})$, Eq. (71) is approximately

$$B_{PPM} \approx \frac{\bar{p}}{2\epsilon}. \tag{72}$$

For $\epsilon = 0.01$ we would require $B_{PPM} \approx 5 \times 10^8$ Hz when $\bar{p} = 10^7$ photons/sec. This can be compared to the bandwidth $B \geqslant 2 \times 10^{14}$ Hz required by the signalling scheme given by Eqs. (48) and (51) to achieve the same rate. A comparison of Eqs. (72) and (61) shows the relative bandwidth advantage of coded PPM versus the signalling scheme given by Eqs. (48) and (51). This is because B increases at least inversely with ϵ^2 while B_{PPM} increases only inversely with ϵ, where ϵ is the desired proximity to channel capacity. These results apply to the case where $\bar{p}/B_{PPM}$ is small. For large values of $\bar{p}/B_{PPM}$ even less bandwidth is required for PPM modulation to approach capacity.

V. Conclusion

We have derived the capacity of a free-space optical channel using a direct detection receiver under both peak and average signal power constraints and without a signal bandwidth constraint. This result is a generalization of Kabanov's work (Ref. 6), where only a peak power constraint was imposed. In the absence of received background noise, an optimally coded PPM system was shown to achieve channel capacity in the limit as signal bandwidth approaches infinity. All of these results did not consider the effect of a signal bandwidth constraint. It would be interesting to derive the channel capacity under a fixed bandwidth constraint also.

Recent work (Ref. 3) has advocated considering the channel capacity per received signal photon. In the no background noise case ($\bar{n} = 0$) it can be seen from Eq. (13) that

$$\frac{C(\bar{s},\bar{p})}{\sigma} = \log \frac{\bar{p}}{\sigma} \text{ nats/photon} \tag{73}$$

in the capacity per unit signal photon. It can be easily seen from Eqs. (14) and (73) that for a fixed peak signal power constraint $\bar{p}$, the capacity per unit signal photon increases to infinity as the average signal power constraint $\bar{s}$ approaches zero. However, as $\bar{s} \rightarrow 0$, the throughput channel capacity $C(\bar{s},\bar{p}) \rightarrow 0$. Thus it does not appear meaningful to consider capacity per signal photon without fixing the throughput channel capacity. The expression Eq. (12) for $C(\bar{s},\bar{p})$ can be used in this regard to determine the average signal capacity per unit signal photon for a fixed throughput capacity. This is another problem of interest that has been addressed by Butman, Katz and Lesh (Ref. 20) in the no background noise case.

References

1. Gordon, J. P., "Quantum Effects in Communication Systems," *Proc. Inst. Radio Eng.*, 50, pp. 1898-1908, 1962.
2. Helstrom, C. W., Liu, J. W. S., and Gordon, J. P., "Quantum Mechanical Communication Theory," *Proc. IEEE*, 58, pp. 1578-1598, 1970.
3. Pierce, J. R., "Optical Channels: Practical Limits with Photon Counting," *IEEE Trans. Comm.*, COM-26, No. 12, pp. 1819-1821, 1978
4. McEliece, R. J., Rubin, A. L., and Rodemich, E. R., "The Practical Limits of Photon Communication," *DSN Progress Report 42-52*, Jet Propulsion Laboratory, Pasadena, Calif., pp. 63-67, 1979.
5. Katz, J., "Information Aspects of Optical Channels," JPL Section 331 seminar.
6. Kabanov, Yu. M., "The Capacity of a Channel of the Poisson Type," *Theory of Probability and Applications*,Vol. 23, No. 1, pp. 143-147, Dec. 1978.
7. Macchi, O., and Picinbono, B. C., "Estimation and Detection of Weak Optical Signals," *IEEE Trans. Inform. Theory*, IT-18, No. 5, pp. 562-573, Sept. 1972.
8. Karp, S. and Clark, J. R., "Photon Counting: A Problem in Classical Noise Theory," *IEEE Trans. Inform. Theory*, IT-16, No. 6, pp. 672-680, Nov. 1970.
9. Rubin, I., "Regular Point Processes and Their Detection," *IEEE Trans. Inform. Theory*, IT-18, No. 5, pp. 547-557, Sept. 1972.
10. Snyder, D. L., *Random Point Processes*, Wiley, New York, 1976.
11. Gallager, R. G., *Information Theory and Reliable Communication*, Wiley, New York, 1968.
12. Lipster, R , and Shiryayev, A. N., *Statistics of Random Processes II*, Springer-Verlag, New York, 1978.
13. Smith, J. G., "The Information Capacity of Amplitude- and Variance-Constrained Scalar Gaussian Channels," *Information and Control*, 18, pp. 203-219, 1971.
14. Segall, A., and Kailath, T., "The Modelling of Randomly Modulated Jump Processes," *IEEE Trans. Inform. Theory*, IT-21, No. 2, pp. 135-143, Mar. 1975
15. Doob, J., *Stochastic Processes*, Wiley, New York, 1953.
16. Segall, A., Davis, M. H. A., and Kailath, T., "Nonlinear Filtering with Counting Observations," *IEEE Trans Inform. Theory*, IT-21, No. 2, pp. 143-149, Mar. 1975.
17. Gagliardi, R., and Karp, S., *Optical Communications*, Wiley, New York, 1978
18. Pierce, J. R., Posner, E. C., and Rodemich, E. R., "The Capacity of the Photon Counting Channel," submitted for publication.
19. Kadota, T. T., Zakai, M., and Ziv, J., "Capacity of a Continuous Memoryless Channel with Feedback," *IEEE Trans. Inform. Theory*, IT-17, No. 4, pp. 372-378, July 1971.
20. Butman, S. A. Katz, J., and Lesh, J. R., "Practical Limitation on Noiseless Optical Channel Capacity," *DSN Progress Report 42-52*, Jet Propulsion Laboratory, Pasadena, Calif., pp. 12-14, 1979.

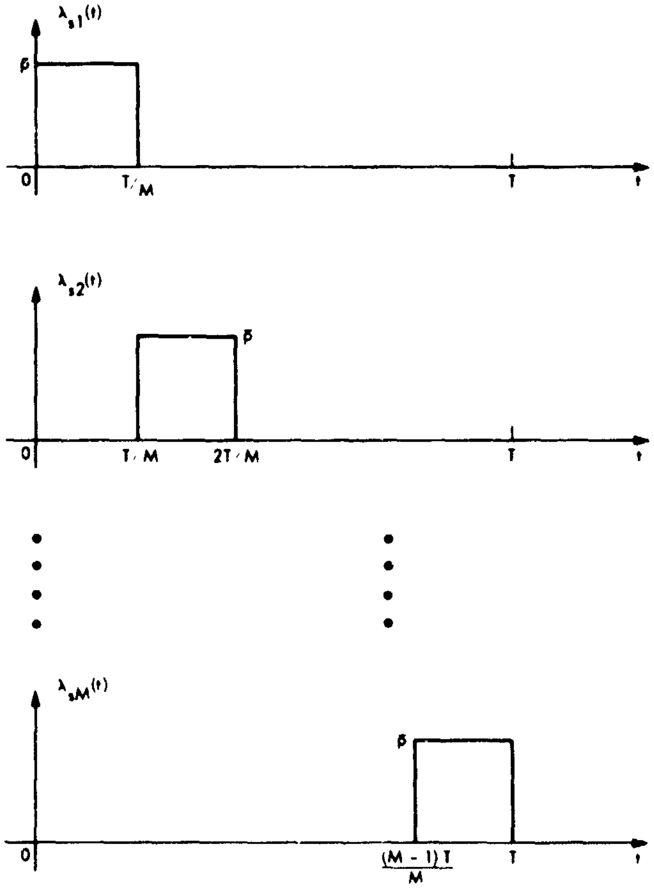

Fig. 1. PPM signal set

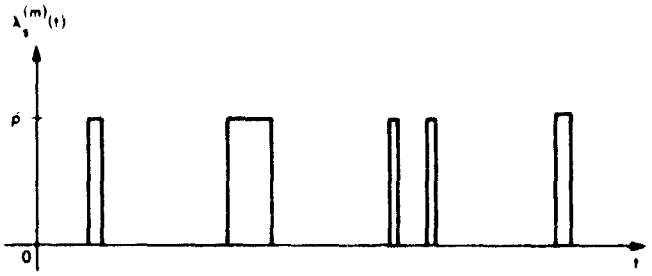

Fig. 2. Typical sample path of $\lambda_s^{(m)}(t)$ when $\alpha << 1$ for Kabanov signals

Appendix A
Derivation of Eq. (19)

Let $p(N_T)$ be the sample function density (Ref. 1) of the compound regular point process $\{N(t):\ 0 \leqslant t \leqslant T\}$ and $p(N_T|S_T)$ be the conditional sample function density of $\{N(t):\ 0 \leqslant t \leqslant T\}$ given the message signal process $\{S(t).\ 0 \leqslant t \leqslant T\}$. Then from Ref. 9 (Theorems 2 and 4) we have[1]

$$p(N_T|S_T) = \exp\left[-\int_0^T (\lambda_s(t)+\bar{n})\,dt + \int_0^T \log(\lambda_s(t)+\bar{n})\,dN(t)\right], \tag{A-1}$$

$$p(N_T) = \exp\left[-\int_0^T (\hat{\lambda}_s(t)+\bar{n})\,dt + \int_0^T \log(\hat{\lambda}_s(t)+\bar{n})\,dN(t)\right]. \tag{A-2}$$

Now since

$$I(S_T, N_T) \overset{\Delta}{=} E\left[\log \frac{p(N_T|S_T)}{p(N_T)}\right], \tag{A-3}$$

we have from Eqs. (A-1) and (A-2) that

$$\begin{aligned}
I(S_T;N_T) &= E\left[\int_0^T (\hat{\lambda}_s(t) - \lambda_s(t))\,dt + \int_0^T \log\left(\frac{\lambda_s(t)+\bar{n}}{\hat{\lambda}_s(t)+\bar{n}}\right) dN(t)\right] \\
&\overset{①}{=} E\left[\int_0^T \log\left(\frac{\lambda_s(t)+\bar{n}}{\hat{\lambda}_s(t)+\bar{n}}\right) dN(t)\right] \\
&= E\left[\int_0^T (\lambda_s(t)+\bar{n}) \log\left(\frac{\lambda_s(t)+\bar{n}}{\hat{\lambda}_s(t)+\bar{n}}\right) dt\right] \\
&\quad + E\left[\int_0^T \log\left(\frac{\lambda_s(t)+\bar{n}}{\hat{\lambda}_s(t)+\bar{n}}\right) (dN(t) - (\lambda_s(t)+\bar{n})\,dt)\right].
\end{aligned} \tag{A-4}$$

where ① is because

$$E[\hat{\lambda}_s(t)] = E[E[\lambda_s(t)|N_t]] = E[\lambda_s(t)].$$

Next, since

$$N(t) - \int_0^t (\lambda_s(\tau)+\bar{n})\,d\tau$$

is a martingale (Ref. 14, (3.20)), then from a theorem on stochastic integrals (Ref. 15, p. 437), the second expectation in Eq. (A-4) is zero. Hence Eq. (A-4) can be rewritten as

$$\begin{aligned}
I(S_T;N_T) &= \int_0^T \{E[(\lambda_s(t)+\bar{n})\log(\lambda_s(t)+\bar{n})] - E[(\lambda_s(t)+\bar{n})\log(\hat{\lambda}_s(t)+\bar{n})]\}\,dt \\
&\overset{①}{=} \int_0^T \{E[(\lambda_s(t)+\bar{n})\log(\lambda_s(t)+\bar{n})] - E[(\hat{\lambda}_s(t)+\bar{n})\log(\hat{\lambda}_s(t)+\bar{n})]\}\,dt,
\end{aligned} \tag{A-5}$$

which establishes Eq. (19). In Eq. (A-5) ① is because

$$\begin{aligned}
&E[(\lambda_s(t)+\bar{n})\log(\hat{\lambda}_s(t)+\bar{n})] \\
&= E[E[(\lambda_s(t)+\bar{n})\log(\hat{\lambda}_s(t)+\bar{n})|N_t]] \\
&= E[E[(\lambda_s(t)+\bar{n})|N_t]\log(\hat{\lambda}_s(t)+\bar{n})] \\
&= E[(\hat{\lambda}_s(t)+\bar{n})\log(\hat{\lambda}_s(t)+\bar{n})].
\end{aligned} \tag{A-6}$$

The above derivation is formal and not rigorous. We have assumed interchanges of integration and expectation without rigorous justifications. A rigorous derivation of Eq. (19) can be found in Ref. 12.

---

[1] The integrals with respect to $N(t)$ in Eqs. (A-1) and (A-2) and henceforth in the remainder of this paper is interpreted in the Ito sense (Refs 9, 10).

Appendix B

Proof of Proposition 2

Let $\mathscr{R}(\bar{p}, k)$ be the set of all random variables Λ such that $0 \leqslant \Lambda \leqslant \bar{p}$ and $E[\Lambda] = k$ where $0 \leqslant k \leqslant \bar{p}$. Then

$$\sup_{\Lambda \in \mathscr{R}(\bar{p})} \left\{ E[(\Lambda + \bar{n}) \log (\Lambda + \bar{n})] - [E(\Lambda + \bar{n})] \log [E(\Lambda + \bar{n})] - \left(\frac{\mu}{T}\right) E[\Lambda] \right\}$$

$$= \sup_{0 \leqslant k \leqslant \bar{p}} \left\{ \sup_{\Lambda \in \mathscr{R}(\bar{p}, k)} E[(\Lambda + \bar{n}) \log (\Lambda + \bar{n})] - (k + \bar{n}) \log (k + \bar{n}) + \left(\frac{\mu}{T}\right) k \right\}. \tag{B-1}$$

Note from Fig B-1 that if $0 \leqslant \Lambda \leqslant p$, then the possible values of $E[(\Lambda + \bar{n}) \log (\Lambda + \bar{n})]$ must lie in the set of all y-coordinates of the closed convex hull of the graph of $y = (x + \bar{n}) \log (x + \bar{n})$ for $0 \leqslant x \leqslant \bar{p}$. Hence the largest possible values lie on the cord AB. These values can be achieved using a random variable Λ with the following distribution

$$P(\Lambda = \bar{p}) = 1 - P(\Lambda = 0) = \alpha \tag{B-2}$$

where $\alpha \epsilon [0, 1]$ must be chosen so that $E[\Lambda] = k$ in order for Λ to be in $\mathscr{R}(\bar{p}, k)$. In order for $E[\Lambda] = k$, we must have

$$\alpha = k/\bar{p}. \tag{B-3}$$

Hence

$$\sup_{\Lambda \in \mathscr{R}(\bar{p}, k)} E[(\Lambda + \bar{n}) \log (\Lambda + \bar{n})] = \left(\frac{k}{\bar{p}}\right)(\bar{p} + \bar{n}) \log (\bar{p} + \bar{n}) + \left(1 - \frac{k}{\bar{p}}\right) \bar{n} \log \bar{n}, \tag{B-4}$$

where the Λ achieving the supremum is given by Eqs (B-2) and (B-3) Hence the optimization problem in Eq. (B-1) can be written as

$$\sup_{0 \leqslant k \leqslant \bar{p}} g(k), \tag{B-5}$$

where $g(k)$ is given by

$$g(k) = \left(\frac{k}{\bar{p}}\right)(\bar{p} + \bar{n}) \log (\bar{p} + \bar{n}) + \left(1 - \frac{k}{\bar{p}}\right) \bar{n} \log \bar{n} - (k + \bar{n}) \log (k + \bar{n}) - \left(\frac{\mu}{T}\right) k \tag{B-6}$$

Since $g(k)$ is concave in k, the supremum in Eq (B-5) is achieved by a $k \epsilon [0, \bar{p}]$ such that $g'(k) = 0$, provided that such a k exists. Setting $g'(k) = 0$ gets

$$k = (\bar{p} + \bar{n}) \exp \left(- \left(\frac{\mu}{T} + 1\right) + \frac{\bar{n}}{\bar{p}} \log \left(1 + \frac{\bar{p}}{\bar{n}}\right)\right) - \bar{n}. \tag{B-7}$$

It follows immediately from Eq (16) since $\mu \geqslant 0$ that $k \leqslant \bar{p}$ in Eq (B-7) Since by hypothesis of the proposition, $k \geqslant 0$, we can conclude that k given by Eq. (B-7) achieves the supremum in Eq. (B 5). This establishes the proposition

Also note from Eq. (B-6) that when $\mu = 0$, $g(0) = 0$ and $g'(0) \geqslant 0$. This means that when $\mu = 0$, the solution k to $g'(k) = 0$ must be nonnegative So when $\mu = 0$ the k given by Eq. (B-7) is nonnegative.

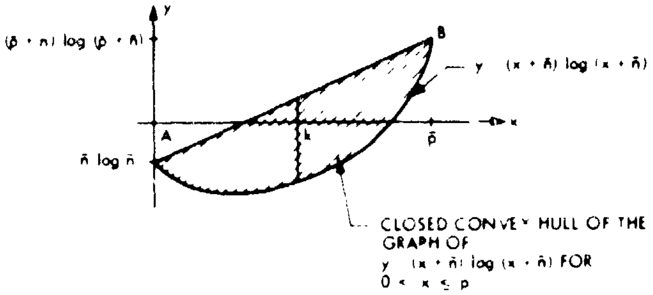

Fig. B-1. Geometry of optimization

Appendix C

Proof that $E[S_m(t)] = \alpha$

Since $M(t)$ is nonnegative integer-valued, $(-1)^{M(t)} = \cos(\pi M(t))$. So Eq. (48) can be rewritten as

$$S_m(t) = \left(\frac{1}{2}\right) + \left[1_{\{1\}}(S_m(0)) - \frac{1}{2}\right]\cos(\pi M(t)), \qquad \text{(C-1)}$$

for $t > 0$. So for each t, $S_m(t)$ is a function of $M(t)$ and hence we may use the Stochastic Differential Rule (e.g., Ref. 10, Theorem 4.2.2) to obtain

$$\begin{aligned}
dS_m(t) &= \left\{\left(\frac{1}{2}\right) + \left[1_{\{1\}}(S_m(0)) - \frac{1}{2}\right]\cos(\pi M(t) + 1)\right. \\
&\qquad \left. - \left(\left(\frac{1}{2}\right) + \left[1_{\{1\}}(S_m(0)) - \frac{1}{2}\right]\cos(\pi M(t))\right)\right\} dM(t) \\
&\overset{①}{=} [1 - 2S_m(t)]\, dM(t) \\
&= [1 - 2S_m(t)]\, \nu(t)\, dt \\
&\qquad + [1 - 2S_m(t)]\, [dM(t) - \nu(t)\, dt] \\
&\overset{②}{=} [1 - 2S_m(t)] \left[m\, 1_{\{0\}}(S_m(t^-))\right. \\
&\qquad \left. + m\left(\frac{1-\alpha}{\alpha}\right) 1_{\{1\}}(S_m(t^-))\right] dt \\
&\qquad + [1 - 2S_m(t)]\, [dM(t) - \nu(t)\, dt], \qquad \text{(C-2)}
\end{aligned}$$

where ① is obtained using Eq. (C-1) and ② is because of Eq. (50). Rewriting Eq. (C-2) in integral form gets

$$\begin{aligned}
S_m(t) &= S_m(0) + \int_0^t [1 - 2S_m(u)]\, [m\, 1_{\{0\}}(S_m(u)) \\
&\qquad + m\left(\frac{1-\alpha}{\alpha}\right) 1_{\{1\}}(S_m(u))]\, du \\
&\qquad + \int_0^t [1 - 2S_m(u)]\, [dM(u) - \nu(u)\, du] \\
&\overset{①}{=} S_m(0) + \int_0^t m\alpha^{-1}(\alpha - S_m(u))\, du \\
&\qquad + \int_0^t [1 - 2S_m(u)]\, [dM(u) - \nu(u)\, du], \qquad \text{(C-3)}
\end{aligned}$$

where ① follows since $S_m(t)$ is either 0 or 1. Now it follows from Eq. (49) that $E[S_m(0)] = \alpha$. Next, since

$$M(t) - \int_0^t \nu(u)\, du$$

is a martingale (Ref. 14, (3.20)), it follows that the expected value of the last integral in Eq. (C-3) is zero (Ref. 15, p. 437). So, taking expected values in Eq. (C-3) gets

$$E[S_m(t)] = \alpha + m\alpha^{-1} \int_0^t [\alpha - E[S_m(u)]]\, du. \qquad \text{(C-4)}$$

The unique solution of this initial value problem Eq. (C-4) is

$$E[S_m(t)] = \alpha. \qquad \text{(C-5)}$$

Appendix D

Derivation of Eq. (55)

Note that since $S_m(t) = 0$ or 1, it follows from Eq. (C-5) that $P(S_m(t) = 1) = \alpha$. So from Eqs. (49) and (51) it follows that

$$E\left[(\lambda_s^{(m)}(t) + \bar{n}) \log (\lambda_s^{(m)}(t) + \bar{n})\right]$$

$$= \left(\frac{\alpha}{\bar{p}}\right)(\bar{p} + \bar{n}) \log (\bar{p} + \bar{n}) + \left(1 - \frac{\alpha}{\bar{p}}\right)\bar{n} \log \bar{n} . \qquad \text{(D-1)}$$

So from Eqs. (19) and (D-1),

$$\frac{1}{T} I(S_{mT}; N_T) - \left(1 - \frac{\alpha}{\bar{p}}\right)\bar{n} \log \bar{n} - \left(\frac{\alpha}{\bar{p}}\right)(\bar{p} + \bar{n}) \log (\bar{p} + \bar{n})$$

$$+ (\alpha + \bar{n}) \log (\alpha + \bar{n})$$

$$= \frac{1}{T}\int_0^T E\{f(\hat{\lambda}_s^{(m)}(t)) - f(\alpha)\}\, dt \qquad \text{(D-2)}$$

where

$$f(x) = (x + \bar{n}) \log (x + \bar{n}), \qquad \text{(D-3)}$$

and

$$\hat{\lambda}_s^{(m)}(t) \overset{\Delta}{=} E[\lambda_s^{(m)}(t) | N_t)$$

$$= \bar{p}\, E[S_m(t) | N_t]$$

$$\overset{\Delta}{=} \bar{p}\, \hat{S}_m(t) . \qquad \text{(D-4)}$$

Now it can be easily shown that for $0 \leqslant x \leqslant \bar{p}$,

$$|f(x) - f(\alpha)| \leqslant A\, |x - \alpha| , \qquad \text{(D-5)}$$

where

$$A = \max\left[\frac{f(\bar{p}) - f(\alpha)}{\bar{p} - \alpha} , \left|\frac{f(0) - f(\alpha)}{\alpha}\right|\right] , \qquad \text{(D-6)}$$

since $0 \leqslant \alpha \leqslant \bar{p}$. So from Eqs. (D-4) (D-5) and (49), we have

$$\frac{1}{T}\int_0^T E\{f(\hat{\lambda}_s^{(m)}(t)) - f(\alpha)\}\, dt$$

$$\leqslant \frac{A\bar{p}}{T}\int_0^T E\{|\hat{S}_m(t) - \alpha|\}\, dt$$

$$\overset{①}{\leqslant} \frac{A\bar{p}}{T}\int_0^T (E[(\hat{S}_m(t) - \alpha)^2])^{1/2}\, dt$$

$$\overset{②}{=} \frac{A\bar{p}}{T}\int_0^T (E[(\hat{S}_m(t))^2] - \alpha^2)^{1/2}\, dt.$$

$$\text{(D-7)}$$

Here ① is from Jensen's inequality and ② is because

$$E[\hat{S}_m(t)] = E[E[S_m(t) | N_t]] = E[S_m(t)] = \alpha$$

from Eq (C-5). The remainder of the derivation now follows Kabanov's proof exactly to show that $E[\hat{S}_m(t))^2] - \alpha^2$ converges to zero as $m \to \infty$ uniformly in t. Specifically, from Eq. (C-3) and (Ref. 16, Eq. 1.6a) we can write

$$d\hat{S}_m(t) = m\alpha^{-1}(\alpha - \hat{S}_m(t))\, dt$$

$$+ \frac{\bar{p}E[S_m(t)(S_m(t) - \hat{S}_m(t)) | N_t]}{\bar{p}\hat{S}_m(t) + \bar{n}}$$

$$\cdot [dN(t) - (\bar{p}\hat{S}_m(t) + \bar{n})\, dt]$$

$$\overset{①}{=} m\alpha^{-1}(\alpha - \hat{S}_m(t))\, dt$$

$$+ \frac{\bar{p}\hat{S}_m(t)(1 - \hat{S}_m(t))}{\bar{p}\hat{S}_m(t) + \bar{n}}$$

$$\cdot [dN(t) - (\bar{p}\hat{S}_m(t) + \bar{n})\, dt] , \qquad \text{(D-8)}$$

where ① is because $S_m(t) = S_m^2(t)$. Next, using the Stochastic Differential Rule (Ref. 10, Theorem 4.2.2), we obtain

$$d(\hat{S}_m(t))^2 = \left[2m\alpha^{-1} \hat{S}_m(t)(\alpha - \hat{S}_m(t)) + \frac{[\bar{p}\hat{S}_m(t)(1 - \hat{S}_m(t))]^2}{\bar{p}\hat{S}_m(t) + \bar{n}} \right] dt$$

$$+ \left[\frac{2\bar{p}(\hat{S}_m(t))^2(1 - \hat{S}_m(t))}{\bar{p}\hat{S}_m(t) + \bar{n}} + \left(\frac{\bar{p}\hat{S}_m(t)(1 - \hat{S}_m(t))}{\bar{p}\hat{S}_m(t) + \bar{n}} \right)^2 \right]$$

$$\cdot [dN(t) - (\bar{p}\hat{S}_m(t) + \bar{n})\, dt] . \quad \text{(D-9)}$$

Now using the martingale property of

$$N(t) - \int_0^t (\bar{p}\hat{S}_m(u) + \bar{n})\, du$$

as in Eqs. (A-4), (A-5) and in (C-4), we can take the expected value of the integral of Eq. (D-9) to obtain

$$E[(\hat{S}_m(t))^2] = \alpha^2 + 2m\alpha^{-1} \int_0^t (\alpha^2 - E[\hat{S}_m(u)]^2)\, du$$

$$+ \int_0^t E\left[\frac{[\bar{p}\hat{S}_m(u)(1 - \hat{S}_m(u))]^2}{\bar{p}\hat{S}_m(u) + \bar{n}} \right] du .$$

(D-10)

Define

$$g(t) = E\left[\frac{[\bar{p}\hat{S}_m(t)(1 - \hat{S}_m(t))]^2}{\bar{p}\hat{S}_m(t) + \bar{n}} \right]$$

$$\leqslant \bar{p} E[\hat{S}_m(t)(1 - \hat{S}_m(t))^2]$$

$$\leqslant \bar{p} E[\hat{S}_m(t)]$$

$$= \sigma . \quad \text{(D-11)}$$

Now since $(\hat{S}_m(0))^2 = (E[S_m(0)])^2 = \alpha^2$, the unique solution to the initial value problem Eq. (D-10) is

$$E[(\hat{S}_m(t))^2] = \alpha^2 e^{-2m\alpha^{-1}t}$$

$$+ e^{-2m\alpha^{-1}t} \int_0^t (g(u) + 2m\alpha)$$

$$\cdot e^{2m\alpha^{-1}u}\, du . \quad \text{(D-12)}$$

Since from Eq. (D-11), $0 \leqslant g(u) \leqslant \sigma$, we have from Eq. (D-12) that

$$E[(\hat{S}_m(t))^2] - \alpha^2$$

$$\leqslant \frac{\sigma^2}{2m\bar{p}} (1 - e^{-2m\alpha^{-1}t})$$

$$\leqslant \frac{\sigma^2}{2m\bar{p}} \quad \text{(D-13)}$$

Therefore Eqs. (D-2), (D-7) and (D-13) establish Eq. (55).

Appendix E

Derivation of Eq. (57)

It follows from Eqs. (51) and (C-5) that

$$K_\lambda(t,\tau) = \bar{p}^2 \{E[S_m(t)S_m(\tau)] - \alpha^2\}. \qquad \text{(E-1)}$$

Since $P(S_m(t) = 1) = \alpha$ from Eq. (C-5), it follows that for $t \geqslant \tau$,

$$E[S_m(t)S_m(\tau)] = E[S_m(\tau)E[S_m(t)|S_m(\tau)]]$$

$$= \alpha E[S_m(t)|S_m(\tau) = 1]. \qquad \text{(E-2)}$$

Then we may write, using Eq. (C-3), for $t \geqslant \tau$

$$S_m(t) = S_m(\tau) + m\alpha^{-1}\int_\tau^t (\alpha - S_m(u))\,du$$

$$+ \int_\tau^t (1 - 2S_m(u))\,[dM(u) - \nu(u)\,du]. \qquad \text{(E-3)}$$

Hence for $t \geqslant \tau$,

$$E[S_m(t)|S_m(\tau) = 1]$$

$$= 1 + m\alpha^{-1}\int_\tau^t (\alpha - E[S_m(u)|S_m(\tau) = 1])\,du. \qquad \text{(E-4)}$$

because

$$E\left\{\int_\tau^t (1 - 2S_m(u))[dM(u - \nu(u)\,du]\,|S_m(\tau) = 1\right\}$$

$$= E\left\{\int_\tau^t (1 - 2S_m(u))[d(M(u)\right.$$

$$\left. - M(\tau)) - \nu(u)\,du]\,|S_m(\tau) = 1\right\} \overset{①}{=} 0, \qquad \text{(E-5)}$$

where ① follows since

$$\left\{M(s) - M(\tau) - \int_\tau^s \nu(u)\,du : s \geqslant \tau\right\}$$

is a martingale given that $S_m(\tau) = 1$.

Since $E[S_m(\tau)|S_m(\tau) = 1] = 1$, the solution of the initial value problem Eq. (E-4) can be shown to be

$$E[S_m(t)|S_m(\ ) = 1] = (1 - \alpha)\, e^{-m\alpha^{-1}(t-\tau)} + \alpha, \qquad \text{(E-6)}$$

when $t \geqslant \tau$. Thus Eqs. (E-1), (E-2) and (E-6) gets

$$K_\lambda(t,\tau) = p^{-2}\,\alpha(1 - \alpha)\,e^{-m\alpha^{-1}(t-\tau)} \qquad \text{(E-7)}$$

for $t \geqslant \tau$. Since $K_\lambda(t,\tau) = K_\lambda(\tau,t)$ and since $\alpha = \rho/p$, Eq. (57) follows from Eq. (E-7).

Effects of the Gaseous and Liquid Water Content of the Atmosphere on Range Delay and Doppler Frequency

W. L. Flock
Telecommunications Systems Section

When high precision is required for range measurement on Earth-space paths, it is necessary to correct as accurately as possible for excess range delays due to the dry air, water vapor, and liquid water content of the atmosphere. Calculations based on representative values of atmospheric parameters are useful for illustrating the order of magnitude of the expected delays. Range delay, time delay, and phase delay are simply and directly related. Doppler frequency variations or noise are proportional to the time rate of change of excess range delay.

I. Introduction

Increasingly sophisticated deep-space missions place high requirements upon the precision of time delay and Doppler frequency measurements. The interplanetary plasma is one of the factors limiting the precision of such measurements. The excess time and range delays due to the plasma are proportional to total electron content along the path and inversely proportional to frequency squared. Doppler frequency variations are generated by the plasma in direct proportion to the rate of change of total electron content and in inverse relation with frequency. When unwanted, as is often the case, such variations are commonly referred to as Doppler frequency noise. In deep-space missions conducted by the Jet Propulsion Laboratory, range has been determined by using coded two-way transmissions at S-band for the uplink and S-band and X-band for the downlink. Because of the need for increased precision in range and Doppler frequency measurement, it is planned to demonstrate the capability of the higher frequency X-band for both the uplink and downlink, retaining S band up- and downlinks as well. K-band links may be utilized at a later date. High precision is needed for range measurements when using very long baseline interferometry (VLBI) techniques, and high precision and sensitivity for Doppler frequency measurements are required if gravitational waves are to be recorded (Refs. 1 and 2).

When high precision is needed for range and Doppler frequency measurements, it becomes necessary to consider effects due to the gaseous and liquid water content of the troposphere as well as effects due to the interplanetary plasma and ionosphere. The tropospheric effects may dominate if the interplanetary plasma Doppler noise is reduced by adding X-band uplink capability (Ref. 3). The purpose of this report is to analyze the tropospheric effects as part of an overall consideration of the capability of precision two-way ranging and Doppler systems.

The term precision is used here in distinction from accuracy. The state of knowledge concerning the velocity of light limits the absolute accuracy of range measurements, but it is possible to overcome propagation effects and hardware limitations sufficiently to obtain high precision and a high degree of consistency.

II. Excess Range Delay Due to Dry Air and Water Vapor

A. Refractivity of Troposphere

Range to a target is commonly determined by radar techniques by assuming that electromagnetic waves propagate with the velocity c (2.99792458×10^8 m/s or approximately 3×10^8 m/s). A velocity of c corresponds to an index of refraction of unity. In the troposphere, however, the index of refraction n is slightly greater than unity with the result that the phase velocity of an electromagnetic wave is slightly less than c. A range error then results if the velocity c is assumed. The slight error in range is unimportant in many applications, but may be important in other situations. In practice, when high precision in range is desired, it is anticipated that the range indicated by using the velocity c is greater than the true range, and an effort is made to estimate as closely as possible the excess range delay ΔR (the amount by which the indicated range exceeds the true range) in order to correct for it.

To consider the excess range delay, which can be referred to also as excess group delay, note that the integral $\int n\, dl$ evaluated along a path, with n representing the index of refraction and dl an increment of length, gives the true distance along the path if $n = 1$, but gives a value which is different from the true distance if $n \neq 1$ (By definition, the index of refraction n of a particular wave type in a given medium is the ratio of c to v_p, the phase velocity of the wave in the medium.) The difference ΔR between the true and indicated distances is given by

$$\Delta R = \int (n - 1)\, dl \qquad (1)$$

The index of refraction of the troposphere is only slightly greater than 1 and for this reason the usual practice is to use N units, defined by $N = (n - 1)10^6$ and commonly referred to as refractivity. The refractivity of the troposphere is given by

$$N = \frac{77.6\, p_d}{T} + \frac{72\, e}{T} + \frac{3.75 \times 10^5\, e}{T^2} \qquad (2)$$

where p_d is the pressure of dry nonpolar air in millibars (mb), e is water vapor pressure in mb, and T is absolute temperature in kelvins (Ref. 4). N is seen to vary inversely with temperature and to be strongly dependent on water vapor pressure e, which equals the saturation water vapor pressure e_s times the relative humidity, RH. The saturation water vapor pressure e_s is a function of temperature as shown in Table 1.

If Equation (2) is expressed in terms of total pressure p, where $p = p_d + e$, it becomes

$$N = \frac{77.6\, p}{T} - \frac{5.6\, e}{T} + \frac{3.75 \times 10^5\, e}{T^2} \qquad (3)$$

The last two terms can be combined to give, approximately,

$$N = \frac{77.6\, p}{T} + \frac{3.73 \times 10^5\, e}{T^2} \qquad (4)$$

The form is widely used and gives values for N that are accurate within 0.5 percent for the ranges of atmospheric parameters normally encountered and for frequencies below 30 GHz (Ref. 6). If one wishes to consider separately the effects of dry air and water vapor, however, with $N = N_d + N_w$ where N_d refers to dry air and N_w to water vapor, Eq. (2) should be used with

$$N_d = \frac{77.6\, p_d}{T} \qquad (5)$$

and

$$N_w = \frac{72\, e}{T} + \frac{3.75 \times 10^5\, e}{T^2} \qquad (6)$$

B. Excess Range Delay Due to Dry Air

We consider first the magnitude of ΔR_d, the excess range due to dry air, for a zenith path. For this purpose, SI units will be used with p_d in newtons/meter^2 (N/m^2) rather than mb. Then $N_d = 0.776\, p_d/T$ and, by using Eq. (A-3) of the Appendix, p_d/T is replaced by $R\rho/M$ so that

$$N_d = \frac{0.776\, R\rho}{M} \qquad (7)$$

where R is the gas constant, 8.3143×10^3 J/(K kg mol) with J standing for joules. M is the molecular weight in kg mol and is taken as 28.8 corresponding to an atmosphere that is 80 percent molecular nitrogen and 20 percent molecular oxygen. The density ρ in Eq. (7) is in kg/m^3. ΔR_d, the excess range delay due to dry air, can be calculated for a zenith path in terms of N_d by

$$\Delta R_d = 10^{-6} \int N_d \, dh = \frac{10^{-6}\, 0.776\, R}{M} \int_0^\infty \rho \, dh \qquad (8)$$

The surface pressure p_0 is related to density ρ by

$$p_0 = g \int \rho \, dh \qquad (9)$$

where g is the acceleration of gravity and has the value of 9.8 m/s^2 at the Earth's surface. The resulting approximate expression for ΔR_d, using this surface value of g, is

$$\Delta R_d = \frac{(0.776)(8.3143 \times 10^3)}{(28.8)(9.8)(10^6)} p_0$$

so that

$$\Delta R_d = 2.29 \times 10^{-5} p_0, \text{ m} \qquad (10a)$$

with p_0 in N/m^2 and

$$\Delta R_d = 2.29 \times 10^{-3} p_0, \text{ m} \qquad (10b)$$

with p_0 in mb. The pressure p_0 is the surface pressure of dry air and equals total pressure p minus water vapor pressure e. Note that the temperature T drops out and the result depends on surface pressure p_0 only. If $p_0 = 1000$ mb, $\Delta R_d = 2.29$ m. Hopfield (Ref. 7) has examined the applicability of this relation and, using 2.2757 as the coefficient corresponding to the value of g at about 6 km above sea level, has concluded that it allows determination of the range error due to dry air on a zenith path to an accuracy of 0.2 percent or about 0.5 cm. Her form for Eq. (10) is

$$\Delta R_d = 2.2757 \times 10^{-3} p_0 \qquad (10c)$$

with p_0 in mb.

C. Excess Range Delay Due to Water Vapor

The delay caused by water vapor is considerably smaller than that for dry air, but total water vapor content along a path is variable and not predictable with high accuracy from the surface water vapor pressure. Therefore, water vapor is responsible for a larger error or uncertainty in range than dry air. N_w can be expressed in terms of water vapor density ρ rather than water vapor pressure e by using

$$e = \frac{\rho T}{216.7} \qquad (11)$$

as derived in the Appendix, with ρ in g/m^3 and e in mb. N_w then takes the form

$$N_w = 0.3323 \rho + \frac{1.731 \times 10^3 \rho}{T} \qquad (12)$$

from which

$$\Delta R_w = 10^{-6} \int N_w \, dl = 3.323 \times 10^{-7} \int \rho \, dl$$

$$+ 1.731 \times 10^{-3} \int \frac{\rho}{T} dl, \text{ m} \qquad (13)$$

Sometimes the first term of Eqs. (12) and (13) is not used, but for highest accuracy it should be retained. For example, if 1.731×10^3 is divided by a temperature near 280 K, then the first term amounts to about 5 percent of the total delay. The value of the integral of Eq. (13) can be determined from radiosonde data, assuming that ρ and T vary only with height above the surface and not horizontally to a significant degree within the limits of the path.

Microwave radiometry has the advantage of being able to provide continuous real-time estimation of ΔR_w by use of remote sensing techniques. The basic relation utilized for microwave radiometry applies to the brightness temperature T_b that is observed, when a source at a temperature of T_s is viewed through an absorbing medium having a variable temperature T. T_b is given by (Ref. 8)

$$T_b = T_s e^{-\tau_\infty} + \int_0^\infty T(h)\, \alpha(h)\, e^{-\tau} \, dh \qquad (14)$$

with

$$\tau_\infty = \int_0^\infty \alpha(h)\,dh$$

and

$$\tau = \int_0^h \alpha(h)\,dh$$

where $\alpha(h)$ is the attenuation constant that is a function of height h. The expression for T_b takes a simpler form when T is constant or when an effective value T_i can be employed. In that case

$$T_b = T_s e^{-\tau} + T_i(1 - e^{-\tau}) \qquad (15)$$

which form is used for remote sensing of attenuation due to precipitation. The source temperature T_s represents cosmic noise in the case considered here and has a small value. Therefore, attention is directed primarily to the second term of Eq. (14). The attenuation constant $\alpha(h)$ is due to three forms of matter: water vapor, the liquid water of clouds, and oxygen. To obtain information on water vapor, for example, it is necessary to separate out the effects of liquid water and oxygen. The separation can be accomplished by making observations at 2 or more frequencies.

Consider first the problem of obtaining the total water vapor and liquid water content along a tropospheric zenith path. For this purpose, one can use a pair of frequencies such as 20.6 GHz and 31.6 GHz, the first near the peak of and thus sensitive to water vapor absorption and the second more sensitive to liquid water than to water vapor. Taking this approach, M_V and M_l, the total vapor and liquid contents in g/cm², can be obtained from (Refs. 9 and 10)

$$M_V = a_1 + a_2 T_{b_2} + a_3 T_{b_3} \qquad (16)$$

and

$$M_l = b_1 + b_2 T_{b_2} + b_3 T_{b_3} \qquad (17)$$

where T_{b_2} is the brightness temperature at the lower frequency and T_{b_3} is the brightness temperature at the higher frequency. The a's and b's are determined by a process of statistical inversion. Simultaneous radiosonde data and readings of brightness temperature are utilized to carry out this process. For Denver, Colorado, the particular relation obtained is

$$M_V = -0.18 + 0.11\,T_{b_2} - 0.053\,T_{b_3}$$

$$M_L = -0.017 - 0.001\,T_{b_2} + 0.0027\,T_{b_3}$$

The relative sensitivities to water vapor and liquid water are shown by the relative magnitudes of a_2 and a_3 for water vapor and b_2 and b_3 for liquid water. The coefficients a_1 and b_1 take account of oxygen and cosmic noise.

For range delay due to water vapor, however, the integral $\int\rho/T\,dh$ makes a larger contribution than $\int\rho\,dh = M_V$. For determining $\int\rho/T\,dh$, using two frequencies similar to those mentioned above, and therefore, utilizing two equations having the form of Eq (14), leads to (Ref. 11)

$$\frac{T_{b_1} - T_{c_1}}{f_1^2} - \frac{T_{b_2} - T_{c_2}}{f_2^2} = \int_0^\infty W(h)\frac{\rho}{T}\,dh + T_0 \qquad (18)$$

where

$$W(h) = \frac{T^2}{\rho}\left[\frac{\alpha_{v_1}}{f_1^2}e^{-\tau_1} - \frac{\alpha_{v_2}}{f_2^2}e^{-\tau_2}\right] \qquad (19)$$

and

$$T_0 = \int_0^\infty T\left[\frac{\alpha_{0_1}e^{-\tau_1}}{f_1^2} - \frac{\alpha_{0_2}e^{-\tau_2}}{f_2^2}\right] \qquad (20)$$

The total attenuation α is the sum of three contributions so that

$$\alpha = \alpha_V + \alpha_L + \alpha_O \qquad (21)$$

where α_V is the attenuation constant associated with water vapor, α_L is that associated with liquid water, and α_O is associated with oxygen. By assuming that α_L for clouds varies as f^2, α_L has been eliminated and the factors of f_1^2 and f_2^2 appear in the denominators as shown. T_{c_1} and T_{c_2} represent values of the first term of Eq. (14) and, being small, are treated as constants. By suitable choice of frequencies and other refinements, $W(h)$ is made to assume an essentially constant known value so that $\int_0^\infty \rho/T\,dh$ can be determined. Pairs of frequencies that have been found to be satisfactory are

20.3 and 31.4 GHz, 20.0 and 26.5 GHz, and 24.5 and 31.4 GHz (Ref. 11).

The development and testing of water vapor radiometers has received considerable attention at the Jet Propulsion Laboratory (Refs. 11 through 15). One of the systems developed utilized 18.5 and 22.235 GHz as the frequency pair, this combination having the advantage of using the same size of waveguide for both frequencies (Ref. 14). It was concluded later, however, that the 20.3 and 31.4 GHz pair provided better performance.

Profiles of tropospheric temperature can also be obtained by microwave radiometry utilizing three frequencies near the 60-GHz oxygen absorption peak and one frequency each near 20 GHz and 30 GHz to separate out water vapor and liquid water effects (Ref. 10). Oxygen is a major constituent of and occurs as an essentially fixed fraction of the tropospheric composition, and the temperature of oxygen at a given height is thus the temperature of the troposphere at that height. The frequencies utilized allow a coarse determination of the water vapor profile as well, but the use of several frequencies near the peak of a strong water vapor absorption line such as that at 183 GHz is stated to be necessary to provide accurate profiles of water vapor content (Ref. 10).

D. Illustrative Calculated and Measured Values of Excess Delay Due to Water Vapor

The precise value of ΔR_w in a particular situation depends on the water vapor and temperature profiles, but an indication of the magnitude of ΔR_w can be obtained by assuming an exponential decrease of N_w with a scale height H of 2 km, a water vapor density ρ at the surface of 7.5 g/m^3, and a temperature of 281.65 K (that for a standard atmosphere at an altitude of 1 km). It is of interest that the value obtained for ΔR_w in this way is the same as if N_w were constant up to the height H and zero beyond. The values of 7.5 g/m^3 and 2 km are mentioned as being representative values in CCIR Report 719 (Ref. 16). The values of ρ and T at the surface result in values of e and N_w of 9.748 mb and 48.57, respectively. Then, for a zenith path,

$$\Delta R_w = 10^{-6} \int_0^{\infty} 48.57\, e^{-h/2000}\, dh$$

$$= 10^{-6}(48.57)(2000) = 0.0972 \text{ m}$$

$$= 9.72 \text{ cm} \qquad (22)$$

The excess range due to water vapor for a zenith path may thus be about 10 cm. For paths at elevation angle θ of about 10 deg or greater, the range delay equals the zenith value divided by sin θ. That is,

$$\Delta R(\theta) = \frac{\Delta R(\theta = 90 \text{ deg})}{\sin \theta} \qquad (23)$$

For an elevation angle of 30 deg, for example, ΔR_w might be about 20 cm.

An extreme value of 44.8 cm for ΔR_w for a zenith path could occur for the highest accepted weather observatory values for e and ρ of 53.2 mb and 37.6 g/m^3, respectively, at the temperature of 34°C (Ref. 17). These values were recorded at Sharjah, Saudi Arabia, on the Persian Gulf. The value of ΔR_w of 44.8 cm is based on an exponential decrease of N_w with a scale height of 2 km as in the previous example.

Mean zenith values of ΔR_w determined from radiosonde measurements in a semiarid location in California ranged from 4 to 16 cm (Ref. 18). With respect to the accuracy to which ΔR_w can be determined, Wu (Ref. 11) stated that the calibration for water vapor delay, using a water vapor radiometer, is accurate to $\leq$ 2 cm at all elevation angles greater than 15 deg. Slobin and Batelaan (Ref. 15) state that the rms error in ΔR_w, as determined by a water vapor radiometer, was less than 1 cm over a total delay range of 9 to 38 cm at a 30 deg elevation angle.

E. Time Delay

Range delay and time delay are directly related. If one prefers to think in terms of time delay Δt or wishes to determine numerical values of time delay corresponding to values of range delay, use

$$\Delta t = \frac{\Delta R}{c} \qquad (24)$$

for one-way paths. For monostatic radar modes of operation for which electromagnetic waves twice traverse the distance from the original transmitter to the target or repeater,

$$\Delta t = \frac{2\Delta R}{c} \qquad (25)$$

A range delay of 10 cm for water vapor on a one-way path corresponds to a time delay of 0.333 ns. The extreme range delay on a one-way zenith path of 44.8 cm is equivalent to a time delay of 1.5 ns.

III. Excess Range Delay Due to Liquid Water

A. Effective Index of Refraction of Medium

The liquid water content of the troposphere can also make a contribution to range delay. To distinguish the range delays due to water vapor and liquid water, we shall henceforth use ΔR_1 for the delay due to water vapor and ΔR_2 for the contribution due to liquid water. To determine ΔR_2 due to the small droplets of clouds, one can make use of the fact that a small spherical particle in the presence of a sinusoidally time-varying electric field acts as a tiny antenna having an electric dipole moment p_1. By application of Laplace's equation (Ref. 19, pp. 218 to 224, for example), it can be shown that, when the drop diameter is small compared to wavelength, p_1 is given by

$$p_1 = 3V\left(\frac{n^2 - 1}{n^2 + 2}\right)\epsilon_0 E_0 \tag{26}$$

where V is the volume of the spherical particle and n is now the index of refraction of the particle, in the case of interest here the index of refraction of water. The quantity ϵ_0 is the electric permittivity of empty space (8.854×10^{-12} F/m) and E_0 is the electric field intensity of the incident wave in V/m. In a region containing N such particles per unit volume

$$P = Np_1 = 3NV\left(\frac{n^2 - 1}{n^2 + 2}\right)\epsilon_0 E_0 \tag{27}$$

where P is the electric dipole moment or electric polarization per unit volume (considering only the effect of the spherical water particles and neglecting all other possible contributions to P). The basic relations, by definition, between E, D (electric flux density), and P for an isotropic medium are that

$$D = \epsilon_0 E + P = \epsilon_0 (1 + \chi)E = \epsilon_0 K E \tag{28}$$

where K is the relative dielectric constant and χ is electric susceptibility. The relative dielectric constant K (commonly designated by ϵ_r) is equal to ϵ/ϵ_0, where ϵ is the electric permittivity of the medium. D and P have units of C/m^2. From Eq. (28),

$$K = 1 + \chi \tag{29}$$

In the case considered here, K is an effective relative dielectric constant of a medium consisting of small spherical water droplets in empty space.

The excess range delay in the medium is proportional to the index of refraction of the medium minus unity as in Eq. (1). As n has already been used in Section III for the index of refraction of water, however, we will use m for the index of refraction of the medium. Index of refraction squared equals relative dielectric constant. Thus

$$m^2 = K \tag{30}$$

Then as, in general, $(1 + a)^{1/2} = 1 + a/2$ for $a << 1$ and in this case χ is much less than 1,

$$m = 1 + \frac{\chi}{2} \tag{31}$$

By comparison of Eqs. (27) and (28),

$$\chi = 3NV\left(\frac{n^2 - 1}{n^2 + 2}\right) \tag{32}$$

and

$$m - 1 = \frac{\chi}{2} = \frac{3NV}{2}\left(\frac{n^2 - 1}{n^2 + 2}\right) \tag{33}$$

The relation comparable to Eq. (1) for determining the excess range delay ΔR_2 due to the liquid water content of the troposphere is

$$\Delta R_2 = \int Re\,(m - 1)\,dl \tag{34}$$

Here m is used in place of the n of Eq. (1) and the expression indicates that the real part of $m - 1$ should be used. This notation is needed because the index of refraction of water is complex and m is therefore complex also. The real part of m determines the phase shift and range delay, and the imaginary part determines attenuation. In deriving Eq. (33), no mention was made of the lossy nature of the droplets, but relations derived for a lossless medium can be applied to the lossy case by merely utilizing the proper complex value in place of the real value. Whereas the index of refraction of dry air and water vapor are independent of frequency in the radio frequency range up to about 50 GHz, the index of refraction of liquid water is a function of frequency and temperature.

B. Illustration of Excess Range Delay Due to a Cloud

To illustrate the range delay due to water droplets in a cloud, consider the range delay for a zenith path through a dense cloud 1-km thick and having a water content of 1 g/m^3. For a frequency of $f = 3$ GHz and a temperature of $T = 20$°C, it can be determined from curves given by Zufferey (Ref. 20) (see also Hogg and Chu (Ref 21), or values presented by Gunn and East (Ref. 22)), that $n = 8.88 - j\,0.63$. As water has a density of 1 g/cm^3, the water content of 1 g/m^3 fills only 10^{-6} of a cubic meter. Then NV of Eq. (33) is 10^{-6} so that

$$m - 1 = \frac{3}{2}10^{-6}\left[\frac{(8.88 - j\,0.63)^2 - 1}{(8.88 - j\,0.63)^2 + 2}\right]$$

and

$$Re\,(m - 1) = 3/2\,(0.967)(10^{-6})$$

$$= 1.45 \times 10^{-6}$$

As a region of uniform water content and a thickness of 1 km is assumed, the integral of Eq. (26) simplifies to become the product of $Re\,(m - 1)$ and 10^3 m so that

$$R_2 = 1.45 \times 10^{-6}\,(10^3)$$

$$= 1.45 \times 10^{-3}\text{ m}$$

$$= 0.145\text{ cm}$$

For $f = 10$ GHz, $n = 8.2 - j\,1.8$ and the value of ΔR_2 is 0.144 cm, while for $f = 30$ GHz, $n = 6 - j\,2.8$ but ΔR_2 is still about 0.144 cm. The excess range delay in this case is quite insensitive to the value of n, which condition might be anticipated by noting that n^2 appears in both the numerator and denominator of Eq. (33). The excess delay is therefore insensitive to frequency as well.

The water content of 1 g/m^3 assumed in the above example is that of a rather dense cloud, but it has been reported that the maximum water content of clouds lies between 6 and 10 g/m^3 (Ref. 23).

C. Excess Range Delay Due to Rain

Raindrops are considerably larger than the small droplets of clouds, and to analyze the effects of raindrops one must generally use the Mie scattering theory or refinements of it. The technique of deriving an equivalent index of refraction can nevertheless be employed for rain, this approach has been utilized most extensively for determining the attenuation constant for propagation through rain. If $m = m_r - im_i$, the field intensity attenuation constant α is given by

$$\alpha = \beta_0\,m_i \text{ neper/m} \qquad (35)$$

where $\beta_0 = 2\pi/\lambda_0$ is the phase constant and λ_0 is wavelength for propagation in empty space. (One neper equals 8.68 dB.) The phase constant β for propagation through a region of rain is given by

$$\beta = \beta_0\,m_r \text{ rad/m} \qquad (36)$$

For calculating the excess range delay ΔR_2 due to rain, one can use

$$\int Re\,(m - 1)\,dl = \int (m_r - 1)\,dl \qquad (37)$$

Tables giving values of $m_r - 1$ have been provided by Setzer (Ref. 24), and Zufferey (Ref. 20) has presented these values in graphical form (Fig. 1). Setzer's value for $m_r - 1$ for a rain of 25 mm/h at a frequency of 3 GHz, for example, is 1.8×10^{-6}. The excess range delay in a 1-km path of uniform rain of that rate is $(1.8 \times 10^{-6})\,(10^3) = 0.18$ cm, a value comparable to that for a zenith path through a cloud 1-km thick. For a heavy rain of 150 mm/h, the delay would be 0.92 cm in 1 km.

For estimating total excess range delay due to rain, one needs an estimate of effective path length through rain. This topic of effective path length has been considered with respect to estimating attenuation due to rain (Refs. 25, 26). Rain is largely confined below the 0°C isotherm, and the height of the isotherm and the elevation angle of the path determine the path length through rain. In addition, it develops that the average rain rate along a path tends to differ from the instantaneous point rain rate, the average rate being less than the point rate for heavy rains. Effective path lengths through rain tend to be in the order of 4 or 5 km for an elevation angle of 45 deg at a latitude of 40°N (Ref. 20) and these figures can be used as a rough guide. Information on the height of the 0°C isotherm as a function of probability of occurrence is given in Fig. 2. In contrast with attenuation in rain which increases with frequency up to about 150 GHz, excess range delay decreases above 10 GHz and stays nearly constant below 10 GHz to 1 GHz or lower, but has modest maxima in the 6- to 10-Ghz range, depending on rain rate (Fig. 1). It appears that the excess range delay due to rain may be of significance in some heavy rainstorms.

The concept of an equivalent index of refraction of a medium containing small particles has been discussed by van de Hulst (Ref. 27) and Kerker (Ref 28), but early consideration of this topic is attributed by Kerker to an 1899 paper by Rayleigh and 1890 and 1898 papers by Lorenz.

IV. Phase Delay and Doppler Frequency

A. Relations Between Range and Time Delay, Phase Delay, and Doppler Frequency

Range delay, time delay, and phase delay are all directly and simply related. It was pointed out in Section II that time delay Δt is related to range delay ΔR by

$$\Delta t = \frac{\Delta R}{c}$$

for a one-way path. The phase delay $\Delta\phi$ associated with a range delay can be determined by taking the product of the range delay ΔR and the phase constant β_0. Thus

$$\Delta\phi = \beta_0 \Delta R = \frac{2\pi}{\lambda_0}\Delta R = \frac{2\pi f}{c}\Delta R \tag{38}$$

Doppler frequency f_D and phase ϕ are related by

$$f_D = \frac{1}{2\pi}\frac{d\phi}{dt}, \text{Hz} \tag{39}$$

This relation can also be written in terms of finite quantities as

$$f_D = \frac{1}{2\pi}\frac{\Delta\phi}{T_c}, \text{Hz} \tag{40}$$

where T_c is a count time or count interval. Also, as $\Delta\phi = (2\pi/\lambda_0)\,\Delta R$,

$$f_D = \frac{1}{\lambda_0}\frac{\Delta R}{T_c} = \frac{v_R}{\lambda_0}, \text{Hz} \tag{41}$$

for a one-way path, where v_R is the average radial component of velocity and f_D is the average Doppler frequency during the time T_c. For a two-way ranging system,

$$f_D = \frac{2v_R}{\lambda_0} \tag{42}$$

It can be noted that if a value f_D is recorded during an interval T_c, a corresponding change in range ΔR has taken place during T_c. In this case, ΔR can represent either a true change in range or a change in excess range delay or a combination of the two. (Elsewhere ΔR has been used for total excess range due to water vapor or liquid water, but in this section ΔR is any arbitrary change or increment or range.) For an accuracy of 10^{-5} m/s in velocity T_c may be as low as 1 to 10 s when a spacecraft is near the Earth or another planet, or it may be as long as 1000 s when the spacecraft is in a cruise phase (Ref. 29).

B. Doppler Frequency Noise

Precise calculation of range delay due to the troposphere requires information concerning the water vapor, liquid water, and temperature profiles, but representative values can be calculated readily. Fewer data concerning Doppler frequency are available and it is somewhat more difficult to establish representative values for Doppler frequency noise. Both bulk changes in water vapor and liquid water content along the path and tropospheric scintillation involving scatter from turbulent irregularities can contribute to this noise. The term scintillation is usually applied to rather rapid variations of amplitude, phase, and angle of arrival. For considering tropospheric effects, it may be distintuished from refractive fading that results from the large-scale structure of the index of refraction and tends to involve amplitude variations of fairly large magnitude but of lower frequency than scintillation.

Because of the relations between phase, excess range delay, time delay, and Doppler frequency, the occurrence of phase scintillation implies also the occurrence of range and time delay jitter and Doppler noise. The noise is generated in proportion to the rate of change of phase as indicated by Eqs. (39) and (40). In some investigations of phase scintillation, records were taken showing the variation of phase with time. These allow the determination of corresponding Doppler frequency values. Using phase records obtained by Thompson, et al., (Ref. 30) in Hawaii, Armstrong, Woo, and Estabrook (Ref. 3) estimated the fractional Doppler frequency stability for propagation through the troposphere on Earth-space paths for a 1000-s count interval to be about 5×10^{-14} or less $[\sigma_y\,(1000\ \text{s}) \sim 5 \times 10^{-14}$ where σ_y is referred to as an Allan variance$]$. It was estimated also that plasma scintillation at S-band, primarily involving the solar plasma contribution which dominates the ionospheric contribution, would cause noise corresponding to $\sigma_y\,(1000\ \text{s}) \sim 3 \times 10^{-14}$. Minimum Doppler frequency noise due to the solar plasma is observed in the antisolar direction. Use of an X-band system is estimated to reduce the plasma noise to that corresponding to σ_y $(1000\ \text{s}) \sim 3 \times 10^{-15}$. Thus it was inferred that tropospheric scintillation may dominate for the case of an X-band system. Also using data from Thompson, et al., (Ref. 30) and radiosonde data from Edwards Air Force Base, California, as well, Berman and Slobin (Ref. 18) have estimated a fractional Doppler frequency stability for two-way propagation and a 1000-s count interval as 6×10^{-14}.

C. Gravitational Waves

It is generally considered that gravitational waves may produce a fractional variation in Doppler frequency equal to or less than about 10^{-15} (Refs 2 and 3). Thus detection of gravitational waves will require careful attention and efforts to minimize the effects of all sources of Doppler noise and instability. On sufficiently long paths, gravitational waves should impart a characteristic triple-impulse signature to the Doppler record. The three impulses arise from buffeting of the spacecraft and Earth by the passing gravitational wave and in[illegible]e the travel times between the Earth and spacecraft. For example, the gravitational wave might first buffet the Earth and the antenna of the telecommunication system and thus produce an immediate corresponding Doppler impulse in the received signal. Then the gravitational wave might buffet the spacecraft, and this would produce an impulse in the Doppler record after a time delay corresponding to the travel time from the spacecraft to Earth. Finally, a third impulse would appear in the Doppler record of the received signal, corresponding to the original buffeting of the Earth antenna, but delayed by the travel time from the Earth to the spacecraft and back. The form of the actual sequence of impulses would depend upon the geometrical configuration of the Earth and spacecraft and the direction of travel of the gravitational wave. An effect due to clock speedup is also expected (Ref. 2). As the periods of gravitational impulses are long (10 to 10,000 s), long telecommunications paths involving round-trip travel times of about 1000 s and longer are required for the detection of gravitational waves by the technique under discussion.

V. Excess Range Delay in Terms of Total Water Vapor and Liquid Water Content

A. Delay Due to Liquid Water

Consideration is given in this section to expressing excess range delay in terms of the total masses of water vapor and liquid water in a vertical column. Expressions of this type have been in use (Ref 15), and the basis for them will now be examined. The case of the small water droplets of a cloud is the simplest to analyze. For this purpose, Eq. (33) is repeated below.

$$m - 1 = \frac{\chi}{2} = \frac{3NV}{2}\left(\frac{n^2 - 1}{n^2 + 2}\right) \tag{33}$$

Range delay ΔR_2 for a zenith path through a uniform cloud of thickness h is given by

$$\Delta R_2 = (m - 1)h \tag{43}$$

which is merely a statement of Eq (34) for a uniform cloud. The total liquid water content in a vertical column M_L is given for the uniform case by

$$M_L = NVh\rho \tag{44}$$

where N is the number of droplets per unit volume, V is the volume of an individual droplet, h is the vertical extent of the cloud, and ρ is the density of water, namely 1000 kg/m^3 in SI units. Of the four factors of Eq (44), all but ρ already appear in the expression for ΔR_2. The remaining quantities in the expression for ΔR_2 are $3/2\ (n^2 - 1)/(n^2 + 2)$, which equals $(3/2)(0.967) = 1.45$ for $f = 3$ GHz. If $\rho = 10^3$ is to be introduced into Eq (35) where it did not originally appear, so that ΔR_2 can be expressed in terms of M_L, a factor of 10^{-3} must be introduced to compensate. Thus

$$\Delta R_2 = 1.45 \times 10^{-3} M_l \text{, m} \tag{45}$$

with M_L for the example of Section III having the value of $(10^{-6})(10^3)(10^3) = 1$ kg/m^2, where the three factors represent NV, h, and ρ respectively. If it is desired to express ΔR_2 in cm and M_L in g/cm^2, then

$$\Delta R_2 = 1.45 M_L \text{, cm} \tag{46}$$

with $M_L = 0.1$ g/cm^2 for the same example of Section III. For other frequencies, the value of $(n^2-1)/(n^2+2)$ will change only very slightly, so Eqs (45) and (46) are generally applicable with reasonable accuracy. The expressions apply to the small droplets of clouds, or in general, when Rayleigh scattering can be assumed to take place. The droplets of clouds actually vary in size such that one should use a summation $\Sigma N_i V_i$ in place of NV, but the simple form of Eq. (33) is sufficient for present purposes.

B. Delay Due to Water Vapor

Consider next the case of water vapor. The applicable expression in this case is

$$\Delta R_w = 3.323 \times 10^{-7} \int \rho\, dl + 1.731 \times 10^{-3} \int \frac{\rho}{T}\, dl \tag{13}$$

with ρ in g/m^3 or

$$\Delta R_w = 3.323 \times 10^{-4} \int \rho\, dl + 1.731 \int \frac{\rho}{T}\, dl \tag{47}$$

with ρ in kg/m^3. The delay is a function of temperature as well as total water vapor content. If T is taken to be 281.65 K (the temperature in a standard atmosphere at an elevation above sea level of 1 km) as was assumed in Section II,

$$\Delta R_v = 6.48 \times 10^{-3} M_V \text{, m} \tag{48}$$

where M_V, the mass of water vapor in a vertical column, equals $\int \rho\, dl$, and, in the example of Section II with ρ =

7.5 g/m^3 = 7.5 × 10^{-3} kg/m^3 at the surface and a scale height of 2 km, is 15 kg/m^2. If it is desired to express ΔR_1 in cm and M_V in g/cm^2, then

$$\Delta R_1 = 6.48\, M_V, \text{cm} \tag{49}$$

For the same example of Section II, M_V = 1.5 g/cm^2 and ΔR_1 = 9.72 cm. Equations (48) and (49) apply strictly only for a constant or average value of temperature of 281.65 K, and choice of this value, while reasonable, was arbitrary. However, the equations can be used for rough estimates of ΔR_1 if deisred, and if the temperature profile does not depart excessively from the constant value assumed here.

C. Combined Delay

The combined delay due to water vapor and small water droplets on a zenith path is given roughly by

$$\Delta R = \Delta R_1 + \Delta R_2 = 6.48\ M_V + 1.45\, M_L, \text{cm} \tag{50}$$

with M_V and M_L in g/cm^2. The delay due to water vapor ΔR_1 is actually a function of temperature as well as the mass of water vapor in a vertical column M_L. If information on temperature and water vapor profiles are available, Eq. (13) should be used for ΔR_1 instead of Eqs. (48 through 50) to obtain a better estimate.

VI. Conclusion

The excess range delay due to water vapor and liquid water content of the troposphere require attention when high precision is required for range measurement on Earth-space paths. The physical factors affecting excess range delay have been discussed and illustrative calculations of range delay have been presented in this report. The use of radiometer techniques for continuous monitoring of the range delay and Doppler frequency due to water vapor appears to be advantageous when high precision is required. The various possible systems for accomplishing this purpose should be carefully considered. The same general principles have been used for remotely sensing the water vapor and liquid water content of the atmosphere from Nimbus satellites (Refs. 31 and 32), but in these applications total water vapor content, $\int \rho\, dh$, and not $\int (\rho/T)\, dh$, is obtained.

Excess range delay at an elevation angle θ, $\Delta R(\theta)$, may generally be related to delay for a zenith path (θ = 90 deg) for elevation angles greater than about 10 deg by

$$\Delta R(\theta) = \frac{\Delta R(\theta = 90\ \text{deg})}{\sin\theta} \tag{23}$$

For clouds, information on the thickness and liquid water density of a cloud is required to estimate range. For estimating excess range delay through rain as accurately as possible, one needs to take into account that average rain rates tend to be less than point rain rates for heavy rains (Refs. 25 and 26).

The separate but related topic of Doppler frequency noise has been considered briefly. Whereas range delay involves the integral of the index of refraction minus unity along a path, Doppler frequency noise involves the time rate of change of the integral. Range delay can be analyzed as involving propagation in a locally homogeneous medium, but consideration of Doppler noise requires attention to scintillation, involving scatter from inhomogeneities as well. Variations in range delay imply Doppler frequency noise, and Doppler frequency noise implies jitter in range. Correction for range delay allows increased precision in range measurement. Minimizing Doppler frequency noise of interplanetary origin by moving to higher frequencies increases the probability of detecting weak effects such as gravitational waves, but Doppler noise of tropospheric origin may then dominate.

When striving for the highest possible precision in range measurement, the limitations posed by the state of knowledge of the velocity of light should be kept in mind. The value of c of 299,792.458 m/s involves a fractional uncertainty $\Delta c/c$ of ±4 × 10^{-9} (Ref. 33). Specifying c to nine significant figures may seem impressive, but the fractional uncertainty in c corresponds to an uncertainty in velocity of 1.2 m/s and an uncertainty in meters in one-way range of 1.2 times the propagation times in seconds. For spacecraft near Saturn, say at 10 AU, the corresponding uncertainty in absolute range is about 6 km. This consideration should not be regarded as unduly discouraging. When using the VLBI technique, for example, it is the difference in range to the spacecraft from two locations that is important and not the absolute range. In other situations, it is the consistency and precision of range measurements that is essential, rather than accuracy of absolute range. One should take care, however, not to imply that the precisions of a few meters or centimeters in range measurement on long paths represent the accuracies to which absolute range can be measured.

C-2

Acknowledgments

I would like to express my appreciation to T. A. Komarek, E. K. Smith, J. G. Meeker, S. D. Slobin, and B. Gary for helpful discussions and for encouraging and supporting the effort on this report.

References

1. Anderson, J. D., and Estabrook, F. B., "Application of DSN Spacecraft Tracking Technology to Experimental Gravitation," *J. of Spacecraft and Rockets*, Vol. 16, pp. 120-125, March-April 1979.
2. Berman, A. L., "The Gravitational Wave Detection Experiment: Description and Anticipated Requirements," in *The Deep Space Network Progress Report 42-46*, Jet Propulsion Laboratory, Pasadena, Calif., pp. 100-108, May and June 1978.
3. Armstrong, J. W., Woo, R., and Estabrook, F. B., "Interplanetary Phase Scintillation and the Search for Very Low Frequency Gravitational Radiation," *Astrophysical Journal*, Vol. 230, pp. 570-749, June 1, 1979.
4. Smith, E. K., and Weintraub, S., "The Constants in the Equation for Atmospheric Refractive Index at Radio Frequencies," *Proc. IRE*, Vol. 41, pp. 1035-1037, August 1953.
5. List, R. J., *Smithsonian Meteorological Tables*, Sixth Revised Edition, Washington, D.C., Smithsonian Institution, 1958.
6. Crane, R. K., "Refraction Effects in the Neutral Atmosphere," in *Methods of Experimental Physics*, Vol. 12, *Astrophysics*, Part B: *Radio Telescopes* (M. L. Meeks, ed.), pp. 186-200. New York: Academic Press, 1976.
7. Hopfield, H. S., "Tropospheric Effect on Electromagnetically Measured Range: Prediction from Surface Weather Data," *Radio Science*, Vol. 6, pp. 357-367, March 1971.
8. Waters, J. W., "Absorption and Emission by Atmospheric Gases," in *Methods of Experimental Physics*, Vol. 12, *Astrophysics*, Part B: *Radio Telescopes* (M. L. Meeks, ed.), pp. 142-176. New York: Academic Press, 1976.
9. Guiraud, F. E., Howard, J., and Hogg, D. C., "A Dual-channel Microwave Radiometer for Measurement of Precipitable Water Vapor and Liquid," *IEEE Trans. on Geoscience Electronics*, Vol. GE-17, pp. 129-136, October 1979.
10. Hogg, D. C., "Ground-based Remote Sensing and Profiling of the Lower Atmosphere using Radio Wavelengths," *IEEE Trans. on Antennas and Propagation*, Vol AP-28, pp. 281-283, March 1980.
11. Wu, S. C., "Frequency Selection and Calibration of a Water Vapor Radiometer," in *The Deep Space Network Progress Report 42-43*, Jet Propulsion Laboratory, Pasadena, Calif., pp. 67-81, Nov. and Dec. 1977.
12. Winn, F. B., et al., "Atmospheric Water Vapor Calibrations: Radiometer Technique," in *The Deep Space Network Progress Report 42-32*, Jet Propulsion Laboratory, Pasadena, Calif., pp. 38-44, Jan and Feb. 1976.

13. Claflin, E. S., Wu, S. C., and Resch, G. M., "Microwave Radiometer Measurement of Water Vapor Path Delay: Data Reduction Techniques," in *The Deep Space Network Progress Report 42-48*, Jet Propulsion Laboratory, Pasadena, Calif., pp. 22-30, Sept. and Oct. 1978.

14. Batelaan, P. D., and Slobin, S. D., "DSN Water Vapor Radiometer Development – Recent Work, 1978," in *The Deep Space Network Progress Report 42-48*, Jet Propulsion Laboratory, Pasadena, Calif., pp. 129-135, Sept. and Oct. 1978.

15. Slobin, S. D., and Batelaan, P. D., "DSN Water Vapor Radiometer – Tropospheric Range Delay Calibration," in *The Deep Space Network Progress Report 42-49*, Jet Propulsion Laboratory, Pasadena, Calif., pp. 136-145, Nov. and Dec. 1978.

16. CCIR, "Attenuation by Atmospheric Gases," Report 719, pp. 97-102, in *Recommendations and Reports of the CCIR, 1978*, Vol. V, *Propagation in Non-ionized Media*, Geneva: ITU, 1978.

17. *U.S. Standard Atmosphere, 1976*, sponsored by NOAA, NASA, USAF. Washington, D.C.: Supt. of Documents, U.S. Government Printing Office, 1976.

18. Berman, A. L., and Slobin, S. D., "Tropospheric Path Length Fluctuation in Temperate Semiarid Locales: Application to the Gravitational Wave Detection Experiment," in *The Deep Space Network Progress Report 42-55*, Jet Propulsion Laboratory, Pasadena, Calif., pp. 79-85, Nov. and Dec. 1979.

19. Ramo, S., Whinnery, J. R. and Van Duzer, T., *Fields and Waves in Communication Electronics*, New York: Wiley, 1965.

20. Zufferey, C. H., *A Study of Rain Effects on Electromagnetic Waves in the 1-600 GHz Range*, M. S. Thesis, Boulder, Co.: Department of Electrical Engineering, U. of Colorado, 1972 (reprinted in 1979).

21. Hogg, D. C., and Chu, T. S., "The Role of Rain in Satellite Communications," *Proc. IEEE*, Vol. 63, pp. 1308-1331, Sept. 1975.

22. Gunn, K. L. S., and East, T. W. R., "The Microwave Properties of Precipitation Particles," *Quart. J. Roy. Meteor. Soc.*, Vol. 80, pp. 522-545, 1954.

23. Valley, S L. (ed.), *Handbook of Geophysics and Space Environment*, Air Force Cambridge Research Laboratories, New York: McGraw-Hill 1965.

24. Setzer, D. E., "Computed Transmission through Rain at Microwave and Visible Frequencies," *Bell System Tech. Jour.*, Vol. 49, pp. 1873-1892, Oct. 1970.

25. Karl, R., Wallace, R., and Kinal, G., *A Propagation Effects Handbook for Satellite System Design, A Summary of Propagation Impairments on 10-100 GHz Satellite Links with Techniques for System Design*, Washington, D.C.: NASA Communications Division, NASA Headquarters, March 1980.

26. Crane, R. K., "Prediction of Attenuation by Rain," *IEEE Trans. on Communications*, Vol. COM-28, pp. 1717-1733, Sept. 1980.

27. van de Hulst, H. C., *Light Scattering by Small Particles*. New York Wiley, 1957.

28. Kerker, M., *The Scattering of Light and Other Electromagnetic Radiation*, New York: Academic Press, 1969.

29. Moyer, T. D., *Mathematical Formulation of the Double-Precision Orbit Determination Program (DPODP)*, Technical Report 32-1527, Jet Propulsion Laboratory, Pasadena, Calif., May 15, 1971.

30. Thompson. M. C., Wood, L. E., Janes, H. B., and Smith. D., "Phase and Amplitude Scintillations in the 10 to 40 GHz band," *IEEE Trans. on Antennas and Propagation*, Vol. AP-23, pp. 792-797, Nov. 1975.

31. Grody, N. C., "Remote Sensing of Atmospheric Water Content from Satellites using Microwave Radiometry," *IEEE Trans. on Antennas and Propagation*, Vol. AP-24, pp. 155-162, March 1976.

32. Chang, A. T. C., and Wilheit. T. T., "Remote Sensing of Atmospheric Water Vapor, Liquid Water, and Wind Speed at the Ocean Surface by Passive Microwave Techniques from the Nimbus 5 Satellite," *Radio Science*, Vol. 14. pp. 793-802, Sept.-Oct. 1979.

33. Evenson, K. M., "The Development of Direct Optical Frequency Measurement and the Speed of Light," *ISA Transactions*, Vol. 14, pp. 209-216, 1975.

Table 1 Saturation water vapor pressure, e_s in mb [adapted from Smithsonian Meteorological Tables, 1958 (Ref. 5)]

T, °C	e_S, mb	T, °C	e_S, mb
-30	0.5	20	23.4
-20	1.3	22	26.4
-10	2.9	24	29.8
0	6.1	26	33.6
2	7.1	28	37.8
4	8.1	30	42.4
6	9.3	32	47.6
8	10.7	34	53.2
10	12.3	36	59.4
12	14.0	38	66.3
14	16.0	40	73.8
18	20.6		

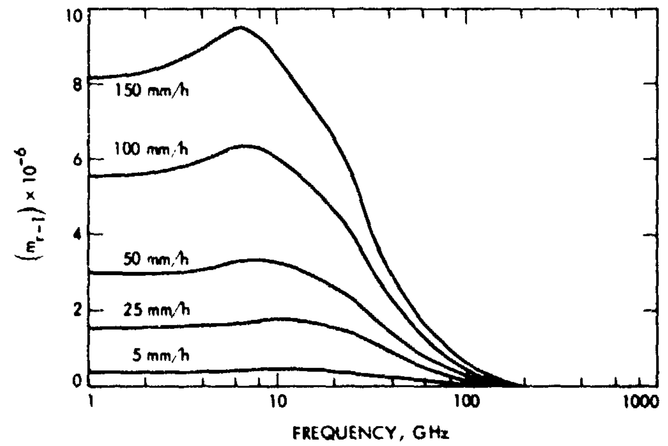

Fig. 1. The real part of the equivalent index of refraction minus unity (m_r - 1) of a medium consisting of raindrops in empty space, as a function of frequency (Ref. 20) (Temperature 20°C; Laws and Parsons distribution)

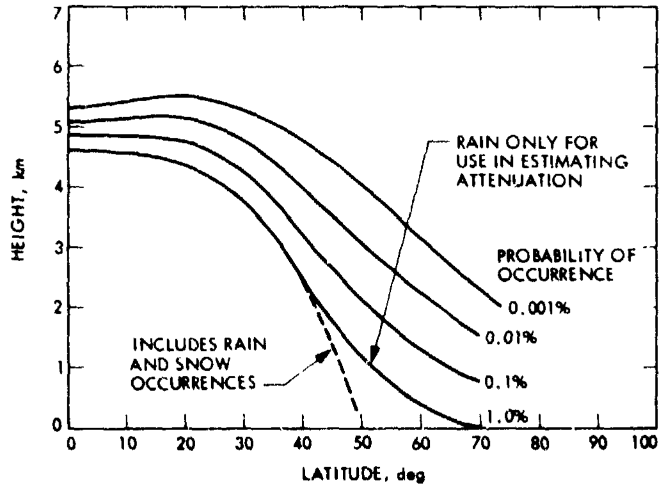

Fig. 2. Height of the 0°C isotherm as a function of latitude and probability of occurrence (Ref. 26)

Appendix

Relation Between Water Vapor Pressure and Density

The perfect gas law in the form applying to one molecular weight of gas is

$$pv = RT \tag{A-1}$$

where, in SI units, p is pressure in N/m^2; v is specific volume in m^3; R is the gas constant, 8.314×10^3 J/(K kg mol), where J stands for joules and T is temperature in kelvins. To obtain density ρ in kg/m^3, use

$$\rho = \frac{M}{v} = \frac{pM}{RT} \tag{A-2}$$

where M is molecular weight in kg mol. Also note that

$$\frac{p}{T} = \frac{R}{v} = \frac{R\rho}{M} \tag{A-3}$$

If we apply Eq. (A-2) to water vapor and thus set p equal to e, the water vapor pressure in N/m^2, and M equal to 18.02 kg,

$$\rho = \frac{e\ 18.02}{8.3143 \times 10^3 T} = \frac{2.167 \times 10^{-3}\, e}{T}, \text{ kg/m}^3 \tag{A-4}$$

If e is to be expressed in mb, however, rather than N/m^2,

$$\rho = \frac{0.2167 e}{T}, \text{ kg/m}^3 \tag{A-5}$$

Finally for $\rho = g/m^3$ and e in mb,

$$\rho = \frac{216.7\, e}{T}, \text{ g/m}^3 \tag{A-6}$$

D/12

N81-27135

Atmospheric Noise Temperature Measurements

C. T. Stelzried
Radio Frequency and Microwave Subsystems Section

Radiometric microwave noise temperature measurements are used to estimate atmospheric transmission loss. It is common practice to use the following lumped element model expression for the noise temperature contribution,

$$T'' = T_p (1 - 1/L).$$

This relationship is used to estimate the transmission loss L in terms of T'' and the atmosphere effective physical temperature T_p. This report evaluates T_p in terms of assumed distributed loss and temperature models. Simplified expressions are presented for low loss applications. For these applications L is determined directly and accurately without integration or iteration.

I. Summary

Radiometric microwave noise temperature measurements are used to estimate atmospheric transmission loss. It is common practice to use the lumped element model expression for the noise temperature contribution

$$T'' = T_p (1 - 1/L)$$

This relationship is used to estimate the transmission loss L in terms of T'' and the atmospheric effective physical temperature T_p. This report evaluates T_p in terms of assumed distributed loss and temperature models For exponential loss and linear temperature distributions

$$T_p = T_1 + k(T_2 - T_1)$$

where

$$k = \frac{1 - I}{1 - 1/L}$$

$$I = \frac{1}{(\ln \alpha_2/\alpha_1) e^{\alpha_2/a}} \int_{\alpha_1/a}^{\alpha_2/a} \frac{e^z}{z} \, dz$$

These equations are evaluated and T_p is presented for a range of values for L and α_2/α_1. For low loss ($L \approx 1$)

$$k \simeq \frac{\alpha_2/\alpha_1}{(\alpha_2/\alpha_1) - 1} - \frac{1}{\ln(\alpha_2/\alpha_1)}$$

As an example, if $\alpha_2/\alpha_1 = 10$, we have $k = 0.6768$. Then for this model

$$T_p \simeq T_1 + 0.6768\,(T_2 - T_1)\,.$$

This provides a useful estimate of T_p (in some applications T_1 is estimated and T_2 measured). Then from the lumped element model

$$L = \frac{1}{1 - T''/T_p}$$

This indicates that for low loss, L can be directly and accurately determined from these models without integration or iteration.

II. Introduction

Radiometer microwave noise temperature measurements are used to estimate atmospheric transmission loss (Ref. 1). It is common to use the lumped element model expression for a lumped element model for the noise temperature contribution

$$T'' = T_p\,(1 - 1/L) \qquad (1)$$

where

L = propagation path loss, ratio

T_p = atmosphere effective physical temperature, kelvins

to estimate the transmission loss

$$L = \frac{1}{1 - T''/T_p} \qquad (2)$$

This article investigates methods to evaluate T_p required for the appropriate transmission path model.

III. Theory

We have (Ref. 1, Eq. 3, using the same symbols and definitions)

$$T'' = \int_0^l \alpha(x)\,T(x)\,e^{-\int_x^l \alpha(x')\,dx'}\,dx \qquad (3)$$

Substitute, $x = yl$

$$T'' = \int_0^1 \alpha(y)\,l\,T(y)\,e^{-\int_{yl}^1 \alpha(y')l\,dy'}\,dy \qquad (4)$$

Using

$$Z = -\int_{yl}^1 \alpha(y')\,l\,dy' \qquad (5)$$

results in

$$T'' = -\int_0^{Z_1} T(Z)\,e^Z\,dZ \qquad (6)$$

where

$$Z_1 = -\int_0^1 \alpha(y')\,l\,dy'$$

IV. Application

Consider the variable parameter model (Ref. 1, model 2) with exponential propagation constant and linear temperature distributions,

$$\begin{aligned} \alpha(y) &= \alpha_1\,e^{aly} \\ T(y) &= T_1 + (T_2 - T_1)\,y \end{aligned} \qquad (7)$$

Then, with Eq. (5),

$$\begin{aligned} Z &= (\alpha_1/a)\,(e^{aly} - e^{al}) \\ &= (\alpha_1/a)\,(e^{aly}) - (\alpha_2/a) \end{aligned}$$

$$Z_1 = \frac{(\alpha_1 - \alpha_2)}{a}$$

and

$$T'' = -\int_0^{(\alpha_1-\alpha_2)/a} \left[T_1 + (T_2 - T_1)\,\frac{\ln\left(\dfrac{aZ}{\alpha_1} + \dfrac{\alpha_1}{\alpha_2}\right)}{al} \right] e^z\,dz \quad (8)$$

Expanding

$$T'' = T_1\,(1 - 1/L) + (T_2 - T_1)\,(1 - I) \qquad (9)$$

where ($al = \ln \alpha_2/\alpha_1$, $\alpha_1/a = \ln L/(\alpha_2/\alpha_1 - 1)$, $(\alpha_2 - \alpha_1)/a = \ln L$)

$$I = \frac{1}{(\ln \alpha_2/\alpha_1) e^{\alpha_2/a}} \int_{\alpha_1/a}^{\alpha_2/a} \frac{e^z}{Z} \, dZ$$

I is solely a function of α_2/α_1 and L. Equating Eqs. (1) and (9)

$$T_p = (1 - k) T_1 + k T_2 \qquad (10)$$

where

$$k = \frac{1 - I}{1 - 1/L}$$

The solution for k is obtained from numerical integration of I. The results are shown in Fig. 1. Over this range of parameters,

$$k \simeq 0.5 + 0.01768 \, L \, (\mathrm{dB}) + 0.01768 \, (\alpha_2/\alpha_1)(\mathrm{dB})$$

$$- \, 0.000368 \, L \, (\mathrm{dB}) (\alpha_2/\alpha_1)(\mathrm{dB}) \qquad (11)$$

For example, if (α_2/α_1) (dB) = L (dB) = 10, we have $k \simeq 0.8168$ so that for $T_1 = 250\,K$ and $T_2 = 290\,K$, $T_p \simeq 282.7\,K$, which agrees with previous calculations (Ref. 1, Table 2, case 3).

For $L \approx 1$, (from expansion of Eq. 8)

$$I \approx 1 - (\alpha_2/\alpha_1) \frac{L - 1}{(\alpha_2/\alpha_1) - 1} + \frac{L - 1}{\ln(\alpha_2/\alpha_1)}$$

so that

$$k \cong L \left[\frac{\alpha_2/\alpha_1}{(\alpha_2/\alpha_1) - 1} - \frac{1}{\ln(\alpha_2/\alpha_1)} \right]$$

$$\approx \left[\frac{\alpha_2/\alpha_1}{(\alpha_2/\alpha_1) - 1} - \frac{1}{\ln(\alpha_2/\alpha_1)} \right] \qquad (12)$$

and similarly for $(\alpha_2/\alpha_1) \approx 1$ (also from Ref. 1, model 3)

$$I \approx \left(\frac{1}{\ln L} - \frac{1}{L \ln L} \right)$$

so that

$$k = \frac{1 - \frac{1}{\ln L} + \frac{1}{L \ln L}}{1 - 1/L} \qquad (13)$$

for both $L \approx 1$ and $\alpha_2/\alpha_1 \approx 1$ this reduces to $k \simeq 0.5$

In Figs. 2, 3 and 4 T_p is shown plotted using model 2 for a range of values of α_2/α_1, L, T_1, and T_2. Precise transmission loss estimates can be made from radiometer noise temperature measurements for this model without integral evaluations using Eqs. (2) and (10) [Eqs. 12 or 13 if appropriate]. The procedure is to calculate the loss using Eq. (2) iteratively with T_p evaluated from Eqs. (10) and (11). The required initial estimate of T_p is given by 280 K, $(T_1 + T_2)/2$ or other choice as appropriate.

For example, if $T'' = 254.4$ K, $(\alpha_2/\alpha_1) = 10$, $T_1 = 250$ K, $T_2 = 290$ K, we have (using for initial estimate, $T_p = (T_1 + T_2)/2 = 270$ K) from Eq. (2)

$$L = 12.4 \text{ dB}$$

First iteration (Eqs. 11, 10 and 2)

$$k = 0.8504$$

$$T_p = 284.0$$

$$L = 9.8 \text{ dB}$$

Second iteration

$$k = 0.814$$

$$T_p = 282.6$$

$$L = 10.0 \text{ dB}$$

which indicates rapid convergence. For most applications, the second iteration is not required. For example, starting with $T_p = 270$ K as above and $T'' = 210.6$ K, 139.5 K and 57.1 K results in (with 1 iteration) $L = 6.02$ dB, 3.01 dB, and 1.00 dB respectively, (in agreement with previous calculations, Ref. 1, Table 2). This technique is useful for other models with application of Eqs. (4) and (6). The solution for k is tabulated in Table 1 for various models. Further, these methods apply not only to atmospheric measurements, but to any determination of loss from radiometer calibrations such as transmission line loss (required for thermal load standards, Ref. 2) or radome loss calibration (Ref. 3).

For an application example at small loss, assume $(\alpha_2/\alpha_1) \simeq 10$, $L \approx 1$. Then

$$T_p \simeq T_1 + 0.6768\,(T_2 - T_1) \qquad (14)$$

In some applications, T_1 would be estimated and T_2 measured. Using Eqs. (14) and (2):

Case 1

$$\left.\begin{aligned} T_1 &= 250\ \text{K}\\ T_2 &= 290\ \text{K}\\ T'' &= 10\ \text{K}\end{aligned}\right] \Rightarrow \begin{aligned} T_p &\simeq 277.1\ \text{K}\\ L &\simeq 0.159\ \text{dB}\end{aligned}$$

Case 2

$$\left.\begin{aligned} T_1 &= 250\ \text{K}\\ T_2 &= 310\ \text{K}\\ T'' &= 10\ \text{K}\end{aligned}\right] \Rightarrow \begin{aligned} T_p &\simeq 290.6\ \text{K}\\ L &\simeq 0.152\ \text{dB}\end{aligned}$$

The small difference between L calculated for cases 1 and 2 illustrates that for small losses L is insensitive to errors in T_p. In these examples, the error in T_p using Eq. (14) is approximately 1.3 K, resulting in an error in L of approximately 0.01 dB. This example demonstrates that for low loss applications, determine or estimate, α_2/α_1, calculate k from Eq. (12), T_p from Eq (10) and L from Eq. (2). This is accomplished directly without integration or iteration.

For comparison, a linear/linear variable parameter model (Ref. 1, model 6) is analyzed in Appendix A and summarized in Fig. A-1 and Table 1. This model results in (using parameters of Case 1 above)

$$k \simeq 0.6364$$

$$T_p \simeq 275.5\ \text{K}$$

$$L \doteq 0.161\ \text{dB}$$

This indicates that for low loss, the solution for L is insensitive to the model choice.

V. Conclusion

Various expressions are derived for the effective physical temperature T_p of the atmosphere for use in the lumped element model expression for the noise temperature contribution

$$T'' = T_p\,(1 - 1/L)$$

We have

$$T_p = T_1 + k\,(T_2 - T_1)$$

where

$$k = \frac{1 - l}{1 - 1/L}$$

l is derived and evaluated for a range of values for L and (α_2/α_1) for 2 models. Low loss, useful and accurate approximations are given by

$$k \simeq \frac{\alpha_2/\alpha_1}{\alpha_2/\alpha_1 - 1} - \frac{1}{\ln \alpha_2/\alpha_1} \qquad \begin{gathered}\text{model 2}\\ \text{(exponential/linear)}\end{gathered}$$

$$\simeq 0.6768\ (\text{for } \alpha_2/\alpha_1 = 10)$$

$$k \simeq 1 - \frac{1 + 1/3\,[(\alpha_2/\alpha_1) - 1]}{(\alpha_2/\alpha_1) + 1} \qquad \begin{gathered}\text{model 6}\\ \text{(linear/linear)}\end{gathered}$$

$$\simeq 0.6364\ (\text{for } \alpha_2/\alpha_1 = 10)$$

For both $L \approx 1$ and $\alpha_2/\alpha_1 \approx 1$, these reduce to $k \simeq 0.5$. With these low loss approximations, T_p can be evaluated in terms of α_2/α_1, T_1 and T_2. Then L can be determined accurately and directly without integration or iteration, using

$$L \simeq \frac{1}{1 - (T''/T_p)}$$

References

1. Stelzried, C., and Slobin, S., "Calculation of Atmospheric Loss From Microwave Radiometer Noise Temperature Measurements," in *TDA Progress Report 42-62*, Jet Propulsion Laboratory, Pasadena, Calif., April 15, 1981.

2. Stelzried, C. T., "Microwave Thermal Noise Standards," *IEEE Trans. Microwave Theory and Techniques*, Vol. MTT-16, No. 9, Sept. 1968, p. 646.

3. Seidel, B. L., and Stelzried, C. T., "A Radiometric Method for Measuring the Insertion Loss of Radome Materials," *IEEE Trans. Microwave Theory and Techniques*, Vol. MTT-16, No. 9, Sept. 1968, p. 625.

Table 1. Summary of various approximations for k required to calculate T_p

Model	Parameter			
	$\alpha(x)$	$T(x)$	l	k
2	$\alpha_1 e^{(x/l)\ln(\alpha_2/\alpha_1)}$	$T_1 + (T_2 - T_1)\frac{x}{l}$	$e^{\frac{(\alpha_2 - \alpha_1)l}{\ln(\alpha_2/\alpha_1)}}$	$\simeq 0.5 + 0.01768\,L\,(\mathrm{dB}) + 0.01768\,\frac{\alpha_2}{\alpha_1}\,(\mathrm{dB}) - 0.000368\,L\,(\mathrm{dB})\,\frac{\alpha_2}{\alpha_1}\,(\mathrm{dB})$ $\simeq L\left[\frac{\alpha_2/\alpha_1}{(\alpha_2/\alpha_1) - 1} - \frac{1}{\ln(\alpha_2/\alpha_1)}\right](L \approx 1)$ or $\approx \left[\frac{\alpha_2/\alpha_1}{(\alpha_2/\alpha_1) - 1} - \frac{1}{\ln(\alpha_2/\alpha_1)}\right](L \approx 1)$ $\left.\begin{array}{l}\approx \dfrac{1 + \frac{1}{L\ln L} - \frac{1}{\ln L}}{1 - 1/L}\end{array}\right\} \frac{\alpha_2}{\alpha_1} = 1$ (Ref. 1, Model 3) $\left.\simeq 0.5\right\} L = 1, \frac{\alpha_2}{\alpha_1} = 1$
6	$\alpha_1 + (\alpha_2 - \alpha_1)\frac{x}{l}$	$T_1 + (T_2 - T_1)\frac{x}{l}$	$e^{\frac{(\alpha_1 + \alpha_2)l}{2}}$	$\simeq 0.5 + 0.01768\,L\,(\mathrm{dB}) + 0.01364\,\frac{\alpha_2}{\alpha_1}\,(\mathrm{dB}) - 0.000309\,L\,(\mathrm{dB})\,\frac{\alpha_2}{\alpha_1}\,(\mathrm{dB})$ $\simeq 1 - \frac{1 + \frac{1}{3}\left(\frac{\alpha_2}{\alpha_1} - 1\right)}{\frac{\alpha_2}{\alpha_1} + 1}\,(L \approx 1)$ $\left.\begin{array}{l}\approx \dfrac{1 + \frac{1}{L\ln L} - \frac{1}{\ln L}}{1 - 1/L}\end{array}\right\} \frac{\alpha_2}{\alpha_1} = 1$ (Ref. 1, Model 3) $\left.\simeq 0.5\right\} L = 1, \frac{\alpha_2}{\alpha} = 1$

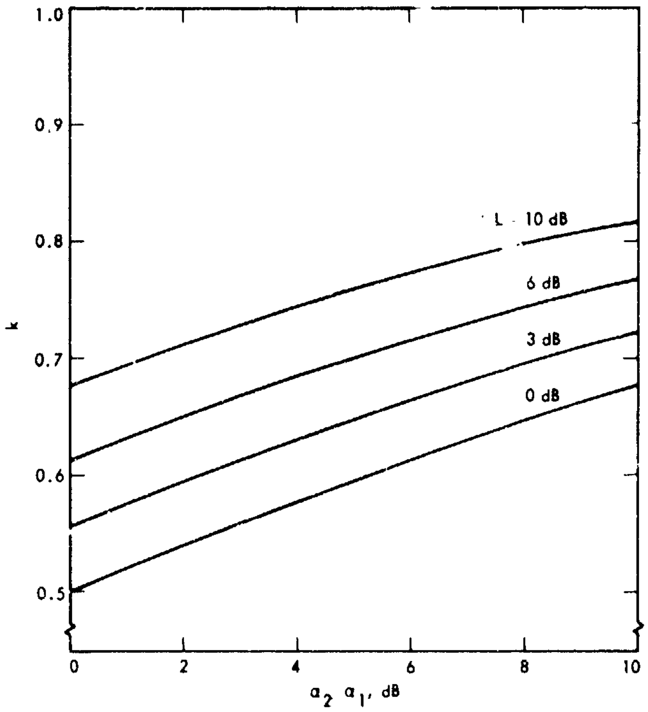

Fig. 1. Plot of k vs α_1/α_2 for various values of L for model 2 (T_1 = 250 K, T_2 = 290 K)

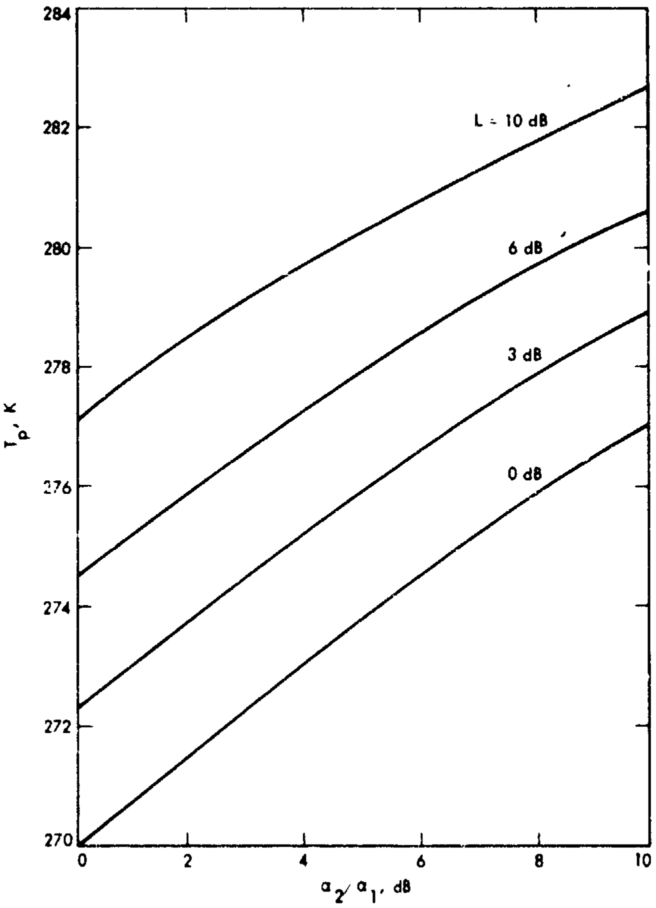

Fig. 2. Plot of T_p vs α_2/α_1 for various values of L for model 2 (T_1 = 250 K, T_2 = 290 K)

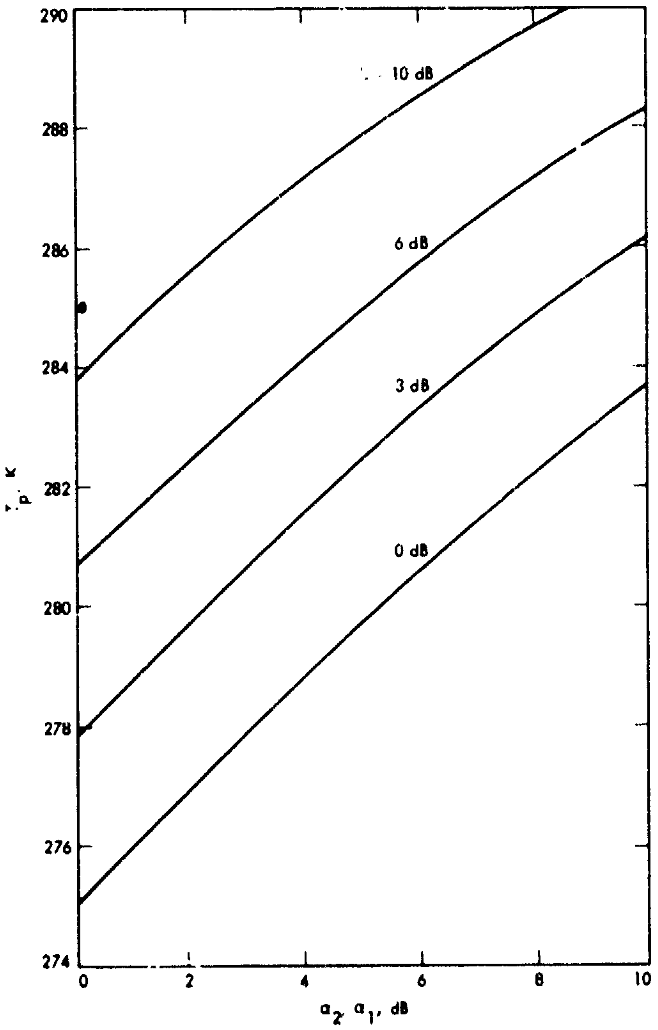

Fig. 3. Plot of T_p vs α_2/α_1 for various values of L for model 2 (T_1 = 250 K, T_2 = 300 K)

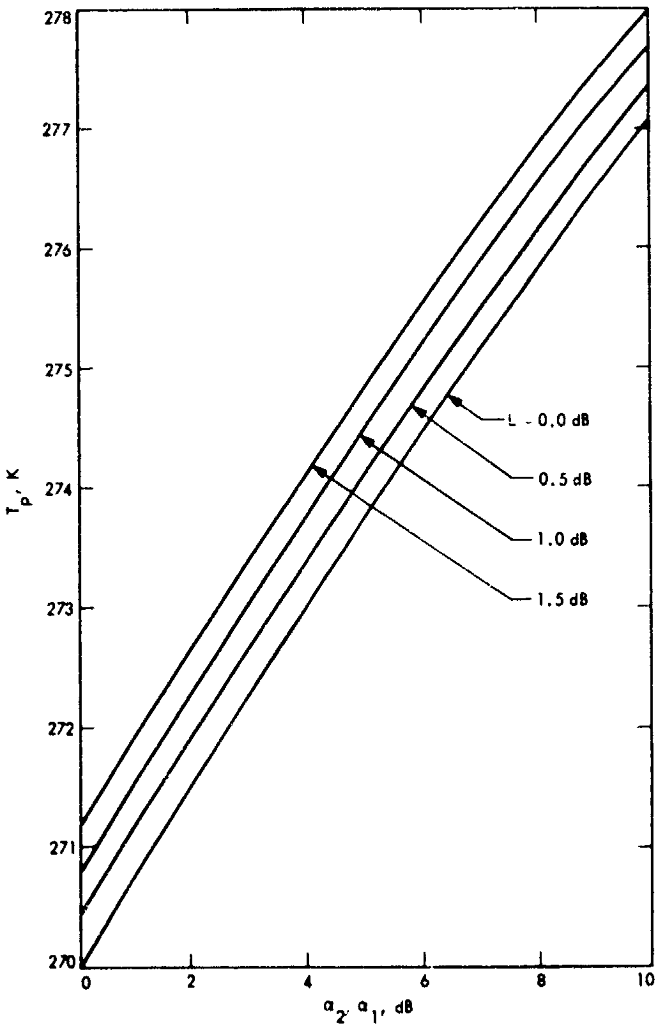

Fig. 4. Plot of T_p vs α_2/α_1 for small increments of L for model 2 (T_1 = 250 K, T_2 = 290 K)

Appendix A

Linear/Linear Variable Parameter Model

Consider the linear/linear variable parameter model (Ref. 1, model 6) with

$$\alpha(y) = \alpha_1 + (\alpha_2 - \alpha_1)y$$

$$T(y) = T_1 + (T_2 - T_1)y \qquad \text{(A-1)}$$

Then

$$T'' = \frac{2 \ln L}{L\left(\frac{\alpha_2}{\alpha_1} + 1\right)}$$

$$\int_0^1 \left[1 + \left(\frac{\alpha_2}{\alpha_1} - 1\right) y\right] e^{\frac{\ln L}{\frac{\alpha_2}{\alpha_1} + 1}\left[2y + \left(\frac{\alpha_2}{\alpha_1} - 1\right) y^2\right]}$$

$$\cdot \left[T_1 + (T_2 - T_1)y\right] dy \qquad \text{(A-2)}$$

Expanding

$$T'' = T_1 (1 - 1/L) + (T_2 - T_1)(1 - I) \qquad \text{(A-3)}$$

where

$$L = e^{\frac{(\alpha_1 + \alpha_2) l}{2}}$$

$$I = \frac{1}{L} \int_0^1 e^{\left[2y + \left(\frac{\alpha_2}{\alpha_1} - 1\right) y^2\right]\left(\frac{\ln L}{\frac{\alpha_2}{\alpha_1} + 1}\right)} dy$$

Equating Eqs. (1) and (A-3)

$$T_p = T_1 + k(T_2 - T_1) \qquad \text{(A-4)}$$

where

$$k = \frac{1 - I}{1 - 1/L}$$

The solution for k from integration of I is shown plotted in Fig. A-1 over a range of values for (α_2/α_1) and L. This can be approximated with the expression

$$k \simeq 0.5 + 0.01768\, L\,(\text{dB}) + 0.01364\, \alpha_2/\alpha_1\,(\text{dB})$$

$$- 0.000309\, L\,(\text{dB})\, \alpha_2/\alpha_1\,(\text{dB}) \qquad \text{(A-5)}$$

for $L \approx 1$

$$k \simeq 1 - \frac{1 + 1/3\,[(\alpha_2/\alpha_1) - 1]}{(\alpha_2/\alpha_1) + 1} \qquad \text{(A-6)}$$

$$k \simeq 0.6364 \text{ (for } \alpha_2/\alpha_1 = 10)$$

$$k \simeq 0.5 \quad \text{(for } \alpha_2/\alpha_1 = 1)$$

T_p is shown plotted in Figs. A-2 for T_1 = 250 K and T_2 = 290 K for a range of values for (α_2/α_1) and L.

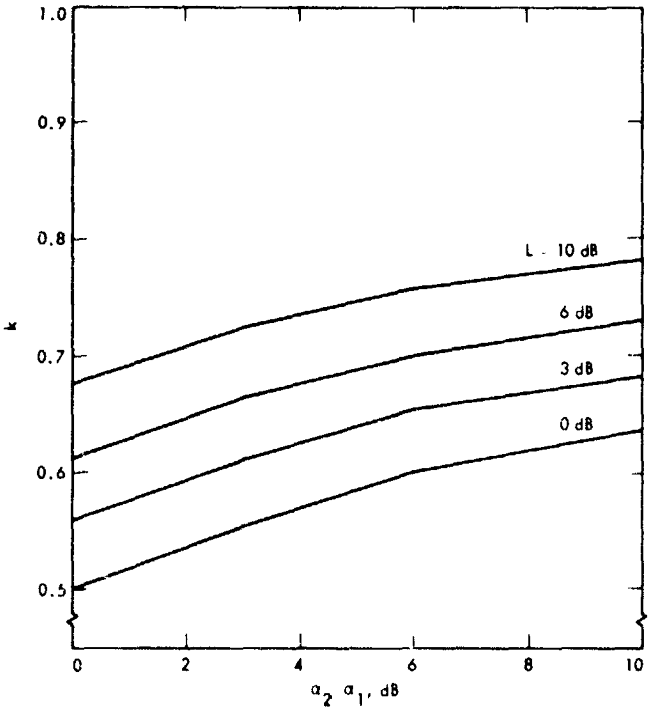

Fig. A-1. Plot of k vs α_2/α_1 for various values of L for model 6 (T_1 = 250 K, T_2 = 290 K)

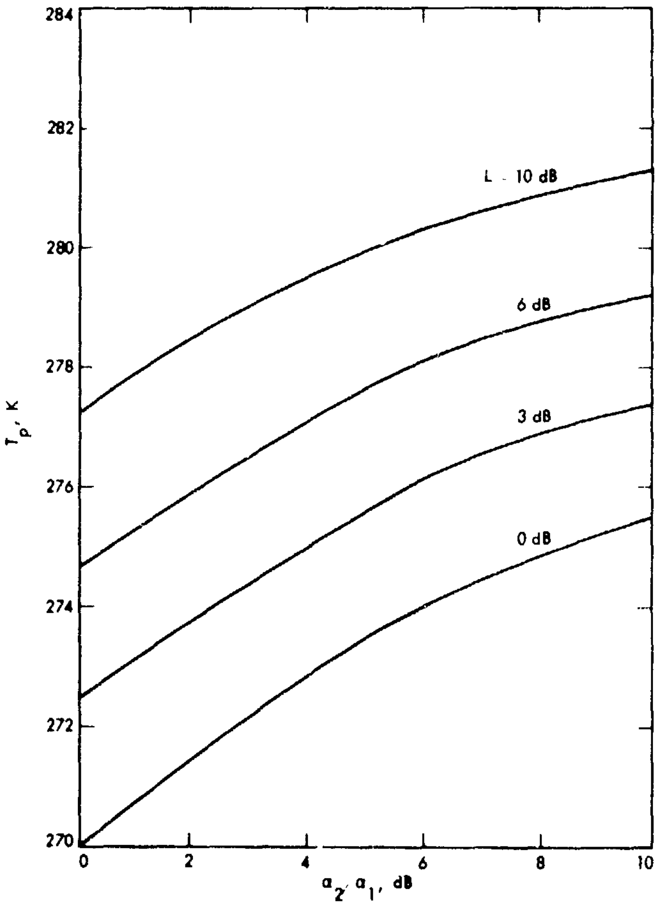

Fig. A-2. Plot of T_p vs α_2/α_1 for various values of L for model 6 (T_1 = 250 K, T_2 = 290 K)

D/3

N81-27136

Second-Generation X/S Feedcone: Capabilities, Layout and Components

J. R. Withington
Radio Frequency and Microwave Subsystems Section

High-power (20-kW) S- and X-band transmitting systems are added to the Second-Generation Common Aperture X/S Feedcone System to demonstrate X- and S-band uplink/downlink capabilities. Design considerations of new X-band components, cone layout, and capabilities are discussed.

I. Introduction

One of the feedcones normally installed at DSS 13 is called the XSR or first-generation X/S feedcone. This listen-only system incorporated for the first time the common aperture feedhorn, enabling simultaneous X- and S-band reception from a geometrically symmetrical antenna. Figure 1 shows this feedcone mounted at DSS 13. The second-generation X/S feedcone, though having the exact same outward appearance, has been made a multifunction feedcone on the inside by the addition of transmitters and diplexers with extended bandwidths and power handling capabilities. There were four aspects to the system development:

(1) The development of a common aperture feedhorn and combiner to handle the added bandwidth and power (Refs. 1 and 2).

(2) The development of the 20-kW X-band transmitter/exciter (Refs. 3, 4, and 5).

(3) The design of new X-band broadband devices to handle the added transmit functions.

(4) The integration of all these elements within the confines of a new feedcone.

Parts 1 and 2 above have already been covered in previous reports and will not be discussed to any length here. We will confine ourselves to system capabilities, block diagrams, functional layout of the cone, and the performance of the new X-band diplexer and polarizer.

II. Planned Capabilities

This new feedcone will transmit 2110 to 2120 MHz and receive 2200 to 2300 MHz at S-band, and transmit 7145 to 7235 MHz and receive 8200 to 8600 MHz (with the best receive performance between 8400 to 8500 MHz) at X-band. Each function is fully independent with each band diplexed. The bandwidth of the horn itself easily covers the full S- and X-band spectrum, with RF efficiencies of 68% and 72% respectively (Ref. 1).

The X/S combiner design requires the polarization of the S-band signal to be a "hard-wired" function. Right circular polarization (RCP) will be the one provided. The addition of left circular polarization (LCP) would involve a new waveguide run and an extra switch, for an estimated 2-K additional system noise. S-band ellipticity measurements have yet to be made with this new horn. As is standard in other S-band cones, the system will consist of either a low-noise listen-only path, or a fully diplexed path for simultaneous transmission/reception. The system is intended for a single S-band maser, and a direct VLBI port is not supplied. Because of limited X-band rejection uncertainty in the combiner section, a waffle-iron filter is placed just in front of the maser for added X-band isolation. This will add 3.4 K to an approximate 24-K (baseline) system noise temperature. It is expected that tests on the antenna will indicate sufficient X-band rejection to warrant its removal. (Ultimately, cryogenic filtering within the amplifiers will be developed.) In the diplexed position, the additional waveguide and S-band diplexer will add approximately 5 K over that for a total of 27 K and 33 K, respectively. These figures are based on performance of the first-generation feedcone and known effects of various S-band components. The S-band system is designed to transmit 20-kW, powered by the present transmitter on DSS 13. An S-band transmit filter will reject S-band beam noise. However, there is presently no fourth-harmonic filter in the system to suppress X-band receive harmonics. An effort is being made to locate one.

The X-band system will have switchable polarization (LCP or RCP), but will have only a diplexed configuration, first because of the high performance of the new X/X-band diplexer, and second because the diplexer's receive band will cover the proposed VLBI band (8200 to 8600 MHz). Again, the design is for a Block II-A maser (100-MHz instantaneous bandwidth) that will cover 8400 to 8500 MHz. The diplexer has its best match, lowest loss, and highest isolation at these frequencies. A VLBI receive-only port is supplied, but no X-band transmit function will be possible in that configuration. An approximate system noise temperature for the diplexed receive band of 8400 to 8500 MHz is 30 K. A listen-only path could conceivably drop this to 27 K (baseline), but at the same time would degrade the diplexed receive link by 7 K, for a total of 34 K. Ellipticity measurements of the feedhorn/polarizer combination await completion of the broadband polarizer. The new transmitter will supply the required 20-kW signal for the X-band uplink demonstration on this project. The X-band transmitter is located in the cone.

A dual -54-dB loop coupler at S-band and a dual -54-dB cross-guide coupler at X-band are supplied to monitor the respective transmitter signals, run phase calibration checks, and perform other required microwave tests. Both an X-band and S-band calibration system will be supplied for maser calibration. They will incorporate noise diodes (three levels), a receive-band signal source, and both will be NAR capable. All microwave switches, the X-band polarizer, and both calibration boxes will be compatible with on-going automation projects. The block diagram (Fig. 2) shows the other couplers and loads supplied by the microwave group. The signal paths and cone interfaces shown are generally those believed necessary to operate the fully operational feedcone. However, only those functions necessary to demonstrate the principles will be supplied in FY 81. Some functions (such as the X-band transmit functions, doppler extraction being an example) are scheduled for implementation in FY 82 and 83. (Ref. 4).

III. Planned Layout

The housing of the microwave subsystem mirrors the first-generation feedcone in construction. To a basic straight base cone shell (approximately 429 cm tall) we again bolt a cone extension (approximately 196 cm in height) to the top of the base cone. An adapter ring (3.73 cm thick) is then used to mount and position the X/S feedhorn/combiner in the cone. A flat plate bolted to the X/S combiner enables us to directly mount a standard DSN X-band polarizer package to the feedhorn. A 23-cm section of WC 137 (a 0.6-K loss) waveguide is used to fill the gap between the feedhorn and the polarizer caused by the shorter throat section of the X/S feedhorn, and a new four-section stepped transition is used instead of the tapered transition to make room for the -54-dB cross-guide coupler. The new broadband polarizer is designed to be a direct replacement for the standard single-frequency polarizer. The X/X-band diplexer (water cooled) is placed between the WR125 two-position switch and the -35-dB calibration coupler on the X-band maser. Approximately 366 cm of WR125 (water cooled) waveguide join the diplexer and the X-band transmitter positioned directly below it on the cone floor. All X-band waveguide microwave components will be constructed of copper.

The S-band system will employ the same waveguide bridge network found in the First-Generation Feedcone System. The horn is fed through four separate circumferential ports 90 deg apart on the side of the horn. The phasing at each port is controlled by "equal-length" waveguide runs, two 90-deg hybrids, and a magic "T" (all in WR430 waveguide). Coupling the magic "T" to the correct two ports of the two 90-deg hybrids "hard wires" either RCP or LCP operation. Between the "E" plane port of the magic "T" and the S-band maser, a -54-dB loop coupler, approximately 91 cm of WR430, a two-position switch, the waffle-iron filter, and a -33-dB cross-guide coupler constitute the listen-only low-noise path; add to that another switch, the S-band diplexer, and 213 cm of WR430 for the diplexed mode and you have the diplexed receive path. Since the transmitter input to the S-band diplexer is some 427 cm above the cone's bottom floor, the transmit waveguide runs 2/3 the length of the cone through the S-band transmit filter to the floor. A WR430 waveguide run connects the cone to the S-band transmitter located in the DSS 13 equipment room below the dish. Most of the S-band waveguide will be made of aluminum, and the S-band system in the cone will not be water cooled (Fig. 3).

IV. Feedcone Components

This feedcone is basically two separate systems sharing a common feedhorn aperture. Except for the X/S feedhorn/combiner, no new S-band hardware was developed. Much the same thing can be said for the X-band system, except for the aforementioned X/X-band diplexer and the broadband polarizer. Both will be the subject of a separate report when all final models and tests are completed. Following are exerpts of the more pertinent characteristics of each.

A. X/X-Band Diplexer[1]

The diplexer consists of three separate components. The center three-port "T" combiner section consists of a high-pass filter in the receive arm and a band-pass filter in the transmit arm. Two "E" plane cavity-type band stop filters (BSF) are added, one each to the transmit and receive ports for the necessary added isolation. The "T" section combiner was electroformed (copper electrodeposited on an aluminum mandrel), while the two BSFs were constructed of three flat plates, all machined separately, and then pinned and bolted together to give a section of WR125 waveguide with inductively coupled "E" plane cavities. A two-cavity BSF is used in the receive link and was originally designed for 40-dB rejection of the transmit band (7145 to 7235 MHz) and a four-cavity BSF is used for the transmit link with better than 70-dB rejection of 8400 to 8500 MHz. The transmit arm of the "T" was tuned in conjunction with the four-cavity BSF, and as such must be used as a single unit. However, the receive arm of the "T" and the two-cavity BSF were matched independently and are meant to be used together or separately depending on the desired isolation. The high-pass receive arm itself has > 38 dB of rejection of the 7145 to 7235 MHz band, but the two-cavity BSF added only 30 dB more. Originally it was felt that the total 68 dB would be enough, however, new tests on the interference effects (RFI) in the TWMs limits to 1 mW the transmit power received before experiencing some drop in maser performance. The degradation in performance is due to overcoupling between the two cavities, and the cavities are now being respaced to give the necessary 5-dB more isolation.

1. Measured performance of the receive band.

VSWR (8200 to 8600 MHz):	<1.17.1
(8400 to 8500 MHz):	<1.07:1
loss (combined):	<0.05 dB[2] (<3.5 K)
isolation/rejection: (7145 to 7245 MHz)	>68 dB (goal: 73 dB)

2. Measured performance of the transmit band.

VSWR: (7145 to 7245 MHz):	<1.07.1
loss:	<0.08 dB[3]
isolation/rejection: (8400 to 8500 MHz)	>>93 dB[4]

The results of the rework of the two-cavity BSF will be reported at a later date when the full report on the diplexer is made.

B. WC137 Broadband Polarizer

A polarizer converts a linearly polarized TE°_{11} mode, generated from $TE^{\square}_{01}$ by the WR125 to WC137 four-step transition, into a circularly polarized TE°_{11} mode by "quarter-wave plate" action. Because of the wide separation of the transmit and receive bands, the performance over this extended range of the quarter-wave plate is questionable, and will be replaced with an iris-type polarizer. At present, only an aluminum prototype exists, but these test results should be representative of the finished product. The results below were obtained using the Automated Network Analyzer.

1. Measured performance for 7000 to 8600 MHz.

ellipticity:	<0.5 dB
VSWR:	<1.07:1

2. Current fabrication. A polarizer is now being fabricated from a solid block of copper. Its loss, VSWR, and ellipticity will be measured as time and equipment allow, and will be reported at a later date when a full report on this polarizer is made.

V. Conclusions

A new Cassegrain feedcone assembly designated the XSU feedcone (for common aperture X- and S-band uplink) is being built to replace a XSR (for common aperture X-and S-receive only) feedcone presently in use at DSS 13.

---

[1] Original design by W. Erlinger of Wenzel/Erlinger Associates.

[2] The loss measurement was made using a maser and a liquid nitrogen load.

[3] The loss measurement was done using an Automated Network Analyzer.

[4] The sensitivity limit of the equipment used (the original design called for 100 dB). Full isolation will be done when a maser is available.

This feedcone is the prototype for six wideband listen-only SXC cones (convertible to XSU) to be implemented throughout the operating DSN network. The microwave design is essentially complete, fabrication of the cone shell is complete, and assembly has begun. The microwave component installation will be completed at JPL and shipped to the DSN Microwave Test Facility where the X-band transmitter will be installed. Following fabrication and installation, testing will take place at the Test Facility and at DSS 13. Ground tests will measure system noise and power handling capabilities.

This feedcone greatly extends the state of the art in performance offered to the DSN, and will greatly enhance experimental as well as DSN capabilities in the coming years.

References

1. Williams, W. F., and Reilly, H., "A Prototype DSN X/S Band Feed: DSS 13 Application Status (Fourth Report)," *The Telecommunications and Data Acquisition Progress Report 42-60*, September and October 1980. Jet Propulsion Laboratory, Pasadena, California.
2. Williams, W., et al., "A Prototype DSN X/S Band Feed: DSS 13 Application Status (Third Report)," *The Deep Space Network Progress Report 42-52*, May and June 1979, Jet Propulsion Laboratory, Pasadena, California.
3. Kolbly, R. B., "20KW X-Band Uplink Transmitter Development," *The Telecommunications and Data Acquisition Progress Report 42-60*, September and October 1980. Jet Propulsion Laboratory, Pasadena, California.
4. Komareck, T., and Meeker, J., (Editors) *X-Band Uplink Technology Demonstration*, Document No. 900-944. March 1, 1981. Jet Propulsion Laboratory, Pasadena, California. (JPL internal document.)
5. Hartop, R., Johns, C., and Kolbly, R., "X-Band Uplink Ground Systems Development," *The Deep Space Network Progress Report 42-56*. March and April 1980. Jet Propulsion Laboratory, Pasadena, California.
6. Williams, W. F., and Withington, J. R., "A Common Aperture S- and X-Band Feed for the Deep Space Network," in the *Proceedings of the 1979 Antenna Applications Symposium*, University of Illinois, Urbana-Champaign, Illinois, September 26-28, 1979.

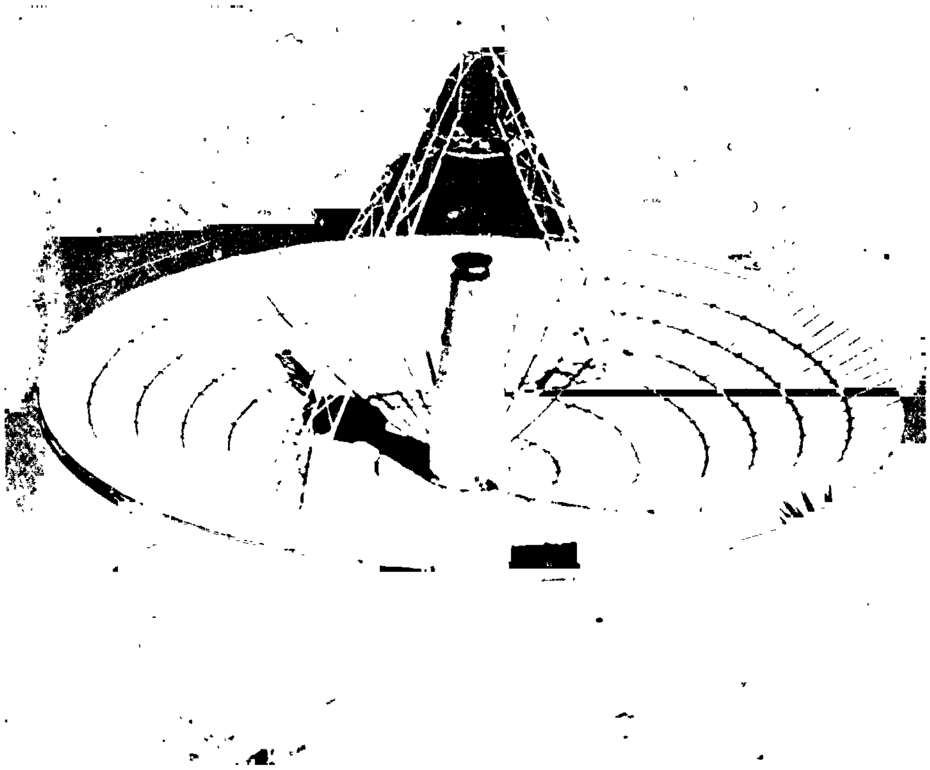

Fig. 1. The first X/S feedcone on DSS 13

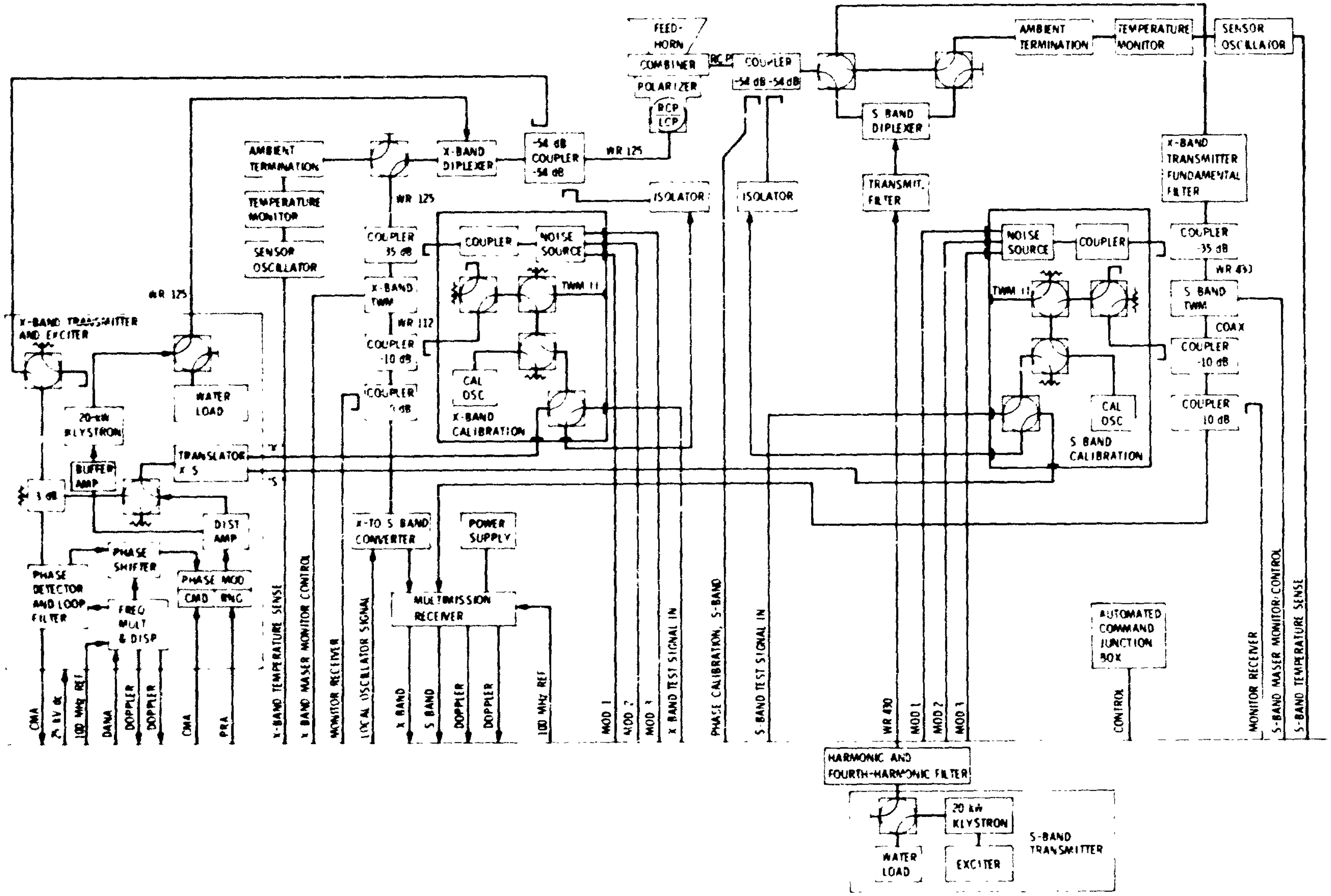

Fig. 2. Second-generation X/S feedcone, block diagram

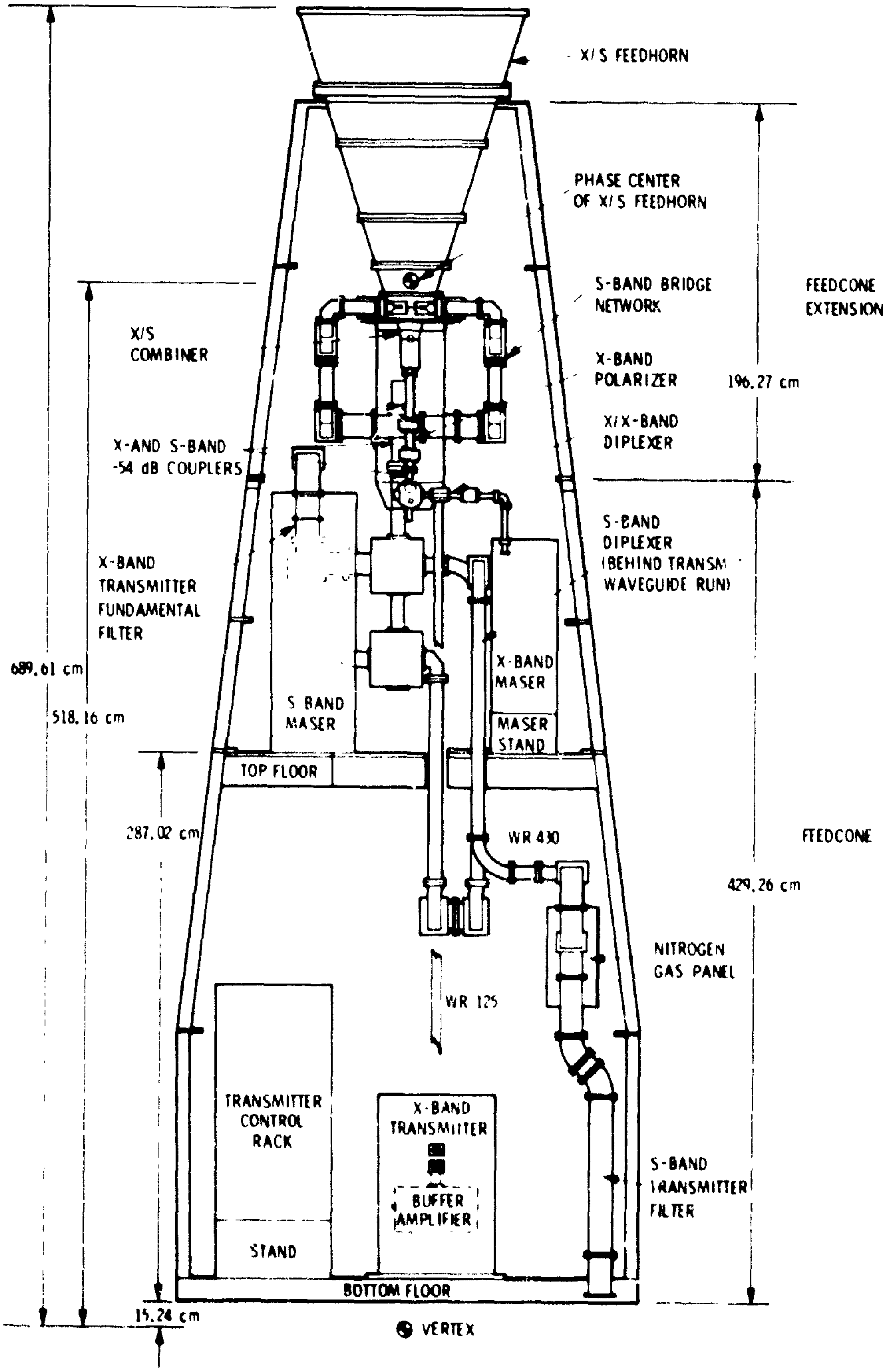

Fig. 3. Second-generation X/S feedcone, general layout

D4 N81-27137

TDA Progress Report 42-63 March and April 1981

Improved Cooling Design for High Power Waveguide System

W. C. J. Chen and R. Hartop
Radio Frequency and Microwave Subsystems Section

An improved cooling method in waveguide system was designed for high power test. Experimental results indicated that this improved design can increase high power handling capability.

I. Introduction

An improved cooling technique has been developed for high power waveguide systems. Testing of X-band high power components in a traveling wave resonator has shown that this improved cooling design reduces temperature in the waveguide and flange. The waveguide power handling capability and power transmission reliability have therefore been increased substantially.

II. Description of Problem

High power transmission capability has been a challenging problem affecting the 400 kW CW X-band radar feed cone at DSS 14. It is well known that breakdown of RF energy often occurs in waveguide systems when power increases to certain levels. There are many factors contributing to the breakdown, e.g., impurities in the waveguide, dimensional mismatching, inadequate cooling, etc.

In the past, several experiments have been conducted to investigate the susceptibility of waveguide to the arc phenomenon during Deep Space Network (DSN) station high power transmission. For example, Yen (Refs. 1, 2, 3) made efforts to study the high power waveguide arcing by using models. Kolbly (Ref. 4) developed an X-band traveling wave resonator (Ref. 5) for high power simulation. In Kolbly's work, heat dissipation in the waveguide was considered to be the major problem in operating the traveling wave resonator, and limited its stable operation to 300 kW CW. Hartop and Bathker (Ref. 6) also pointed out that a major problem in high power X-band planetary radar work was excess heating of waveguide components.

In present high power CW waveguide systems, the waveguide is provided with coolant flowing through ducts soldered on both broad walls of the waveguide. However, it is difficult to apply coolant to the flange area and still provide for easy assembly/disassembly and maintain standard bolt hole patterns. Figure 1 diagrams the common technique of interconnecting WG sections with flexible tubes.

When the waveguide is filled with a dielectric gas, breakdown occurs at a higher power level. Electric strength of dielectric gas at radio frequencies has been researched thoroughly by various authorities (Refs. 7, 8, 9). This research concludes that resistance to breakdown depends mainly on the capability of the gas to absorb free electrons generated by the applied electric field, and then convert the free electrons to heavy negative ions. Under the influence of the increased thermal energy produced from RF insertion loss in the waveguide, the dielectric gas exhibits a thermal effect that speeds up the ionization process, lowers the corona onset, and considerably lowers the gas breakdown potential.

III. Improved Waveguide Cooling Technique

To reduce localized heating (i.e., temperature discontinuities in the waveguide) thereby reducing the single electron avalanche probabilities in the dielectric gas, a new cooling method* for the waveguide system has been designed as diagrammed in Fig. 2. In this improved design, the coolant flows through holes into the waveguide flanges with suitable O-rings designed to prevent coolant leakage at the flange mating surface. A small pressure relief groove is provided between the O-ring and the waveguide to insure that no coolant can leak into the waveguide even in the event of O-ring failure.

IV. Experiment

The JPL-CPR type flange for WR-125 waveguide was modified according to the improved cooling concept. For the purpose of high power testing, the X-band traveling wave resonator was rebuilt with the modified flanges and cooling ducts. Thermocouples were installed on the traveling wave resonator to measure the temperature variation at different power levels, flow rate and types of gas.

A 20-kW CW klystron was used to drive the X-band traveling wave resonator. Before actual field testing, the modified flange design was measured for RF performance. No increased RF leakage through the flange mating surfaces due to the modified design was measured. The level was less than the capability of the instrumentation used for the measurement. The capability of measurement was -90 dB.

V. Results

Water coolant flow rates of 5.67, 7.57, 9.46, 11.35, and 12.11 liters per minute (1.5, 2, 2.5, 3 and 3.2 gpm) were used during the operation of the high power traveling wave resonator. Nitrogen and sulfur hexafluoride were tested separately and at different flow rates. Test results showing stable, 600-kW power levels were obtained in the X-band traveling wave resonator by using this improved cooling design. The maximum power level was limited only by the 20-kW source. It is expected that higher resonant power would be achieved if the input power could be increased. The temperature in the flanges was 53.3°C (128°F) at 600-kW of power with 2-gpm flow rate. Temperature variations on the waveguide at 7.57 lpm (2-gpm) flow rate are reported here since this flow rate is common at the DSN stations. Flange temperature as a function of resonant power is shown in Figs. 3(a), 3(b).

No arcing was observed during high power testing when either nitrogen or sulfur hexafluoride was used in the waveguide.

---

*Patent applied for, NASA NPO-15401.

Acknowledgement

M. Britcliffe at the Microwave Test Facility at Goldstone provided valuable assistance in operating the traveling wave resonator.

References

1. Yen, H. C., "A Preliminary Model for High-Power Waveguide Arcing and Arc Protection," *The DSN Progress Report 42-48*, pp. 118-125, Jet Propulsion Laboratory, Pasadena, California, December 15, 1978.
2. Yen, H. C., "A Circuit Model for Electromagnetic Properties of Waveguide Arcs," *The DSN Progress Report 42-51*, pp. 193-195, Jet Propulsion Laboratory, Pasadena, California, June 15, 1979.
3. Yen, H. C., "Waveguide Arc Study," *The DSN Progress Report 42-51*, pp. 196-199, Jet Propulsion Laboratory, Pasadena, California, June 15, 1979.
4. Kolbly, R. B., "X-Band Traveling Wave Resonator (TWR)," TR 32-1526, pp. 134-136, Jet Propulsion Laboratory, Pasadena, California, October 1973.
5. Miller, S. J., "The Traveling-Wave Resonator and High-Power Microwave Testing," *Microwave Journal*, pp. 50-58, September 1960.
6. Hartop, R., and Bathker, D. A., "The High-Power X-Band Planetary Radar at Goldstone: Design, Development, and Early Results," *IEEE Transactions On Microwave Theory and Techniques*, Vol. MTT-24, No. 12, pp. 958-963, December 1976.
7. Gibson, J. W., and Miller, C. F., "The Electric Strength of Sulfur Hexafluoride at Radio Frequencies," *Journal of Electrochemical Society*, Vol. 100, No. 6, pp. 265-271, June 1953.
8. Morris, J. C., Krey, R. U., and Bach, G. R., "The Continuum Radiation of Oxygen and Nitrogen for Use in Plasma Temperature Determination," *J. Quant. Spectrasc. Radiat. Transfer*, Vol. 6, pp. 727-740.
9. Brown, S. C., "High Frequency Gas Discharge Breakdown," *Handbuch der Physik*. XXII, 1955.

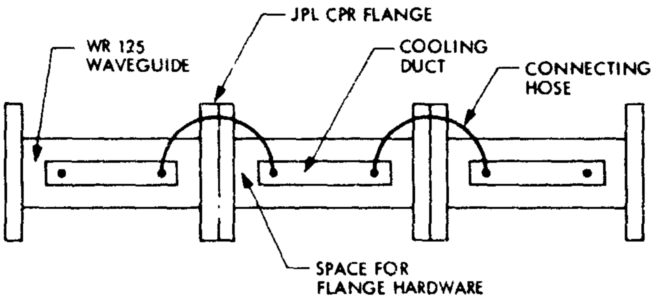

Fig. 1. Original cooling design of waveguide system

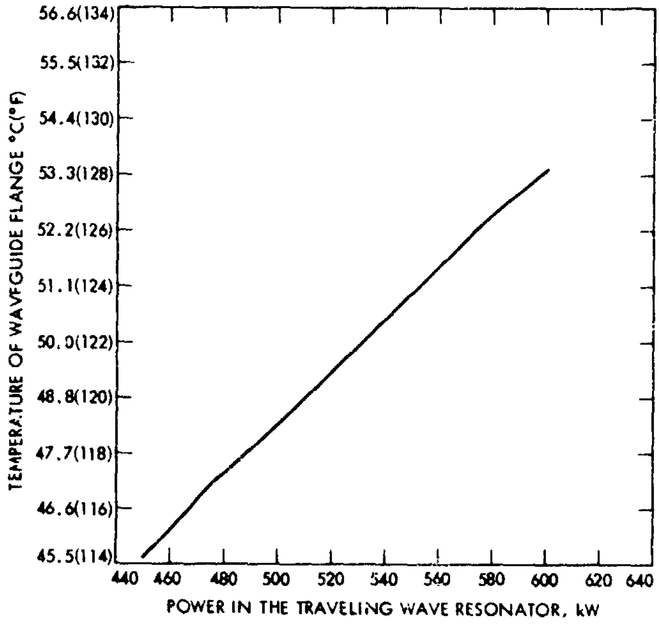

Fig. 3(a). Temperature variation of flange as a function of resonant power. Flow rate 7.57 lpm (2 gpm), nitrogen dielectric gas, modified cooling design. The spot temperature of flange exceeded 148.8°C (300°F) with 300 kW power limitation in the original cooling design

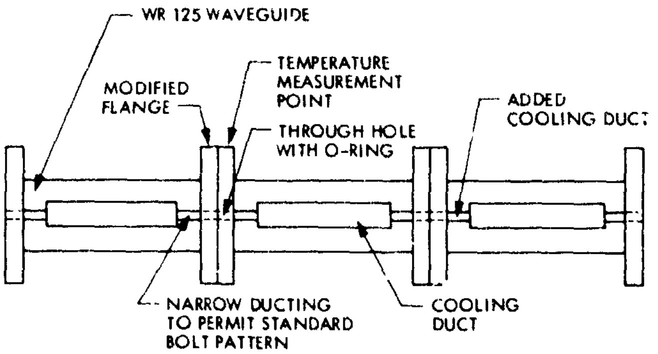

Fig. 2. Modified cooling design of high power waveguide system

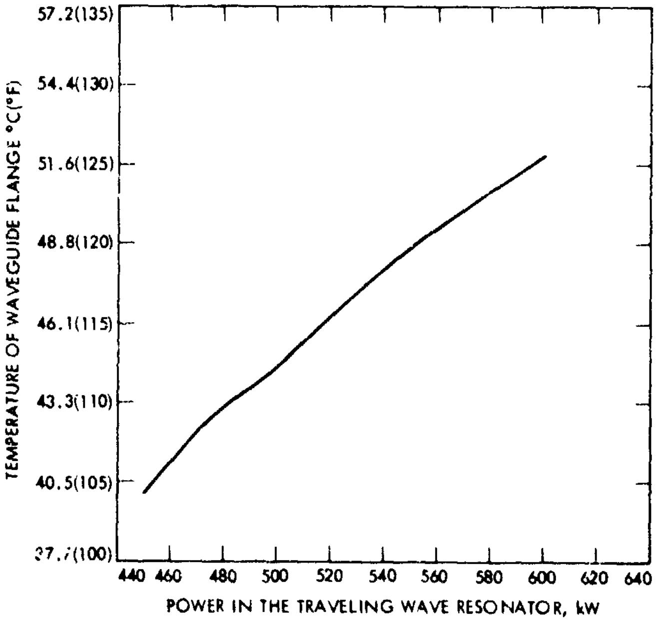

Fig. 3(b). Temperature variation of flange as a function of resonant power. Flow rate 7.57 lpm (2 gpm), sulfur hexaflouride dielectric gas, modified cooling design

D15

TDA Progress Report 42-63 March and April 1981

An Evaluation of the Intel 2920 Digital Signal Processing Integrated Circuit

J. Heller
Communications Systems Research Section

The Intel 2920 integrated circuit is a device for digital signal processing. Consisting of a digital-to-analog converter, accumulator, read-write memory and UV-erasable read-only memory, the circuit can convert an analog signal to a digital representation, perform mathematical operations on the digital signal and subsequently convert the digital signal to an analog output. In addition to the 2920 circuit, Intel also offers development software tailored for programming the 2920. This is a report of experiences with the 2920 circuit and its software.

I. Introduction

Intel's 2920 digital signal processor is the first commercially available integrated circuit which allows the user to implement custom digital signal processing algorithms. (Two other circuits, American Microsystem's S2811 and NEC's UPD7720 are not available yet.) Unlike the 7720, Intel's device performs both analog-to-digital and digital-to-analog conversion on the chip. All the circuits are designed for the high-speed multiplications and additions which are the basis of digital filtering algorithms.

The 2920 is being evaluated for use as a low-pass filter. This report describes the experiences obtained from the circuit itself and the support software from Intel. Although the software proved to be exceptional, the chip has drawbacks of a serious nature which could limit its use.

II. 2920 Functional Description

The functional block diagram is reproduced in Fig. 1. The chip can accept up to 4 analog signals at ±1 to ±2 volts peak depending on an external reference voltage. These signals can be multiplexed to a sample-and-hold circuit which, in conjunction with a digital-to-analog converter, can be configured, under programmed control, to act as an analog-to-digital converter with 8-bit precision plus a sign bit. The digital section of the 2920 features a 40-word, 25-bit wide read/write memory (RAM), and a shift register capable of shifting up to 13 bits to the right or 2 bits to the left in a single instruction cycle. The shifter is connected to one port of an arithmetic and logic unit (ALU), while the other ALU input port receives data from the RAM. The output of the ALU returns to the RAM. The ALU features addition, subtraction, absolute value, "exclusive or," "and," "limit" and other operations. Individual bits can also be tested, although not in the ALU. The digital-to-analog converter used for the conversion of analog signals is also used to convert the digital representation back to the analog form for one of eight sample and hold circuits. The chip sections are controlled by a program stored in an UV erasable read-only memory (EPROM) which can accommodate 192 24-bit instructions. All instructions take the same amount of time to execute which, for the 2920-16, is 600 nsec.

III. Programming Considerations

The 2920 program runs as an endless loop with no jumps allowed. One instruction (EOP) can be used at the end of the program to jump to the beginning if not all 192 EPROM locations are needed. This instruction must be located at word addresses divisible by 4 and must be followed by 3 NOPs.

In order to convert analog signals to digital values, an instruction sequence consisting of a group of IN codes followed by a CVT-NOP-NOP group for each bit is required. Thus, a 9-bit conversion requires 35 instructions. To output an analog signal, approximately 7 NOPs are needed prior to the OUT instructions to allow the digital-to-analog buffer amplifier to settle. Seven OUT instructions are recommended in order to ensure that the sample-and-hold circuit captures the correct value.

Instructions can be executed on a conditional basis depending on the state of a specified bit in the DAR register. If the instruction condition is not fulfilled, a NOP is executed instead. During program segments in which the DAR is not used, it is possible to execute IN or OUT instructions simultaneously with ALU instructions.

IV. 2920 Inadequacies

The 2920 circuit has a number of problems which can cause difficulties of varying degrees. These include faulty instructions as well as gain and offset errors. It should be noted that the following comments apply to the 2920-16 (600-nsec instruction cycle time). The 400-nsec part (2920-10) is unavailable.

Two instructions fail to work properly. The ABA instruction, which takes the absolute value of the contents of a source register and then adds it to the contents of a destination register, does not execute correctly at 600 nsec. In order to use this instruction, the clock rate must be reduced to 4 MHz or less; otherwise the instruction should be replaced by the sequences ABS and ADD. The second faulty instruction, EOP, is used as a jump from the end to the beginning of the program, a useful feature when not all 192 ROM locations are needed. The EOP instruction requires a pull-up resistor on pin 21 where the pin is connected internally to an open drain MOS transistor. The pin is also an input, presumably to a MOS transistor gate, for the reset function. Thus in order for the EOP instruction to operate properly, the voltage at pin 21 must go low at the proper time in order to reset the program counter. At present, in addition to the pull-up resistor at pin 21, a 15-pf capacitor must be connected between pin 21 and ground for the EOP instruction to work. According to Intel, another open drain output at pin 22, OF, does not operate properly. This pin goes low when the accumulator overflows.

The 2920 is subject to analog complaints as well. Given a reference voltage of +1.000 volts, the maximum analog output voltage is approximately ±0.93 volts instead of ±1 volt. For a 2-V reference, the range is ±1.8 V. The 2920 also suffers from a large output offset error which varies with the signal sign and magnitude. As an example, the offset error measured for one 2920 output channel ranged from +13 mV at -0.9 V to -62 mV at 0.0 V to -77 mV at +0.9 V. The results of an experiment point to a nonlinearity in the sample-and-hold buffers driving the output pins. Whatever the cause, errors of this size are serious in low-pass filter applications; hence a number of fixes have been suggested.

With the first method an uncommitted output pin is connected to an unused input. The desired output signal from the DAR is first sent to the previously uncommitted output channel and then read-in to the DAR via the previously unused input channel. The difference between the new value in the DAR and the original DAR contents is used as a correction - the corrected value is then output to the appropriate channel. The success of this method depends on how closely the "uncommitted" output channel matches the channel which outputs the corrected signal.

Another scheme chops the signal by alternately multiplying it by +1 then -1. The output is capacitively coupled to a rectifier which detects the waveform envelope, followed by a low-pass filter for smoothing out the sampling pulses. The chopping can be accomplished by first loading the DAR with the true digital signal representation and converting it to its analog value. Then the same number is exclusive or'd with -1, loaded into the DAR and converted to its analog value. Both signals are alternately output on the same channel.

A third method is based on "correction curve" code appended to the filter program. The curve is determined experimentally by programming the 2920 to act as a wire and then applying accurately measured input voltages over the range of operation and measuring the output voltages. These data can be used with the Intel-supplied signal processing compiler software to generate code which multiplies the digital value by a correction factor prior to loading into the DAR for output. This approach requires a substantial amount of read-only memory for good accuracy.

A revision of the 2920 from the present "D step" to an "E step" version is planned by Intel for this summer. To what extent the above problems will be solved remains to be seen.

V. Program Development: Hardware

The only necessary hardware for 2920 programming is an EPROM programmer (and an ultraviolet light EPROM eraser). However, in order to take advantage of the support software, an Intel Intellec Development System is required. The 2920 applications software is shipped on both single and double density floppy disc formats. Software modules are included which utilize the floating-point hardware board option in the Intellec; otherwise, software is used for these calculations. A special PROM programming card and adapter socket are also required for the Intellec PROM programmer.

VI. Program Development: Software

Three programs are used to develop code for the 2920: the 2920 signal processing applications software/compiler, a 2920 assembler and a simulator. The applications software/compiler program is the centerpiece of the 2920 software development scheme. The use of the term "compiler" is appropriate as the program enables the engineer to examine and specify filters with familiar design terminology which the compiler in turn converts into 2920 assembly code.

The compiler provides the user with three planes, *s*, *Ts*, and *z*, and the commands for creating, moving and deleting poles and zeros on these planes. The *s* plane is used to characterize any circuitry preceding the 2920 in the signal path. This is a particularly useful feature for modeling anti-aliasing filters. Poles and zeros are also placed in the *Ts* and *z* planes, and it is these values which are used to represent the 2920 digital filter. The *Ts* plane is provided for designers who prefer a sampling plane that corresponds more closely to the *s* plane than the *z* plane does. Prior to code generation, the poles and zeros placed on the *Ts* plane are mapped to the *z* plane using the transform $e^{2\pi Ts(x+jy)}$ where T is the sampling period and $s(x+jy)$ are the pole/zero coordinates on the *Ts* plane. Readers may recognize this mapping as the "matched *z* transform." Finally, since the 2920 uses sample-and-hold circuits on the analog outputs, it is possible to model this effect as well by using the HOLD ON command.

The usefulness of the compiler is apparent after the poles and zeros for the signal path have been specified, for then it is possible to graph, with simple commands, gain and phase as functions of frequency. In addition, the step and impulse responses of the filter can be displayed. After a suitable pole/zero constellation is determined, the compiler is used to generate the 2920 assembly code. It is also possible to generate code for implementing operations such as limiting or rectification.

Another powerful capability of the compiler is the macro feature. A macro is a compiler directive which executes sequences of compiler commands upon invocation of the macro name. Macros are utilized where repetitive sections of code are required or for designing a family of filters, where the structure is the same but parameters such as cutoff frequency and ripple vary. The compiler comes with a number of macros including ones for generating Butterworth and Chebyshev filters. The user can also write and save new ones.

Another helpful aid is an arithmetic interpreter which allows the user to enter a Fortran-like mathematical expression for evaluation. An extremely valuable option is the ability of the compiler to create a file which contains a record of all subsequent compiler commands and responses. This is an aid for reviewing previous design sessions.

The compiler has some drawbacks which the user should be aware of. First, the matched *z* transform which is used to map from the *Ts* to *z* plane can give incorrect results (e.g., when the zeros in the *Ts* plane have center frequencies greater than half the sampling frequency (Ref. 1)). Another difficulty occurs when the compiler generates 2920 assembly code. The code for each pole and/or zero is produced independently of the previous poles and zeros; hence it is necessary to use equivalence statements such as OUTP1 EQU INPZ2 to link the output variable of a pole or zero to the input variable for the next pole or zero. A similar procedure is required for connecting the analog input and output routines to the rest of the filter code. Finally, the gain calculation occasionally suffered from overflow.

The 2920 assembler is an easy-to-use program that can be invoked, along with options, with a single command. The assembler terminates after the creation of an object file suitable for loading into the 2920 EPROM and a list file showing the original assembly code and its address assignment in the 2920. An important debug option is available which, when used in conjunction with the simulator (see below) enables the designer to reference 2920 memory locations with the same symbolic names as specified in the assembly code provided the names are preceded by "RAM." or "ROM." ROM instructions can be altered using symbolic code also.

The 2920 simulator is the other significant piece of software that Intel provides. Using as input the object code generated by the assembler, the simulator interprets the 2920 code instruction by instruction. It is similar in operation to software debuggers as it provides a breakpoint, a breakpoint qualifier (i.e., those conditions which must be met at, and prior to, the breakpoint), and a trace feature which saves the values of selected analog inputs and outputs as well as the contents of 2920 memory locations as a function of time or iteration number. Also the simulation can be halted so that chosen memory locations, etc., may be displayed. The simulator also provides a "calculator" feature similar to the compiler; however, it does not accept numbers in scientific format (e.g., 4.2E5), unlike the compiler version, an omission which is quite annoying.

It is recommended that the simulator be used in conjunction with a floating point hardware board in order to speed up calculations. Another time-wasting operation is the simulation of input and output conversion codes. Thus, in order to reduce execution time it is worth the bother to create a "streamlined" version of the assembly code for submittal to the simulator. Even this will not be satisfactory for simulations which must evaluate the 2920 over minutes, not just seconds. One simulation carried out during the course of the project required 4 days to generate 15 minutes worth of data. Users should also be aware that the RAM locations in the simulator representing the 2920 RAM are not cleared prior to execution of the simulation. It appears, however, that the 2920 circuit RAM is not cleared and indeed has random values on power-up, so this is perhaps a "realistic" (if unwitting) simulation. The simulator allows users to initialize RAM locations if desired.

The simulator's analog output values include an added offset error representing the error incurred by conversion of the two's complement digital representation to a sign magnitude format in the 2920 D-to-A converter. As the offset errors seen on actual 2920 devices are large, the simulator offset error is negligible.

One other inconvenience is that the simulator must be informed of the time required to execute one complete pass of the code. It would be desirable to specify the execution time for a single instruction instead and let the simulator figure out the rest. Nevertheless, the simulator along with the compiler and assembler are indispensible for the development of 2920 code in a reasonable amount of time.

All the software operated flawlessly. None of the programs entered states from which there was no return. Some of the terminology could have been coordinated better. One LOADs a file in the simulator but INCLUDEs a file in the compiler, for example, and the "calculator" feature was not identical in both the simulator and compiler. Nevertheless, these are small gripes about smooth-operating software. The compiler and simulator have HELP commands which provide the user with explanations about program commands. These were not found to be useful.

VII. Software Documentation

Three manuals accompanied the software – one each for the assembler, compiler and simulator. There is very little overlap of information.

The 2920 Assembly Language Manual (Intel No. 9800987-01) discusses the 2920 functional elements, instructions and assembly language symbols and format. One chapter describes design techniques including multiplication and division methods. The bit patterns of the 2920 instructions are presented in an appendix. Two other appendices are devoted to carry and overflow and two's complement data handling considerations. This information is important and is not repeated elsewhere.

The 2920 Signal Processing Applications Software/Compiler User's Guide (No. 121529-003, Rev. B) is the least accessible of the three manuals. The guide does not give a satisfying overview of the design approach – instead, a "sample session" of 19 pages is presented for the reader to glean whatever information he can. Most of the manual is devoted to compiler command definitions, which are not always clear. Listings are included for the macros which have been supplied with the compiler. Some of the more useful data are in the appendices under "Notes and Cautions," "Design of Complex Digital Filters Used in the 2920," and "Formulas Used by the SPAS20 Compiler." In short, it is more of a reference manual than a user's guide.

On the other hand, the "2920 Simulator User's Guide" (No. 9800988-02 Rev. B) is easier to assimilate due, in part, to its brevity. The commands are not involved so the user can get started quickly.

A fourth document is necessary for programming the 2920: "Universal PROM Programmer User's Manual" (No. 9800819-01). Sections 5-33 through 5-38 are devoted to programming the 2920 EPROM. Although somewhat understandable, an example showing the required commands would be of great value if only as a time-saver. To summarize, users will find it necessary to familiarize themselves with all three software manuals.

VIII. Other Documentation

Intel publishes two other pieces of literature which are worth reading. The "2920 Analog Signal Processor Design Handbook" is a nonmathematical tutorial in digital signal processing followed by a discussion of the 2920 architecture. Subsequent chapters deal with realizing arithmetic functions (similar to the discussion in the assembly language manual), oscillators and nonlinear functions, different filter types, implementation techniques, etc. Design examples are shown including one section on breadboarding. A weak chapter on the software support programs (i.e., compiler, simulator, etc.) is included. For designers who are considering the 2920 as a filter candidate and need a detailed discussion of the 2920, this book is the recommended one.

The final document which should be consulted is the "2920-16 Signal Processor" data sheet (October 1980, marked "Preliminary"). Unlike the earlier data sheet "2920-10" (which incidentally refers to a 10-MHz 2920 not mentioned on the newer sheet) this paper provides specifications on the analog performance of the device, although no mention is made of the inadequacies cited in Section IV above. The document presents the only good discussion of input and output code-timing requirements.

IX. Conclusion

The concepts embodied by the 2920 device represent a formidable tool for realizing compact digital filters. The software support is excellent. However, new users should be cognizant of 2920 device problems.

Reference

1. Rabiner, L., and Gold, B., *Theory and Application of Digital Signal Processing*, New York, 1975, pp. 224-6.

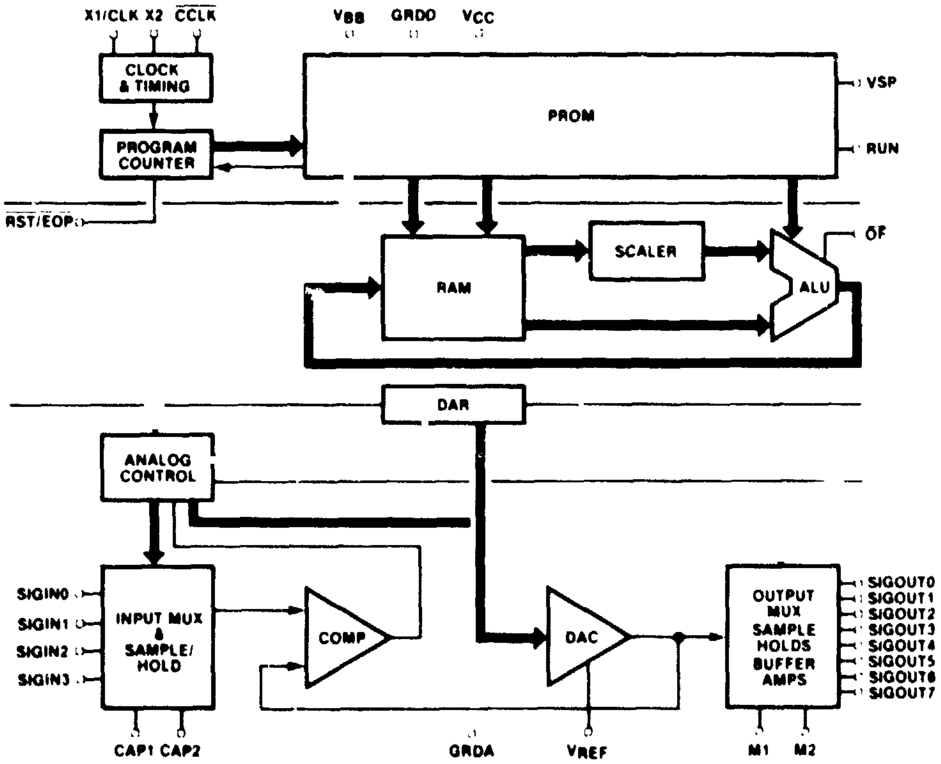

Fig. 1. Block diagram of 2920 signal processor

D16

N81-27139

High-Power Transmitter Automation – Part II

M. A. Gregg
Radio Frequency and Microwave Subsystems Section

This report describes the current status of the transmitter automation development. The work being done is applicable to all transmitters in the Deep Space Network. New interface and software designs are described which improve reliability and reduce the time required for subsystem turn-on and klystron saturation.

I. Introduction

The benefits of transmitter automation are the reduction of life cycle costs and increased availability. Life cycle costs will be reduced not only by the requirement for fewer operators, but also by more effective preventive maintenance through increased and more accurate reporting of critical subsystem parameters. Increased availability will be provided by eliminating the need for operations personnel on evening and weekend shifts. Automatic fault diagnosis and programmed recovery procedures will also increase availability.

The development work currently being done for the DSS 13 100-kW S-band transmitter is applicable to all other known or planned transmitters in the Deep Space Net (DSN) including the X-band uplink development at DSS 13. The difference in operational parameters of the various transmitters is provided for by including a configuration table installed on an individual PROM (programmable read-only memory) for each klystron (or multiple klystrons) at an individual station. Since each klystron has its own table, a change of klystron due to failure, repair, or replacement requires only a single PROM programmed and delivered to the station with the klystron. This will allow the PROM to be installed directly at the klystron in the future. The configuration table (shown in Fig. 1) was discussed in Ref. 1.

II. History

Prior history was discussed in Ref. 1. Current equipment used includes the latest multibus microprocessors (ICS-80) using an 80/20-4 CPU with 9 k-bytes of RAM, 24 digital output lines, and a PROM card for program storage. Communication is provided by a SBC-534 module with four RS-232C ports. A SBC-519 input-output card provides for 72 digital input signals. A 32-channel differential input multiplexer and analog-to-digital converter is used for analog inputs (only 16 channels are used in the transmitter at this time). This controller is located in the Local Control Console (LCC), with a second controller (without the interfaces) located at the control room in the Remote Control Console (RCC), where this controller acts solely as a communications buffer for the 15-line standard interface to the Station Controller.

III. New Hardware

The new controller is based on the Intel Industrial Control Series (ICS), changing only the package design from an ICS-80 chassis to an ISBC 660 chassis, which still uses the standard ISBC 640 power supply. The interface modules have been changed from the Intel ICS 910 and 920, to a common distributed plug-in type module having a higher driving capability. The interface between the transmitter controllers is a serial interface (RS-232C) through short haul modems as shown in the block diagram of the transmitter controller (Fig. 2).

The automation of the heat exchangers is complete and operational, with the louvers thermostatically controlled upon demand of the system. The heat exchanger at DSS 13 is in three bays and has a separate set of louvers for each bay (see Fig. 3). As the system power increases, the heat exchanger automatically adds more cooling capability to the heat exchanger by opening another set of louvers and turning on another cooling fan.

IV. Software

The software conforms to the top-down structured methodology, using 100% PL/M. The communications is being investigated with regard to the use of an RMX-80 interrupt system, which may speed up the communications and allow better access to the program through the CRT. A composite top-level flow chart is shown in Fig. 4. The programs are separated into three parts consisting of the RMX, XMTR, and COMM programs. The RMX program resides in PROMs on the CPU board and provides the communications and control of the priorities of the individual tasks. The XMTR program is the operating program of the system and operates the transmitter and verifies the operating parameters. The COMM program resides in PROMs on a CPU board and provides the communications between the main controller and the remote controller.

V. Present Status

Testing of the controller with the transmitter simulator is presently being conducted in order to improve the operating system and add engineering changes into the programs. Also being added are system calibrations, using new temperature sensors and water flow devices.

Reference

1. Gosline, R., "High-Power Transmitter Automation," in *The TDA Progress Report 42-57*, March and April 1980, pp. 71-81, Jet Propulsion Laboratory, Pasadena, Calif., June 15, 1980.

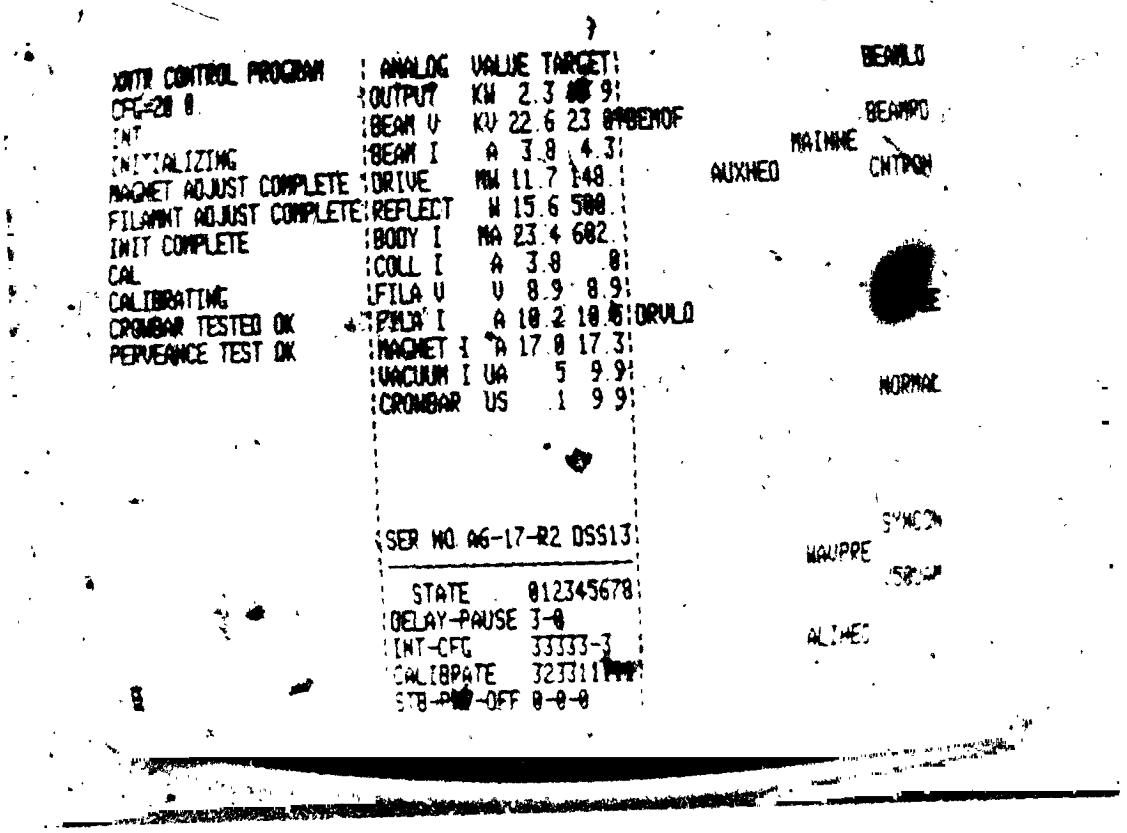

```
XMTR CONTROL PROGRAM      : ANALOG   VALUE TARGET:
CFG=20 0.                 :OUTPUT    KW  2.3 [illegible] 9:
INT                       :BEAM V    KV 22.6 23 000BEMOF
INITIALIZING              :BEAM I     A  3.8  4.3:
MAGNET ADJUST COMPLETE    :DRIVE     MW 11.7 148.  :
FILAMNT ADJUST COMPLETE:REFLECT    W 15.6 500.  :
INIT COMPLETE             :BODY I    MA 23.4 602.  :
CAL                       :COLL I     A  3.8    .0:
CALIBRATING               :FILA V     V  8.9   8.9:
CROWBAR TESTED OK         :FILA I     A 10.2 10.[illegible]:DRVLO
PERVEANCE TEST OK         :MAGNET I   A 17.0 17.3:
                          :VACUUM I UA     5   9.9:
                          :CROWBAR  US    .1   9 9:
                          :                       :
                          :SER NO. A6-17-R2 DSS13:
                          :-----------------------
                          :  STATE       012345678:
                          :DELAY-PAUSE 3-0
                          :INT-CFG       33333-3  :
                          :CALIBRATE     323311[illegible]:
                          :STB-P[illegible]-OFF 0-0-0
```

Fig. 1. Configuration table

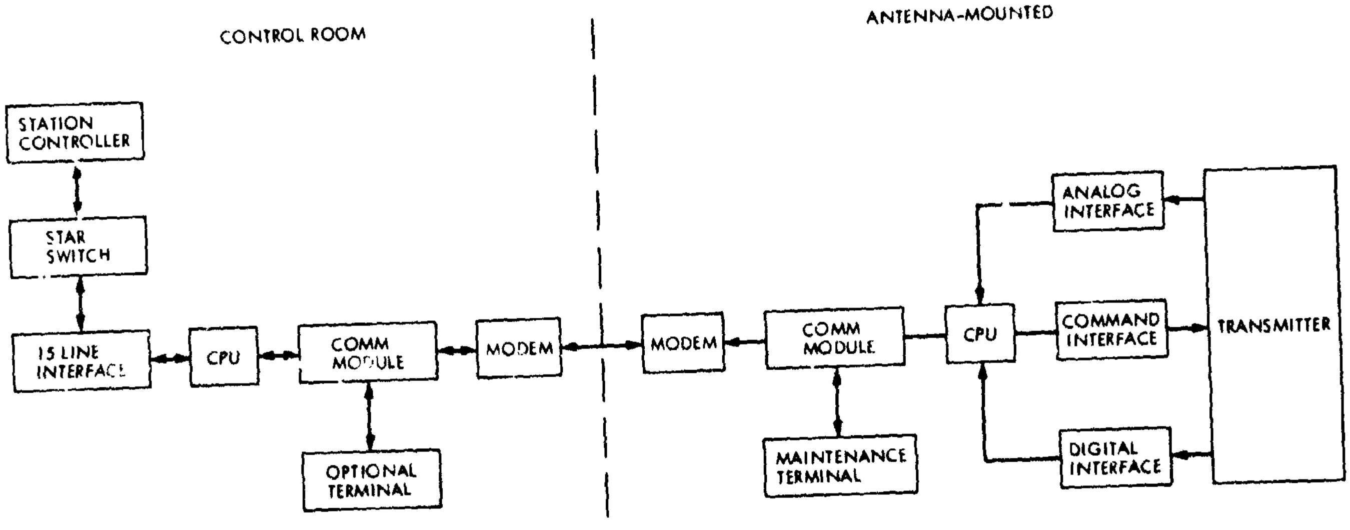

Fig. 2. Transmitter controller block diagram

ORIGINAL PAGE IS
OF POOR QUALITY

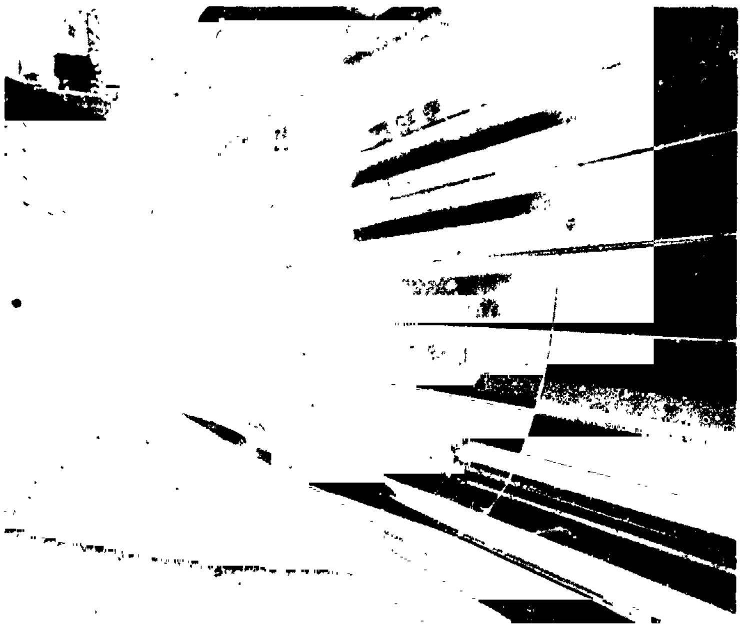

Fig. 3. Heat exchanger louvers, showing Bay 1 open and Bay 2 closed

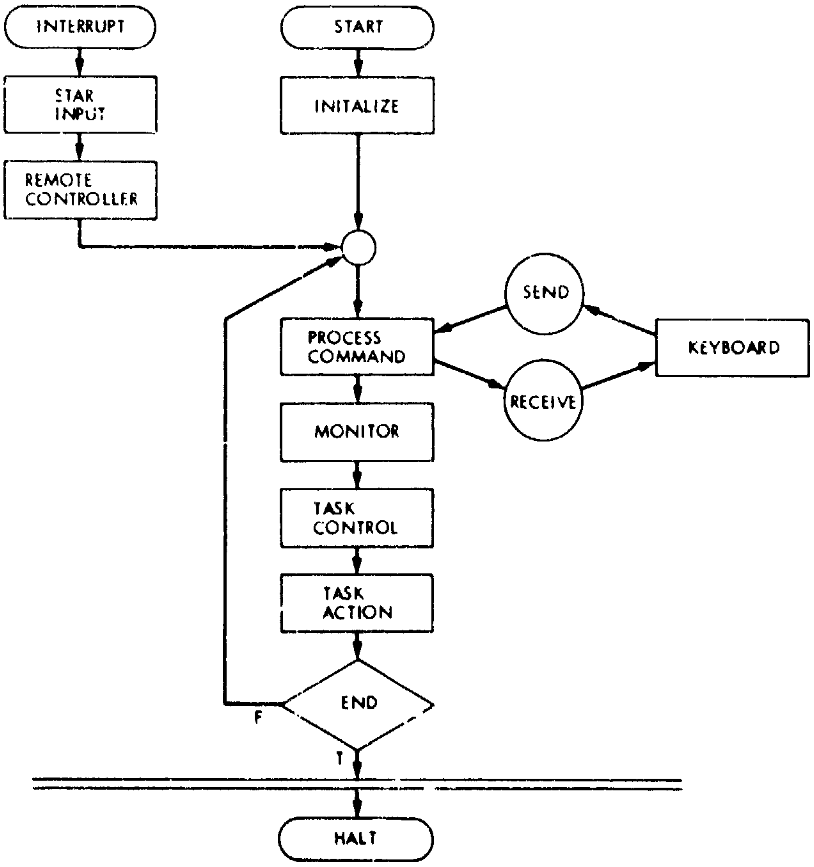

Fig. 4. Transmitter control program top-level flowchart

TDA Progress Report 42-63 March and April 1981

A Multiple Access Communication Network Based on Adaptive Arrays

S. Zohar
Communications Systems Research Section

We consider here a single-frequency communication system consisting of K possibly moving users distributed in space simultaneously communicating with a central station equipped with a computationally adapted array of $n \geqslant K$ *antennas. Such a configuration could result if K spacecraft were to be simultaneously tracked by a single DSN complex consisting of an n antennas array. The array employs K sets of n weights to segregate the signals received from the K users. The weights are determined by direct computation based on known position information of the K users. Currently known techniques require (for* $n = K$*) about* $(4/3)K^4$ *computer "operations" (multiply and add) to perform such computations. We develop here an improved technique that accomplishes this same goal in* $8K^3$ *operations, yielding a reduction by a factor of* $K/6$*.*

I. Introduction

Consider a narrow-band communication system consisting of a central station trying to simultaneously receive signals from K spatially distinct users sharing the same frequency. Assume, further, that the continuously varying geometry of the network (positions of the users relative to the central station) is known to the central station. A reasonable approach to such a multiple access system may be based on equipping the central station with an n-element antenna array where[1]

$$n \geqslant K, \qquad (1)$$

and providing this array with K processors, each of which treats one specific signal source as the desired signal and the remaining $(K-1)$ sources as jammers. The kth processor would thus enhance the message of source k while attenuating all other sources (see Fig. 1).

The actual implementation of such a processor involves multiplying the output of each array element by a complex weight and summing these weighted outputs to deliver the processor's output. The crucial task here is the determination of the nK weights (n weights for each one of the K processors). The equations yielding these weights as functions of the system's parameters have been known for quite some time (Refs. 1, 2) and have been widely applied in the field of adaptive arrays. Here we propose to proceed differently and apply these equations to solve for the weights directly. Let us elaborate: An adaptive array usually operates under the premise that the locations of the various transmitters are unknown to its processor. Its operation may be visualized as consisting, in principle, of two distinct parts:

(1) Extracting from the received signals the unknown parameters pertaining to the geometry of the network (using cross-correlators).

---

[1] When $n < K$ we do not have enough degrees of freedom to accommodate all K users (see Ref. 4). In this preliminary analysis it is reasonable to assume $n = K$. However, there are indications that a somewhat larger n would decrease the incidence of momentary pathological geometric configurations of the network (see Appendix). With this in mind, we preserve the distinction between n and K throughout this paper.

(2) Using this information to set up and solve (iteratively) the eigenvalue equation yielding the optimal weights.

In our case, the first step is superfluous since the network geometry is assumed known at any instant of time. Furthermore, it is well known (Refs. 1, 2) that the eigenvalue equation for the weight of each processor is a particularly simple one which reduces to a set of n linear equations (with complex coefficients). It can be shown that a straightforward application of these equations to our problem yields the Kn weights with an investment of $(4/3)Kn^3 \geqslant (4/3)K^4$ computer "operations." (A computer "operation" is defined here as one real addition plus one real multiplication.)

Now, it should be borne in mind that the feasibility and ultimate limitation of the scheme proposed here depend on the speed with which these computations can be carried out. Assume that we have the proper weights for a given geometrical configuration of sources. As time goes on, the sources move, leading to a different configuration requiring a new set of weights. The obvious speed constraint requires that the time taken to compute a new set of weights should be shorter than the time it takes the system geometry to change to such an extent that the older weights lead to unacceptable reductions in the SNR's.

The fact that the computational load increases with the 4th power of the number of members in the network imposes a severe constraint on the network size that can be accommodated with this approach. Our main purpose here is to show that by utilizing a recent analysis of adaptive arrays (Ref. 4) we get a computational load that increases only as the 3rd power of K. More specifically, the new scheme proposed here reduces the number of computations by the factor $K/6$.

It should be pointed out that the value $K/6$ is arrived at under the constraint $K \gg 1$. Thus, the seeming implication that for $K < 6$ the new scheme is inferior to the old one is false. As a matter of fact, the new scheme requires fewer operations in all cases, saving at least $(4/3)Kn^3\ (1 - K^2/n^3)$ operations each time we compute the weights. For $n = K$, this is a saving of $(4/3)K^4\ (1 - 1/K)$ operations.

The weights are derived here in the context of a one-way communication network from the outlying members to the central station. Thus, the array operates as a receiving antenna. It should be pointed out, though that there are well-known techniques whereby the reception-mode weights can be utilized to generate the same directivity pattern in a transmission mode. Thus the method proposed here is applicable to a two-way communication system.

It should be apparent that a communication network of the type considered here will require a number of detailed studies before it materializes as an operational deployed system. Our objective here is a limited one, namely, the development of the new method of weights determination which makes such a system feasible for a network of reasonable size.

II. Formulation of the Problem

As our development here is based on the formulation developed in Ref. 4, we start with an introduction of the notation and formalism used there. The reader interested in the underlying derivations should consult Ref. 4.

Let the array consist of n antennas and let $G_r(\bar{\rho})$ be the voltage antenna pattern of element r of the array, where $\bar{\rho}$ is a unit position vector. (Throughout this article, barred variables and bold face variables represent vectors.) We assume that the receivers fed by each antenna have identical thermal noise characteristics and denote by σ^2 the thermal noise power referred to the terminals of each antenna.

To prescribe the geometry of the array and the network, we choose an arbitrary reference point in the array and use it as the origin for two sets of position vectors $\{\bar{\beta}_r\}_{r=1}^n$, $\{\bar{\rho}_k\}_{k=1}^K$, where $\bar{\beta}_r$ is the position vector of the rth array element divided by the wavelength, and $\bar{\rho}_k$ is the unit vector pointing to source k (see Fig. 2). To complete the description of the network, we assume now a hypothetical isotropic antenna located at the array's reference point and use it to define the incident powers of the network sources. Specifically, we denote by V_k^2 the power delivered from source k to the terminals of the reference antenna (V_k is real positive). We see then that the overall system is prescribed in terms of the following parameters

$$\{G_r(\bar{\rho})\}_{r=1}^n, \{\bar{\beta}_r\}_{r=1}^n, \sigma^2$$

$$\{\bar{\rho}_k\}_{k=1}^K, \{V_k^2\}_{k=1}^K$$

As shown in Ref. 4, the analysis of the system is most conveniently handled in terms of entities derived from these parameters, namely, a set of complex, normalized vectors $\{\mathbf{u}_k\}_{k=1}^K$ in an abstract n-dimensional space the excitation vectors, and a set of scalars $\{\epsilon_k\}_{k=1}^K$, the power parameters.

Let $\{\mathbf{g}_r\}_{r=1}^{n}$ be an orthonormal basis in the n-dimensional space; that is,[2]

$$\mathbf{g}_i^* \cdot \mathbf{g}_j = \delta_{ij} \qquad (i,j = 1,2,\ldots,n) \tag{2}$$

and let

$$\mathbf{v}_k = \sum_{r=1}^{n} v_{kr}\,\mathbf{g}_r \qquad (1 \leq k \leq K) \tag{3}$$

where

$$v_{kr} = V_k\,G_r(\bar{\rho}_k)\,e^{j2\pi\bar{\rho}_k \cdot \bar{\beta}_r} \qquad (1 \leq k \leq K;\, 1 \leq r \leq n) \tag{4}$$

is the voltage at the terminals of the rth antenna due to source k. The ϵ_k power parameters are defined as

$$\epsilon_k = \frac{\sigma^2}{|\mathbf{v}_k|^2} \tag{5}$$

$\mathbf{u}_k$ is a normalized version of $\mathbf{v}_k$; that is,

$$\mathbf{u}_k = \frac{\mathbf{v}_k}{|\mathbf{v}_k|} \tag{6}$$

More explicitly, this means

$$\mathbf{u}_k = \sum_{r=1}^{n} u_{kr}\,\mathbf{g}_r \tag{7}$$

with

$$u_{kr} = \frac{\sqrt{\epsilon_k}}{\sigma}\,v_{kr} \tag{8}$$

Finally, we find that we have to deal with all possible scalar products of the $\mathbf{u}_k$-vectors. Hence the notation

$$m_{ij} = \mathbf{u}_i^* \cdot \mathbf{u}_j \tag{9}$$

Consider now the kth processor and let γ_k be its output SNR defined as follows:

$$\gamma_k = \frac{[\text{power of signal from source } k]}{\left\{\begin{array}{c}[\text{thermal noise power}]\\ +\\ [\text{power of signals from other } (K\text{-}1)\,\text{sources}]\end{array}\right\}} \tag{10}$$

The basic task facing us is the determination of the optimal weights in each of the K processors, that is, the weights that maximize the γ_k's. Here, we adopt a more meaningful design parameter, namely,

$$\nu_k = \frac{\gamma_k}{\hat{\gamma}_k} \tag{11}$$

where $\hat{\gamma}_k$ is the "available SNR" (Ref. 4) of processor k, that is, the maximal γ_k achieved when all other sources are removed. We refer to ν_k as the normalized SNR. Obviously,

$$0 \leq \nu_k \leq 1 \tag{12}$$

and the combination of weights that maximizes γ_k will also maximize ν_k.

Let w_{kr} be the optimal weight multiplying the output of the rth antenna in the kth processor. We define now the optimal weights-vector for the kth processor

$$\mathbf{w}_k = \sum_{r=1}^{n} w_{kr}^*\,\mathbf{g}_r \qquad (1 \leq k \leq K) \tag{13}$$

It is shown in Ref. 4 that these vectors lie in the subspace spanned by the set $\{\mathbf{u}_k\}_{k=1}^{K}$. Therefore, we are at liberty to adopt the following alternative representation for $\mathbf{w}_k$:

$$\mathbf{w}_k = \sum_{i=1}^{\hat{r}} \omega_{ki}\,\mathbf{u}_i \tag{14}$$

where $\hat{r}$ is the rank of the $\{\mathbf{u}_k\}_{k=1}^{K}$ set; that is, $\hat{r}$ is the size of its largest subset which is linearly independent. (In (14) it is implied that the sources are numbered in such a way that the rank of $\{\mathbf{u}_k\}_{k=1}^{\hat{r}}$ is $\hat{r}$.)

It turns out that the value of $\hat{r}$ has far-reaching implications for the system's performance. We examine these in the Appendix and proceed here under the assumption (shown there to be reasonable)

$$\hat{r} = K \tag{15}$$

---

[2] The asterisk (*) denotes complex conjugation. In handling vectors over the field of complex numbers, we adopt the approach of Morse and Feshbach (Ref. 5). A short summary is given in Appendix A of Ref. 4.

so that

$$\mathbf{w}_k = \sum_{r=1}^{K} \omega_{kr} \mathbf{u}_r \tag{16}$$

In adopting the (16) representation we are transforming the weights problem into that of finding the coefficients ω_{kr}. It turns out that this simple change of representation is the crucial step which ultimately leads to the significant speed advantage mentioned in Section I. The underlying, more fundamental reason for the emergence of a different algorithm (which, fortunately, happens to be more efficient) is that, in adopting the (16) representation, we are led to a different set of equations involving the w_{kr}'s. This is explained more fully at the end of Section III.

III. The Weights Equation

We have shown in Ref. 4 that when the desired signal is source number 1, the optimal ω_{1j}'s are given by[3]

$$\begin{cases} \displaystyle\sum_{j=1}^{K} (m_{ij} - \nu_1 \delta_{ij}) \omega_{1j} = 0 \qquad (i = 1) & (17) \\[2ex] \displaystyle\sum_{j=1}^{K} (m_{ij} + \epsilon_i \delta_{ij}) \omega_{1j} = 0 \qquad (2 \leqslant i \leqslant K) & (18) \end{cases}$$

Equations (17), (18) form a homogeneous set of equations for the ω_{1j}'s. We now combine and reformulate them as the following nonhomogeneous set:

$$\sum_{j=1}^{K} (m_{ij} + \epsilon_i \delta_{ij}) \omega_{1j} = \delta_{i1} (\nu_1 + \epsilon_1) \omega_{11} \quad (1 \leqslant i \leqslant K) \tag{19}$$

The generalization of (19) to the ω_{kj}'s of the kth processor is trivial, namely,

$$\sum_{j=1}^{K} (m_{ij} + \epsilon_i \delta_{ij}) \omega_{kj}$$

$$= \delta_{ik} (\nu_k + \epsilon_k) \omega_{kk} \quad (i, k = 1, 2, \ldots, K) \tag{20}$$

Now, since the $\{\omega_{kj}\}_{j=1}^{K}$ set is a solution of a homogeneous set of equations, we may impose for each k the arbitrary condition[4]

$$(\nu_k + \epsilon_k) \omega_{kk} = 1 \quad (1 \leqslant k \leqslant K) \tag{21}$$

thus, getting:

$$\sum_{j=1}^{K} (m_{ij} + \epsilon_i \delta_{ij}) \omega_{kj} = \delta_{ik} \quad (1 \leqslant i \leqslant K) \tag{22}$$

Let us denote by M the $K \times K$ matrix whose (i, j) element is

$$M_{ij} = m_{ij} + \epsilon_i \delta_{ij} \tag{23}$$

Equation (22) now reads

$$\sum_{j=1}^{K} M_{ij} \omega_{kj} = \delta_{ik} \tag{24}$$

But this implies that

$$\omega_{kj} = (M^{-1})_{jk} \tag{25}$$

In other words, the ω-weights of processor k are just the kth column of M^{-1}. Inverting M will thus yield all the ω_{kj}'s.

The validity of (21) (see footnote 4) can now be verified. From (6), (9) we infer that

$$m_{ii} = 1 \tag{26}$$

Hence (23, A-2), $|M|$ is closely approximated by the Gramian (Ref. 6) of $\{\mathbf{u}_k\}_{k=1}^{K}$, which is nonzero since $\hat{r} = K$. This means that a solution of (20) exists only if $\omega_{kk} \neq 0$.

An incidental result of the obtained solution is simple formulae for the SNR's realized by the optimal weights. From (21) we get

$$\nu_k = \frac{1}{\omega_{kk}} - \epsilon_k \tag{27}$$

Equivalently (see 11, A-1),

$$\gamma_k = \frac{\hat{\gamma}_k}{\omega_{kk}} - 1 \tag{28}$$

---

[3] These follow directly from (4.18)-(4.22) of Ref. 4 when we recall that we proceed here under the assumption $\hat{r} = K$.

[4] There is an implied assumption here that $\omega_{kk} \neq 0$. This is justified later on.

Having solved for the ω_{ij}'s, we now have to find the corresponding physical weights $\{w_{ij}\}$. This follows in a straightforward manner from the two representations of $\mathbf{w}_k$ (13, 16). Starting with (13), we find that

$$\mathbf{w}_k \cdot \mathbf{g}_j^* = \sum_{r=1}^{n} w_{kr}^* \mathbf{g}_r \cdot \mathbf{g}_j^* = \sum_{r=1}^{n} w_{kr}^* \delta_{rj} = w_{kj}^* \quad (29)$$

But (16), (17) yield

$$\mathbf{w}_k \cdot \mathbf{g}_j^* = \sum_{i=1}^{K} \omega_{ki} \mathbf{u}_i \cdot \mathbf{g}_j^*$$

$$= \sum_{i=1}^{K} \sum_{r=1}^{n} \omega_{ki} u_{ir} \mathbf{g}_r \cdot \mathbf{g}_j^* = \sum_{i=1}^{K} \omega_{ki} u_{ij} \quad (30)$$

Hence, combining these two results, we obtain

$$w_{kj} = \sum_{i=1}^{K} \omega_{ki}^* u_{ij}^* \quad (1 \leqslant k \leqslant K; 1 \leqslant j \leqslant n) \quad (31)$$

Let us now regard w_{kj} as the (k, j) element of a $K \times n$ matrix W. Similarly, let u_{ij} be the (i, j) element of a $K \times n$ matrix U. Recalling now that ω_{kj} is the (j, k) element of the matrix M^{-1}, we conclude that (31) is equivalent to[5]

$$W = (\tilde{M}^{-1})^* U^* = (\tilde{M}^*)^{-1} U^* \quad (32)$$

But M is hermitian.[6] Hence

$$W = M^{-1} U^* \quad (33)$$

or equivalently,

$$MW = U^* \quad (34)$$

This is our main result. We already know that (34) is much more efficient than the result based on the direct approach. But the ω_{kj}'s do not appear in (34) and if we recall definitions (9), (23), we conclude that both approaches yield equations relating $\{w_{kj}\}$ to $\{u_{ij}\}$. What is the difference then between these two sets of equations involving the same entities? An examination reveals a very simple answer: The kth equation of the direct approach set involves the weights of all antenna elements in the kth processor, $\{w_{kr}\}_{r=1}^{n}$. The rth equation of the indirect approach involves all the weights in all the processors connected to the rth antenna element, $\{w_{kr}\}_{k=1}^{K}$.

IV. Operations Count

We propose now to solve (34) by the LU decomposition method (Ref. 3). Specifically, we express the matrix M as

$$M = \mathcal{L}\mathcal{U} \quad (35)$$

where $\mathcal{L}$ is a $K \times K$ lower triangular matrix with units along the diagonal and $\mathcal{U}$ is a $K \times K$ upper triangular matrix. This decomposition requires $(4/3)K^3$ operations[7] and transforms (34) into

$$\mathcal{L}\mathcal{U}W = U^* \quad (36)$$

Denoting

$$\mathcal{U}W = X, \quad (37)$$

we obtain

$$\mathcal{L}X = U^* \quad (38)$$

The solution now is quite simple: Starting with (38), we solve for X. Since $\mathcal{L}$ is lower triangular, this solution is trivial requiring $2K^2n$ operations. Having done that, we substitute X in (37), getting W trivially with an additional investment of $2K^2n$ operations.

In addition to the above operations, we have to consider the extra computations required to transform the physical parameters into those of (34). Since the operations count for the solution of (34) involves 3rd order terms (K^3, K^2n), we may ignore computations leading to lower order terms. Strictly speaking, this leaves us with only the $2K^3$ operations

---

[5] The symbol ~ indicates transposition

[6] From (23),

$$(\tilde{M}^*)_{ij} = m_{ji}^* + \epsilon_i \delta_{ji} = (\mathbf{u}_j^* \cdot \mathbf{u}_i)^* + \epsilon_i \delta_{ij}$$

$$\mathbf{u}_i^* \cdot \mathbf{u}_j + \epsilon_i \delta_{ij} = m_{ij} + \epsilon_i \delta_{ij} = M_{ij}$$

[7] Here and subsequently, the operations counts are actually multinomials in K, n. Since in systems of interest $n > K \gg 1$, we approximate each multinomial by its highest order term. Note also that multiplying two complex numbers and adding their product to another complex number, requires 4 operations.

required to compute $\{m_{ij}\}$ from $\{u_{kr}\}$.[8] However, the computation of the u_{kr}'s themselves requires Kn polar-cartesian conversions.[9] Taking a conservative attitude, we allot $(2/3)K^2/n$ operations per conversion, getting a grand total of $2K^3(1 + 3\, n/K)$ operations per set of weights. For $n = K$, this reduces to $8K^3$ operations.

Let us compare these results to the direct method. It can be shown that, in this case, we have to perform LU decomposition on K different nth order complex matrices. Hence we have here an investment of $(4/3)Kn^3$ operations. The remaining computations have 3rd order computation counts which, however, are larger than the corresponding terms in the new scheme. Therefore, the number of operations saved in the new scheme is greater than

$$\frac{4}{3}Kn^3 - \frac{4}{3}K^3 = \frac{4}{3}Kn^3\left(1 - \frac{K^2}{n^3}\right)$$

For $n = K$ this reduces to a saving of at least $(4/3)K^4\,(1 - 1/K)$ operations. Alternatively, for $K >> 1$, the ratio of the number of operations in the two scheme is

$$\frac{\frac{4}{3}Kn^3}{2K^3\left(1 + 3\frac{n}{K}\right)} = K\frac{2\left(\frac{n}{K}\right)^3}{3\left(1 + 3\frac{n}{K}\right)}$$

in favor of the new scheme. For $n = K$, this reduces to $K/6$.

V. Parallel Computation

Given the available hardware and the number of operations as computed in the last section, we can easily get the frequency of possible updates for a single arithmetic unit performing all computations serially. If it turns out that knowledge of the velocity vectors of the network members can yield sufficiently accurate short-term predictions of their position vectors, then pipelining can be employed to increase the frequency of updates and/or increase the network size. Let us examine the possibilities here. For $n = K$, the $8K^3$ operations are divided roughly equally among four tasks which can be pipelined as follows:

(1) Computing M.

(2) LU decomposition of M.

(3) Solving for X.

(4) Solving for W.

We assign one arithmetic unit (AU) to each one of these four tasks and allot them the time required to perform $2K^3$ operations. This is the correct value for tasks 1, 3, 4 if we assign to task 1 an additional special-purpose chip for the K^2 polar-cartesian conversions.[10] It is longer than needed for task 2 ($(4/3)K^3$ operations) so we have the option of using here a slower (and cheaper) AU.

With this scheme, we could update every $2K^3$ operations. It is important to remember, though, that the m_{ij}'s computed in task 1 should not be based on the current $\bar{\rho}_k$'s but rather on the $\bar{\rho}_k$'s predicted to hold when the corresponding W comes out at the end of task 4. Thus, our prediction has to be good 4 pipelining cycles ahead.

It should be pointed out that tasks 3, 4 allow n-fold paralleling. If other parts of the system call for a slow microprocessor allotted to each antenna,[11] then these n microprocessors could perform tasks 3 and 4 as an additional duty. To see this, consider equation (38): X, U^* are $K \times n$ matrices. The microprocessor of the rth antenna can solve for the rth column of X in K^2 operations and, having done that, proceed to equation (37) and solve for the rth column of W in another K^2 operations. Thus, in $2K^2$ operations this microprocessor will have obtained all the weights needed by the rth antenna. During that time, the fast processors assigned to tasks 1, 2 perform about $2K^3$ operations. We see, therefore, that the antenna microprocessor may be quite slow and yet keep up with the pipelining rhythm and its other tasks.

Needless to say, there is still much to be studied and analyzed prior to embarking on the design of a multiple access system of the type described here. We believe, though, that sufficient merit and promise have been demonstrated here to warrant such further studies.

---

[8] We assume all array elements to be identical and aligned so that $G_r(\bar{\rho}_k)$ in (4) is replaced by $G(\bar{\rho}_k)$ leading to only K pattern computations. Quite complex pattern formulae would thus have a negligible effect on the operations count.

[9] u_{kr} is initially computed in a polar form according to (8), (4) and then converted to cartesian form for the subsequent computations

[10] These can be carried out in parallel with the main effort of task 1 computing $\{m_{ij}\}$

[11] For example, to digitally set the weights multiplying its output.

References

1. Applebaum, S. P., "Adaptive Arrays, *IEEE Trans. Ant. Prop.*, Vol. AP-24, pp. 585-598, September 1976.
2. Dupree, J. E., "Enhancement of Spread-Spectrum Systems Through Adaptive Antenna Techniques," Presented at ICC 1977, Chicago, Illinois, June 15, 1977, paper 48.4.
3. Forsythe, G. E., and Moler, C. B., *Computer Solution of Linear Algebraic Systems*, Prentice-Hall, 1967.
4. Zohar, S., "Adaptive Arrays: A New Approach to the Steady State Analysis" (Available from the author).
5. Morse, P. M., and Feshbach, H., *Methods of Theoretical Physics*, McGraw-Hill, 1953.
6. Gantmacher, F. R., *The Theory of Matrices*, Chelsea Publishing Co., 1959, Vol. I, Chap. IX, Sec. 3.

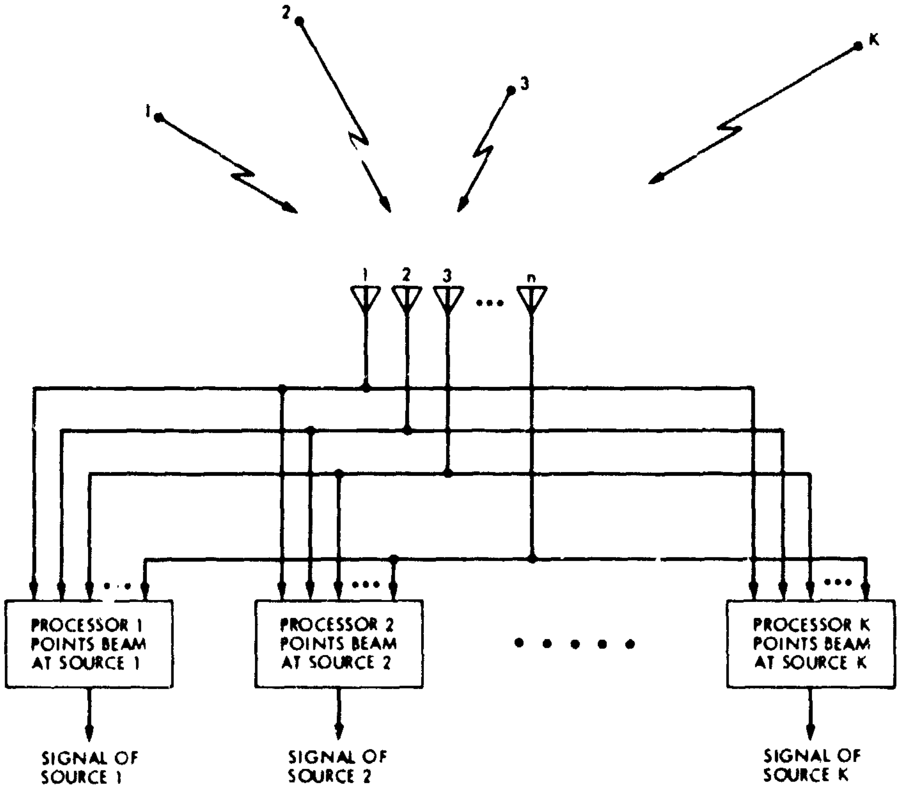

Fig. 1. System outline

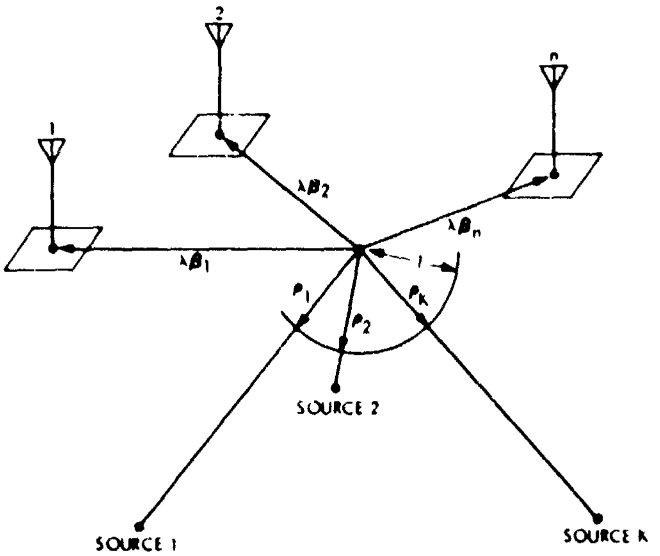

Fig. 2. The vector sets $\{\bar{\beta}_r\}_{r=1}^{n}$, $\{\bar{\rho}_k\}_{k=1}^{K}$ (note: λ is the wavelength)

Appendix A
Pathological Excitation-Vectors Configurations

The dimensionality of the $\mathbf{u}_k$ vectors is n, whereas their number is $K \leqslant n$. This implies that if we were to select the $\mathbf{u}_k$ vectors at random, they would most likely be linearly independent and thus display $\hat{r} = K$. However, in a constantly varying geometrical configuration of sources, it is reasonable to expect from time to time short-lived pathological configurations which have $\hat{r} < K$. We refer to such configurations as rank-deficient. A simple, obvious example is a configuration in which the angular separation of two users (indexed i, j) becomes small so that $\bar{\rho}_i \approx \bar{\rho}_j$ and hence $\mathbf{u}_i \approx \mathbf{u}_j$. Needless to say, there are many situations where the cause of rank-deficiency is not so obvious.

The effect of rank-deficiency on the system is two-fold:

(a) The system will fail to provide adequate services to some users. Obviously, if we go to the extreme of $\bar{\rho}_i = \bar{\rho}_j$ in the above example, no choice of weights could distinguish between users i and j.

(b) The whole system could collapse if we are not aware of the rank-deficiency and are thus led to ill-conditioned equations for the weights.

Let us consider (a) first: It is easy to show (Ref. 4) that $\hat{\gamma}_k$, the "available SNR" of processor k, is given by

$$\hat{\gamma}_k = \frac{1}{\epsilon_k} \qquad \text{(A-1)}$$

Therefore, in the system design we must make sure that

$$\epsilon_k << 1 \qquad (1 \leqslant k \leqslant K) \qquad \text{(A-2)}$$

But, under these conditions, we can invoke theroem (8.15) of Ref. 4, which may be rephrased to state that if $\mathbf{u}_k$ of the desired source is expressible as a linear combination of the $\mathbf{u}_j$'s of the other sources, then $\nu_k << 1$. Now, if the rank of $\{\mathbf{u}_k\}_{k=1}^{K}$ is $\hat{r} < K$, then at least $(K - \hat{r})$ of the $\mathbf{u}_k$'s fall into this category. Therefore, even if we succeed in obtaining error-free values for the weights, the relevant $(K - \hat{r})$ processors will still perform very poorly, delivering $\gamma_k << \hat{\gamma}_k$ (11). In other words, $(K - \hat{r})$ of the links will be non-serviceable. But this does not mean that the other $\hat{r}$ links will provide satisfactory service. One could certainly conceive of a rank-deficient vector set in which each and every member of the set is expressible as a linear combination of the other members of the set. All we can say here is that $(K - \hat{r})$ is a lower bound on the number of malfunctioning links.

We turn now to (b). First, let us point out that given $\hat{r}$ and given a specific set of $\hat{r}$ linearly independent vectors[12], we can certainly modify our formulation so as to avoid the singularity. We present here a brief sketch of this approach based on the developments in Ref. 4: Equation (34) is still valid but M is now an $\hat{r} \times \hat{r}$ matrix with

$$M_{ij} = m_{ij} + \epsilon_i (\delta_{ij} + \hat{q}_{ij}) \qquad \text{(A-3)}$$

where[13]

$$\hat{q}_{ij} = \begin{cases} \displaystyle\sum_{s=\hat{r}+1}^{K} \frac{\alpha_{si}\, m_{sj}}{\epsilon_s} & (\hat{r} < K) \\ 0 & (\hat{r} = K) \end{cases} \qquad \text{(A-4)}$$

and α_{si} is defined by

$$\mathbf{u}_s = \sum_{i=1}^{\hat{r}} \alpha_{si}\, \mathbf{u}_i \qquad (\hat{r} < s \leqslant K) \qquad \text{(A-5)}$$

Finally, (21) is replaced by

$$(\nu_k + \epsilon_k) \sum_{j=1}^{\hat{r}} (\hat{q}_{kj} + \delta_{kj})\, \omega_{kj} = 1 \qquad (1 \leqslant k \leqslant \hat{r}) \qquad \text{(A-6)}$$

Equation (34) will now yield the $\{\mathbf{g}_r\}$ components of $\{\mathbf{w}_k\}_{k=1}^{\hat{r}}$. As we have indicated before, the $(K - \hat{r})$ processors $\hat{r} + 1$, $\hat{r} + 2, \ldots, K$ will yield unacceptably low SNR's so there is no need to compute $\{\mathbf{w}_k\}_{k=\hat{r}+1}^{K}$ and we see that (34) yields the complete solution.

Though this approach is mathematically sound, it does raise serious questions concerning the extra cost of determining $\hat{r}$ and selecting a corresponding set of linearly independent $\mathbf{u}_k$'s. We have not looked into this in detail but, assuming the cost is prohibitive, we propose here an alternative line of attack based on a combination of three partial "fixes" – one for a special but rather important circumstance and the other two of more general applicability.

---

[12] We assume for convenience that they are numbered 1, 2, . . . , $\hat{r}$

[13] $\hat{q}_{ij}$ is a trivial modification of q_{ij} of Ref. 4

The special circumstance we consider is that of $\bar{u}_i \approx \bar{u}_j$ $(i \neq j)$. This covers the example cited earlier but is more general since the functional dependence of $\mathbf{u}_i$ on $\boldsymbol{\rho}_i$ is such that widely different $\bar{\rho}_i$'s may yield identical $\mathbf{u}_i$'s. Our strategy here is to forego links i, j altogether but combine their effect on the rest of the system in a single vector (say) $\mathbf{u}_i$ and a modified ϵ_i to account for the combined power of both sources. Obviously, if the original rank deficiency was due to $\mathbf{u}_i = \mathbf{u}_j$ then removal of $\mathbf{u}_j$ would rectify the situation.

The implementation of such a scheme is quite simple and straightforward: In computing the m_{ij}'s for the M matrix, we set a gate to "sound the alarm" whenever $|1 - m_{ij}|^2$ falls below a certain small tolerance[14]. The reaction to this "alarm" is simple too: Eliminate (say) $\mathbf{u}_j$ and replace ϵ_i by ϵ_i' where

$$\frac{1}{\epsilon_i'} = \frac{1}{\epsilon_i} + \frac{1}{\epsilon_j} \qquad \text{(A-7)}$$

Note that this same algorithm is applicable to any number of colinear $\mathbf{u}_i$'s.

The other two "fixes" are:

(1) Increase the difference $(n - K)$. This increases the dimensionality of each $\mathbf{u}_k$ and thereby decreases the likelihood of $\hat{r} < K$.

(2) Devise a network protocol geared to overcome the effects of short-term fading.

Obviously, these are just outlines and the whole subject merits further study.

---

[14] Recall that m_{ij} is complex

N81-27141

The Effect of Noisy Carrier Reference on Telemetry with Baseband Arraying

D. Divsalar, D. Hansen, and J. H. Yuen
Telecommunications Systems Section

Antenna arraying is coherently adding individually received signals from different receiving stations to improve telemetry performance. The array configuration of the current DSN Network Consolidation Project (NCP) will consist of a 64-meter station and three 34-meter stations.

This article examines the effect of noisy carrier reference on telemetry link performance in this NCP configuration when individually received signals are combined at baseband. This imperfect carrier reference causes a degradation in detection performance in coherent communication systems. A measure of this degradation is the radio loss, which is the amount of increase in data signal-to-noise ratio (SNR) per bit required to achieve the same bit error rate when carrier reference is perfect. Performance analysis and numerical results are obtained for the Voyager high rate telemetry link with maximum likelihood convolutional decoding.

The arraying of antennas provides not only improved performance due to an increase in effective antenna aperture, but also a decrease in radio loss with respect to a single antenna. This telemetry link performance improvement is a function of the carrier loop SNR and data bit error rate. When the carrier loop SNR's are low, it provides a significant improvement in the telemetry link performance since the decrease in radio loss with respect to a single station is substantial.

I. Introduction

Antenna arraying is a technique for coherently adding the received signals from different stations in order to achieve improved downlink telemetry performance. Previous articles in the DSN Progress Report (Refs. 1 and 2) discuss the use of arraying. Wilck talked about the baseband combiner used to array the signals from DSS's 12, 13 and 14 for Mariner 10. Arraying provided a 0.8-dB gain in telemetry signal-to-noise ratio. Brockman discussed carrier arraying for improved tracking capability.

In this report we consider baseband arraying of N stations. Results are applied to an array consisting of a 64-meter station and three 34-meter stations, which is the current DSN NCP configuration. Radio loss for a high rate telemetry link is analyzed when baseband arraying is used to add the signals. In this analysis we have assumed that the subcarrier tracking and symbol synchronization are perfect. It is also assumed that there is no carrier arraying. Numerical results are obtained for the Voyager high rate telemetry link with maximum likelihood decoding. Performance analysis shows that the bit error rate is less sensitive to the noisy carrier phase reference when baseband arraying is employed than when a single station is used.

II. System Model and Performance

A system for baseband arraying of N stations is depicted in Fig. 1. Consider the case where the telemetry signal is an RF carrier that is phase-modulated by a squarewave subcarrier ($\text{Sin}\,\omega_{sc} t$) at a peak modulation index θ. The subcarrier is bi-phase modulated with a binary data stream $D(t)$. The telemetry signal can be expressed (without loss of generality, assume station 1) as

$$S_1(t) =$$

$$\sqrt{2P_1} \sin(\omega_c t + \phi_{1c} + D(t)\,\theta\, \text{Sin}(\omega_{sc} t + \phi_{1sc})) + n_1(t) \tag{1}$$

where P_1 is the total received power, ω_c is the carrier radian frequency, ϕ_{1c} is the carrier phase, ω_{sc} is the subcarrier radian frequency, ϕ_{1sc} is the subcarrier phase, and $n_1(t)$ is the additive white Gaussian noise with two-sided spectral density $N_{01}/2$.

The signal $S_1(t)$ is coherently demodulated to the subcarrier frequency by a reference signal generated by the carrier tracking loop,

$$r_1(t) = \sqrt{2} \cos(\omega_c t + \hat{\phi}_{1c}) \tag{2}$$

where $\hat{\varphi}_{1c}$ is the PLL estimate of the carrier phase.

The resulting data signal for station 1 is

$$\begin{aligned} Y_1(t) &= S_1(t)\, r_1(t) \\ &= \sqrt{P_1} \sin\theta\, D(t)\, \text{Sin}(\omega_{sc} t + \phi_{1sc}) \cos\phi_1 + \tilde{n}_1(t) \end{aligned} \tag{3}$$

where $\phi_1 = \phi_{1c} - \hat{\phi}_{1c}$ and $\tilde{n}_1(t)$ is white Gaussian noise with two-sided spectral density $N_{01}/2$ (Refs. 3 and 4).

Similarly, the demodulated signal for the ith station, $i = 2, 3, \ldots, N$ is

$$\begin{aligned} Y_i(t) = \sqrt{P_i} \sin\theta\, D(t - \tau_i)\, \text{Sin}(\omega_{sc}(t - \tau_i) \\ + \phi_{isc}) \cos\phi_i + \tilde{n}_i(t) \end{aligned} \tag{4}$$

where

$$\phi_i = \phi_{ic} - \hat{\phi}_{ic}$$

and $\tilde{n}_i(t)$ is the Gaussian noise process resulting from $n_i(t)$ after carrier demodulation. ϕ_{isc} is ϕ_{1sc} delayed by τ_i, and ϕ_i, ϕ_j are independent phase processes for any $i \neq j$. Without loss of generality, let station 1 be the reference station, i.e., $\tau_1 = 0$, and let $\tau_N > \tau_i$, $i = 1, 2, \ldots, N$.

The corresponding loop signal to noise ratios are

$$\rho_{li} = \frac{P_i \cos^2\theta}{N_{0i} B_{L,i} \Gamma_i}\,; \qquad i = 1, 2, \ldots, N \tag{5}$$

where N_{0i} is the one-sided noise spectral density for $n_i(t)$ in station i, and Γ_i is the limiter performance factor (Refs. 3 and 4).

The received signals should be synchronized. To do so, the relative time delay τ_i for each station should be known. Here it is assumed that τ_i, $i = 1, 2, \ldots, N$, is perfectly estimated; i.e.,

$$\hat{\tau}_i = \tau_i\,; i = 1, 2, 3, \ldots, N \tag{6}$$

Now, we delay the signal from station i by $\hat{\tau}_N - \hat{\tau}_i$, weight the signal from station i by the constant β_i (let $\beta_1 = 1$) and add coherently. Clearly the independent additive noises $n_i(t)$ from each receiver add incoherently, or in a mean square sense.

The resultant signal can be written as

$$\begin{aligned} Z(t) &= \sum_{i=1}^{N} \beta_i Y_i(t - \hat{\tau}_N + \hat{\tau}_i) \\ &= \left[\sin\theta\, D(t - \hat{\tau}_N) \sum_{i=1}^{N} \beta_i \sqrt{P_i} \cos\phi_i\right] \\ &\quad \times \text{Sin}(\omega_{sc} t - \omega_{sc} \tau_N + \phi_{Nsc}) \\ &\quad + \sum_{i=1}^{N} \beta_i \tilde{n}_i(t + \hat{\tau}_i - \hat{\tau}_N) \end{aligned} \tag{7}$$

After subcarrier tracking (assuming perfect tracking) and demodulation we have

$$\begin{aligned} X(t) = \sin\theta\, D(t - \hat{\tau}_N) \sum_{i=1}^{N} \beta_i \sqrt{P_i} \cos\phi_i \\ + \sum_{i=1}^{N} \beta_i \hat{n}_i(t + \hat{\tau}_i - \hat{\tau}_N) \end{aligned} \tag{8}$$

where $\hat{n}_i(t)$, $i = 1, 2, \ldots, N$ are independent low-pass Gaussian noise processes derived from $\tilde{n}_i(t)$ after the subcarrier demodulation process.

The sampled signal at the output of the integrate and dump circuit is

$$x_k = a_k \sin\theta \sum_{i=1}^{N} \beta_i \sqrt{P_i} \cos\phi_i + \sum_{i=1}^{N} \beta_i n_{ik} \tag{9}$$

where n_{ik}, $i = 1, 2, \ldots, N$ are Gaussian noise samples and a_k is the data symbol. At the input of the Viterbi decoder the sample x_k is 3-bit quantized. Given ϕ_i and a_k, the signal-to-noise ratio of sample x_k is

$$SNR = \frac{(\bar{x}_k)^2}{\sigma^2_{x_k}} \tag{10}$$

Here

$$\bar{x}_k = \left(\sum_{i=1}^{N} \beta_i \sqrt{P_i} \cos\phi_i\right) a_k \sin\theta \tag{11}$$

and

$$\sigma^2_{x_k} = \overline{(x_k - \bar{x}_k)^2} = \frac{1}{2T_s} \sum_{i=1}^{N} \beta_i^2 N_{0i} \tag{12}$$

where T_s = symbol time.

Therefore, the signal-to-noise ratio is

$$SNR = \frac{\left(\sin\theta \sum_{i=1}^{N} \sqrt{2P_i T_s} \cos\phi_i\right)^2}{\sum_{i=1}^{N} \beta_i^2 N_{0i}} \tag{13}$$

Note that for a rate 1/2 convolutional code, bit energy is

$$E_{bi} = 2P_i T_s \sin^2\theta \qquad i = 1, 2, \ldots, N \tag{14}$$

Let $f(E_b/N_0)$ represent the bit error rate for a given bit SNR E_b/N_0. Then the conditional bit error rate is

$$P_b(\phi_1, \phi_2, \ldots, \phi_N) = f\left(\frac{\left(\sum_{i=1}^{N} \beta_i \sqrt{E_{bi}} \cos\phi_i\right)^2}{\sum_{i=1}^{N} \beta_i^2 N_{0i}}\right) \tag{15}$$

$$\text{where } f(x) = \begin{cases} \exp[-(\alpha_0 + \alpha_1 x)], & x > \dfrac{\ln(2) - \alpha_0}{\alpha_1} \\ \dfrac{1}{2}, & |x| < \dfrac{\ln(2) - \alpha_0}{\alpha_1} \\ 1 - \exp[-(\alpha_0 + \alpha_1 x)], & x < -\dfrac{\ln(2) - \alpha_0}{\alpha_1} \end{cases} \tag{16}$$

where $\alpha_0 = -4.4514$ and $\alpha_1 = 5.7230$, for standard constraint length 7, code rate 1/2 convolutional code.

Note that ϕ_i, $i = 1, 2, \ldots, N$ are independent, having probability density functions

$$p(\phi_i) = \frac{e^{\rho_{Li} \cos\phi_i}}{2\pi I_0(\rho_{Li})}; \quad i = 1, 2, \ldots, N \tag{17}$$

where ρ_{Li} is the previously defined carrier loop SNR for station i (Eq. 5). The average bit error rate is

$$P_b = \int_{-\pi}^{\pi} \int_{-\pi}^{\pi} \cdots \int_{-\pi}^{\pi} P_b(\phi_1, \phi_2, \ldots, \phi_N)\, p(\phi_1) p(\phi_2) \ldots p(\phi_N)\, d\phi_1 d\phi_2 \ldots d\phi_N \tag{18}$$

Clearly P_b depends on the weighting parameters $\beta_2, \beta_3, \ldots, \beta_N$. For a given set of ρ_{Li}, $i = 1, 2, \ldots, N$ we can find the β_i's which minimize P_b. Analytically this is a very complex task. However, it is straightforward to optimize the β_i's when there are no tracking phase errors. We will use these values of β_i here. These choices of β_i will be suboptimum when the carrier loop SNR is below 15 dB, but the difference in the resulting bit error rate, P_b, is very small.

We want to minimize P_b when there are no phase errors. Note that $f(\cdot)$ (Eq. 16) is a convex, monotonically decreasing function of effective bit SNR. Therefore, minimizing P_b is equivalent to maximizing the effective bit SNR with respect to the β_i's, $i = 1, 2, \ldots, N$.

With no phase errors, the effective bit SNR is

$$SNR = \frac{\left(\sum_{i=1}^{N} \beta_i \sqrt{E_{bi}}\right)^2}{\sum_{i=1}^{N} \beta_i^2 N_{0i}} \tag{19}$$

Note that this function is convex. Therefore, taking the derivative with respect to $\beta_i, i = 1, 2, \ldots, N$ and setting it equal to zero, we get

$$\beta_i = \sqrt{\frac{E_{bi}}{E_{b1}}}\,\frac{N_{01}}{N_{0i}} \tag{20}$$

These choices of β_i minimize the bit error rate. Using (20) in (15), we obtain

$$P_b(\phi_1, \phi_2, \ldots, \phi_N) = f\left[\frac{\left(\sum_{i=1}^{N} \frac{E_{bi}}{N_{0i}} \cos\phi_i\right)^2}{\sum_{i=1}^{N} \frac{E_{bi}}{N_{0i}}}\right] \tag{21}$$

Using (21) in (18) we get the average bit error rate. (Gauss-Chebyshev quadrature formula is used to compute (22).

$$P_b = \int_{-\pi}^{\pi} \int_{-\pi}^{\pi} \cdots \int_{-\pi}^{\pi} f\left[\frac{\left(\sum_{i=1}^{N} \frac{E_{bi}}{N_{0i}} \cos\phi_i\right)^2}{\sum_{i=1}^{N} \frac{E_{bi}}{N_{0i}}}\right]$$

$$p(\phi_1)p(\phi_2)\ldots p(\phi_N)d\phi_1 d\phi_2 \ldots d\phi_N \tag{22}$$

III. Numerical Results for NCP

The current NCP configuration consists of four antennas: a 64-m antenna and three 34-m antennas. Let station 1 be the one with a 64-m antenna. One of the 34-m stations has both transmit and receive capabilities, i.e., T/R, while the other two can only receive, i.e., listen only or L/O.

We assume the additive noises associated with each received signal are independent with equal noise spectral densities, i.e., $N_{01} = N_{02} = N_{03} = N_{04}$. A Block IV receiver with a 30-Hz threshold loop noise bandwidth is assumed for each station. It is also assumed that the received powers for the 34-m T/R station and the two 34-m L/O stations are less than the received power for the 64-m station by 5.8 dB, and 4.6 dB, respectively.

From (20) we have

$\beta_1 = 1$

$\beta_2 = 1/2\,(-5.8 \text{ dB}) = 0.513$

$\beta_3 = \beta_4 = 1/2\,(-4.6 \text{ dB}) = 0.589$

Using these parameters, numerical results have been obtained. The telemetry bit error rate is evaluated as a function of E_{b1}/N_{01}. This is shown in Fig. 2 for different values of ρ_{l1}, the carrier loop SNR for station 1. Comparisons between the radio loss for a single 64-m station and the array for bit error rates of 5×10^{-3} and 5×10^{-5} are illustrated in Figs. 3 and 4, respectively. When the carrier loop SNR is greater than 15 dB there are essentially no differences between the two curves. When the carrier loop SNR is less than 15 dB, the array has a decrease in radio loss with respect to a single station.

Reference 5 provided the telemetry total power to noise spectral density ratio as a function of time during Uranus encounter for DSS 43 in Australia (a typical case). The carrier margin was derived assuming an 80° modulation index. The carrier margin for DSS 43 during Uranus encounter is plotted as a function of time in Fig. 5. Corresponding to Fig. 5, the radio loss is plotted as a function of time in Fig. 6 for a four-element array in Australia during Uranus encounter.

IV. Conclusion

The arraying of N antennas, in this case a 64-m station and three 34-m stations, provides not only gain due to an increase in effective antenna aperture, but also a decrease in radio loss. The amount of this decrease is a function of the desired bit error rate and carrier loop SNR. When the carrier loop SNR is very high, the radio loss is negligible so the array gain is due only to the increased antenna aperture. For lower loop SNR's the decrease in radio loss is substantial, as shown in the radio loss curves. For the NCP configuration, with the Voyager spacecraft during Uranus encounter, radio loss can be expected to be less than 0.6 dB for the majority of the pass. This assumes a BER of 5×10^{-3}. The radio loss should always be under 1.0 dB.

References

1. Wilck, H., "A Signal Combiner for Antenna Arraying," *DSN Progress Report 42-25*, Jet Propulsion Laboratory, Pasadena, Calif., February 15, 1975, pp. 111-117.
2. Brockman, M., "Radio Frequency Carrier Arraying for High Rate Telemetry Reception," *DSN Progress Report 42-45*, Jet Propulsion Laboratory, Pasadena, Calif., June 15, 1978, pp. 209-223.
3. Viterbi, A. J., *Principles of Coherent Communication*, McGraw-Hill, New York, 1966.
4. Lindsey, W. C., *Synchronization Systems in Communication and Control*, Prentice-Hall, Inc., Englewood Cliffs, New Jersey, 1972.
5. Madsen, B., Voyager Project unpublished notes, March 1981.

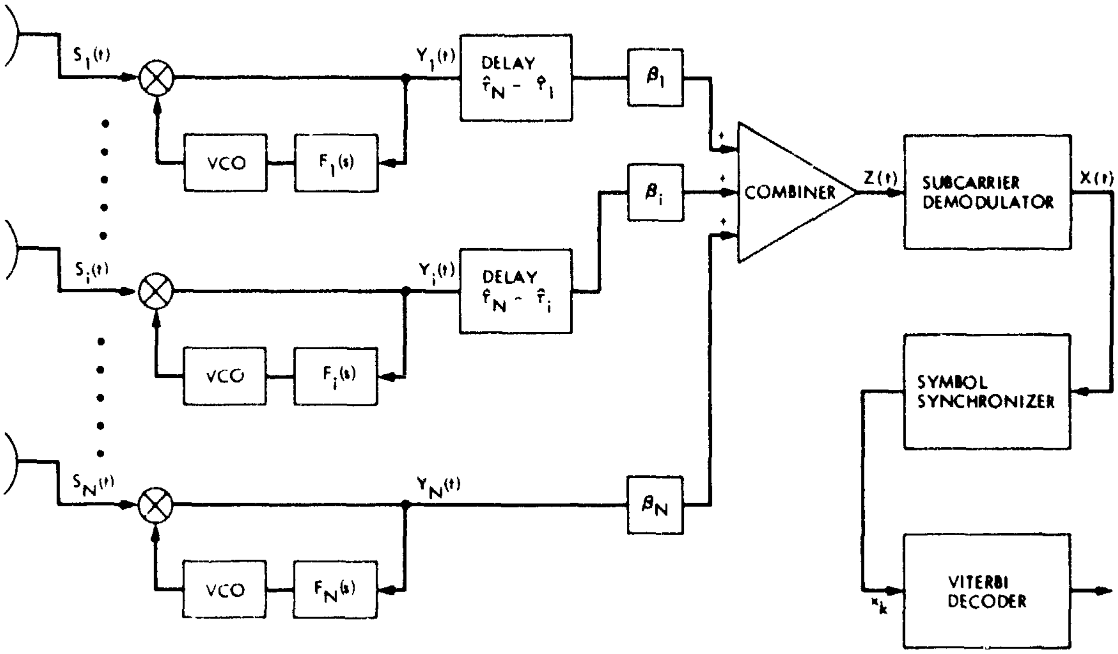

Fig. 1. Configuration for arrayed network with baseband arraying

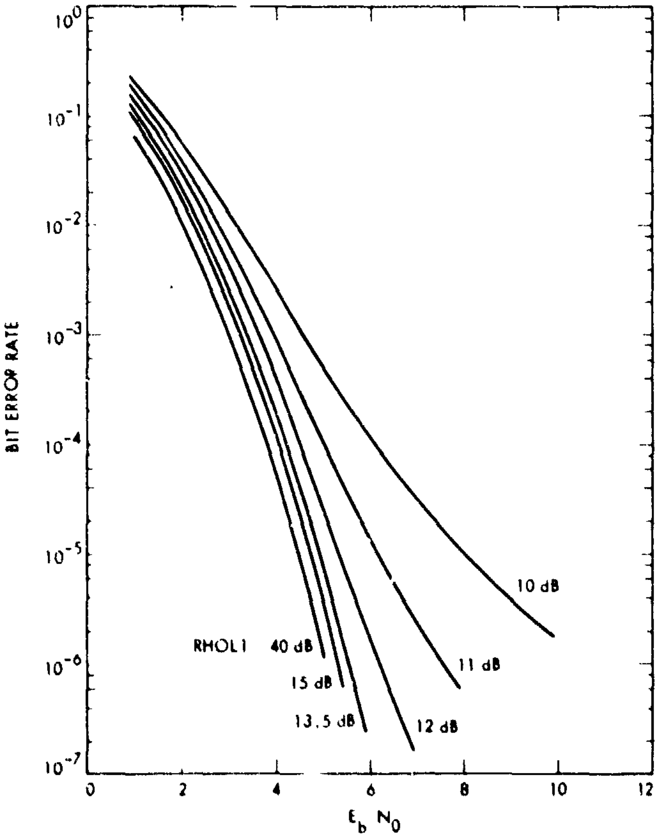

Fig. 2. Performance curves for a four-element array using a baseband combiner

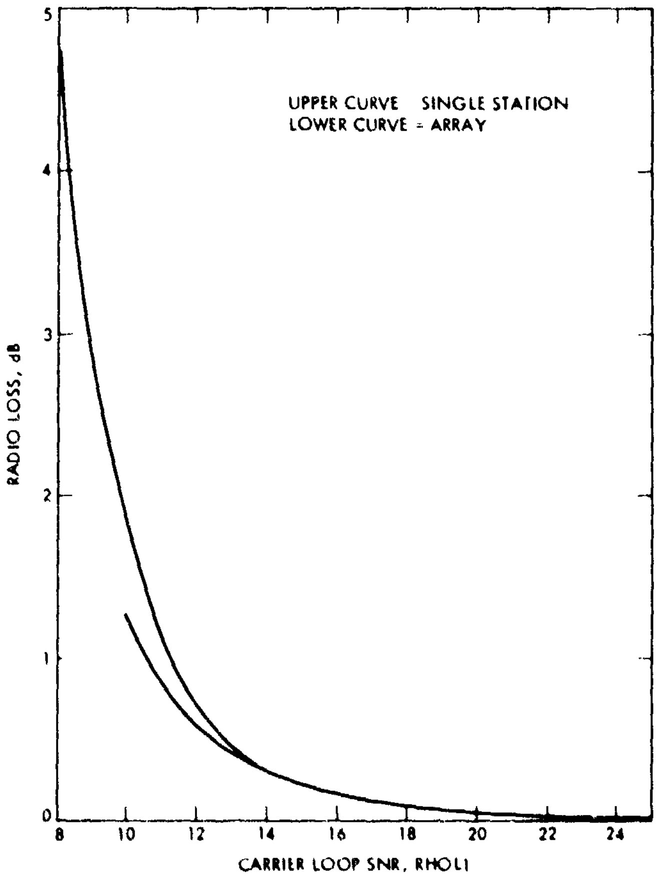

Fig. 3. One-way high rate radio loss for a BER of 5 × 10^{-3}

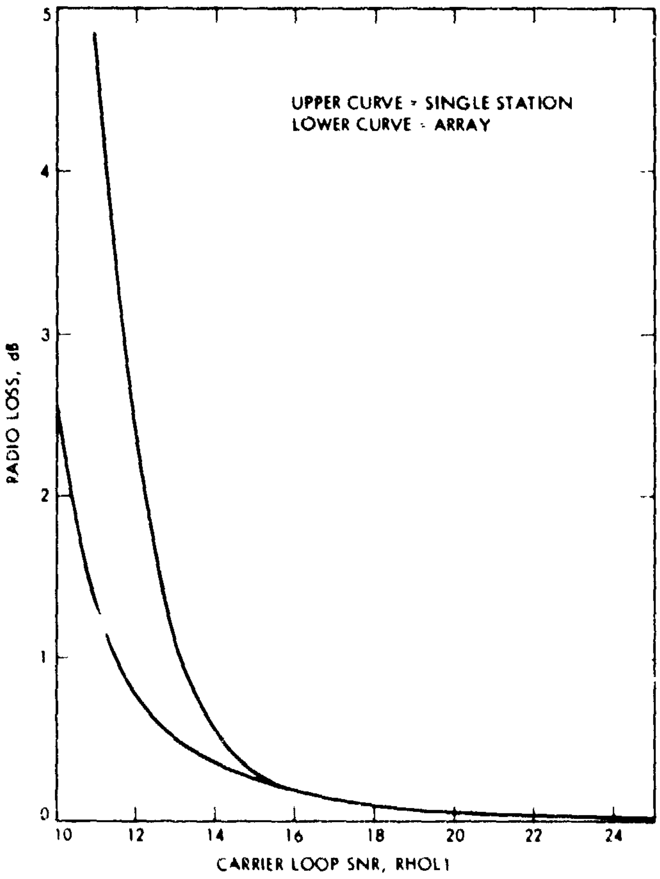

Fig. 4. One-way high rate radio loss for a BER of 5 × 10^{-5}

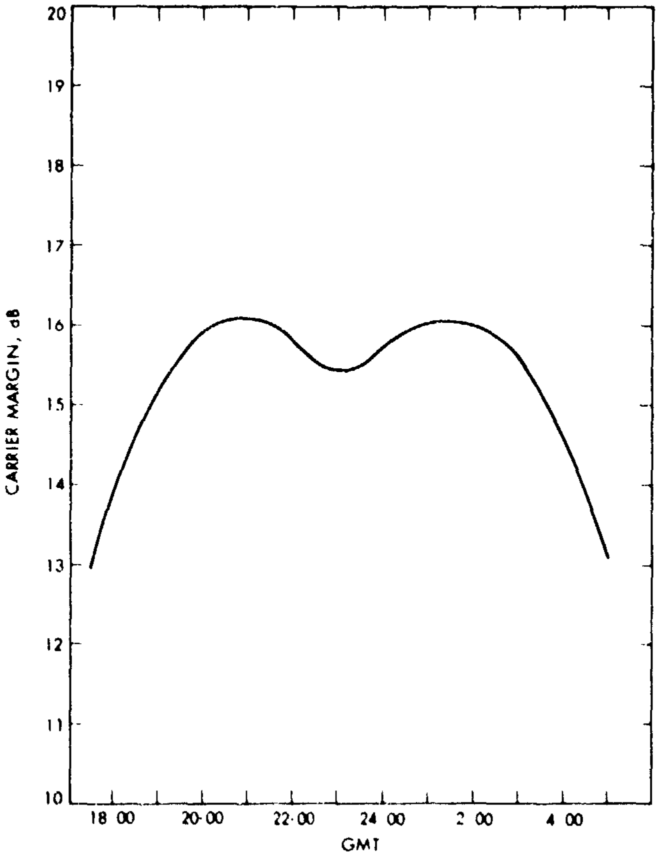

Fig. 5. Carrier margin for DSS 43 at Uranus

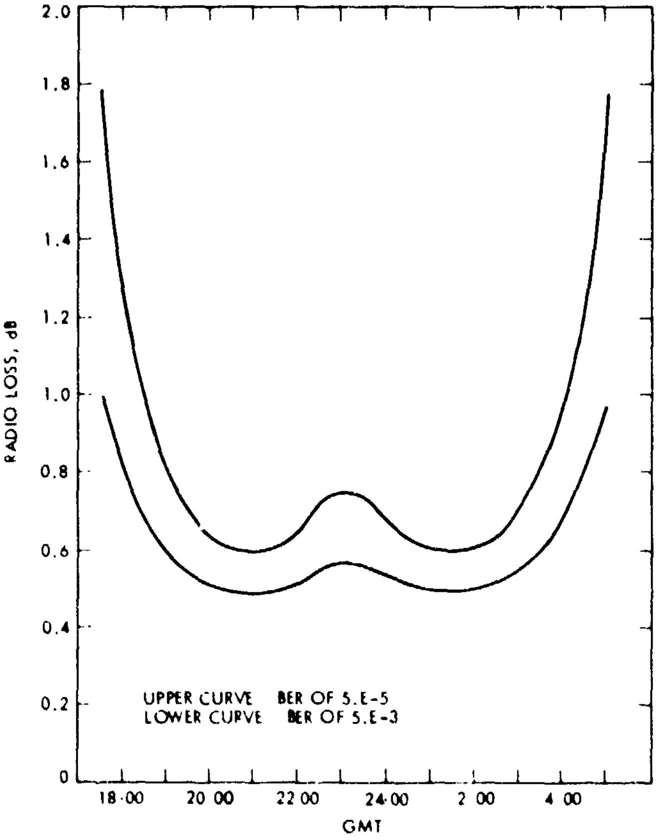

Fig. 6. Radio loss for Australian array at Uranus

D19 N81-27142

The Effects of Pointing Errors on the Performance of Optical Communications Systems

V. A. Vilnrotter
Telecommunications Systems Section

Optical communications systems operating over interplanetary distances require the use of extremely narrow optical beams for maximum power concentration near the receiver. Consequently, pointing errors must be kept to a small fraction of a beamwidth to avoid severe deterioration in receiver performance, due to the decrease in received power associated with pointing errors. In this article, the mathematical models required for studying the effects of random pointing errors are developed and applied to the problem of quantifying the effects of pointing errors on the performance of coherent and incoherent optical receivers.

I. Introduction

Long-distance optical communications systems generally operate with narrow optical beams, in order to maximize the signal power-density in the vicinity of the receiver. While the minimum attainable beamwidth is limited by diffraction effects, optical antennas can generate beams with divergence angles on the order of microradians. Therefore, accurate beam pointing becomes a formidable task, and even minute pointing errors can lead to severe deterioration in system performance. Here we consider an idealized long-distance optical communications system model consisting of a diffraction-limited optical transmitter and an optical receiver located in the far-field of the transmitted beam. In order to simplify the analysis, it is assumed that there is no relative motion between the receiver and the transmitter. We concentrate on modelling the optical field at the receiver in the presence of random pointing errors and on developing a useful model for the probability density of the pointing error. The model is applied to the optical communications problem in order to determine the effects of constant pointing offsets and random pointing errors on the performance of both coherent and direct-detection (or incoherent) optical communications systems.

II. Mathematical Models for the Received Field

Consider the field-propagation model shown in Fig. 1. A circular transmitter aperture $\mathcal{A}_t$ is assumed to be centered in the transmitter plane (coordinates x_1, y_1). The transmitter aperture is illuminated by a temporally modulated, normally incident plane-wave $U_t(t; x_1, y_1)$, which we model as

$$U_t(t, x_1, y_1) = \begin{cases} U_1(t_1); & x_1^2 + y_1^2 \leqslant (d_t/2)^2 \\ \\ 0 \;; & \text{elsewhere} \end{cases} \tag{1}$$

where we define $t_1 = t + (z/c)$ in order to account for propagation delay, d_t is the diameter of the transmitter aperture and c is the speed of light. The temporal component is defined as

$$U_1(t) = \left(\frac{U_1}{\sqrt{A_t}}\right) m(t) \exp\left[j(\omega t + \phi_1(t))\right] \tag{2}$$

where A_t is the area of the transmitter aperture, $U_1/\sqrt{A_t}$ is the normalized field amplitude, $m(t)$ is the modulating waveform ($|m(t)| \leqslant 1$), ω is the radian frequency of the optical carrier, and $\phi_1(t)$ is a random phase process associated with the optical source. The normalized field amplitude $U_1/\sqrt{A_t}$ can be interpreted as an equivalent field amplitude that generates an average photon rate of $n_t = U_1^2/h\nu$ photons/second, independent of the area of the transmitting aperture (here h is Planck's constant, and $\nu = \omega/2\pi$ is the optical carrier frequency). The beam axis is defined to be a line normal to the transmitter plane, passing through the origin. The receiver aperture $\mathscr{A}_r$ (with collecting area A_r) is assumed to be located a distance z from the origin of the transmitter plane, perpendicular to the line between the centers of the transmitter and receiver apertures. The pointing error θ_e is defined as the angle between this line and the beam axis, as shown in Fig. 1.

The receiver aperture is assumed to be in the "far-field," or Fraunhofer region, of the transmitted beam. If the dimensions of the receiver aperture are much smaller than the beam dimensions, then amplitude and phase variations over the aperture can be neglected, and the complex field at the receiver can be represented as

$$U(t; z, \theta_e) = A_t U_1(t) f(z) G(\theta_e) \tag{3}$$

where

$$f(z) = \frac{e^{j2\pi z/\lambda}}{j\lambda z} \tag{4}$$

$$G(\theta_e) \simeq 2\,\frac{J_1(\pi d_t \theta_e/\lambda)}{(\pi d_t \theta_e/\lambda)} \tag{5}$$

and $J_1(\cdot)$ is the Bessel function of order one (Ref. 1). The amplitude gain function $G(\theta_e)$ is the normalized diffraction pattern of the transmitter aperture. The amplitude gain function $G(\theta_e)$ and the intensity gain function $G^2(\theta_e)$ are shown in Fig. 2. Note that the first zero occurs at $\zeta \triangleq (\pi d_t/\lambda)\theta_e = 3.82$, clearly defining the dimensions of the main lobe.

When the standard deviation of the pointing error is much less than one radian ($\theta_e << 1$ radian), the pointing error can be conveniently decomposed into orthogonal components θ_x and θ_y, where

$$\theta_x = \theta_e \cos\psi \tag{6a}$$

$$\theta_y = \theta_e \sin\psi \tag{6b}$$

and

$$\psi = \tan^{-1}\left(\frac{\theta_y}{\theta_x}\right) \tag{6c}$$

We assume that θ_x and θ_y are independent random variables with mean values η_x and η_y, and variance σ_x^2 and σ_y^2 respectively. The total pointing error process can then be expressed in terms of θ_x and θ_y as

$$\theta_e(t) = \left[\theta_x^2(t) + \theta_y^2(t)\right]^{1/2} \tag{7}$$

It is convenient to define the parameter η as

$$\eta = \left[\eta_x^2 + \eta_y^2\right]^{1/2} \tag{8}$$

which can be interpreted as the pointing error induced by constant pointing offsets in the θ_x and θ_y directions.

The analysis becomes somewhat tractable if we assume that $\theta_x(t)$ and $\theta_y(t)$ are Gaussian random processes. Suppressing the time dependence for notational simplicity, and letting $\sigma_x^2 = \sigma_y^2 = \sigma^2$ the probability density for the independent Gaussian random variables θ_x and θ_y is given by the expression

$$p_{xy}(\theta_x, \theta_y) = \frac{1}{2\pi\sigma^2} \exp\left[-\frac{(\theta_x - \eta_x)^2 + (\theta_y - \eta_y)^2}{2\sigma^2}\right] \tag{9}$$

The density of θ_e can be determined by a straightforward transformation (Ref. 2); using Eq. (6), the joint density of the random variables θ_e and ψ can be expressed as

$$p(\theta_e, \psi) = \frac{\theta_e}{2\pi\sigma^2} \exp\left[-\frac{(\theta_e \cos\psi - \eta_x)^2 + (\theta_e \sin\psi - \eta_y)^2}{2\sigma^2}\right] \tag{10}$$

It follows therefore that

$$p(\theta_e) = \int_0^{2\pi} p(\theta_e, \psi)\, d\psi = \frac{\theta_e}{\sigma^2} \exp\left[-\frac{(\theta_e^2 + \eta^2)}{2\sigma^2}\right] \left(\frac{1}{2\pi} \int_0^{2\pi} \exp\left[\frac{\theta_e}{\sigma^2}(\eta_x \cos\psi + \eta_y \sin\psi)\right] d\psi\right) \tag{11}$$

Defining the angle ψ_1 as

$$\psi_1 = \tan^{-1}\left(\frac{\eta_y}{\eta_x}\right) \tag{12}$$

we can rewrite the exponent inside the integral as

$$\eta_x \cos\psi + \eta_y \sin\psi = \eta \cos(\psi_1 - \psi) \tag{13}$$

The integral is now recognized as a representation of the modified Bessel function of order zero

$$\frac{1}{2\pi} \int_0^{2\pi} \exp\left[\frac{\theta_e}{\sigma^2}\, \eta \cos(\psi_1 - \psi)\right] d\psi = I_0\left(\frac{\theta_e \eta}{\sigma^2}\right) \tag{14}$$

Substituting Eq. (14) into Eq. (11) yields

$$p(\theta_e) = \frac{\theta_e}{\sigma^2} \exp\left[-\frac{1}{2\sigma^2}(\theta_e^2 + \eta^2)\right] I_0\left(\frac{\theta_e \eta}{\sigma^2}\right) \tag{15}$$

which is seen to be the well-known Rice density. Note that since $I_0(0) = 1$, Eq. (15) reduces to the familiar Rayleigh density in the limit as the pointing error $\eta \to 0$. In the following sections, we shall apply the above results to examine the effects of pointing error on the performance of direct detection and coherent optical receivers.

III. Performance of Optical Receivers in the Presence of Pointing Errors

In this section, the effects of pointing errors on receiver performance are examined. First, we consider the effects of pointing errors on direct-detection receivers, assuming that M-ary PPM signal sets are observed. Such signals can be generated by letting $m(t) = 1$ over one of M time slots, and zero over the remaining $(M - 1)$. The performance of M-ary PPM receivers in the presence of background radiation has been studied elsewhere (Ref. 3). Here we shall assume that the effects of background radiation are negligible, and concentrate on the effects of random pointing errors.

The symbol-error probability can be expressed in terms of the symbol erasure probability as

$$P_d(E) = \frac{M-1}{M} \tag{16a}$$

where

$$= \exp[-K_s] \tag{16b}$$

and K_s is the average count per symbol, in the absence of any pointing errors. For pulses that are much narrower than the correlation time of the pointing-error process, the average pulse count can be related to the received field, conditioned on a given pointing error, θ_e, as

$$K_s(\theta_e) = \frac{\rho}{h\nu}\iint_{A_r}\left[\int_0^{\tau} |U(t,\theta_e)|^2\, dt\right] dx\, dy = \left(\frac{\rho}{h\nu}\right) A_r \left(\frac{U_1^2}{\Omega_t z^2}\right) G^2(\theta_e) = K_s G^2(\theta_e) \tag{17}$$

where τ is the pulse duration, ρ is the quantum efficiency of the photodetector, h is Planck's constant, ν is the optical frequency, and $\Omega_t = \lambda^2 / A_t$ is the divergence of the transmitted beam, measured in steradians. The unconditional erasure probability is obtained by averaging the conditional erasure probability over the density of the pointing-error

$$= \int_0^{\infty} \exp[-K_s(\theta_e)]\, p(\theta_e)\, d\theta_e \tag{18}$$

This expression is accurate whenever the Gaussian approximation for θ_x and θ_y can be invoked. For the pointing-error density of Eq. (15), the erasure probability becomes

$$= \frac{1}{\sigma^2}\int_0^{\infty} \theta_e \exp\left[-K_s G^2(\theta_e) - \frac{(\theta_e^2 + \eta^2)}{2\sigma^2}\right] I_0\left(\frac{\theta_e \eta}{\sigma^2}\right) d\theta_e \tag{19}$$

In the limit as $\sigma^2 \to 0$, $p(\theta_e) \to \delta(\theta_e - \eta)$, and the erasure probability reduces to

$$= \exp[-K_s G^2(\eta)] \tag{20}$$

This erasure probability is shown in Fig. 3 as a function of the normalized pointing error η_e for several values of K_s, where $\eta_e = (\pi d_t / \lambda)\eta$. In terms of these units, a normalized mean value of $\eta_e = 3.82$ corresponds to the planar half-angle of the main lobe (the actual main lobe half-angle is, of course, $(\lambda / \pi d_t)$ times as great). The points where $= 1$ correspond to the zeros of the antenna pattern.

The effects of random pointing errors on the erasure probability are shown in Fig. 4(a) through 4(c). (Numerical integration of Eq. (19) was employed to obtain these graphs.) For a given K_s, the erasure probability is shown as a function of the normalized mean pointing error $\eta_e = (\pi d_t/\lambda)\eta$ for various values of the normalized variance $\sigma_e^2 = (\pi d_t/\lambda)^2 \sigma^2$. Recall that in typical applications, $(\lambda/\pi d_t) \simeq 10^{-6}$, which means that typical beam half angles are on the order of microradians. Note that for high values of K_s, $(K_s \geq 10)$ the erasure probability increases dramatically with increasing (normalized) variance, emphasizing the importance of reducing the variance of the pointing error to a small fraction of the main-lobe divergence when operating at low error probabilities. At low values of K_s, $(K_s \leq 5)$, the effects of mean pointing offsets and random pointing errors become much less pronounced, suggesting that under these conditions the requirements on pointing accuracy can be relaxed.

The performance of coherent receivers can be analyzed in a similar manner. Coherent homodyne reception requires the addition of a local field prior to photodetection. We model the local field as an equivalent plane-wave with temporal variation

$$U_l(t) = \left(\frac{U_L}{j}\right) \exp\left[j(\omega t + \phi_l(t))\right] \tag{21}$$

where U_L is the field amplitude, and $\phi_l(t)$ is a random phase process due to phase instabilities within the local laser. Assuming that $U_l >> U_1/\sqrt{\Omega_r}z$ (which is generally true for long-range communications systems) the average count generated by a binary antipodal signal $(m(t) = \pm 1)$, given that hypothesis H_i is true $(i = 0, 1)$ can be expressed as

$$K_i(\theta_e) = \frac{\rho}{h\nu} \iint_{\mathcal{A}_r} \left[\int_0^T |U(t,\theta_e) + U_L(t)|^2\, dt\right] dx\, dy = \frac{\rho}{h\nu} A_r \left[U_l^2 + 2(-1)^{(i+1)} \frac{U_L U_1}{\sqrt{\Omega_t}z} G(\theta_e) \cos\phi_e\right] \tag{22}$$

where $\phi_e = [\phi_1 - \phi_l + (2\pi z/\lambda)]$ is the phase process of the detected field. If the phase-tracking error $\phi_e(t)$ is assumed to be negligible, then we can let $\cos\phi_e \simeq 1$. If the pointing errors were also negligible $(\theta_e = 0)$, then the error probability of the above coherent receiver could be expressed as (Ref. 4)

$$P_e(E) = Q(\sqrt{4K_s})$$

$$Q(u) = \frac{1}{2\pi} \int_u^\infty e^{-z^2/2}\, dz \tag{23}$$

where K_s is again the average number of signal counts over a given bit interval. We have observed before that the effect of the pointing error θ_e is to decrease the average number of observed counts in proportion to the normalized antenna pattern of the transmitter aperture. Therefore, the conditional error probability of the coherent binary (MAP) receiver can be expressed as

$$P_e(E|\theta_e) = Q(\sqrt{4K_s}\, G(\theta_e)) \tag{24}$$

(Note that the argument of Eq. (24) may take on negative values due to the phase-sensitive detection technique we have employed, which responds to negative values of $G(\theta_e)$). The unconditional error probability is again the average of the conditional error-probability over the pointing-error statistics

$$P_e(E) = \frac{\left[\exp -\left(\frac{\eta^2}{2\sigma^2}\right)\right]}{\sigma^2} \int_0^\infty \theta_e Q(\sqrt{4K_s}\, G(\theta_e)) \exp\left[-\frac{\theta_e^2}{2\sigma^2}\right] I_0\left(\frac{\theta_e \eta}{\sigma^2}\right) d\theta_e \tag{25}$$

When only pointing offsets are present, the error probability again becomes a function of η

$$P_e(E) = Q(\sqrt{4K_s}\, G(\eta)) \tag{26}$$

Figure 5 shows the error probability of the coherent receiver as a function of η_e, in the limit as $\sigma_e^2 \to 0$, which again corresponds to the idealized pointing error density $p(\theta_e) = \delta(\theta_c - \eta)$. Note that the error probability may exceed a half because the antenna pattern can assume negative values, in which case the receiver almost certainly commits an error. As the variance of the pointing error increases ($\sigma_e^2 > 0$) receiver performance deteriorates, as can be seen in Fig. 6(a) through 6(c). (Again, numerical integration was employed to evaluate Eq. (25)). As before, we observe that the performance deterioration due to pointing error is most severe when the receiver is operating at low error probabilities, and tends to become less serious as the average on-axis signal bit count K_s decreases.

IV. Summary and Conclusions

We have developed a general model for evaluating the effects of random pointing errors on the received field in long-range optical communications systems. The probability density of the pointing-error random process has been derived for the case of independent, equal-variance Guassian pointing error components. This model was then applied to the problem of determining the effects of pointing errors on the performance of direct-detection and coherent optical receivers. The results indicate that pointing errors tend to cause a severe deterioration in receiver performance only when the optical receivers are operating at very low error probabilities. Therefore, the ultimate performance of long distance optical communications systems may well be limited by the ability of the transmitter to point the downlink beam toward the intended receiver.

References

1. Born, M., and Wolf, E., *Principles of Optics*, Pergamon Press, New York, 1975.
2. Papoulis, A., *Probability, Random Variables and Stochastic Processes*, McGraw-Hill, New York, 1965.
3. Gagliardi, M., and Karp, S., *Optical Communications*, J. Wiley, New Yc , 1976.
4. Vilnrotter, V. A., "A Binary Coherent Optical Receiver for the Free-Space Channel," in *The TDA Progress Report 42-61*, pp. 27-38, Jet Propulsion Laboratory, Pasadena, Calif., Feb. 15, 1981.

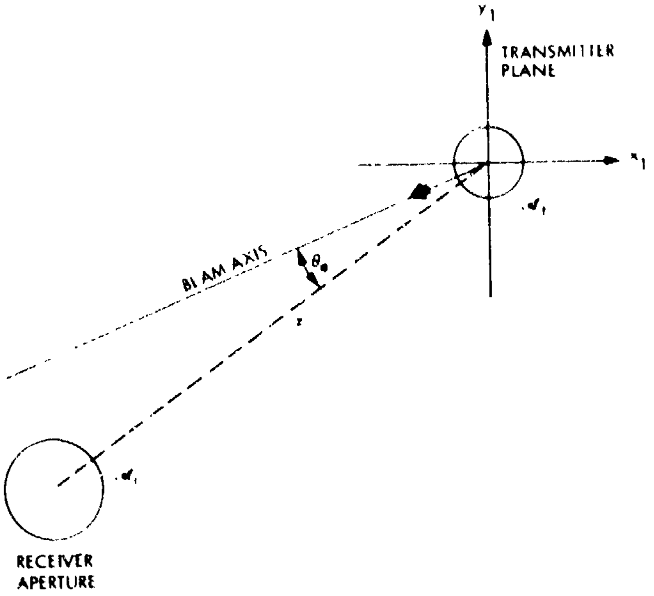

Fig. 1. Optical field propagation geometry

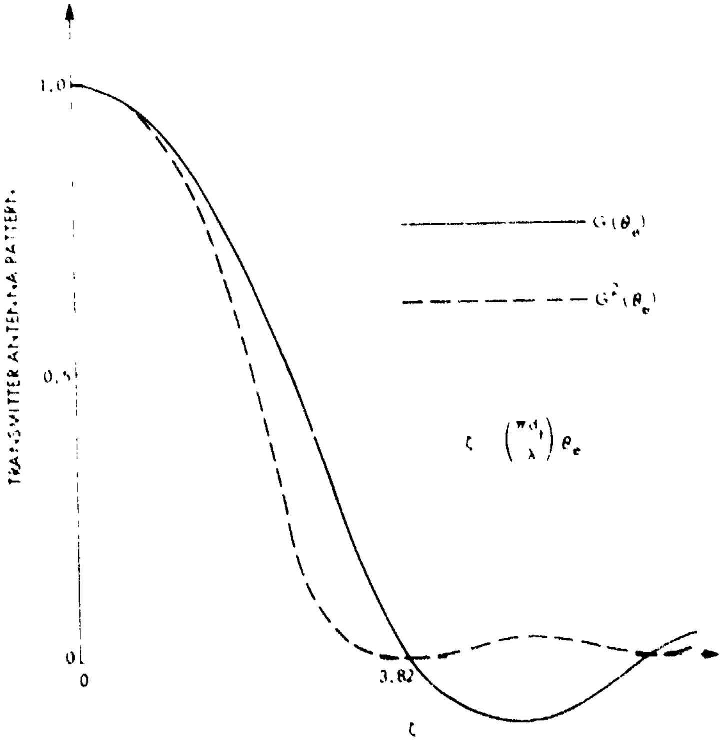

Fig. 2. Amplitude and intensity patterns generated by a circular transmitter aperture

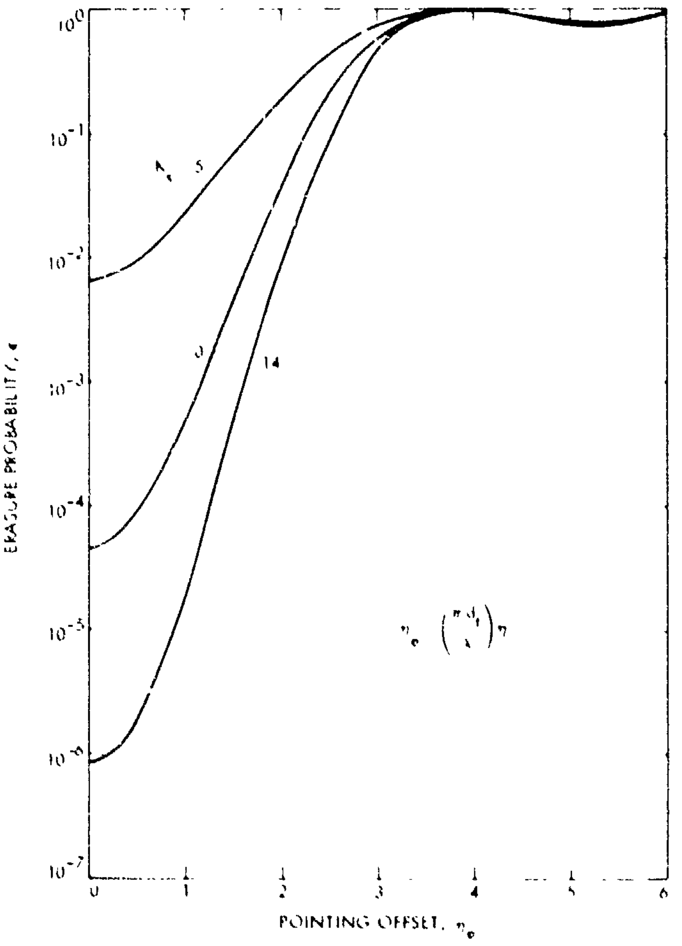

Fig. 3. Erasure probability in the presence of pointing offset

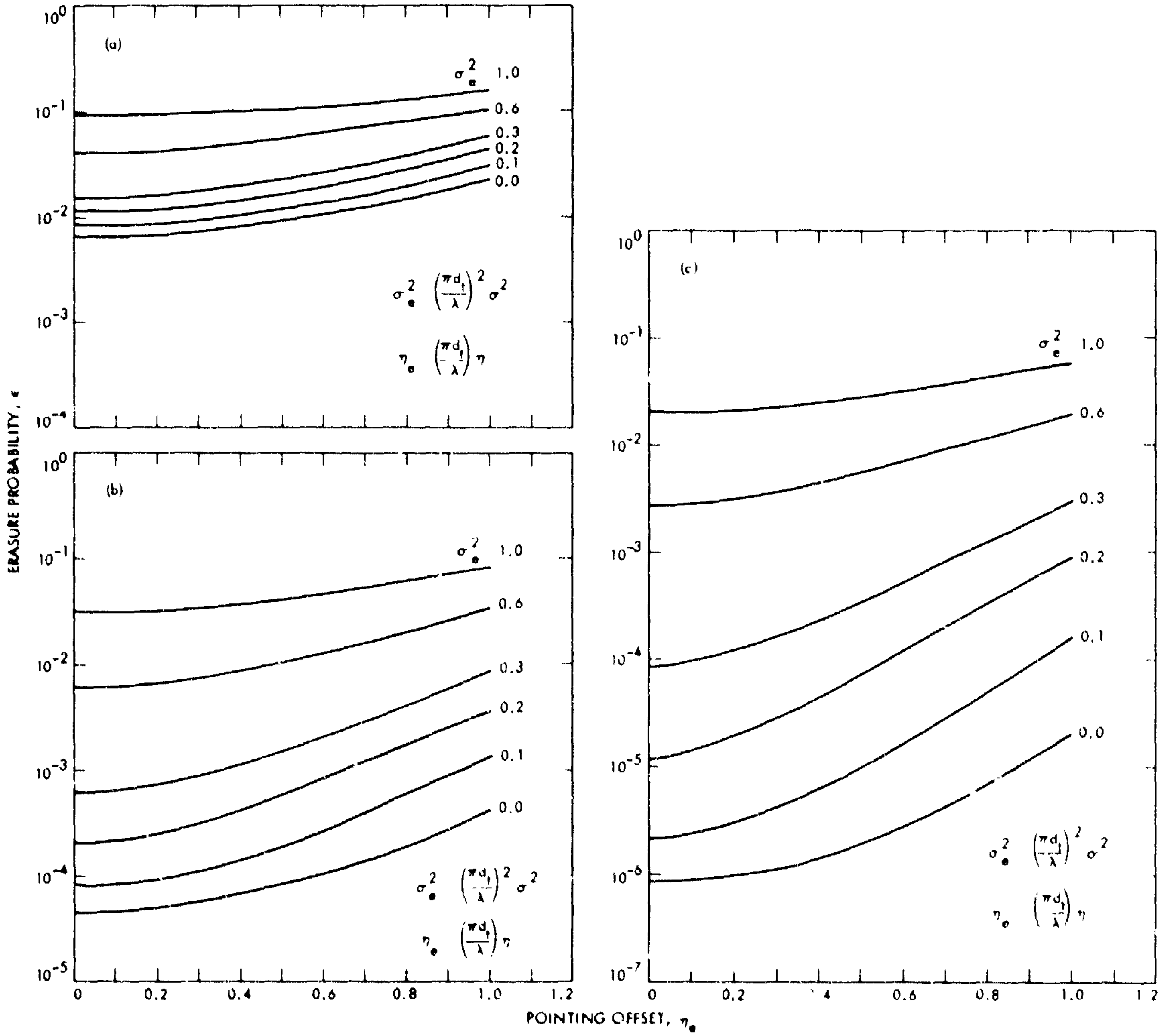

Fig. 4. Erasure probability in the presence of pointing error: (a) $K_s = 5$; (b) $K_s = 10$; (c) $K_s = 1$

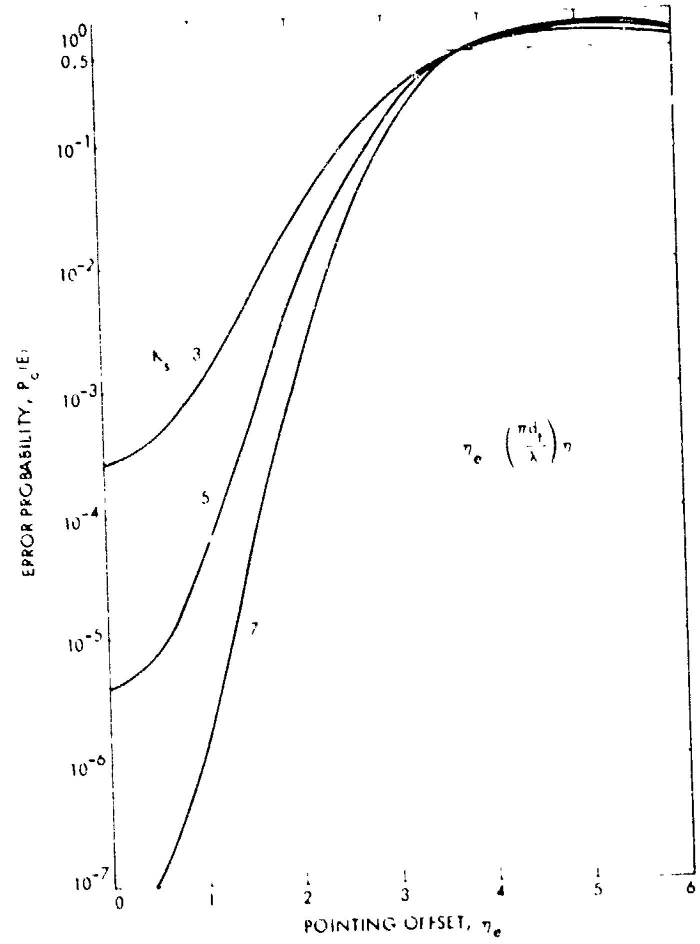

Fig. 5. Performance of binary coherent receiver in the presence of pointing offset

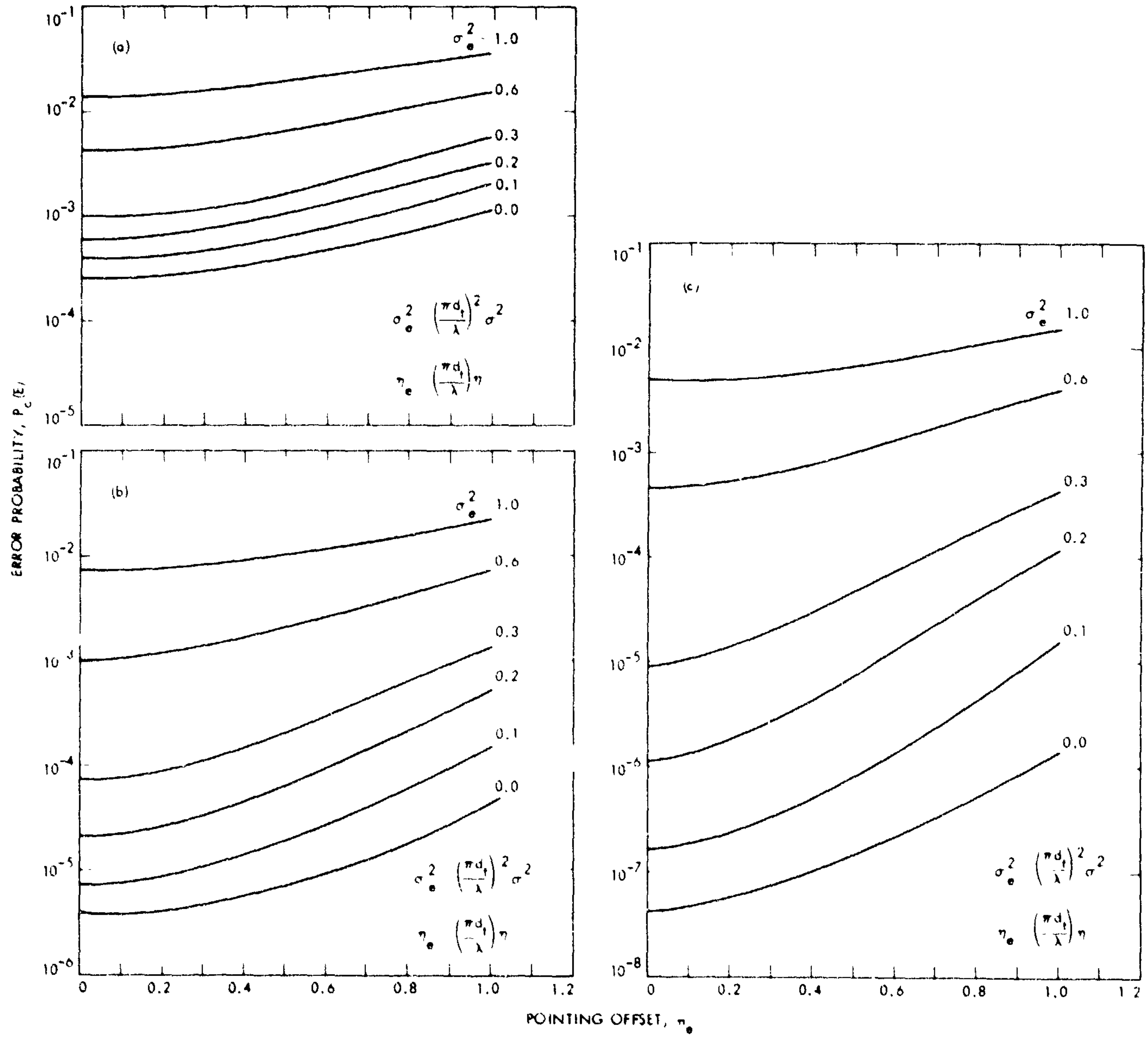

Fig. 6. Performance of binary coherent receiver in the presence of pointing error: (a) $K_s = 3$; (b) $K_s = 5$; (c) $K_s = 7$

N81-27143 D 20

On the Correction for Quantization Effects in Signal-To-Noise Ratio Estimation

L. Howard
Radio Frequency and Microwave Subsystems Section

In sampled data digital telemetry systems the signal-to-noise ratio (SNR) is typically derived as a function of the moments of the digitized input stream (e.g., the receiver output). This analog-to-digital conversion process is itself an additional noise source known as the "quantization" noise. Thus a digitally measured SNR will only approximately represent the SNR of the analog input signal. This report presents a procedure (Sheppard's corrections) for correcting moments of any order for this quantization effect.

I. Introduction

Experience gained over the last two years using the existing subsystems for arraying (Ref. 1) at Jupiter (Voyager 2) and Saturn (Pioneer 11, Voyagers 1 and 2) shows that one of the weak points of the current system is the ability to accurately monitor telemetry signal-to-noise ratio (SNR) at levels acceptable for real-time array performance validation. As part of a development task to improve performance in this area a review and analysis of the problems expected from digital signal processing and SNR estimation has been undertaken. The first of a series of reports on this work is a treatment of quantization effects.

II. Quantization Effects

Quantization error is the term applied to the errors introduced by representation of analog values by a finite (usually few) number of bits. Other sources of numerical error may be introduced during internal calculations; but they are seldom of the significance of the initial quantization errors from the analog-to-digital conversion process, and they can usually be avoided by careful hardware design.

The most extreme case of quantization error occurs when only the sign of the analog signal (+ or −) survives the digital conversion process. This process is often referred to as hard-limiting the signal, and the output is called the sign bit. Single bit estimators are important in that they minimize hardware complexity, often with an acceptable degradation in performance.

There should be a separate treatment of n bit quantization for each $n = 1, 2, 3 \ldots$ ad nauseum. Fortunately an n bit quantizer has 2^n states or quantization levels, each state occupying 2^{-n} of full-scale input range (nonlinear or companding converters will not be treated here, although companding offers interesting possibilities). For $n > 4$ the quantization levels become close enough together that we may assume the sampled distribution is constant over the width of a level. This allows us to treat all cases of sufficiently large n as if the conversion was infinitely accurate ($n \rightarrow \infty$) but also introduces an additive noise component (dependent on n) called the quantization noise.

For an n bit quantizer the quantization levels are spaced 2^{-n} of full range apart; call this value ϵ. The quantized output can exactly represent the input only if the input is exactly at one of these quantization levels. Imagine now that for any arbitrary analog input (within range), an additional "noise" source was added so that the resulting analog signal was moved to the nearest quantization level.

This is the "quantization noise." From what has already been said, its distribution will be uniform from $-\epsilon/2$ to $+\epsilon/2$ about zero (and thus $dF = dx/\epsilon$) and the associated noise power is thus

$$P_{QNoise} = \int_{-\epsilon/2}^{\epsilon/2} x^2 \left(\frac{1}{\epsilon}\right) dx = \frac{\epsilon^2}{12} \qquad (1)$$

The effect of quantization noise is to increase the effective noise component of the signal-to-noise ratio during the act of digitization.

A block diagram of the process is:

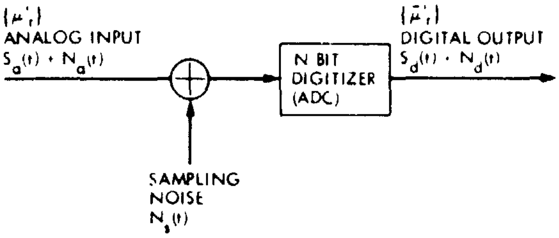

where $\{\mu'_r\}$ = moments of the left-hand side of the distribution, and $\{\bar{\mu}'_r\}$ = moments of the right-hand side of the distribution. Since the analog input power is usually held constant (to keep within the ADC range), the digitally estimated SNR asymptotically approaches a constant value as the analog SNR increases.

Consider the general effect on moments over the distribution. Analog moments on the left-hand side (l.h.s.) of the block diagram are given by

$$\mu'_r = \int_{-\infty}^{\infty} x^r \, dF(x) = \sum_{K=0}^{2^N} \int_{V_K}^{V_{K+1}} x^r dF(x) \qquad (2)$$

where

$F(x)$ = input distribution

μ_r = r^{th} central moment (l.h.s.)

V_K = K^{th} quantization level, $K = 1, \ldots, 2^N$
($V_0 \rightarrow -\infty$, $V_{2+1} \rightarrow +\infty$)

Digital moments on the right hand side (r.h.s.) of the block diagram are given by

$$\bar{\mu}'_r = \sum_{K=1}^{2^N} V_K^r \int_{V_K}^{V_{K+1}} dF(x) = \sum_{K=1}^{2^N} V_K^r \left[F(V_K) - F(V_{K-1})\right] \qquad (3)$$

The problem of approximating integrals like Eq. (2) by finite sums like Eq. (3) is the subject of the Euler-Maclaurin sum formula (see Ref. 2). The estimation of continuous moments from quantized or group data is fortunately a familiar problem in statistics. The results are known as Sheppard's corrections, and the detailed development may be found in statistics texts such as Ref. 3. The formulas for Sheppard's corrections are summarized in the next section.

III. Quantization Effect Corrections

The results are as follows.

$$\mu'_r = \sum_{j=0}^{\left[\frac{r}{2}\right]} \binom{r}{2j} \left(\frac{1}{2}\epsilon\right)^{2j} \frac{1}{2j+1} \mu'_{r-2j} \qquad (4)$$

where

$\left[\frac{r}{2}\right]$ is the integral part of $\frac{r}{2}$

which approximates the r.h.s. moments in terms of l.h.s. moments, and

$$\mu'_r = \sum_{j=0}^{r} \binom{r}{j} (2^{1-j} - 1) \, B_j \epsilon^j \bar{\mu}'_{r-j} \qquad (5)$$

which approximates l.h.s. moments in terms of r.h.s. moments.

The B_j are the Bernoulli numbers, and obey the generating equation

$$\frac{t}{e^t - 1} = \sum_{j=0}^{\infty} \frac{B_j t^j}{j!} \qquad (6)$$

The first 14 are: $B_0 = 1$; $B_1 = -1/2$; odd B's = 0 except B_1; $B_2 = 1/6$; $B_4 = -1/30$; $B_6 = 1/42$; $B_8 = -1/30$; $B_{10} = 5/66$; $B_{12} = -691/2730$; $B_{14} = 7/6$

For the lower moments

$$\mu_1' = \mu_1'$$

$$\mu_2' = \mu_2' + \frac{\epsilon^2}{12}$$

$$\mu_3 = \mu_3' + \frac{1}{4}\mu_1' \epsilon^2$$

$$\mu_4 = \mu_4' + \frac{1}{2}\mu_2' \epsilon^2 + \frac{1}{80}\epsilon^4$$

$$\mu_5' = \mu_5' + \frac{5}{6}\mu_3' \epsilon^2 \; \frac{1}{16}\mu_1' \epsilon^4$$

$$\mu_6' = \mu_6' + \frac{1}{4}\mu_4 \epsilon^2 \; \frac{3}{80}\mu_2' \epsilon^4 + \frac{1}{448}\epsilon^6 \tag{7}$$

and

$$\mu_1' = \mu_1'$$

$$\mu_2' = \mu_2' - \frac{\epsilon^2}{12}$$

$$\mu_3' = \bar{\mu}_3' - \frac{1}{4}\bar{\mu}_1' \epsilon^2$$

$$\mu_4' = \bar{\mu}_4' - \frac{1}{2}\mu_2' \epsilon^2 + \frac{7\epsilon^4}{240}$$

$$\mu_5' = \bar{\mu}_5' - \frac{5}{6}\bar{\mu}_3' \epsilon^2 + \frac{7}{48}\mu_1' \epsilon^4$$

$$\mu_6' = \mu_6' - \frac{5}{4}\mu_4' \epsilon^2 + \frac{7}{16}\mu_2' \epsilon^4 - \frac{31\epsilon^6}{1344} \tag{8}$$

IV. Conclusion

This article has presented the corrections for quantization effects in the estimation of distribution moments. The limitations are that the quantization steps be equally spaced and that the continuous functions whose integrals are estimated must in some sense be smooth with respect to quantization grid (see Ref. 3). The extension of this approach to absolute moments (which are not "smooth" at the origin) and to unequal quantization spacing (companding converters) is currently under study. The effect of these corrections on specific SNR estimation algorithms depends upon the detailed representation of the estimator in terms of distribution moments. Results will be reported as they become available.

References

1. Howard, L. D., Prototype Real-Time Baseband Signal Combiner, in *The Telecommunications and Data Acquisition Progress Report 42-60*, pp 145-151, Jet Propulsion Laboratory, Pasadena, Calif., Dec. 15, 1980.
2. Boole, George, *A Treatise on the Calculus of Finite Differences* (Second Ed., 1872), Dover Publications, Inc., New York, 1960
3. Kendall, M G., and Stuart, A., *The Advanced Theory of Statistics*, Vol. I, Ch. 3, Hafner Publishing Co , New York, 1969.

D21 N81-27144

Networks Consolidation Program System Design

E. C. Gatz
TDA Engineering Office

This article describes the general system design for the Mark IV-A Deep Space Network to be implemented in the Networks Consolidation Program. The arrangement and complement of antennas and the list of subsystem equipment at the Signal Processing Center are described.

I. Introduction

The description of the Networks Consolidation Program (NCP), its history, management planning, and system design approach is given in Ref. 1. The objective of the program is to develop a single cost-effective network of ground tracking stations for communicating with interplanetary spacecraft and with earth-orbiting satellites not served by the Tracking Data Relay Spacecraft System (TDRSS). In the process of this development, it is expected to reduce operations costs and to provide increased antenna aperture on the ground for greater data return for deep space missions.

The current Deep [illegible] Network, called Mark III, will therefore be rec[illegible] [illegible] these objectives, as well as to include [illegible] [illegible]ments. The reconfigured network will be known as the [illegible] Mark IV. The current plan is to perform [illegible] [illegible] for the [illegible] 83 and 1984 with completion [illegible] the [illegible] of [illegible]

II. Mark IV-A Network Configuration

The new network configuration is shown in Fig. 1. It consists of five antennas and Signal Processing Center (SPC) at each of three Deep Space Communications Complexes: Goldstone, California; Madrid, Spain; and Canberra, Australia. Communication facilities to connect these complexes to the Network Operations Control Center are included.

At each complex, the antennas are to be colocated within 1 or 2 kilometers in order to ease operations and maintenance and to enhance the capability of arraying multiple antennas. Each antenna has some locally mounted equipment: antenna drive, low-noise amplifier, receiver front-ends, and transmitters. However, the bulk of the antenna-associated equipment: antenna controller, microwave instrumentation, transmitter controls, etc., is located at the SPC. The SPC also includes telemetry, command, radio metric, and radio science processing equipment, as well as other associated control and processing equipment.

III. Antennas

Each complex is planned to have five antennas, configured as follows:

(1) 64-Meter. This is the existing antenna configured for S-band transmission and reception and X-band reception. This is the prime antenna for deep space communications and for radio science and Very Long Baseline Interferometry (VLBI) applications.

(2) 34-Meter Transmit/Receive. This is the existing 34-meter antenna at each complex, configured for S-band transmission and reception and X-band reception. It is used for all deep space applications and is planned for support of High Earth Orbiters also.

(3) 34-Meter Listen-Only. This will be derived by enlarging and moving the DSN 26-meter antenna at each complex. These antennas will be equipped for X-band only and will be used in array applications.

(4) 34-Meter Listen-Only. This will be derived by enlarging and moving the Ground Spaceflight Tracking and Data Network (GSTDN) 26-meter antenna at each complex. It will be configured for both X-band and S-band reception and will be used for both deep space and High Earth Orbiter reception and for VLBI applications.

(5) 9-Meter. The existing GSTDN 9-meter antennas will be relocated and used for S-band transmission and reception in support of High Earth Orbiters.

IV. Signal Processing Center

A simplified block diagram of a Signal Processing Center is shown in Fig. 2. This shows the general subsystem complement. Detailed configurations and connections will be described in later articles. The SPC is configured to support operation of each antenna individually, or to array any combination of the large antennas. Two subarrays can be supported.

As indicated, antenna control, receiver/exciter and radio metric tracking subsystem equipment is associated with each antenna as appropriate. Only transmitting antennas have exciters and tracking equipment. The Telemetry, Command, and Monitor and Control Subsystems are each organized into four groups. Each group can be independently assigned; the groups are thus assigned to form up to four "links." Each "link" has the necessary equipment to support one spacecraft mission, with receiver, antenna, tracking, command, and telemetry equipment. The link can handle a single antenna or an array. Each link is controlled by a single operator stationed at the link Monitor and Control Console. The link assignments, including the antenna and associated equipment, are performed by the complex Monitor and Control according to an established schedule. Other subsystems provide test support, technical facilities, frequency and timing, maintenance, and radio science support. Details for the SPC System configurations will be presented in future articles.

V. Current Design Work

This article has outlined the system design for the Mark IV-A Deep Space Network. Design work is continuing on the details of connection and control of all elements and on antenna and SPC floor plans and equipment layouts.

Reference

1. Yeater, M. L., Herman, D. T., and Sanner, G. E., "Networks Consolidation Program," in *The Telecommunications and Data Acquisition Progress Report 42-59*, July and August 1980, p. 107-120, Jet Propulsion Laboratory, Pasadena, Calif., Oct. 15, 1980.

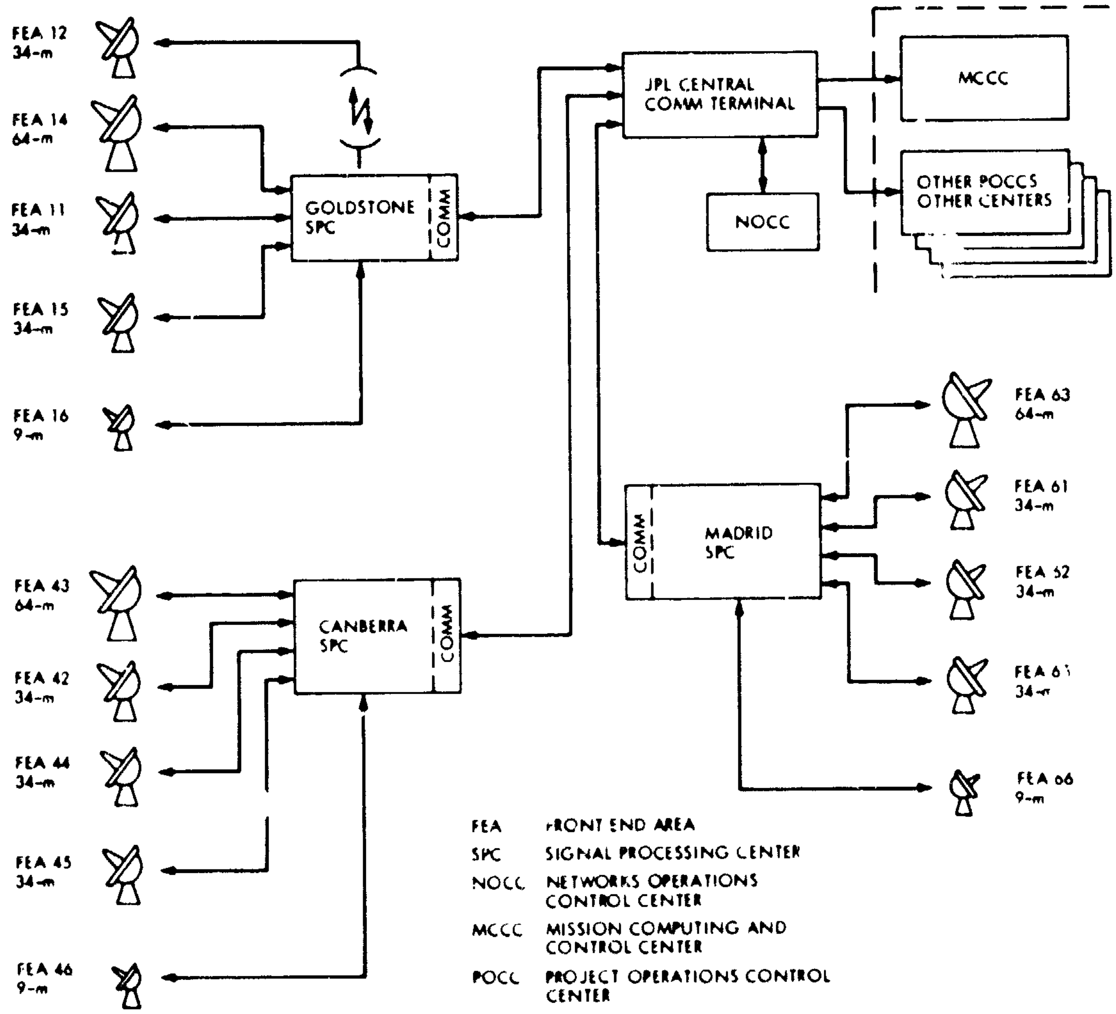

FEA	FRONT END AREA
SPC	SIGNAL PROCESSING CENTER
NOCC	NETWORKS OPERATIONS CONTROL CENTER
MCCC	MISSION COMPUTING AND CONTROL CENTER
POCC	PROJECT OPERATIONS CONTROL CENTER

Fig. 1. Mark IV-A Deep Space Network Configuration

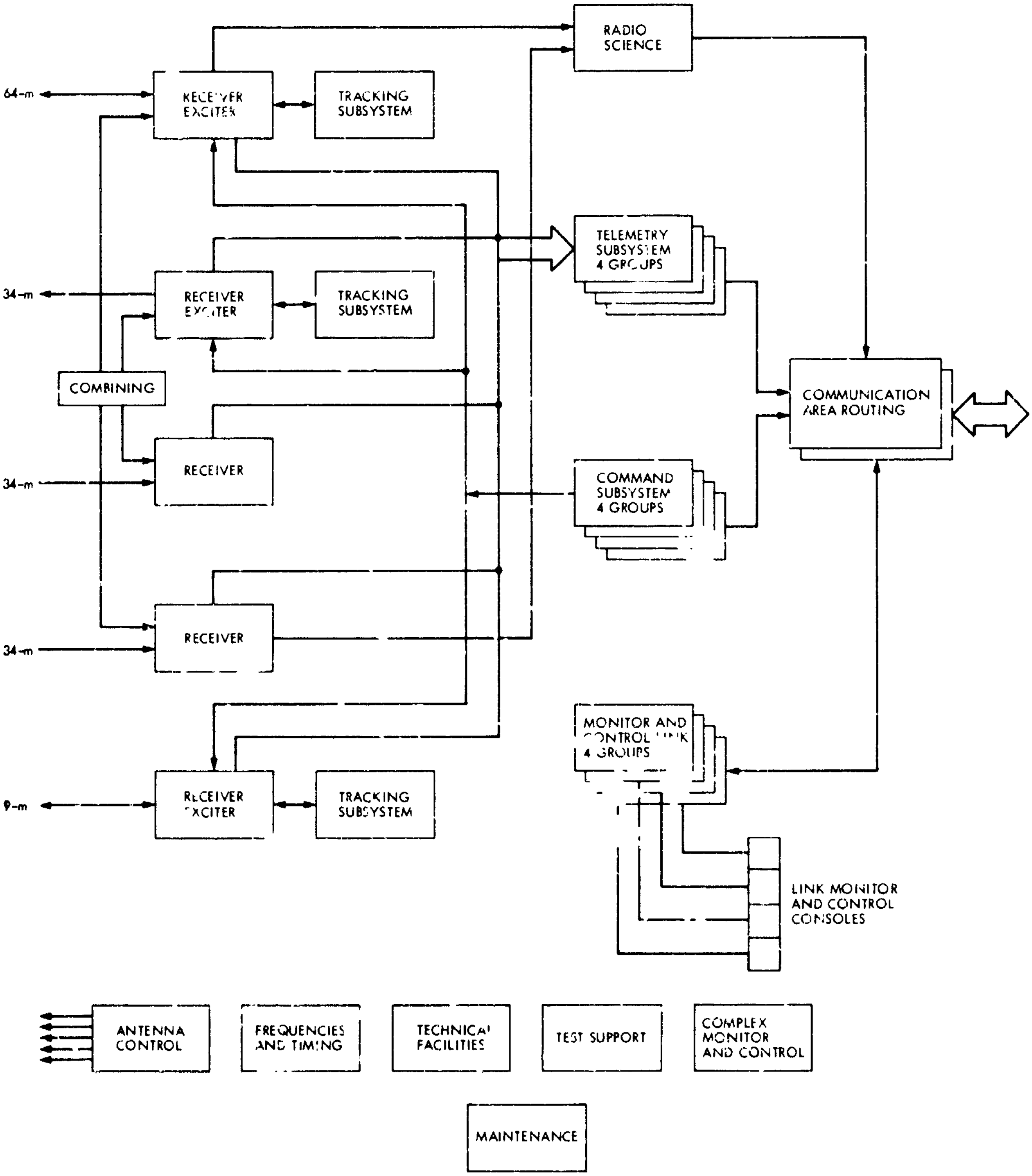

Fig. 2. Signal Processing Center, simplified block diagram

Assessment of Solar-Assisted Gas-Fired Heat Pump Systems

F. L. Lansing
DSN Engineering Section

Industrial and scientific communities are showing a new wave of interest in developing engine-driven heat pumps that utilize hybrid sources of energy combining fossil fuels, solar energy, and waste heat. As a possible application for the Goldstone Energy Project, the performance of a 10-ton heat-pump unit using a hybrid solar-gas energy source is evaluated in an effort to optimize the solar collector size. The heat-pump system is designed to provide all the cooling and/or heating requirements of a selected office building located at the Deep Space Communication Complex, Goldstone, California. The system performance is to be augmented in the heating mode by utilizing the waste heat from the power cycle. A simplified system analysis is described in this report to assess and compute interrelationships of the engine, heat pump, and solar and building performance parameters, and to optimize the solar concentrator/building area ratio for a minimum total system cost. In addition, four alternative heating-cooling systems, commonly used for building-comfort, are described, their costs are compared, and are found to be less competitive with the gas-solar heat-pump system at the projected solar equipment costs.

I. Introduction

Heat pumps, sometimes called "energy pumps," are mechanically driven devices that extract heat from one medium at a certain temperature and "pump" this heat and a little more to another medium at a higher temperature. If used for a heating purpose, heat pumps are known to have a high potential for saving natural energy resources and for reducing primary energy consumption as compared to direct electrical resistance heaters, or fossil-fuel-fired boilers. Several configurations exist, as illustrated in Appendix A, which differ mainly in the type of fluid or media exchanging heat with the heat pump's recirculating refrigerant.

The recent interest by industrial and scientific communities in energy-consumption reduction, as a result of the global energy-shortage situation, has stimulated more research and development of heat pumps in many areas, such as (1) coupling with natural nonfossil-fuel energy resources such as solar-electric, biomass combustion or wind power, as prime movers, and (2) using the pump as a booster for any low-temperature heat, including waste heat, to obtain a more useful higher-temperature-level heat for industrial, residential, and commercial applications (Ref. 1).

Toward the commercialization of small-size heat-pump units (around 10 tons of refrigeration or 35.16 kWh_t)a new study is being jointly reviewed by the Energy and Technology Application office of the Jet Propulsion Laboratory (JPL) and Airesearch Manufacturing Company of the Garrett Corp., and is being sponsored and managed by the Department of

Energy. The hybrid heat-pump system concept under investigation replaces conventional electrical motor-drives with gas-fired engines (or turbines) coupled with solar concentrators. The solar connection is superimposed for saving additional gas heat during the sunny hours. Combining the expertise of JPL in high-temperature solar concentrators, solar receivers, high-temperature energy storage with and without phase-change materials (PCM), and building-energy analysis, with the experience of the Garrett Corp. in developing engines and gas-turbine hardware and in their computer simulation, the investigation is expected to be thorough and very informative.

As part of the Energy Conservation Project for the Deep Space Network (DSN) facilities, continually keeping aware of and making engineering assessments of new technologies, concepts, controls, components, and systems and their economics, particularly in the area of building heating, ventilation and air conditioning (HVAC), is of prime importance for upgrading the facilities and keeping their energy consumption at a minimum. The commercialization of the above hybrid heat-source system and its relevant advanced building controls presents an area worth investigating since it has a high potential for reducing the energy consumption of facilities and enhancing their energy self-sufficiency position

Until the detailed computerized results of the above DOE-managed task are published, a short term definition study has been initiated in order to provide our facilities management and engineers with the key advantages of the candidate heat-pump configuration, its potential cost savings, and its performance and operational superiority The task objectives are tentatively set to (1) configure a complete add-on heat-pump system to an existing building at the DSN facility, (2) outline and identify by a simplified analytical approach, if possible, the key design and weather parameters, (3) compare its economics against alternate dual heating-cooling configurations that are commonly used, (4) provide an optimum solar-collector size for a minimum yearly total cost or a minimum 10-year life-cycle cost, and (5) study variances and sensitivities of the economics or configuration parameters including different types of buildings, weather patterns, energy rates, etc. This preliminary assessment is not intended to substitute for or replace the detailed work currently being done elsewhere, but rather to supplement it, and pave the way for examining to a first order of magnitude the concept applicability to existing DSN facilities that have different weather profiles, building loading, and building types.

The attractiveness of this solar-assisted gas-fired heat-pump system concept for future application in Deep Space Network buildings is based on several features, each of which offers potentially high efficiency, better utilization of existing fossil-fuel resources, or low cost. The system features are composed of the following elements:

(1) A heat pump that "pumps" heat, when used in the heating mode, from outdoor air. This is a single, compact device that functions as either a heating or a cooling unit as necessitated by the building needs.

(2) A heat recovery device that benefits from the heat rejected by the driving engine (or power cycle) and feeds a large portion of that heat directly to the conditioned space. This enables the system to out-perform conventional heating devices, which means higher performance, smaller solar collector area, and lower operation cost.

(3) No large thermal or electrical storage is required for this hybrid system since direct gas combustion is used when needed. Operation during the night or during cloudy periods is uninterrupted, thus providing high reliability

The above features are expected to lead to savings in maintenance and operation costs.

Since numerous parameters are expected to enter into the system performance evaluation, two approaches could be followed. (1) a detailed computerized approach using hourly, daily, monthly, and yearly load distribution, component efficiency, and site weather, or (2) a simplified "lumping" approach for faster assessment. The first approach is already in progress with full results yet to be published The second approach is the one chosen for this report in order to provide coarse boundaries, and size limits in the optimization of the solar share. The complexity of the second approach could be later increased for a better refinement of results accuracy by utilizing one of the available dynamic analysis computer programs such as TRNSYS, SOLTES, etc. However, this article reports only about the first-order assessment of the concept without any detailed computerized calculations.

II. System Description

An outline of a complete conceptual system driven by a hybrid solar/gas heat source is shown in Fig. 1. The flow of energy streams to and from each component is sketched in Fig. 2. The following 4 subsystems are identified:

(1) Solar collection and storage subsystem

(2) Power conversion subsystem.

(3) Heat pump subsystem.

(4) Building air-handling subsystem.

The function of each subsystem is briefly described next, assisted by Figs. 1 and 2.

A. Solar Collection and Storage Subsystem

This subsystem consists of a solar concentrator, a solar receiver, and a high-temperature storage compartment. The concentrator is initially configured as a point-focusing 2-axis tracking paraboloid mirror. Appropriate mechanisms for adjusting the azimuth and elevation angles are provided to line up the paraboloid axis with the sun-earth vector during the sunny hours. The solar energy reflected by the concentrator mirror is focused on the finite aperture of the solar receiver, which is placed at the paraboloid focus. The solar receiver has a cavity-like shape to approximate a black-body radiator. It is also enclosed by a thermal insulation blanket to reduce the outward thermal radiation-convection losses to surrounding air. Through a set of heat-pipes connected to the interior solar receiver walls, a high-temperature energy-storage compartment is attached. The thermal storage capability of this subsystem may be limited to not more than one hour, to provide only damping and smoothing effects for the solar intensity fluctuations. Phase-change materials are recommended for a compact design and for their favorable small temperature changes during charging and discharging modes. The "useful" collected portion of the incident solar radiation, after subtracting the optical and thermal losses, represents heat available to be converted further to a mechanical energy form in the power conversion subsystem.

B. Power Conversion Subsystem

The hybrid heat source needed to operate this subsystem consists of (1) high-temperature solar energy as delivered by the receiver-storage subsystem and (2) high-temperature products of combustion resulting from direct ignition, in a combustor, of a fossil fuel such as natural gas, propane, methane, etc.

The power conversion subsystem location is preferred to be next to the solar receiver-storage subsystem to minimize thermal losses. Gaseous or liquid fuels are also preferred for easy handling if transmitted in pipes to the focal region. For the present study, natural gas has been selected and is assumed available in the location under investigation.

In general, conversion of thermal energy to mechanical work is made via power cycles, of which the most important are

(1) Brayton cycle, whether it is closed or open, simple or regenerative,

(2) Rankine cycle using water or organic fluids, and

(3) Stirling cycle

With any power cycle used, some heat must be rejected which, if recovered and utilized, represents a bonus to the overall system performance. The recoverable heat could be utilized directly for heating the building in the heating mode, and if needed, for temperature modulation in the cooling mode.

The system layout in Fig. 1 illustrates the components of one selected power cycle. The regenerative air-Brayton cycle, which is used as the prime mover for the heat pump. The power cycle is composed of an air compressor, an air turbine, a regenerator, a gas combustor and a heat sink. Air passes through the high-temperature energy-storage element to be heated before it enters the gas combustor. Gas combustion will take over as the sole heating source if insufficient solar energy is collected. The mechanical work of the power cycle is used to drive the refrigeration compressor by a single shaft as shown in Fig. 1. The solar receiver-storage subsystem and the power conversion subsystem could be placed in one assembly, located at the concentrator focal region. Combustion air is preheated before mixing with the fuel in the combustion chamber, by passing through the regenerator. The power conversion subsystem also includes the necessary air-flow controls to utilize the ambient air as a heat sink (if the heat rejected from the cycle is totally not needed) or else divert the air leaving the regenerator through air conduits to another heat exchanger (not shown in Fig. 1) connected to the building air-handler for additional heating, supplementing the heat-pump portion.

Note that configurations other than the selected Brayton cycle have been experimentally demonstrated by many researchers in this field. Steam turbines, for instance, are coupled with heat pumps for an integrated community energy system (Refs. 2, 3). Other examples of using the organic Rankine turbo-compressor-driven heat pump include those of Mechanical Technology, Inc (Ref. 4), the Institute of Gas Technology (Ref. 5), the United Technologies Research Center work using refrigerant R-11 (Ref. 6), the Battelle Columbus Laboratories work with R-11 as a power cycle fluid and R-12 as a refrigerant (Ref. 7), and the analysis of many working organic fluids for power cycles (Refs. 8 and 9). For a gas-fired free piston Stirling engine driving a refrigeration compressor, experimental work was also demonstrated by the Gas Research Institute and General Electric Company for a 3-ton unit (Ref. 10). An internal combustion engine following the Otto-cycle, coupled with a heat recovery unit, a gas-fired auxiliary furnace, and a heat pump, was analyzed by Honeywell, Inc. for the Gas Research Institute (Ref. 11). A Stirling engine driving a unique Stirling refrigeration cycle was also demonstrated (Ref. 12).

C. Heat Pump Subsystem

A heat pump consists of the same basic components as a refrigeration machine, which are itemized as follows:

(1) An indoor element that adds heat to (in the heating mode) or extracts heat from (in the cooling mode) a medium in a conditioned space. This medium could be air or water.

(2) An outdoor element that extracts heat from or ejects heat to a medium outside a conditioned space. This medium also, could be air or water.

(3) A reciprocating or rotary compressor for compressing the refrigerant and moving it in the desired direction so that it "pumps" heat out or in, for cooling or heating modes.

(4) Control elements for satisfactory subsystem operation.

The functions of the refrigerant evaporator and condenser could be interchanged by reversing the direction of flow of the refrigerant between the indoor or outdoor elements. As illustrated in Fig. 3, in both cooling and heating modes, the major components are the refrigerant compressor, condenser, evaporator, throttling valve, and a mode-selector valve (i.e., a reversing valve). The mode-selector valve reverses the flow of refrigerant so that the indoor coil acts as an evaporator in the cooling mode and as a condenser in the heating mode.

The heat-pump subsystem could be any one of the four configurations described in Appendix A according to the medium type in contact with indoor and outdoor elements. The most common configuration, however, is the air-to-air (A-A) type. Performance data of A-A heat pumps appear in numerous references (e.g., Refs. 13 and 14), and in general the capacity and coefficient of performance are strong functions of outdoor temperature. As the temperature difference between indoor and outdoor air increases, it becomes more difficult to move the heat, thus, the capacities (for either heating or cooling) and the efficiency decrease.

Generally, a heat pump is designed to suit the peak cooling load. If the peak heating load exceeds the heating capacity of the pump, supplementary heat is commonly supplied by electrical resistance heaters. One should examine, however, the cost tradeoff of overdesigning the heat pump to cover the coldest winter load or using a suitably designed heat pump supplemented by another heating source. For multi-zone air conditioning systems using a heat pump, air changeover controls sometimes replace the refrigerant changeover valves, depending on the type of media exchanging heat with the pump. The refrigerant flow is not reversed in these systems.

The coefficient of performance, P, which is a measure of the heat-pump effectiveness, is defined as the ratio of "useful" heat effect delivered to the mechanical work used to operate the heat-pump subsystem:

$$\begin{aligned} P_c &= \frac{Q_L}{W} \text{ (cooling mode)} \\ P_h &= \frac{Q_H}{W} \text{ (heating mode)} \end{aligned} \qquad (1)$$

Note that the P values should be based on the same operating conditions before making any comparison with other heat pump types. If compared to the ideal Carnot cycle behavior, the actual value of P is inversely proportional to the temperature difference between the heat source and heat sink. The larger this difference, the lower the performance will be. Because the P value varies with operating conditions, an average performance for the season seems more appropriate in comparing different systems in different climatic regions. In lieu of detailed thermodynamic evaluations (as given in Refs. 14 and 15) a simplified analysis is given in Appendix C based on graphs provided by Ref. 16.

D. Building Air-Handling Subsystem

As sketched in Fig. 1, the air movement to and from the conditioned space forms a closed loop. Fresh make-up air, which is the outdoor ventilation air, mixes with the return-air leaving the space, and the mixture is blown by a fan through the air-handler section. The air-handler is commonly composed of two coils, one for heating and the other for cooling, to adjust the air temperature to that required by the space according to its internal loads. Different temperature or flow controllers are used in practice for modulation. From an energy-balance viewpoint the air-handler requires a net heating or a net cooling effect which equals the heat lost or heat gained, respectively, from the gross control volume encompassing the space boundaries, air-handler, air ducts, and make-up air. In the heating mode, the heat-pump indoor element acts as a refrigerant condenser, i.e., as a heating coil, while use is made of a portion of the power cycle waste heat as a heating supplement. In the cooling mode, the heat-pump indoor element acts as a refrigerant evaporator i.e., as a cooling coil. The power cycle waste-heat in this case could be entirely by-passed or partially used for temperature modulation. The physical location of the heat pump and the air-handler subsystem would probably be in a mechanical room in the building. Two fluid circuits connected to the focal assembly of the solar collection subsystem are envisioned. These are: (a) refrigerant lines connecting the refrigerant compressor to the heat-pump subsystem and (b) an air conduit connecting the power cycle regenerator at the focal assembly with the air-handler "booster" coil.

The major system components having been described, a set of analytical expressions will be presented next to describe the system operation and design guidelines.

III. System Analysis

The following assumptions and idealizations are made in the analysis of the system in order to yield a simplified approach and to enable a complete assessment without a great loss of accuracy.

(1) The exterior outside air temperature variations throughout the year are divided into only two seasons: summer and winter. Spring and fall periods will be merged as appropriate. Distinction between summer and winter is assumed to take place when the average daily temperature, t_o, exceeds or is below a reference temperature. On the other hand, the cooling and heating modes of system operation occur for M_c and M_h months, respectively, which are not necessarily equal but total 12. Modes of operation are determined by comparing the daily average outside air temperature with the building changeover temperature, T_o*. There is always a possible overlap between seasons and modes of operation depending on the type of air-handler modulation, local weather profiles, and space internal loads. The daily average outside air temperature $t_{o,c}$ or $t_{o,h}$ for either cooling or heating modes, respectively, are obtained from local weather data. The building changeover temperatures (one for each season is assumed) are obtained from space internal loads, interior temperature, and rate of heat loss to ambient.

(2) The efficiency of the concentrator mirror, if defined by the ratio of solar flux on receiver interior walls to the solar flux falling on mirror projected areas, becomes the product $\rho\phi$ where ρ is the mirror reflectivity and ϕ is the intercept factor. The intercept factor is defined as the fraction of the reflected radiation from the concave mirror that is intercepted by the internal cavity surface of the solar receiver. The intercept factor is a property of both the concentrator mirror's orientation for producing an image and the receiver's position relative to the concentrator. The optimum aperture size with a mirror of given optical properties, is commonly made by maximizing the "useful" energy collected by the mirror-receiver or minimizing the sum of their optical and thermal losses. A large receiver aperture results in large thermal losses but small optical losses, and vice versa.

(3) Cavity solar receivers are generally high-efficiency absorbers. The receiver, when coupled with the adjacent high-temperature energy storage element, has an efficiency that is defined as the ratio of useful collected thermal energy (which crosses the receiver-storage boundary to the power conversion subsystem) to that energy incident upon the receiver interior walls. Writing the energy collection subsystem efficiency R approximately as a linear relationship with the temperature difference between the receiver working fluid and the ambient air, yields.

$$R = F\rho\phi\alpha - FU\left(\frac{T_f - T_o}{I}\right) \tag{2}$$

where T_f is the inlet fluid temperature to the receiver, ρ is the mirror reflectivity, α is the effective receiver absorptivity, F is a flow factor, I is the solar intensity, and U is the overall heat-loss rate due to convection and radiation per unit concentrator area. Note that the coefficient U takes into consideration the concentration ratio, receiver geometry, etc. Equation (2) could be also written in the linear form:

$$R = m_s - n_s\left(\frac{T_f - T_o}{I}\right) \tag{3}$$

where the intercept m_s represents the product ($F\rho\phi\alpha$) and the slope n_s represents the product (FU).

Solar concentrators with a concentration ratio between 100 and 1000 could reach fluid temperatures between 500°C (932°F) and 1000°C (1832°F). The intercept m_s, for high-temperature solar concentrators, ranges from 0.8 to 0.9, and the slope n_s ranges from 0.10 to 0.20 W/m^2°C.

(4) The efficiency of a general power conversion subsystem is here simplified by a fraction λ_e of the corresponding Carnot's cycle operating between the temperature limits T_f and T_o. By this method, the distinction between different types of power cycles is made primarily by knowing the fraction λ_e, which is commonly limited to a value between 0.4 and 0.6 in practice; thus

$$E = \lambda_e\left(1 - \frac{T_o}{T_f}\right) \tag{4}$$

(5) Similar to the power conversion subsystem performance, the coefficient of performance of a general heat pump P, in either cooling or heating modes at

full load, could be approximated as a constant fraction λ of the Carnot's ideal refrigeration cycle operating between the same evaporator and condenser temperatures. T_{ev} and T_{co}. Hence,

$$P_h = \lambda_h \left(\frac{T_{co}}{T_{co} - T_{ev}} \right)_h \tag{5}$$

$$P_c = \lambda_c \left(\frac{T_{ev}}{T_{co} - T_{ev}} \right)_c \tag{6}$$

For a given space inside temperature, T_i, and a given outside air temperature, T_o, the performance of an air-air heat pump for instance could be evaluated by determining the temperature drop across the evaporator Δt_{ev} and across the condenser Δt_{co} as presented in Appendix C. Note that the fractions λ_h, λ_c embody other design factors such as the type of medium used (water or air), partial loading, and all temperature, pressure, and flow control schemes. In the heating mode, the coefficient of performance P_h as given by Eq. (5) decreases as the outside air temperature (or condenser temperature T_{co}) decreases, thus reducing the amount of heat "pumped" to space. For the cooling mode, Eq. (6) gives a lower P_c as the outside air temperature increases, thus reducing the cooling effect of the refrigerator. This means that in both modes, the trend of the heat pump performance is always against the response of building loads at different outside temperatures. This supply and demand contrast could be illustrated by Figs. 4 and 5, which will be further explained in the analysis later on.

(6) The internal heat gain to (or loss from) a building space, is given in detail in Ref. 17 and is sketched in Fig. 4. The load is assumed the sum of the following four parts:

First, the internal heat generated due to occupant-activity, lighting equipment, electronic equipment, mechanical equipment with motor drives, and internal fuel-fired appliances. This is treated as a constant load independent of outside air temperature variations, but subject to variations in the schedule of activities inside the space.

Second, the heat transmitted to the building structure directly due to solar-radiation incidence upon glazing areas and indirectly due to solar-radiation incidence on opaque exterior walls and roofs. This part is also assumed a constant load, independent of the outside air temperature variations although it takes into consideration reradiation to the sky.

Third, the heat transmission due to varying outside air boundary-layer temperature next to exterior walls, roofs, and windows. If averaged over 24 hours, transient effects are damped and this part is found to be proportional to the difference between the daily average inside and outside air temperatures.

The fourth part of the space load is the undesirable heat loss (or gain) due to infiltration and ventilation. Infiltration or exfiltration air is caused by leakages through cracks or repeated opening of doors, and windows, or due to buoyancy effects. Ventilation air, on the other hand, is essential for hygienic purposes. Since the introduction of outdoor air, whether it is desirable or not, is an energy extensive process, the amount of such air should always be kept at a minimum rate. The sensible heat load as a result of this fourth part will be proportional to the difference between inside and outside air temperatures.

By neglecting latent loads in comparison with sensible loads, and by taking the minimum period of analysis as one day (24 hours), heat gain to a space per unit floor area Q_b could be written simply by the straight line relation.

$$Q_b = m_b + n_b (T_o - T_i) \tag{7}$$

where m_b is a constant building load intercept combining the first and second constant parts of heat gain, n_b is a building load slope combining the third and fourth parts of the heat gain, T_i and T_o are the daily average inside and outside dry bulb temperatures, respectively. The monthly calculations of Q_b are made for one selected day for each month. Monthly space loads could be assumed repeated images of this single representative day in each month. Although daily or monthly values for the parameters m_b and n_b could be used, only two possible patterns for m_b and n_b are allowed for the yearly building load computation, one for the summer and the other for the winter season. Numerically, the values of m_b and n_b are subject to simple design criteria that are usually given per unit floor area (Ref. 17). Furthermore, variations of m_b and n_b are known to be mainly dependent on the type of building activity (e.g., an office building, a central control building, a cafeteria, etc.) and to a lesser extent on the local climate.

Of special importance to the building mode of operation is a particular outside air temperature at which the gross building load reaches zero. This is sometimes called the changeover temperature, T_o^*, which is given by equating Eq. (7) to zero, hence

$$T_o^* = T_i - \frac{m_b}{n_b} \tag{8}$$

The characteristic temperature T_o^* represents the outside air-building "equilibrium" temperature where a lower outside air temperature (i.e., $T_o < T_o^*$) means the building is in a heating mode, and a higher outside air temperature (i.e., $T_o > T_o^*$) means the building is in a cooling mode. Differentiation between a heating mode and a cooling mode is therefore a necessary step once the temperature T_o^* is determined, and should be distinguished from summer and winter seasons.[1]

(7) For a given heat-pump cooling capacity, or heat-pump rating, *CC* (taken at the ARI temperature specification of 35°C (95°F)), the design space floor area to match this capacity is determined based on the peak cooling demand of the space. Let the heat-pump cooling capacity change with the outside air temperature (Ref. 16) as

$$CC_{to} = CC_{35}\,[1 - 0.018\,(t_o - 35)] \tag{9}$$

where CC_{to} is the cooling capacity in tons of refrigeration[2] at any outside air temperature, CC_{35} is the rated capacity at 35°C (95°F), and t_o is in °C. Figure 6 illustrates the difference between the building heat gain and the heat-pump cooling output[3] at various outside air temperatures. At the summer design outside air temperature of the site, $t_{o,c}$, the pump's cooling capacity (point A in Fig. 6) should be somewhat larger than the building's peak heat gain (point B in Fig. 6) by a 10-20% margin to allow for extreme weather conditions. By taking an arbitrary 15% capacity margin, the appropriate space area that could be handled by a given heat pump capacity is calculated from Eqs. (7) and (9) as:

$$A_b = \frac{3057\,CC_{35}\,[1 - 0.018\,(t_{o,c} - 35)]}{m_{b,c} + n_{b,c}\,(t_{o,c} - t_{i,c})} \tag{10}$$

where the coefficients $m_{b,c}$ and $n_{b,c}$ are expressed in SI units in W/m² and W/m²°C, respectively, CC_{35} in tons of refrigeration and A_b in m². Eq. (10) could be also used if the building floor area is given and the appropriate cooling capacity needs to be known.

(8) The annual cost of purchased gas energy at a particular mode of operation is determined by the part of the building load which is unmet by solar energy assistance, taking into consideration the efficiencies of the various components. During M_h months of the heating period, the total cost of gas energy C_h becomes the sum:

$$C_h = C_g \sum_{M_h} \left[\frac{730 A_b \cdot |Q_{b,h}|}{COP_{g,h}} - \frac{30.42\,A_s\,S_h\,COP_{s,h}}{COP_{g,h}} \right] \tag{11}$$

where C_g is the unit gas energy cost in \$/W, $COP_{g,h}$ and $COP_{s,h}$ are the gross coefficients of performance of the system in the heating mode, driven by either gas combustion or solar radiation, respectively, and S_h is the effective daily solar radiation incident upon the concentrator projected area A_s. Eq. (11) assumes a standard month of 30.42 days and 730 continued working hours. The gross coefficient of performance in the heating mode COP_h is determined from Fig. 7, where two types of energy sources are identified: the first being solar radiation and the second gas combustion. COP_h is defined as the ratio of the cumulative heating effect to the space divided by the input primary energy source. From Fig. 7, $COP_{s,h}$ and $COP_{g,h}$ are written as:

$$COP_{s,h} = [\eta_w + E_{s,h}\,(P_h\,\eta_t - \eta_w)]\,R_h \tag{12}$$

$$COP_{g,h} = [\eta_w + E_{g,h}\,(P_h\,\eta_t - \eta_w)]\,\eta_g \tag{13}$$

Similarly, during M_c months of the cooling period, the total yearly cost of gas energy becomes

$$C_c = c_g \sum_{M_c} \left(\frac{730\,A_b \cdot Q_{b,c}}{COP_{g,c}} - \frac{30.42\,A_s\,S_c\,COP_{s,c}}{COP_{g,c}} \right) \tag{14}$$

where $COP_{g,c}$ and $COP_{s,c}$ are the gross coefficients of performance of the system in the cooling mode, driven by either gas combustion or solar radiation,

---

[1] Most weather stations make the distinction of a heating-degree-day and a cooling-degree-day based on the difference between the daily average outside air temperature and 18.33°C (65°F) as a reference temperature

[2] One ton of refrigeration equals 12,000 Btu/hr or 3516 W

[3] The cooling capacity and heating capacity of a heat pump are approximately equal to each other at rated conditions The pump is usually designed to satisfy the peak building cooling needs, and if it is not able to satisfy the peak heating needs, a supplement heater is used Otherwise, the pump is slightly overdesigned to satisfy both needs completely

respectively, and S_c is the effective daily solar radiation incident upon the concentrator projected area. Fig. 8, as in Fig. 7, illustrates quantitatively the energy flows for the cooling period where the gross coefficients $COP_{g,c}$ and $COP_{s,c}$ are given by:

$$COP_{s,c} = R_c E_{s,c} \eta_t P_c \tag{15}$$

$$COP_{g,c} = \eta_g E_{g,c} \eta_t P_c \tag{16}$$

By using Appendix B, several expressions for the maximum $COP_{s,h}$ and $COP_{s,c}$ could be derived to obtain the optimum receiver-engine working temperature. The energy calculations are made monthly and then summed to obtain the yearly profile.

(9) The yearly cost of gas heating, given by Eq. (11), could be further written as

$$C_h = A_b \sum_{M_h} \left(\beta_{b,h} - \beta_{s,h} \frac{A_s}{A_b} \right) \tag{17}$$

where the monthly cost parameters $\beta_{b,h}$ and $\beta_{s,h}$ are given by

$$\beta_{b,h} = 730\, C_g\, |Q_{b,h}|\, / COP_{g,h} \tag{18}$$

$$\beta_{s,h} = 30.42\, C_g S_h\, COP_{s,h} / COP_{g,h} \tag{19}$$

The parameter $\beta_{b,h}$ at a particular month represents the gas heating energy cost per unit building area if no solar equipment exists, where heating is exclusively provided by the gas-fired heat pump. However, the parameter $\beta_{s,h}$ represents the gas cost savings, per unit collector area, resulting from adding a solar collector. The cost C_h starts with a value of $\beta_{b,h} A_b$ if no solar collector is connected and drops nonlinearly to zero cost at the maximum collector area $A_{s,h}$, where the cost C_h remains zero thereafter. The area $(A_{s,h}/A_b)$ given by $(\beta_{b,h}/\beta_{s,h})$ for the month of peak load represents the maximum collector area required to satisfy the building's peak heating load. Note that by subtracting the terms $\beta_{b,h} A_b$ and $\beta_{s,h} A_s$ for any month during the heating mode, negative values of C_h (when $\beta_{b,h} A_b < \beta_{s,h} A_s$) must be counted as zero, which makes the C_h curve with the area A_s a nonlinear relationship, as shown in Fig. 9.

(10) The yearly cost of gas energy for cooling, given by Eq. (14), could also be rewritten similarly to Eq. (17) as

$$C_c = A_b \sum_{M_c} \left(\beta_{b,c} - \beta_{s,c} \frac{A_s}{A_b} \right) \tag{20}$$

where the monthly parameters $\beta_{b,c}$ and $\beta_{s,c}$ are given by:

$$\beta_{b,c} = 730\, C_g\, Q_{b,c} / COP_{g,c} \tag{21}$$

$$\beta_{s,c} = 30.42\, C_g S_c\, COP_{s,c} / COP_{g,c} \tag{22}$$

By analogy, the parameter $\beta_{b,c}$ represents the monthly gas energy cost per unit building area when cooling is exclusively provided by the gas-fired heat pump, without solar equipment. Also, the parameter $\beta_{s,c}$ represents the monthly cost savings, per unit collector area, resulting from adding a solar collector. The yearly cost of gas-cooling is initially $\beta_{b,c} A_b$ with no solar equipment and drops nonlinearly as the concentrator area increases to a collector area $A_{s,c}$, where the cost remains zero thereafter. The area ratio $A_{s,c}/A_b$ as calculated from $(\beta_{b,c}/\beta_{s,c})$ at the peak cooling month, represents the maximum collector area required to satisfy the building's peak cooling load. Analogously to the heating mode, by subtracting the monthly values of $\beta_{b,c} A_b$ from $\beta_{s,c} A_s$ some differences may result in negative values (when $\beta_{s,c} A_s > \beta_{b,c} A_b$), which should be counted as zero. This again gives a convex-shape curve for C_c vs A_s as sketched in Fig. 9.

(11) To compare the economics of candidate heating/cooling systems, several life cycle cost methodologies are available in the literature. One such method is to compute the accumulated implementation, maintenance, and operation costs over a certain number of years, N (e.g., 10 years, 15 years, or the life time of the major system components). Consideration could be taken of some or all of several economic factors such as general inflation rate, taxes, insurance, money interest rates, escalation of maintenance costs, escalation of energy costs, etc. A second method in economic comparisons is to divide the N-year life cycle cost into a "levelized" total cost, LTC, for each year of system operation. By adopting this method, the total annual cost of the gas-fired heat pump system with and without solar equipment is given by:

$$LTC = C_h + C_c + C_m + C_{im} \times CRF \tag{23}$$

where C_h and C_c are the annual costs of energy consumed for heating and cooling, respectively, C_m is the annual maintenance cost, C_{im} is the implementation cost of the new or add-on system including the hardware and installation costs, and *CRF* is the cost recovery factor. The *CRF*, defined as the annual payment of 1$ borrowed with *i*% interest rate, and *N* years payment period, is obtained from.

$$CRF = i(1+i)^N/[(1+i)^N - 1] \tag{24}$$

To compare the economics of the solar-assisted gas-fired heat pump under study with another gas-fired pump without solar equipment, the costs C_h and C_c, are obtained from Eqs. (17) and (20), respectively. As sketched in Fig. 9, the yearly gas cost for heating, C_h, starts with $A_b \sum_{M_h} \beta_{b,h}$ if no solar concentrator is present and decreases in a nonlinear relationship as the concentrator area A_s increases until a zero cost is reached when all heating loads are provided by the solar energy. Similar nonlinear behavior is shown for the yearly gas cost for cooling, C_c, when the monthly load profile is actually computed. If the monthly building loads during a particular mode of operation, however, is averaged as shown by profile 2, Fig. 9, the relationships between C_h or C_c and A_s become linear but lead to a gross error in computing the optimum collector area, as analyzed later on

To account for the costs of financing, property taxes, insurance, maintenance, etc., one can simply multiply the system implementation cost by an Annual Cost Factor, *ACF* (Ref. 18), thus giving a slightly different value to *CRF* as given by Eq. (24). Either an effective *CRF* or *ACF* will be used to combine the yearly costs of implementation and maintenance.

(12) A general profile of the levelized total cost, *LTC*, versus the concentrator area A_s (or the ratio A_s/A_b) is sketched in Fig. 10 for an add-on solar equipment option. The total gas energy cost $(C_c + C_h)$, the solar-equipment implementation and maintenance costs $[C_m + C_{im} \times CRF]$, are sketched as shown in Fig. 10. The energy cost decreases as the concentrator area increases but, on the other hand, the implementation cost increases. Hence, the levelized total cost, *LTC*, reaches a minimum at the optimum concentrator size A_s^*. On the other hand, A_s^* could be given by differentiating Eq. (23) with respect to A_s (assuming C_m, *CRF* as constants), and equating to zero

$$C_s \times CRF = \frac{-d}{dA_s}(C_c + C_h) \tag{25}$$

where $C_s\ (\$/\mathrm{m}^2)$ is the differential concentrator cost per unit area. The optimum concentrator size could be obtained either graphically or by the next analytical method. If the costs C_c and C_h are fitted, each, approximately by a quadratic relation in A_s:

$$\left.\begin{aligned} C_c/A_b &= a_{1,c} + a_{2,c}\left(\frac{A_s}{A_b}\right) + a_{3,c}\left(\frac{A_s}{A_b}\right)^2 \\ C_h/A_b &= a_{1,h} + a_{2,h}\left(\frac{A_s}{A_b}\right) + a_{3,h}\left(\frac{A_s}{A_b}\right)^2 \end{aligned}\right\} \tag{26}$$

Hence, the coefficients a_1, a_2 and a_3 should be known from 3 key properties of the annual energy cost profile. The first coefficient, a_1, for both heating and cooling modes, could be determined by using Eqs. (17) and (20) and Fig. 9 when the concentrator area A_s is set equal to zero:

$$\left.\begin{aligned} a_{1,h} &= \sum_{M_h} \beta_{b,h} \\ a_{1,c} &= \sum_{M_c} \beta_{b,c} \end{aligned}\right\} \tag{27}$$

The second coefficient, a_2, in both heating and cooling modes, represents the initial slope at $A_s = 0$; therefore, at very small A_s close to zero, one may write from Eqs. (17) and (20):

$$\left.\begin{aligned} a_{2,h} &= \sum_{M_h} \beta_{s,h} \\ a_{2,c} &= -\sum_{M_c} \beta_{s,c} \end{aligned}\right\} \tag{28}$$

Accordingly, the coefficients a_1 and a_2 will represent the gas cost coefficients if the space load is approximated as a constant, uniformly distributed load over a particular mode of operation. Since the actual space load varies on a daily or a monthly basis and is not constant over all the year, the third coefficient, a_3, will represent the side effect of actual load deviations from those average conditions. In fact, the coefficient a_3 of Eq. (26) is the sole driver behind the nonlinear relationship previously described. Finally, in order to fit Eq. (26) to the peak load condition where a large solar concentrator area is built to entirely cover the load needs, the coefficient a_3 is found from

$$\left.\begin{aligned} a_{3,h} &= \frac{-a_{1,h}}{(A_{s,h}/A_b)^2} - \frac{a_{2,h}}{(A_{s,h}/A_b)} \\ a_{3,c} &= \frac{-a_{1,c}}{(A_{s,c}/A_b)^2} - \frac{a_{2,c}}{(A_{s,c}/A_b)} \end{aligned}\right\} \quad (29)$$

where $A_{s,h}$ and $A_{s,c}$ are the concentrator areas that satisfy peak heating and peak cooling loads, respectively. Upon the determination of the fitted coefficients a_1, a_2, and a_3 from Eqs. (27) - (29), coupling of Eqs. (25) and (26) yields the optimum concentrator area A_s^* as:

$$\frac{A_s^*}{A_b} = \frac{\sum\limits_{M_h} \beta_{s,h} + \sum\limits_{M_c} \beta_{s,c} - C_s \times CRF}{2\left[\dfrac{\sum\limits_{M_h} \beta_{s,h}}{(A_{s,h}/A_b)} - \dfrac{\sum\limits_{M_h} \beta_{b,h}}{(A_{s,h}/A_b)^2} + \dfrac{\sum\limits_{M_c} \beta_{s,c}}{(A_{s,c}/A_b)} - \dfrac{\sum\limits_{M_c} \beta_{b,c}}{(A_{s,c}/A_b)^2}\right]} \quad (30)$$

Eqs. (25) and (30) and Fig. 10 suggest that the solar concentrator designer should build an ever increasing concentrator size until the "marginal cost" (or the slope of cost curve) of added-on solar equipment (which is in turn the marginal cost of gas energy displaced by solar) equals the "marginal cost" of saving gas energy, i.e., when the slope of the two energy saving and implementation curves becomes the same.

Equation (30) is an important expression needed to find the optimum collector area A_s^*. While it includes the key parameters of the system, Eq. (30) is only valid in the range $(A_s/A_b) = 0$ up to the limiting (A_s/A_b) for either heating or cooling, whichever is smaller. Note that the form of Eq. (30) could be further written in terms of the space cooling/space heating load ratio, for different types of buildings or for different weather patterns. However, this was not done because of its complex form.

(13) For the solar-assisted system to have economic feasibility, two conditions should be met in general. These are explained as follows

(a) Non-negative concentrator area condition ($A_s^* \geqslant 0$). This constrains the concentrator area cost, C_s, to be always below a maximum value. Since the denominator of Eq. (30) is always positive, then:

$$(C_s)_{\max} = \left(\sum_{M_h} \beta_{s,h} + \sum_{M_c} \beta_{s,c}\right) / CRF \quad (31)$$

(b) Ceiling LTC condition: The levelized total cost of the solar-assisted system must not be more than the LTC of the original system without solar equipment. This means that after the determination of the optimum ratio $(A_s/A_b)^*$, the resulting minimum LTC must satisfy the following condition:

$$LTC^* < A_b \left(\sum_{M_h} \beta_{b,h} + \sum_{M_c} \beta_{b,c}\right) \quad (32)$$

The above assumptions, idealizations, and economic feasibility conditions are illustrated for a sample office-type building at a selected DSN facility.

IV. System Application

An office building at the Deep Space Network Communication complex, Goldstone, California has been selected for the numerical evaluation of the system design and optimization. The detailed itemization of the building loads in both the summer and winter seasons appears in Ref. 17, for an arbitrarily selected floor area. However, the unit area parameters m_s and n_b were assumed independently of the building area to enable computations of the matching space size using Eq. (10) for a given heat-pump capacity. Other information is categorized as follows:

Weather		
Outside air design temperature,[4] t_o		
	summer	37.78°C (100°F)
	winter	2.22°C (28°F)
Months of season[4]		
	summer	5 ($t_o > 18.33$°C)
	winter	7 ($t_o < 18.33$°C)
Seasonal average outside air temperature		
	summer	25.8°C (78.46°F)
	winter	11°C (51.84°F)

---

[4] See Table 1 for monthly outdoor temperature and solar radiation profiles, taken from Refs. (19) and (20)

Effective daily solar input[5]	
summer	7548 Wh/m² day
winter	6616 Wh/m² day
Seasonal average solar intensity, I	
summer	943 W/m²
winter	880 W/m²

Building Specifications

Constant load per unit area,[6] m_b	
in summer	37.0 W/m²
in winter	31.7 W/m²
Rate of heat loss to or gain from ambient[7], n_b	4.783 W/m²°C (0.84 Btu/h ft²°F)
Indoor design temperature[8], T_i	
in summer	25.56°C (78°F)
in winter	22.22°C (72°F)
Changeover Temperature[9], T_o^*	
in summer	17.82°C (64.1°F)
in winter	15.59°C (60.1°F)
Matching Building Area,[10] A_b	304 m² (3275 ft²)

Concentrator-Receiver

Mirror reflectivity, ρ	0.88
Aperture intercept factor, ϕ	0.97
Receiver flow factor, F	0.94
Receiver effective absorptivity, α	0.90
Thermal loss rate, U	0.17 W/m²°C
Collector efficiency intercept,[11] m_v	0.722
Collector efficiency slope,[11] n_v	0.160 W/m²°C

Fluid operating temperature,[12] t_f,	
heating mode	500°C (932°F)
cooling mode	800°C (1472°F)

Power Conversion Subsystem

Efficiency of power transmission to the heat pump compressor,[13] η_t	0.9
Gas combustor efficiency, η_g	0.85
Ratio of recoverable heat to heat rejected from power cycle,[14] η_w	0.80
Power cycle efficiency relative to Carnot's, λ_e	0.5
Heat source operating temperature T_f	
in winter	500°C
in summer	800°C

Heat Pump

Nominal cooling capacity (ARI conditions)	10 tons of refrigeration
Average coefficient of performance in heating mode,[15] P_h	2.85
Gross coefficient of performance in heating mode using[16]	
solar, $COP_{h,s}$	0.864
gas, $COP_{h,g}$	1.157
Average coefficient of performance in cooling mode[17] P_c	3.00
Gross coefficient of performance in cooling mode[18] by	
solar, $COP_{c,s}$	0.561
gas, $COP_{c,g}$	0.827

Energy Cost

Unit cost of gas energy,[19] C_g	2×10^{-5} \$/W
Unit cost of electrical energy	7×10^{-5} \$/W

---

[5] Allows for 20% of the incident solar energy from Table 1 to be ineffective for tracking during sunrise and sunset hours

[6] Includes lighting, mechanical equipment, electronics equipment, and solar heat gain to space directly through fenestration areas and indirectly through opaque walls, from Ref (17)

[7] Includes heat transmission to and from varying ambient temperatures, ventilation, infiltration and exfiltration air effects This is assumed the same for both summer and winter seasons (Ref 17)

[8] Follows ASHRAE 90-75 standards (Ref 13)

[9] T_o^* corresponds to a zero building load Q_b from Eq (8)

[10] Using Eq (10) with a 10-ton heat-pump cooling capacity, and a margin capacity of 15% over peak building cooling load when both building and pump are at an outdoor air design temperature, t_o, of 37.78°C (100°F)

[11] From Eq (3)

[12] Selected based on the performance optimization given in Appendix B

[13] Includes friction in bearings, coupling, lubricating oil pump, and other parasitics

[14] Only required during the building heating mode

[15] See Appendix C, and Table 2 Average P_h is taken from $\Sigma Q_{b,h}/\Sigma(Q_{b,h}/P_h)$

[16] See Appendix B, Fig 3, and Table 2 Average COP_h is taken from $\Sigma Q_{b,h}/\Sigma(Q_{b,h}/COP_h)$

[17] See Appendix C, and Table 2 Average P_c is taken from $\Sigma Q_{b,c}/\Sigma(Q_{b,c}/P_c)$

[18] See Appendix B, Fig 2, and Table 2 COP_c, on the average, is taken from $\Sigma Q_{b,c}/\Sigma(Q_{b,c}/COP_c)$

[19] This amounts to \$0.60/Therm or \$6.00/Million Btu

Other Economic Data	
• System life, N	15 years
• Annual interest rate on borrowed money, i	10%
• Capital recovery factor,[20] CRF	0.13147
• Hardware and installation costs of	
• Heat pump[21]	\$11,000
• Master control panel, plant start-up, duct work, motorized dampers, etc.	\$ 8,000
• Power conversion module[22]	\$ 3,000 10,000
• Solar collection subsystem[23]	\$15,000 + (100 – 250) A_s
• Cost of alternate systems[24]	
• A nominal 20 kW$_e$ electrical resistance heater	\$1,000
• A nominal 20 kW (68,000 Btu/h) gas-fired heater	\$2,000

The calculation procedure is summarized as follows

(1) Because the calculations are made on representative days, one for each month, the daily average outside air temperature, T_o, and the direct normal solar radiation (required only for the 2-axis tracking collector) are tabulated for the site under investigation as in Table 1. Summer and winter seasons are distinguished by the average value of t_o as compared to a given reference temperature.

(2) Estimates are made for the constant sources of heat gain to a space, per unit floor area (m_h), and the rate of heat loss (or gain) to the exterior environment, n_h. Detailed back-up information appears in Refs. 13, 17, and 19. Different values of m_h and n_h could be estimated on a monthly basis; however, two changes, one for each season, are found satisfactory. Once the building's inside design temperature, t_i, is fixed, the heat gain to (or loss from) a space, Q_h, is calculated using Eq. (7). The results are listed in Table 2 and sketched in Fig. 11. A comparison of the outside air temperature and the changeover temperature, as obtained from Eq. (8), determines the mode of system operation . . . cooling or heating.

(3) The results of the coefficient of performance optimization versus the working fluid temperature from Appendix B, indicate that the changes in the optimum receiver-engine working temperature, T_f, has a minor effect on the optimum design point. Therefore, a working value of T_f, not necessarily the optimum value T_f^*, for each mode of operation should be chosen in advance, based either on average a" season conditions or on given metallurgical specifications. Monthly computations of P_c, P_h, R_c, R_h, F, COP_h and COP_c follow directly using Eqs. (C-7) and (C-12) of Appendix C and Eqs. (3), (4), (12), (13), (15), and (16).

(4) The monthly cost parameters β_c and β_h for both heating and cooling modes of operation, using Eqs. (18), (19), (21), and (22), are calculated next. The effective sun-tracking period, S, (assumed here as 80% of the daily sunshine period) is introduced to yield practical values for S. The price of the gas energy unit, c_g, is assumed to be representative for the time of the study. Energy cost escalation above general inflation is assumed the same as the escalation of the money interest rate above general inflation.

(5) Having determined the β coefficients, two approaches could be followed: the first approach is to graphically plot, as in Fig. 12, the yearly costs of energy, C_c, C_h, versus the area ratio A_s/A_b. Together with the levelized implementation and maintenance costs, the levelized total cost LTC could be plotted as shown in Fig. 13. For instance, two different concentrator costs were tried (C_s of 100 \$/m^2 and 150 \$/m^2 in addition to a \$1500 basic cost). For each unit concentrator cost, C_s, the optimum size A_s^*/A_b differs and a graphical representation for each is necessary. The second approach in determining the optimum area ratio is nongraphical and slightly less accurate than the first approach, but yields faster results. The second approach utilizes the quadratic curve fit of C_c and C_h previously described in Section III-12. The resulting economic feasibility conditions are given by Eqs. (30) - (32). Numerically, Table 2 is constructed for the given sample building

---

[20] Calculated from Eq. (24)

[21] For a nominal 15 kW$_e$ compressor, 10-ton unit, approximately \$730/kW$_e$. Subtract \$1,000 if the heat pump operates only as a chiller

[22] Smaller figure represents the projected mass production cost (\$200/kW$_e$). The large figure represents current cost of units under development

[23] To include costs of paraboloid mirror, receiver, storage, structure and foundation. It consists of a fixed cost and a variable part C_s depending on the solar collector area A_s in m^2

[24] To be used in conjunction with Table 3

following the above steps. The key quantities which appear in Eq. (30) are found as

$$A_b = 304\ \text{m}^2 \qquad CRF = 0.13147$$

$$\sum_{M_c} \beta_{b,c} = 3.5291\ \$/\text{m}^2 \qquad \sum_{M_h} \beta_{b,h} = 2.0311\ \$/\text{m}^2$$

$$\sum_{M_c} \beta_{s,c} = 18.236\ \$/\text{m}^2 \qquad \sum_{M_h} \beta_{s,h} = 18.011\ \$/\text{m}^2$$

$$\bar{A}_{s,h}/A_b = 0.245 \qquad \bar{A}_{s,c}/A_b = 0.332$$

For a unit concentrator cost C_s of 100 \$/m², (A_s^*/A_b) is 0.1845, from Eq. (30), which if compared to 0.19 using a graphical solution, gives a good test to Eq. (30). At C_s of 150 \$/m², Eq. (30) also gives (A_s^*/A_b) as 0.132 vs 0.12 if a graphical solution is made. This deviation is not large considering a faster engineering assessment. A maximum C_s for any economically feasible solution where $A_s^* > 0$ is also obtained from Eq. (31) as 276 \$/m², i.e., the total concentrator cost should not be more than $(1500 + 276\,A_s)$ \$. Using the fitted coefficients $(a_{1,c} + a_{1,h})$, $(a_{2,c} + a_{2,h})$ and $(a_{3,c} + A_{3,h})$ from Eqs. (27) - (29) as 5.5602, -36.2467, and 62.5892, respectively, the fitted $(C_c + C_h)$ curve is plotted as the dotted line in Fig. 13, to show the difference between the graphical and analytical approaches. The fitted curve is only valid for $A_s/A_b \leqslant 0.245$, which satisfies the peak heating load.

V. Summary of Results

The work described in this first assessment of solar-assisted gas-fired heat pumps has been initiated to benefit the DSN facility in regard to enhancing its performance. The work could be briefly summarized as follows:

(1) A complete air-air heat-pump system powered by a dual heat source has been outlined. Major system components have been identified and a breakdown of energy and flow streams given. Analytical expressions have been provided for the optimization of solar concentrator size at a minimal total system cost.

(2) For a selected office-type building located at the DSN Communication Complex at Goldstone, California, monthly load computations, modes of system operation, and component performance efficiencies have been determined for a given heat-pump size. The results of this step have been used to compute the yearly energy cost with and without a solar collection subsystem.

(3) The larger the solar concentrator size, the more gas energy will be displaced by solar energy, thus reducing the yearly energy cost and, on the other hand, increasing the implementation cost. The levelized total cost combining implementation, maintenance, and operation costs, will have a minimum value at the optimum collector area. This is shown graphically and analytically.

(4) The levelized total cost is sensitive to the concentrator cost per unit area, and if the latter ranges under a mass production program from 100 to 150 \$/m², the optimum concentrator area ratio A_s^*/A_b will be on the order of 0.19 to 0.12, respectively. No solar connection is found to be economical if the concentrator cost exceeds 275 \$/m². For instance, at a concentrator cost of 100 \$/m², the optimum concentrator size $(A_s^*/A_b = 0.19)$ provides 91% of the building's heating during the year and 72% of the building's cooling load for the year. Favorable economics are evident if the concentrator cost decreases and the gas energy cost increases further.

To supplement the engineering assessment of the proposed heat-pump dual heat-source concept, four alternate systems are compared in Table 3. Each is designed to provide the same heating and cooling needs for the selected building. The alternate systems are: (a) an all-electric system with an electrical resistance heater and a vapor compression chiller, (b) a combined gas-electricity system with a gas-fired heater and a vapor compression chiller, (c) an all-electric system using a heat pump for both heating and cooling, (d) an all-gas system using a gas-engine-driven heat pump. The proposed solar-assisted gas-engine driven heat pump is simply a superimposed feature on the alternate system (d). By a simplified 10-year life-cycle cost analysis including an energy escalation rate only 10% higher than that of money interest, system (a) was the highest and systems (b), (c), and (d) were found to be of comparable cost. A cost refinement for all systems (b), (c), and (d) requires detailed cost information that is of secondary importance as far as system-selection is concerned at this stage of the assessment.

The solar-assisted system under study possesses several advantages over other direct solar-heating or cooling devices, such as: 1) the elimination of large thermal energy storage, since gas combustion could run the system instantaneously during cloudy hours, or during nighttime, and 2) the close proximity of the power cycle and the conditioned space, which makes the utilization of rejected heat more feasible, and almost doubles the heat-pump performance. This results in a low total-energy cost. The field implementation, however, needs to satisfy other developmental, environmental and economic constraints that are currently being investigated.

C-3

References

1. Calm, J. M., and Bauer, P. T., "District Heating and Cooling with Heat Pump System," paper No. 799357, presented at the 14th IECEC Conference, Boston, Mass., August 1979, pp. 1681-1686.

2. Yudow, B. D., et al, "Feasibility of a Heat-Actuated Heat-Pump-Centered Integrated Community Energy System," paper No. 799358, presented at the 14th IECEC Conference, Boston, Mass., August 1979, pp. 1687-1692.

3. Lior, N., "Solar Rankine Cycle (steam) Drive and Assistance to Heat Pump Systems," paper presented at the Solar Energy Heat Pump Systems for Heating and Cooling Buildings, Pennsylvania State University, June 1975, ERDA document C00-2560-1.

4. Sullivan, D., "Technology Impact Study of a High Efficiency Industrial Heat Pump," paper No. 799365, presented at the 14th IECEC Conference, Boston, Mass., August 1979, pp. 1725-1929.

5. Wurm, J., "Assessment of Selected-Engine Driven Heat Pumps," presented at the Solar Energy Heat Pump System for Heating and Cooling Buildings, Pennsylvania State University, June 1975, ERDA Document C00-2560-1.

6. Biancardi, R. F., and Meader, M. D., "Demonstration of a Turbocompressor Air Conditioning System," paper presented at the Solar Energy Heat Pump Systems for Heating and Cooling Buildings, Pennsylvania State University, June 1975, ERDA Document C00-2560-1.

7. Fischer, R D., et al., "A Solar Heat Pump Featuring Pivoting-Tip Vanes," paper presented at the Solar Energy Heat Pump Systems for Heating and Cooling Buildings, Pennsylvania State University, June 1975, ERDA Document C00-2560-1.

8. Barber, R. E., "Solar Rankine Engines--Examples and Projected Costs," an ASME paper presented at the Gas Turbine Conference, San Diego, Calif., March 1979.

9. Allen, R. A., and Stiel, L. I., Working Fluids for Solar Rankine Heat Pumps," presented at the Solar Energy Heat Pump Systems for Heating and Cooling Buildings, Pennsylvania State University, June 1975, ERDA Document C00-2560-1.

10. Richards, W. D., and Chiu, W. S., "System Performance of a Stirling Engine-Powered Heat Activated Heat Pump," paper No. 799359, presented at the 14th Intersociety Energy Conversion Engineering Conference (IECEC), August 1979, pp. 1693-1698.

11. Patani, A., and Bonne, U., "Modeling the Performance of Gas-Fired Heat Pump Systems," paper No. 799360, presented at the 14th IECEC Conference, Boston, Mass., August 1979, pp. 1699-1707.

12. Martini, W. R., "An Efficient Stirling Heat Engine-Heat Pump," presented at the Solar Energy Heat Pump Systems for Heating and Cooling Buildings, Pennsylvania State University, June 1975, ERDA Document C00-2560-1.

13. Stamper, E. and Koral, R. L., editors, *Handbook of Air Conditioning, Heating and Ventilating*, Third Edition, Industrial Press, Inc., N. Y., 1979, Section 3.

14. Ekroth, I. A., "Thermodynamic Evaluation of Heat Pumps Working With High Temperatures," paper No. 799363, presented at the 14th IECEC Conference, Boston, Mass., August 1979, pp. 1713-1719.

15. Freeman, T. L., et al., "Computer Modeling of Heat Pumps, and the Simulation of Solar-Heat Pump Systems," ASME paper No. 75-WA/SOL-3, presented at the ASME Winter Annual Meeting, Houston, Texas, November 1975.

16. American Society of Heating, Refrigeration and Air Conditioning Engineers (ASHRAE) Guide and Data Book, 1972, Ch. 43.

17. Lansing, F. L., "A Sensitivity Model for Energy Consumption in Buildings," *TDA Progress Report 42-61*, Jet Propulsion Laboratory, Pasadena, Calif., pp. 58-87, February 1981.

18. Elliot, D. G., "Design and Economics of Solar Cooling for Electrically Powered Southern California Buildings" publication No. 5030-186, Jet Propulsion Laboratory, Pasadena Calif., March 1978.

19. *Handbook of Fundamentals*, American Society for Heating, Refrigeration and Air Conditioning Engineers (ASHRAE), N. Y., N. Y., 1972.

20. Kusuda, T. and Ishii, K., "Hourly Solar Radiation Data for Vertical and Horizontal Surfaces on Average Days in the United States and Canada," NBS Building Science Series, 96 NBS, U. S. Dept. of Commerce, April 1977.

21. Rapp, D. *Solar Energy*, Prentice-Hall, Inc., N. J. 1981, Chapter 9.

22. Barnett, R. C., "Performance Characteristics of Air-to-Air Heat Pumps," presented at the Solar Energy Heat Pump Systems for Heating and Cooling Buildings, Pennsylvania State University, June 1975, ERDA Document C00-2560-1.

23. Miller, J. F., "Extended Range Water Source Heat Pumps," presented at the Solar Energy Heat Pump Systems for Heating and Cooling Buildings, Pennsylvania State University, June 1975, ERDA Document C00-2560-1.

24. Trelease, S. W., "Water Source Heat Pump Evaluation," *Heating, Piping, & Air Conditioning Journal*, October 1980, pp. 75-85.

Definition of Symbols

A	Projected area, m^2
a	cost coefficient, \$/m^2
C	cost, \$
CC	cooling capacity of a heat pump, tons of refrigeration
COP	Gross coefficient of performance
CRF	Cost recovery factor
E	Efficiency of energy conversion subsystem
F	Flow factor in solar receivers
I	Solar intensity, W/m^2
i	Interest rate on borrowed money, %
LTC	Levelized total cost, \$
M	Time in months of a given mode of operation
m	Intercept of a straight line
N	System life in years
n	Slope of a straight line
P	Coefficient of performance of heat pump subsystem
Q	Thermal energy per unit floor area, W/m^2
R	Solar concentrator-receiver efficiency
S	Effective daily solar radiation input, Wh/m^2 day
t	Temperature °C
T	Absolute Temperature, K
U	Heat loss coefficient for solar receiver, W/m^2°C
ρ	Spectral reflectivity of concentrator surface
ϕ	mirror-receiver intercept factor
η	efficiency
α	effective absorptivity of solar receiver
β	cost parameter, \$/m^2
θ	dimensionless parameter
λ	fraction of a corresponding Carnot's cycle

Superscripts

$-$	peak or design conditions
$*$	changeover/optimum conditions

Subscripts

b	building
c	cooling mode
co	condenser
e	heat engine or power conversion subsystem
ev	evaporator
f	working fluid in solar receiver (or gas combustor)
g	gas combustor
h	heating mode
H	high temperature heat reservoir
i	inside the space
im	implementation
m	maintenance
L	low temperature heat reservoir
o	outside environment to space
s	solar-powered mode/solar concentrator
t	energy transmission and storage subsystem
w	waste heat recovery subsystem

Table 1. Monthly average weather parameters for Goldstone, California

Month	Direct solar radiation data[a] Noon intensity, I_n, W/m^2	Daily input, Wh/m^2, day	Sunny hours, h/day	Average intensity over the sunny, I, hours, W/m^2	Daily average outside air temperature, T_o, °C	Season[b] S = summer W = winter
Jan	960	7473	8	934	6.4	W
Feb	987	8697	10	870	11.1	W
Mar	980	9399	10	940	12.1	W
Apr	933	9732	12	811	14.3	W
May	901	9880	12	823	19.8	S
Jun	883	9799	12	817	26.1	S
Jul	876	9564	12	979	29.7	S
Aug	890	9180	12	765	29.1	S
Sep	928	8751	10	875	24.4	S
Oct	949	8246	10	825	17.4	W
Nov	943	7301	8	913	10.7	W
Dec	940	7042	8	880	5.3	W
Average for 5 summer months		9435	10	943	25.8	S
Average for 7 winter months		8270	8.4	880	11.0	W

[a] Uses ASHRAE model (Refs 19 and 20).

[b] Classified as summer or winter depending on whether the average daily outside air temperature is higher than or less than 18.33°C, respectively.

Table 2. Monthly results of the sample office building

Month	t_o^a, °C	Season[a]	t_i, °C	Q_b^b, W/m^2	Mode[c] of operation	P	T_f °C	COP_g^d	COP_s^e	S^f Wh/m^{2}day	β_b^g	β_s^g
May	19.8	S	25.56	9.45	C	3.813	800	1.059	0.710	7904	0.1303	3.2237
Jun	26.1	S	25.56	39.58	C	3.117	800	0.858	0.576	7839	0.6735	3.2014
Jul	29.7	S	25.56	56.80[h]	C	2.782	800	0.764	0.536	7651	1.0854	3.2654
Aug	29.1	S	25.56	53.93	C	2.835	800	0.779	0.514	7344	1.0108	2.9478
Sep	24.4	S	25.56	31.45	C	3.289	800	0.908	0.620	7001	0.5057	2.9081
Oct	17.4	W	22.22	8.64	C	3.660	800	1.022	0.685	6597	0.1234	2.6898
Nov	10.7	W	22.22	-23.40	H	2.878	500	1.161	0.869	5841	0.2943	2.6596
Dec	5.3	W	22.22	-49.23[h]	H	2.810	500	1.150	0.855	5634	0.6250	2.5482
Jan	6.4	W	22.22	-43.97	H	2.841	500	1.156	0.867	5978	0.5553	2.7275
Feb	11.1	W	22.22	-21.49	H	2.883	500	1.162	0.864	6958	0.2700	3.1473
Mar	12.1	W	22.22	-16.70	H	2.896	500	1.165	0.876	7519	0.2093	3.4394
Apr	14.3	W	22.22	- 6.18	H	2.925	500	1.169	0.861	7786	0.0772	3.4885

[a] From Table 1 data.

[b] Calculated monthly from Eq. (7).

[c] C = cooling, h = heating, according to sign of Q_b.

[d] Using Eqs. (13), (16), Table 1, and Appendices B, C.

[e] Using Eqs. (12), (15), and Appendices B, C.

[f] Taking 80% of available solar radiation values in Table 1.

[g] Using Eqs. (18), (19), (21), and (22).

[h] Peak loads needed for equipment design.

Table 3. Comparison of alternate HVAC systems without a solar coupling

HVAC systems		System 1 Electrical resistance heating and electrical-powered chillers	System 2 Gas-fired heater and electrical-powered chillers	System 3 Electrical-powered heat pump for both heating and cooling	System 4 Gas-fired turbo-compressor heat pump
Annual[a] building load, kWh/yr	heating	← 35,722 →			
	cooling	← 44,351 →			
Average efficiency or COP of heating equipment		0.9[b]	0.85[b]	2.85[b]	1.157[d]
Average COP of cooling equipment		3.00[c]	3.00[c]	3.00[c]	0.827[d]
Itemized energy cost[e] per year, $	heating	2,778	840	877	617
	cooling	1,034	1,034	1,034	1,073
Yearly energy cost, $		3,812	1,874	1,911	1,690
Initial cost, × 10^3 $		19[f]	20[g]	19[h]	22[i]
Approx. 10-yr life cycle[j] cost × 10^3 $		79.75	49.87	49.46	48.93

[a] Using building loads from Table 2, 304 m^2 floor area.

[b] Assumed values

[c] Averaged from Table 2 as $\Sigma Q_b / \Sigma (Q_b/P)$

[d] Averaged from Table 2 as $\Sigma Q_b / \Sigma (Q_b/COP_g)$

[e] Based on 2¢/kWh for gas heating and 7¢/kWh for electricity.

[f] $1K for heater, $8K for ducts, controls and $10K for a chiller

[g] $2K for a boiler, $8K for ducts, controls and $10K for a chiller

[h] $11K for a heat pump, $8K for ducts and controls.

[i] Same as system 3, add $3K for gas engine.

[j] With 10% energy escalation rate.

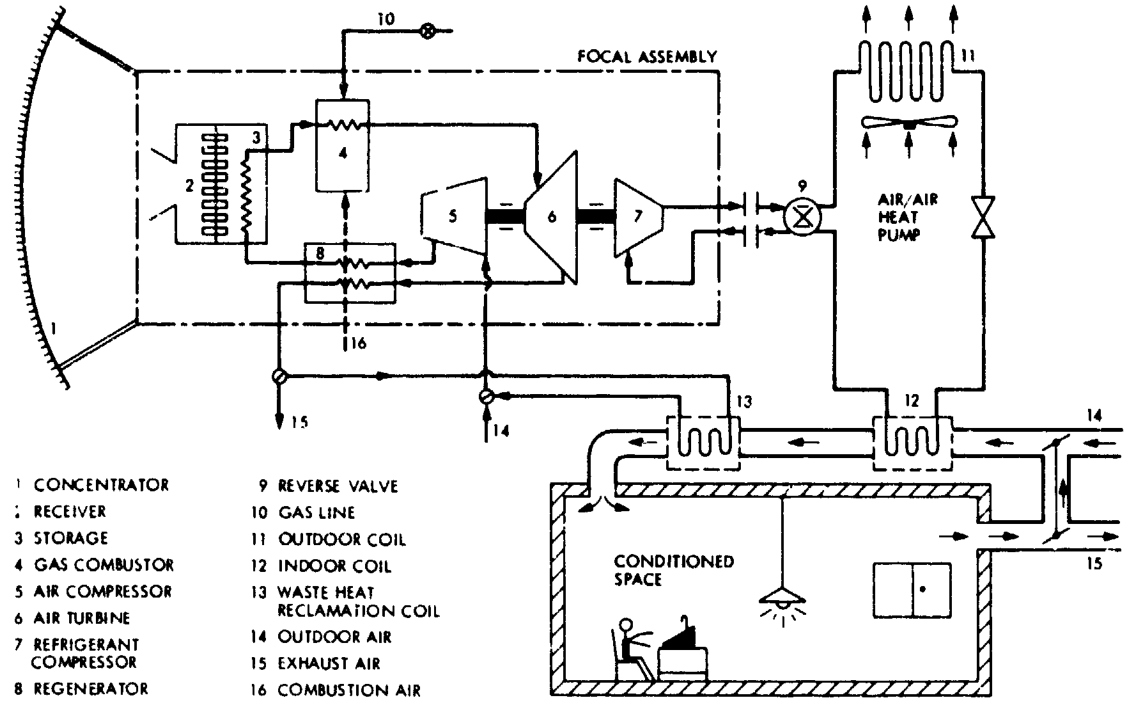

Fig. 1. Layout of a solar-assisted gas-fired heat-pump system (not to scale)

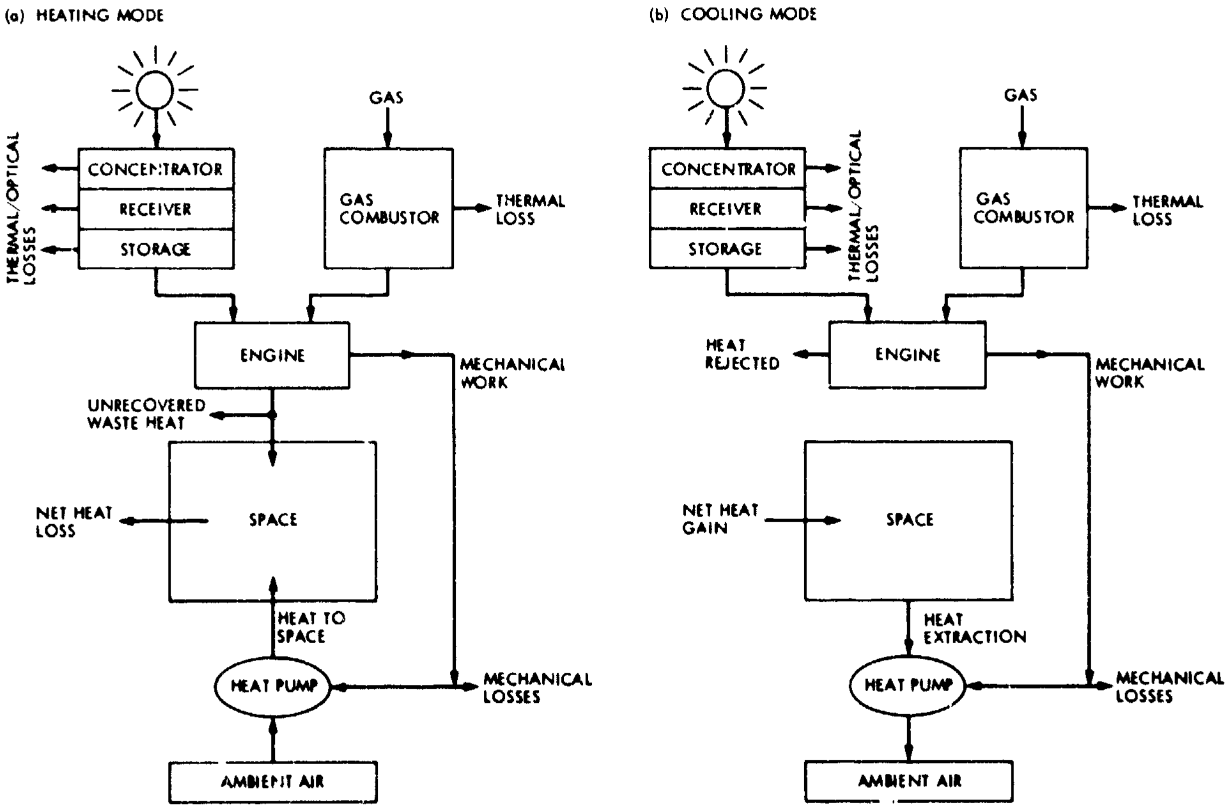

Fig. 2. System energy balance during modes of operation

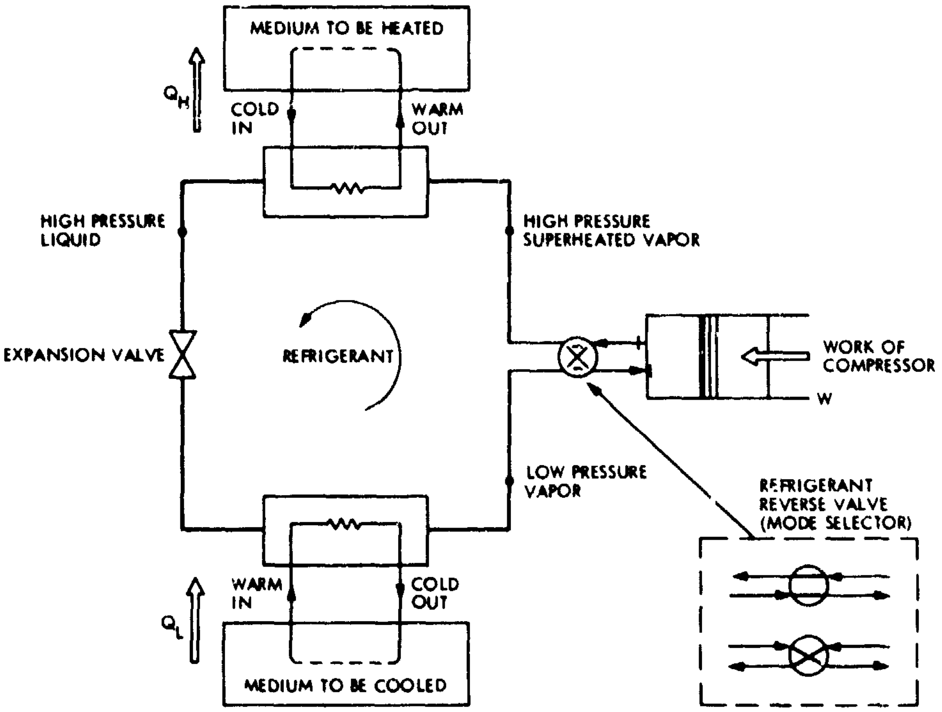

Fig. 3. Principle of operation of a heat pump

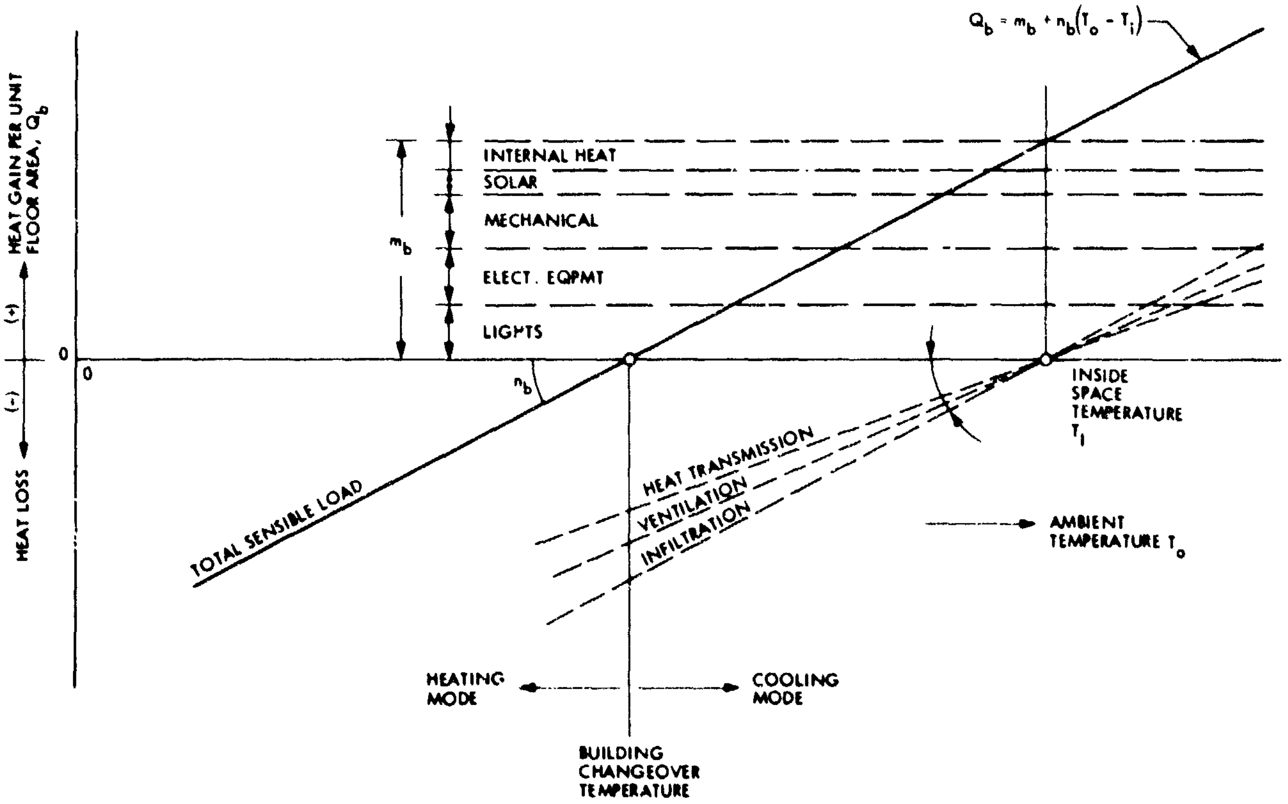

Fig. 4. General daily load profile for buildings

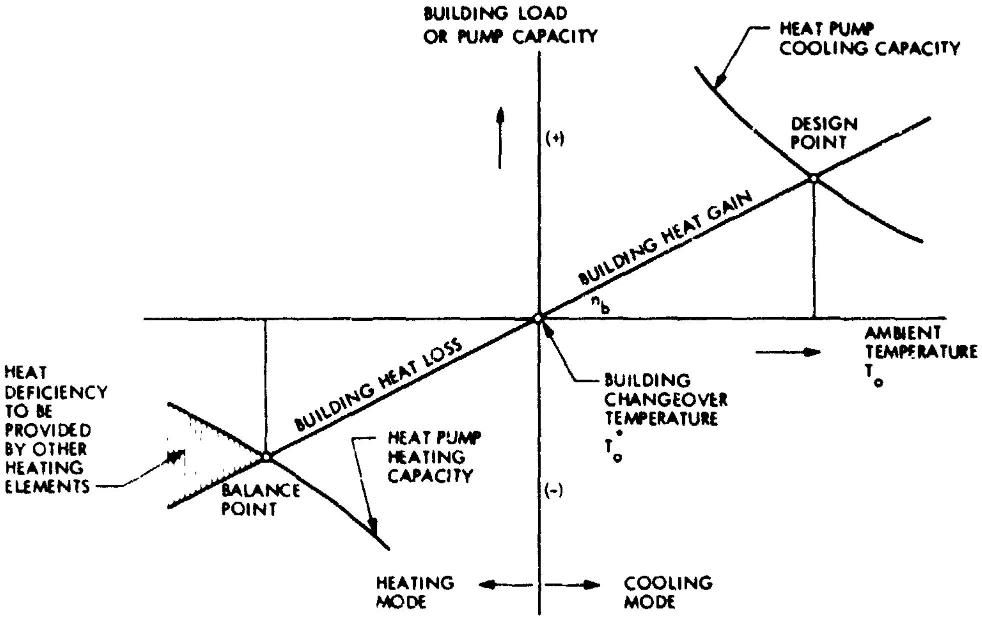

Fig. 5. Heat-pump capacity versus building load

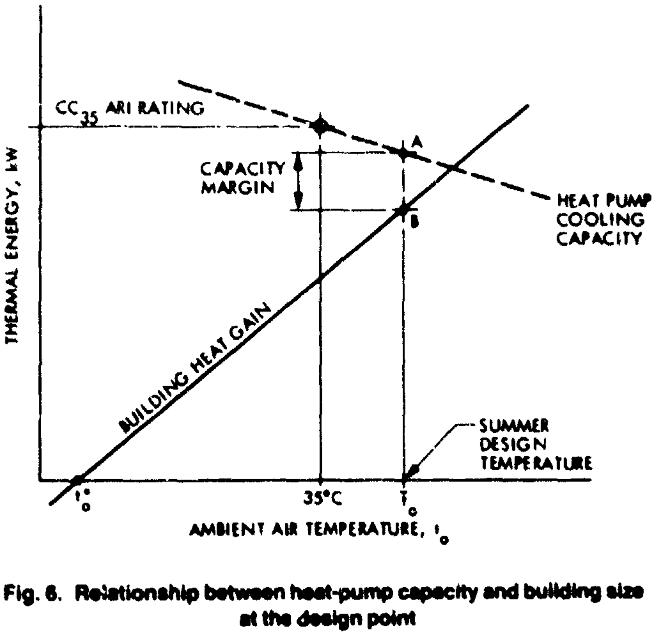

Fig. 6. Relationship between heat-pump capacity and building size at the design point

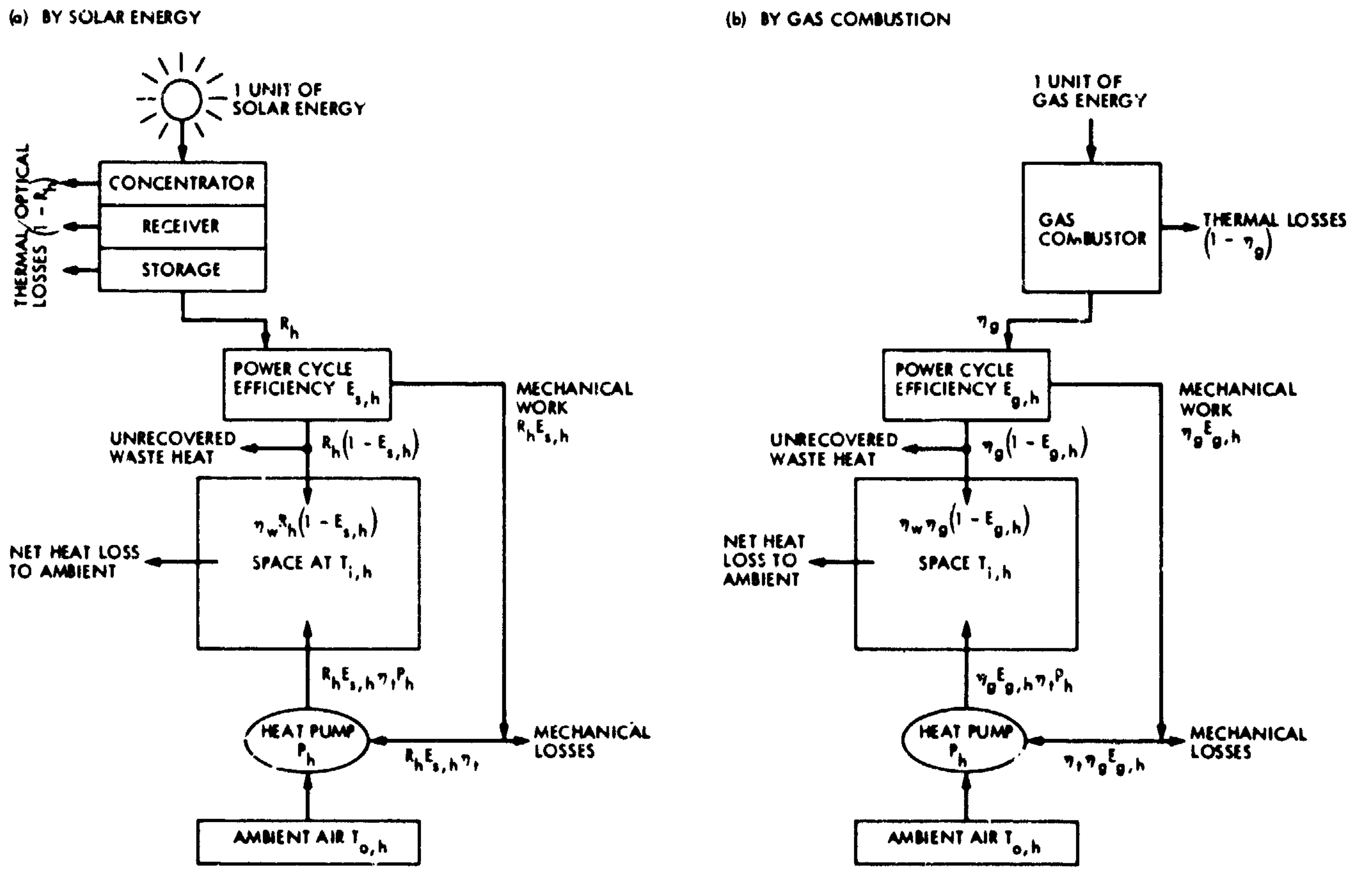
(a) BY SOLAR ENERGY

(b) BY GAS COMBUSTION

Fig. 7. Gross coefficient of performance during heating mode

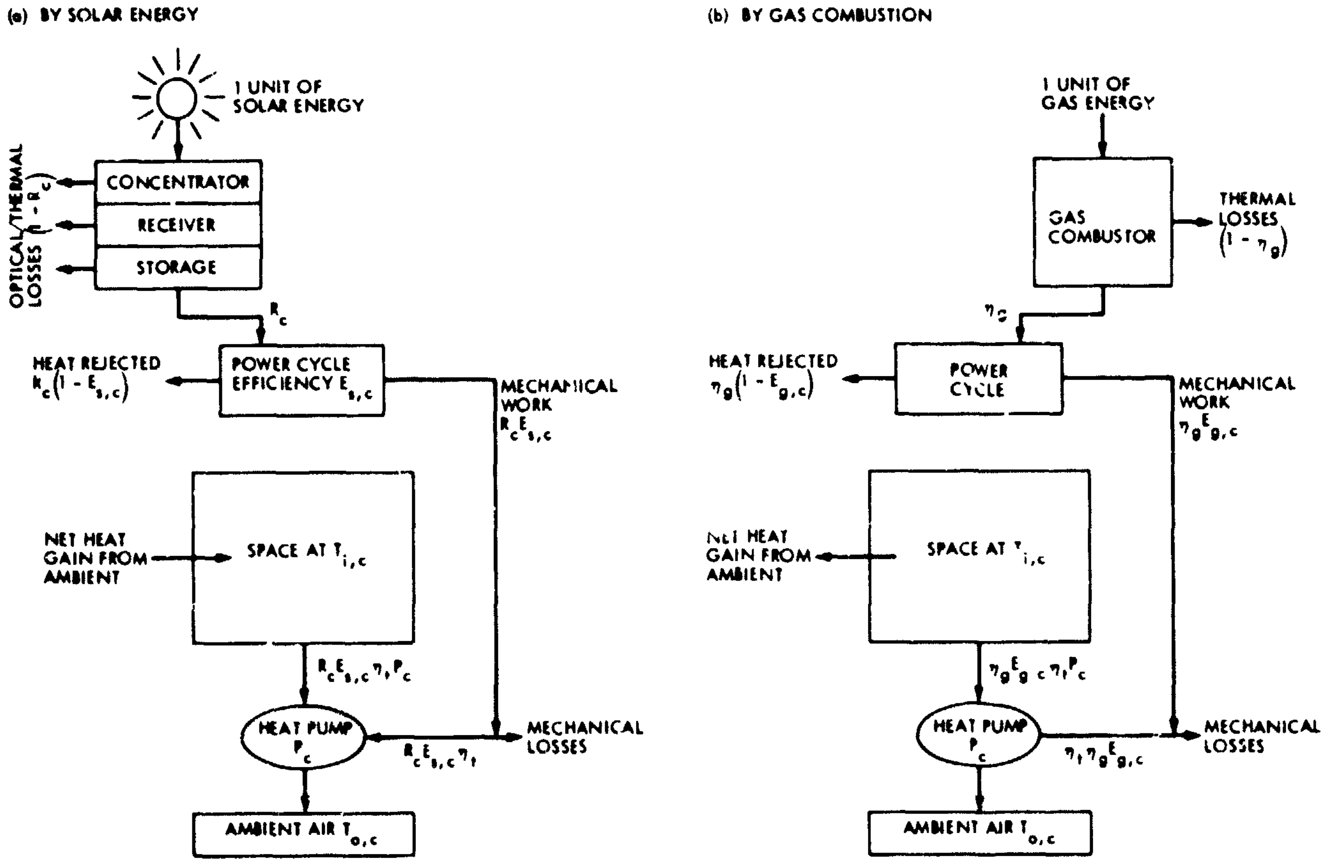

Fig. 8. Gross coefficient of performance during cooling mode

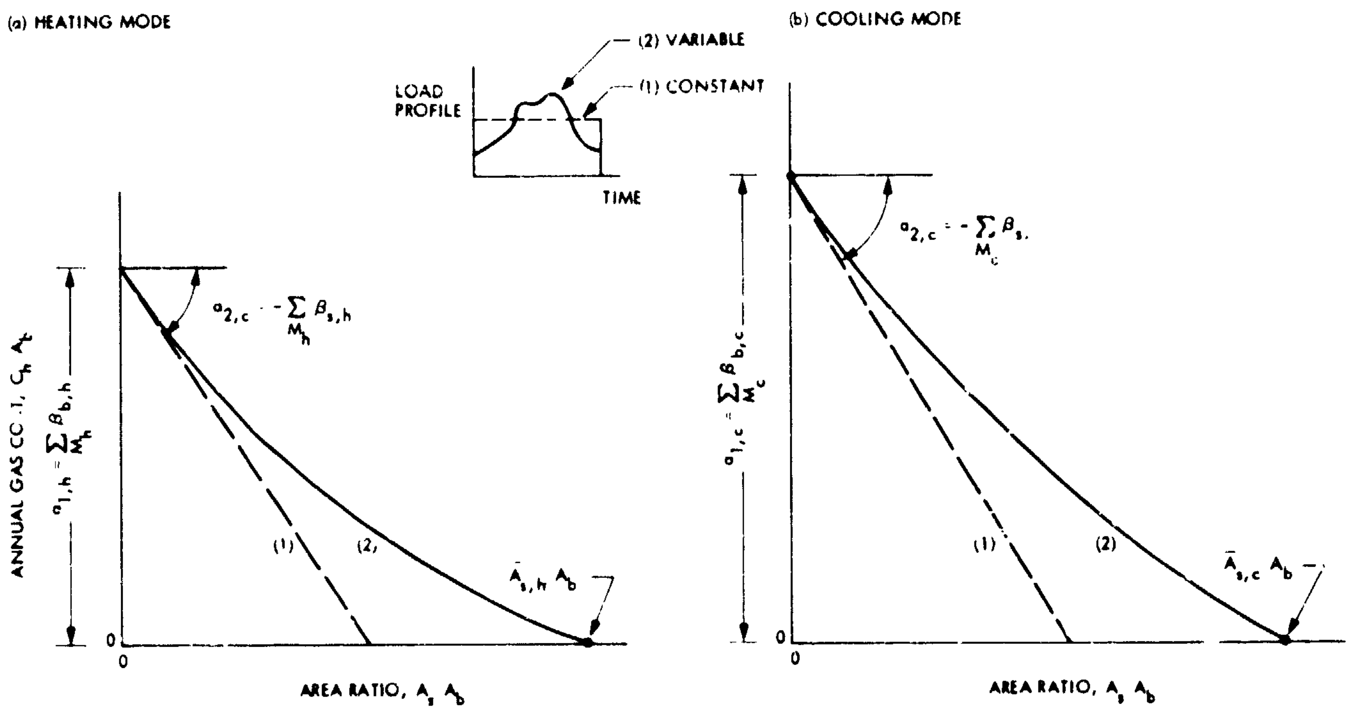

Fig. 9. Trends of gas cost versus solar concentrator area in both heating and cooling modes

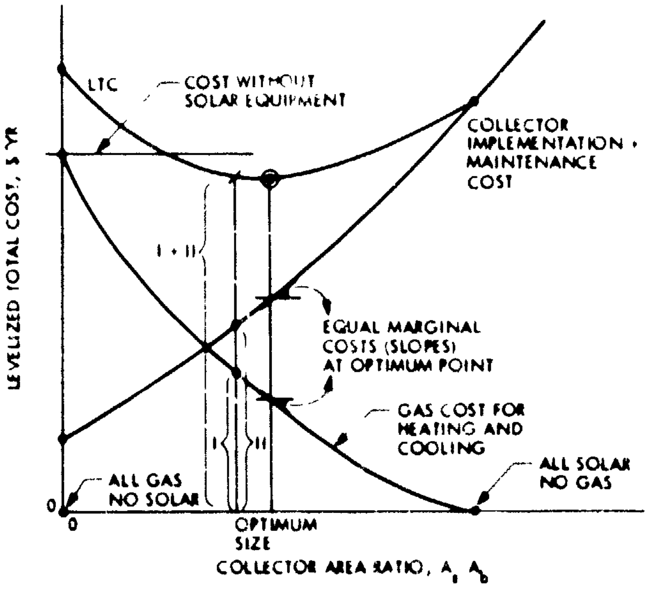

Fig. 10. The search for optimum concentrator size

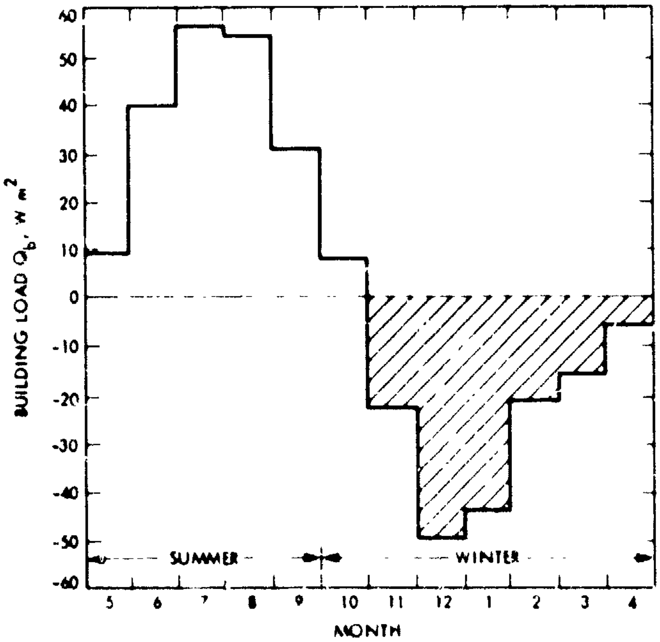

Fig. 11. Monthly heat gain (or heat loss) profile for the sample office building

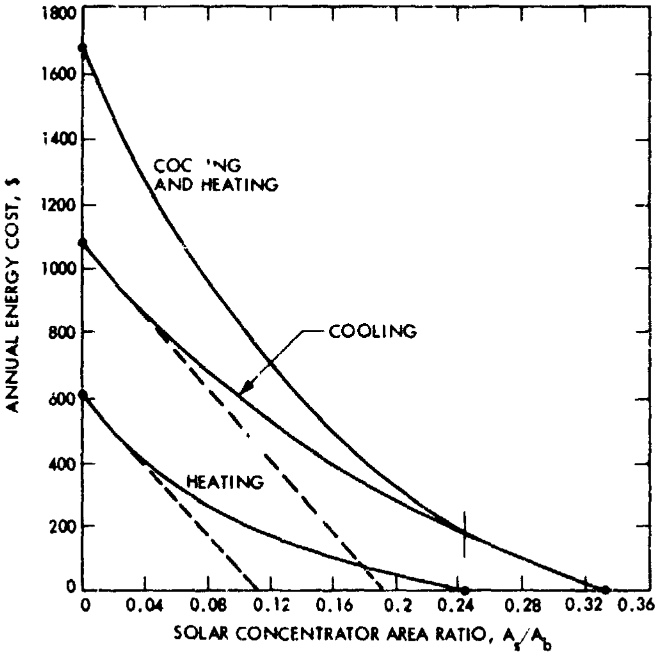

Fig. 12. Results of gas energy costs at different concentrator sizes for the sample building

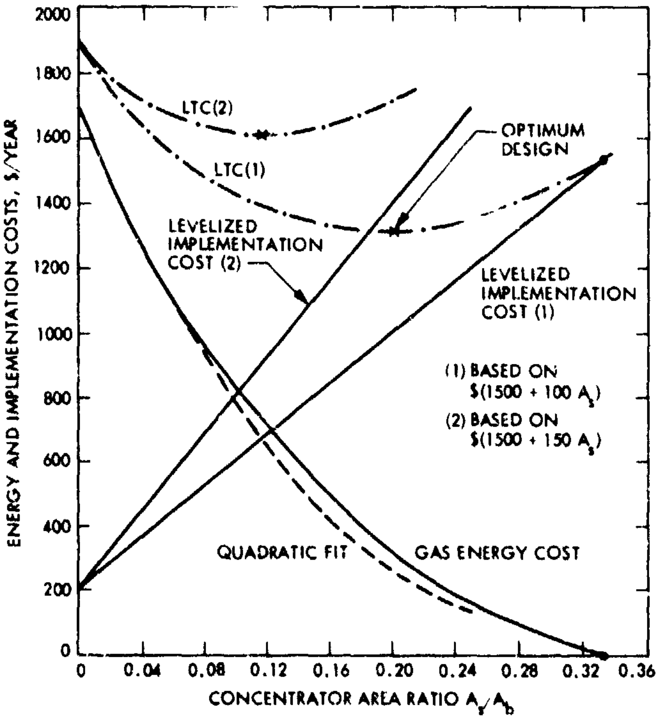

Fig. 13. Solar concentrator optimization for the sample building

Appendix A

Heat Pump Configurations

Four different types of heat pumps are generally available, which are classified basically according to the type of medium in contact with the refrigerant in either the indoor or outdoor elements. This medium acts as a heat source or a heat sink during operation. The heat pump classification is as follows:

(1) Air-to-air heat pump (A-A)

(2) Water-to-water heat pump (W-W)

(3) Water-to-air heat pump (W-A)

(4) Air-to-water heat pump (A-W)

The first medium always represents the outdoor fluid in contact with the refrigerant in the outdoor heat exchanger. This first medium acts either as a heat source (in a heating mode) or as a heat sink (in a cooling mode). The second medium is the indoor fluid which comes in contact with the refrigerant in the indoor heat exchanger. Consequently, the second medium acts either as a heat sink (in a heating mode) or as a heat source (in a cooling mode) (Refs. 13 and 21). Each of the above four heat-pump configurations is described briefly below.

I. Air-to-Air Heat Pump

This is the most widely used heat pump, and is illustrated in Fig. A-1 for both cooling and heating modes of operation with refrigerant reversing controls (Ref. 22). Forced air, from fans, flows over both the indoor and outdoor refrigerant coils. A complete system requires an indoor air distribution network (ducts) to supply filtered warm or cool air as needed. Operating the A-A heat pump in a heating mode where the outdoor air temperature is very low (less than 7°C or 45°F) may cause frost formation on the outdoor coils. Coil frosting impairs the pump effectiveness, since it blocks the air flow and presents several operational difficulties. One solution to this problem is to reverse the mode-selector valve to the cooling mode frequently and for a few minutes until the hot outdoor coil (operating then as a heat rejection element) melts the frost. Other solutions such as the use of electric-resistance heaters or taking advantage of other waste-heat sources could be used.

In multi-zone air conditioning where different zones make different heating or cooling demands simultaneously, the use of A-A heat pumps with an air changeover system is sometimes preferred instead of having a refrigerant changeover selector. In this air-changeover system, the flow of air is controlled by a dual-duct network accompanied by a set of motorized dampers to direct the air across the condenser coils for heating or across the evaporator coils for cooling before entering the air-conditioned space as shown in Fig. A-2. The refrigerant flow is not reversed, however, in this system. Depending on the relative magnitude of heating and cooling demands, the heat pump extracts low temperature heat from zones that require cold air and gives it at high temperature to those zones that require warm air. Although a good potential for energy conservation exists in this configuration because the heat pump partially acts as a heat reclamation device, the air changeover system has not been widely recognized.

A-A heat pumps are generally designed in integral packaged form with small tonnage (up to 30 tons of refrigeration (105 kW)) for residential or commercial applications (Ref. 13). Since water is not used, the maintenance and operation problems of piping, plumbing, fluid leakage, or corrosion do not exist, which generally results in low maintenance costs.

II. Water-to-Water Heat Pump

As illustrated in Fig. A-3, a water-to-water heat pump uses water from a well, lake, river, or any large body of water as either a heat source or a heat sink. Water is also used to exchange heat to and from the refrigerant in the indoor coil. W-W heat pumps have been less popular commercially than A-A types due to:

(1) A shortage of clean water supply in some populated areas; generally, water from wells is returned to the ground in order not to deplete underground water supplies.

(2) Low water quality of city water, which in general contains soluble minerals. Deposits on piping and heat exchangers cause scaling and fouling; soft water, on the other hand, without some mineral content, can be corrosive.

(3) Plumbing costs could increase the first cost of the system.

In spite of the above operation and maintenance problems of W-W heat pumps, they offer several advantages over their competitors: They provide a higher coefficient of performance and less heat exchange surface area since water is a good heat transfer medium and, because of the constant temperature of well water, different from ambient air, they provide higher performance during periods of peak heating (water temperature is higher than air temperature) or peak cooling (water temperature is lower than air temperature). These advantages result in W-W heat pumps being lower in operating cost than the comparable A-A type.

W-W heat pumps could also operate with either the refrigerant reversing valve as shown in Fig. A-2 or water reversing valves. In a water changeover system, the direction of water leaving the condenser and chiller (evaporator) is controlled by valves to provide heating or cooling to multiple zones as required. In general, the refrigerant control is preferred to avoid contamination of indoor coils with the external water supplies (from a river, lake, ocean, etc.), which may be chemically untreated.

III. Water-to-Air Heat Pumps (W-A)

This heat pump also uses well or lake water as a heat sink/source similar to W-W heat pumps, but the heat is delivered to the indoor coil through direct expansion of the refrigerant as shown in Fig. A-4. The W-A heat-pump system has the same basic problems as the W-W type in regard to water availability, quality, and its disposal. However, it operates with higher performance than an A-A system if enough water (at temperatures higher than 10°C (50°F)) is available (Refs. 23 and 24). A W-A system could operate with air-reverse controls to supply cold/warm air as needed or else use refrigerant reverse controls as shown in Fig. A-4. The advantages of low initial cost and low maintenance cost of A-A systems are still applied, since it is a hybrid system of the above A-A and W-W systems.

IV. Air-to-Water Heat Pumps (A-W)

This heat pump is the same as W-A type above, except it uses outdoor air as the heat source/sink and exchanges heat with the indoor coil through the use of clean water as a secondary medium, as shown in Fig. A-5. A-W systems have the same advantages and limitations as W-A units. Since warm/cold water piping replace the interior air duct work, corrosion problems, though not entirely eliminated, are less frequent than in W-W or W-A systems.

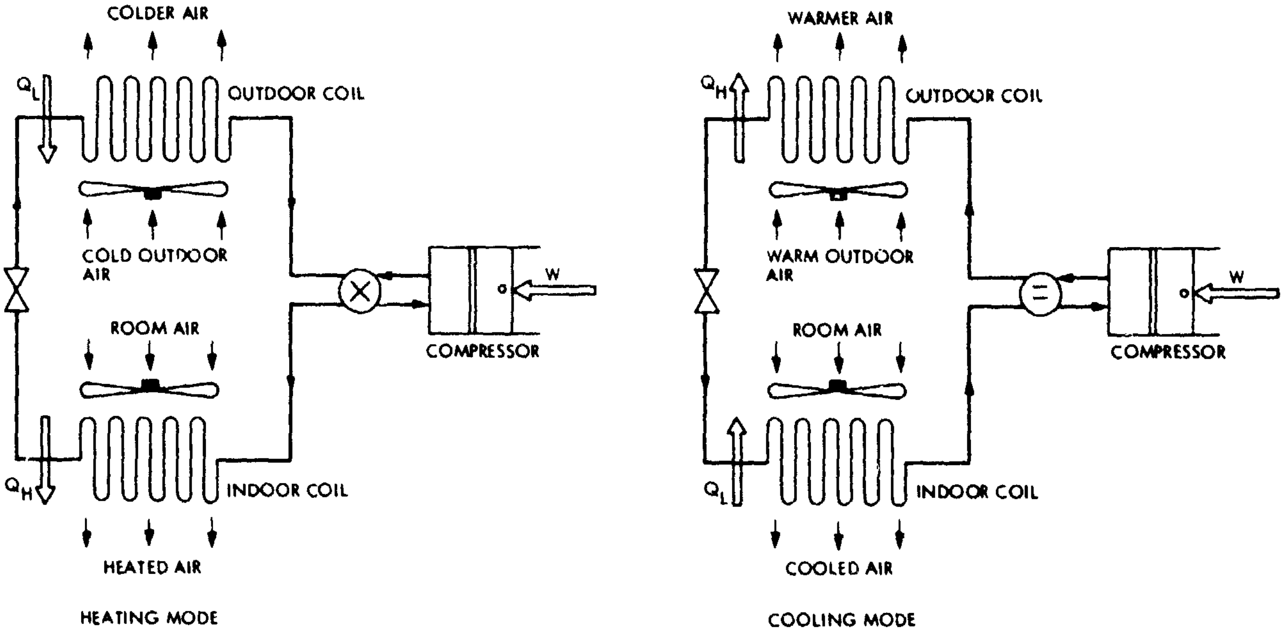

Fig. A-1. Air-to-air heat pump

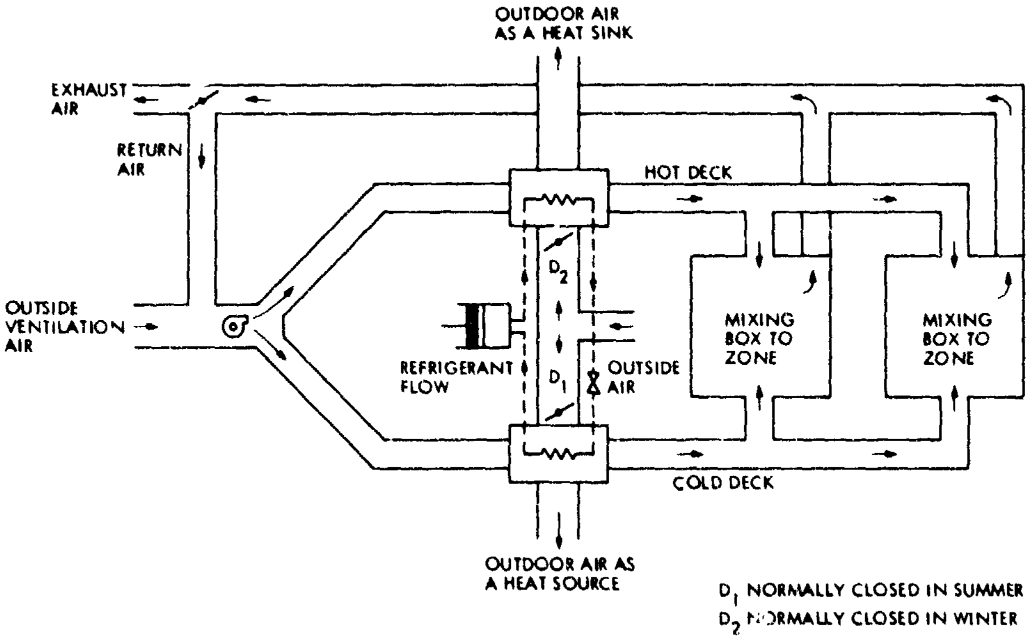

Fig. A-2. Multizone air-changeover A-A heat pump system with dual duct and mixing box controls

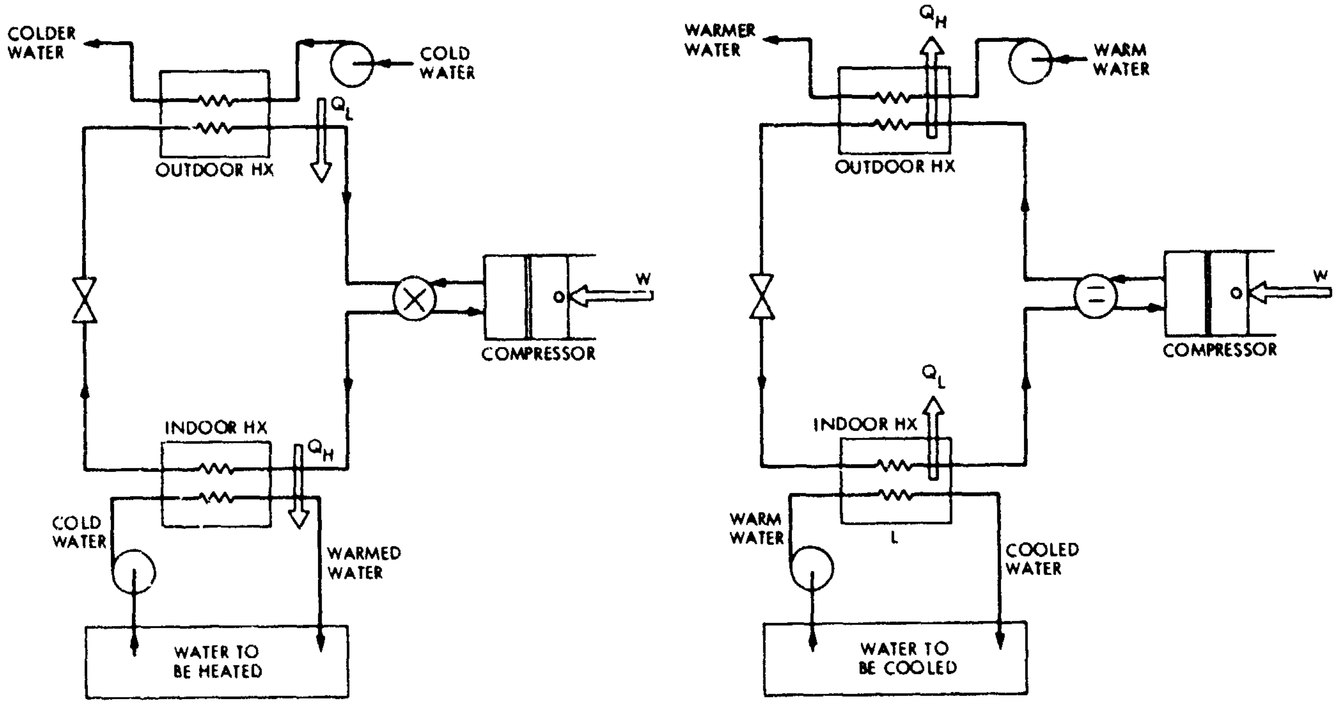

HEATING MODE

COOLING MODE

Fig. A-3. Water-to-water heat pump

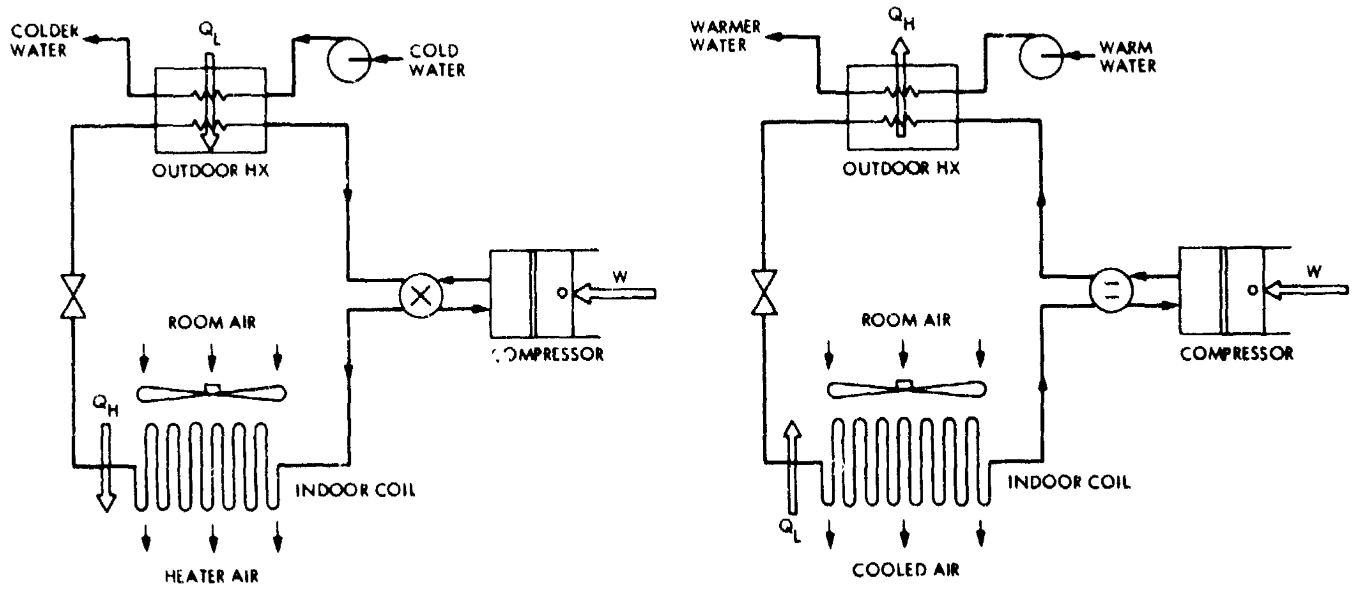

HEATING MODE

COOLING MODE

Fig. A-4. Water-to-air heat pump

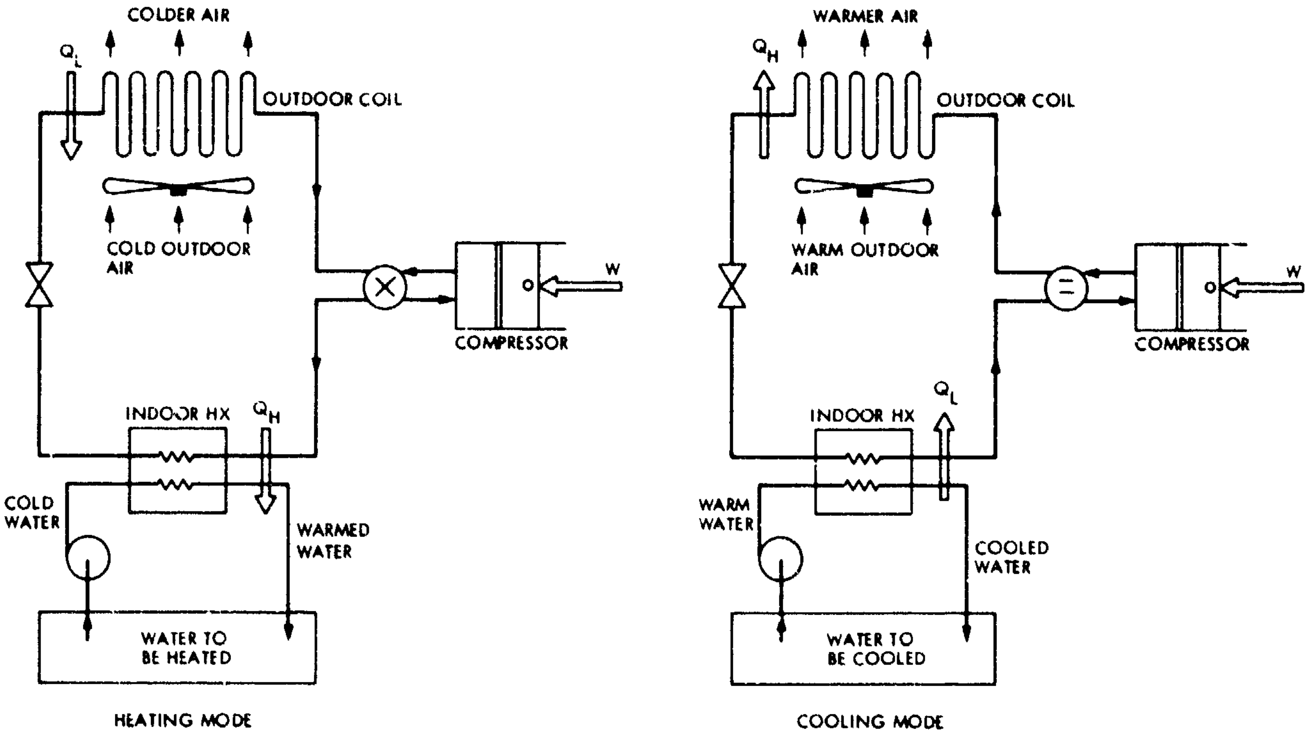

Fig. A-5. Air-to-water heat pump

Appendix B

Optimum Receiver-Engine Working Temperature

The operating temperature of the fluid circulating inside the solar receiver-storage subsystem is an important parameter in determining the coefficient of performance of the heat-pump system at any mode. In the cooling mode, and for a given solar-energy input, a high receiver temperature gives a high-power cycle efficiency, E, but results in a low collector efficiency, R, due to the increased receiver thermal losses. An optimum operating temperature is, therefore, required to maximize the product RE when operating in the cooling mode.

For the building-heating mode, the recoverable portion of the engine's rejected heat is also utilized as an additional heating effect to boost the basic heat-pump heating effect. For a given solar-energy input, the higher the receiver temperature becomes the higher the power cycle efficiency E, the higher the heating effect by the heat pump, and the less the heat rejected from the engine. Again, an optimum receiver operating temperature is required to maximize the sum of the two heating effects. For each mode of operation, the optimum operating temperature is analyzed below, to enable the computations of P and COP expressions in the text.

I. Building Cooling Mode

According to Fig. 8(a), the coefficient of performance of the heat pump when operating during the sunny hours is given by:

$$COP_{s,c} = \eta_t \cdot P_c R_c E_{s,c} \tag{B-1}$$

Therefore, the procedure requires the maximization of only the product $R_c E_{s,c}$ with respect to the receiver fluid temperature T_f since the component efficients η_t, and P_c are independent of T_f. Note that the concentrator-receiver-efficiency R, is taken from Eq. (3) as

$$R = m_s - n_s \frac{(T_f - T_o)}{I} \tag{B-2}$$

where I is an hourly average solar intensity. The power cycle efficiency E, on the other hand, is simplified as a fraction of the corresponding Carnot's cycle when operating between the two temperature limits T_f as a heat source, and T_o as a heat sink. From Eq. (4),

$$E = \lambda_e \left(1 - \frac{T_o}{T_f}\right) \tag{B-3}$$

The maximum product RE, at the optimum fluid temperature T_f^*, is obtained by differentiation and by assuming m, n, T_o, I, and λ_e to be constants. The result is written as:

$$T_{f,c}^* = T_o \sqrt{1 + \frac{m_s I}{n_s T_o}} \tag{B-4}$$

A plot in Fig. B-1 of the quantities R, E, and RE versus T_f is also made for a selected numerical example. Figure B-1 illustrates that the maximum value of the product RE lies on a plateau and not on a sharp peak. For instance, the assigned values of $m_s = 0.722$, $n_s = 0.16$ W/m²°C, $\lambda_e = 0.5$, $t_o = 25.8$°C (299 K), and $I_c = 943$ W/m², yield an optimum temperature T_f^* of 893°C and an optimum RE product of 21.4%. Operating the receiver-engine at 800°C (1472°F) instead of 893°C will yield an RE product of only 21.3%, which is an insignificant loss in performance compared to other cost and metallurgical gains obtained by lowering the operating temperature.

II. Building Heating Mode

When operating during the sunny hours, the gross coefficient of the heat-pump waste-heat recovery system is obtained from Fig. 7(a) as

$$COP_h = \eta_w R_h + R_g E_{s,h} (P_h \eta_t - \eta_w) \tag{B-5}$$

Upon the substitution of R and E expressions from Eqs. (B-2) and (B-3), respectively, and assuming that the component efficiencies η_w, P_h and η_t are independent of T_f, an optimum operating fluid temperature $T_{f,h}^*$ could be obtained by differentiation. The result is expressed as

$$T_{f,h}^* = T_o \sqrt{\left(1 + \frac{m_s I}{n_s T_o}\right) / \theta} \tag{B-6}$$

where θ, is a coupling parameter larger than or equal to 1, given by

$$\theta = 1 + \frac{\eta_w}{\lambda_e (P_h \eta_t - \eta_w)} \qquad \text{(B-7)}$$

Without utilization of any portion of the engine rejected heat, the efficiency η_w is zero and the optimum temperature expression is reduced to Eq (B-4). However, since θ is $\geqslant 1$, the temperature $T^*_{f,h}$ will always be less than $T^*_{f,c}$, keeping other parameters the same. Similarly to COP_c, the trend of COP_h changes very slowly with the temperature T_f, with an almost flat plateau around the optimum point rather than a sharp peak. The above finding allows the designer to choose a lower operating temperature for material consideration without a great sacrifice of the system performance. Numerically, Fig. B-2 is plotted for the same concentrator-receiver design ($m_s = 0.722$, $n_s = 0.16$ W/m²°C) under the average conditions of the site's winter season (I_h = 880 W/m² $t_{o,h}$ = 11°C) together with the assumed component efficiencies ($\eta_t = 0.9$, $\eta_w = 0.8$, $\lambda_e = 0.5$, $P_h = 2.88$) or at $\theta = 1.893$. The optimum $T^*_{f,h}$ is found to be 525°C (977°F), resulting in a maximum COP_h of 0.864. At the selected receiver-engine operating temperature of 500°C, the gross COP_h becomes 0.863, which gives a negligible difference in performance.

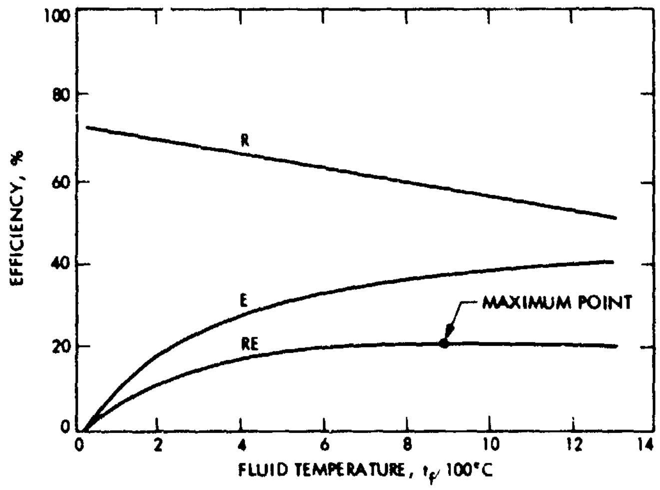

Fig. B-1. Optimum RE product in cooling mode

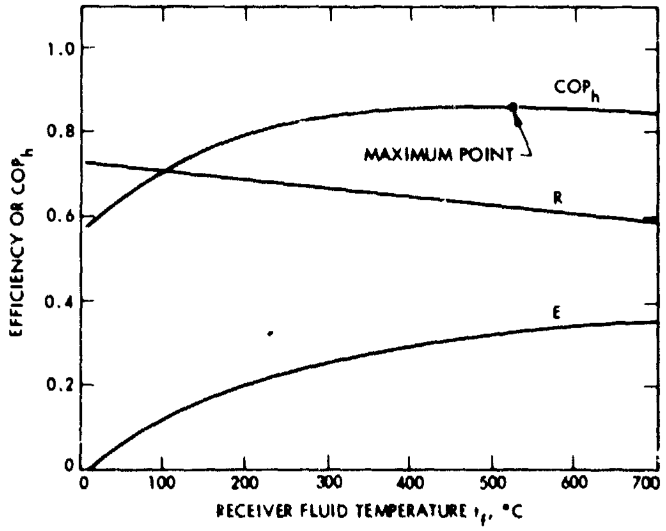

Fig. B-2. Optimization of the gross coefficient of performance during the solar-heating mode

Appendix C

Temperature Levels and Coefficient of Performance of Heat Pumps

Actual heat transfer in heat-pump components requires a temperature difference to transfer heat both from the heat source to the evaporating refrigerant and from the condensing refrigerant to the cooling fluid. Accordingly, the temperature span of the refrigeration cycle will increase over that cycle which is represented only by the heat-source and heat-sink temperatures. For each mode of operation, the temperature levels are here represented by empirical expressions in terms of source/sink temperatures instead of the graphical representation given in Ref. 16. For a direct comparison with the corresponding Carnot's refrigeration cycle, the procedure is discussed as follows.

I. Cooling Mode

The evaporator side temperature difference Δt_{ev}, as sketched in Fig. C-1, could be represented analytically by.

$$\Delta t_{ev} = 23.11 - 0.2\, t_o = t_i - t_{ev} \qquad \text{(C-1)}$$

hence

$$t_{ev} = t_i + 0.2\, t_o \quad 23.11 \qquad \text{(C-2)}$$

Similarly, the condensing side temperature difference, Δt_{co}, could be represented by:

$$\Delta t_{co} = 21.44 - 0.2\, t_o = t_{co} - t_o \qquad \text{(C-3)}$$

or

$$t_{co} = 21.44 + 0.8\, t_o \qquad \text{(C-4)}$$

An actual heat pump will be as efficient as roughly a fraction (between 40 to 60%) of the Carnot-cycle heat pump operating between T_{ev} and T_{co} (Ref. 16). If the fraction λ_c is approximated by the relationship, then

$$\lambda_c = 0.536 - 0.0058\, t_o \qquad \text{(C-5)}$$

The resulting coefficient of performance P_c will be given by:

$$P_c = \lambda_c \frac{T_{ev}}{T_{co} - T_{ev}}$$

or

$$P_c = (0.536 - 0.0058\, t_o) \frac{(t_i + 0.2\, t_o + 250.0)}{(0.6\, t_o - t_i + 44.55)} \qquad \text{(C-6)}$$

For instance, taking the inside and outside air temperatures of the office building during the cooling mode as $t_o = 25.83$°C (78.5°F), $t_i = 25.55$°C (78°F), then $t_{ev} = 7.61$°C (45.7°F), $\Delta t_{ev} = 17.9$°C (32.3°F), $\Delta t_{co} = 16.27$°C (29.3°F), $t_{co} = 42.1$°C (107.8°F), $\lambda_c = 0.5$, and the heat pump performance P_c from Eq. C-6 is found to be 3.14. Although heat pumps with different capacity and design features, differ in their performance, the above relationships are considered valuable not only for A-A heat pumps but for any other media in contact with the refrigerant coils.

II. Heating Mode

The new evaporator and condenser temperature levels in the heating mode will be as illustrated in Fig. C-2. The evaporator-side temperature difference Δt_{ev}, could be approximated by:

$$\Delta t_{ev} = t_o - t_{ev} = 9.29 + 0.21\, t_o \qquad \text{(C-7)}$$

hence,

$$t_{ev} = -9.29 + 0.21\, t_o \qquad \text{(C-8)}$$

Also, at the condenser side, the temperature difference Δt_{co} is obtained from:

$$\Delta t_{co} = t_{co} - t_i = 20.24 + 0.67\, t_o \qquad \text{(C-9)}$$

or

$$t_{co} = 20.24 + 0.67\, t_o + t_i \qquad \text{(C-10)}$$

An actual heat pump in the heating mode will be roughly as efficient as a fraction λ_h of the Carnot cycle heat pump operating between T_{ev} and T_{co}. The fraction λ_h is found close to a constant value of 0.45 and the resulting coefficient of performance P_h becomes

$$P_h = \lambda_h \frac{T_{co}}{T_{co} - T_{ev}} \tag{C-11}$$

or

$$P_h = 0.45 \frac{(293.4 + 0.67\, t_o + t_i)}{(29.53 + t_i - 0.12\, t_o)} \tag{C-12}$$

If, for instance, the space inside and outside temperatures t_i and t_o are 22.22°C (72°F) and 11°C (51.8°F), respectively, they result in a P_h value, using Eq. C-12, of 2.88. Both of the temperature differences Δt_{ev} and Δt_{co} then become 11.6°C (20.9°F) and 27.61°C (49.7°F), respectively. Equations C-6 and C-12 are used to determine monthly P_c and P_h values for each mode of operation as described in the text.

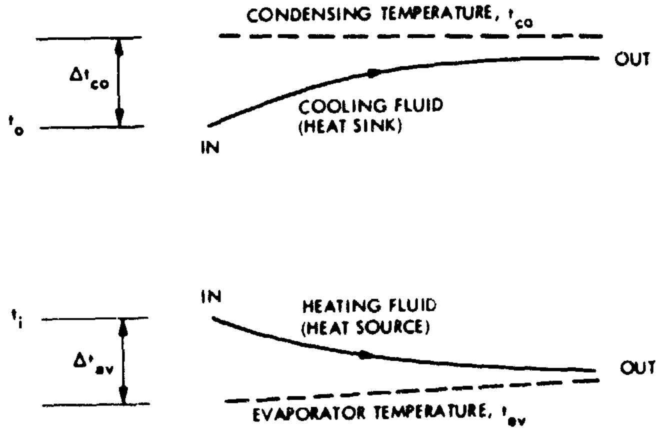

Fig. C-1. Temperature levels of a heat pump in a cooling mode

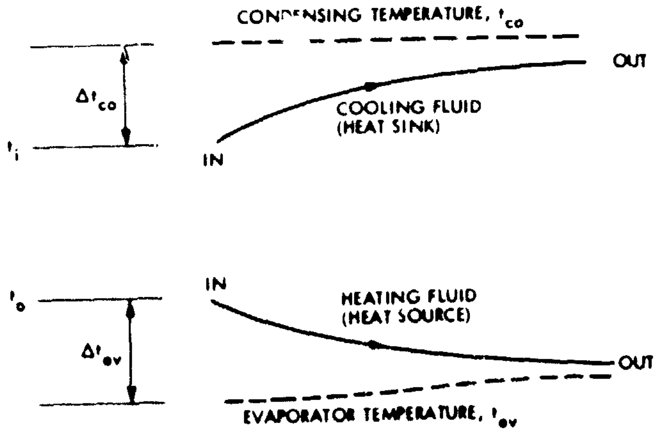

Fig. C-2. Temperature levels of a heat pump in a heating mode

N81-27146 D23

Performance of the Real-Time Array Signal Combiner During the Voyager Mission

C. D. Bartok
Control Center Operations

The technique of station arraying is used to improve the signal-to-noise ratio by reinforcing the coherent spacecraft signal while cancelling out location-dependent incoherent noise. The signal combiner provides a delay compensation that keeps the signals correctly phased throughout the spacecraft pass. The signals are combined to optimize the signal-to-noise ratio of the sum. The combined signal is then processed in the normal manner by the rest of the telemetry chain.

During the Voyager Mission each Deep Space Station used its 64-meter antenna together with a 34-meter antenna to form an array. Data were selected from the Saturn encounter period from November 2 to November 13, 1980, to analyze the signal combiner performance. A statistical analysis of the residual gain data from all of the arrayed Deep Space Stations indicates that the Real-Time Combiner is operating within the designed accuracy range of 0.2 ±0.05 dB around the theoretical gain. A decrease in the residual gain value appears to correlate with an increase in antenna elevation, which may be directly related to the changing antenna gain with elevation. Overall, the combined signal-to-noise ratio is improved by an average of 0.62 ±0.15 dB over the 64-meter signal-to-noise ratio alone.

I. Introduction

A spacecraft signal can be degraded in one of two ways. There can be loss of desired signal relative to noise, where a portion of the signal is diverted, scattered or reflected from its intended route, or there can be an increase of noise relative to the desired signal. Noise can originate as unwanted signal energy injected into the link, or as thermal noise generated within the link. There is a consistent level of degradation of the spacecraft signal from space loss, due to a decrease in the electric field as a function of distance and due to noise injection from the 3°K temperature of space, which is independent of the location of the receiving station. However, there are sources of loss and noise which are highly location-dependent. Some of these are atmospheric loss due to water vapor and oxygen, scintillation fades due to atmospheric multipath phenomena, terrestrial noise, line loss between antenna and receiver, and thermal noise generated within the receiver. Of all the sources described, the spacecraft signal is particularly susceptible to degradation from the last two since the signal is at its lowest energy level at these stages.

The fact that a spacecraft signal received simultaneously at several Deep Space Stations is affected by an independent noise contribution at each station is the significant factor that makes the technique of station arraying possible. An improvement in signal-to-noise ratio (SNR) is achieved by combining the outputs from various receiving locations in an appropriate manner to reinforce the coherent spacecraft signal while cancelling out incoherent noise from the stations. This involves compensating for phase delays at each station caused by differing spacecraft-to-station distances and by differing signal relay times to a common site.

II. Functional Description of the Signal Combiner

A simplified block diagram of the baseband signal combiner is illustrated in Fig. 1. The signal combiner provides a delay compensation that automatically tracks the changing signal delays to keep the signals correctly phased throughout the spacecraft pass. This variable delay compensates for the change in signal arrival time at the different antennas as the Earth rotates during the mission viewing period.

Once properly phased, the signals are combined in a weighted average depending upon their relative average SNRs. The weighting gain factors are chosen to optimize the SNR of the sum in a manner discussed in detail by R. A. Winkelstein (see Bibliography). The combined signal proceeds from the output of the Real-Time Combiner to the baseband input of the Subcarrier Demodulator Assembly (SDA). From there on, the signal is processed in the normal manner by the rest of the telemetry chain.

III. Operational Detail of the Signal Combiner

The heart of the signal combiner is the phase tracking channel. This is illustrated in Fig. 2. Its function is to provide a continuously variable amount of time delay to match the signals at the summing amplifier to the reference baseband signal. The values of the delays are determined by a central processing unit (CPU) controlled tracking loop.

The combiner input signals pass through essentially identical input amplifiers and are converted from analog to digital. For the reference channel the sign bit is switched onto a bus to be used by the correlator sections of the other channels. The baseband signals from each station are sampled by a multiplexed digital FIFO memory at approximately a 10-MHz rate.

The FIFO memory system consists mainly of the multiplexed FIFO and a fill counter. The memory holds digital samples which are input to the memory using the input strobe and output from the memory using the output strobe. The buffer output rate is determined by a fixed common clock line. The buffer input rate is governed by a separate variable clock, but the input strobes are independent of each other and are generated asynchronously with respect to the output clock.

The resident time of a particular sample in memory is the delay time. The length of time a sample remains in the buffer is a function of the number of samples in memory, as indicated by the fill counter, and the phase difference between the input and output strobes. Therefore, the time delay can be continuously adjusted by controlling the input clock frequency.

At the output of the FIFO, the delayed signals are correlated with the reference signal. When the signals agree in phase, the correlation is at its maximum. For each channel, the correlation of the reference signal with the input signal advanced by 90 degrees of phase and the correlation of the reference signal with the input signal retarded by 90 degrees of phase are developed. The difference of these two correlation curves, designated quadrature correlation, crosses zero when the input signal is aligned with the reference signal (see Fig. 3). Therefore, quadrature correlation is suitable as a control function for the delay on each channel of the tracking loop.

Each second the quadrature correlator produces a digital count, which is a function of the relative signal delay. The quadrature correlator count represents an integral of the input signal phase difference averaged over a time period of one second. The quadrature correlator should produce a count of zero when the input signals are exactly aligned. When they are not aligned, the count is proportional to the phase timing error between the signals.

The digital count is scaled by the CPU and converted to analog voltages by digital-to-analog converters. These voltages are applied to the input of the voltage-controlled oscillators (VCO's). The output frequency of the VCO produces a slight change in the FIFO input strobe rate, thus closing the control loop. As a result, the signal delay is changed in the direction to force the error count out of the quadrature correlator to zero.

At the output of the FIFO buffer, with the signals aligned in phase, the signals are reconverted to analog by a digital-to-analog converter. They are then weighted by gains calculated to optimize the SNR of the combined signal and applied to the input of the summing amplifier. Once combined, the signal flows through the telemetry processing chain in a normal manner.

IV. Voyager Mission Performance

During the Voyager Mission, each Deep Space Station used its 64-meter antenna together with a 34-meter antenna to form an array. The input signal from each 64-meter antenna became the reference baseband signal in the phase tracking channel of its respective combiner.

To analyze array performance, data were selected from the Saturn encounter period from November 2 to November 13, 1980. The design of the Real-Time Combiner specifies a signal degradation of no more than 0.2 ±0.05 dB from the theoretical combined gain. The actual gain data contains this system-induced degradation plus external coherent noise injection which is not cancelled out by the combining process, such as from space and atmospheric phenomena.

The 64- and 34-meter uncombined SNR averages are recorded for comparison with the combined array SNR averages. At optimal performance the combined SNR is maximized to a theoretical value of

$$SNR_s = SNR_{64} + SNR_{34}$$

$$= SNR_{64}\left(1 + \frac{SNR_{34}}{SNR_{64}}\right)$$

where

$$A_{th} = \left(1 + \frac{SNR_{34}}{SNR_{64}}\right)$$

is the theoretical gain over the uncombined 64-meter signal. The actual gain is calculated from the data:

$$A_c = SNR_s - SNR_{64} \text{ (SNRs in dB)}$$

and the residual difference is calculated.

$$Residual = A_{th} - A_c \text{ (gains in dB)}$$

It is these residual values that demonstrate the performance capabilities of the Real-Time Combiner.

The data from the Deep Space Stations are plotted as a function of antenna elevation in Figs. 4, 6 and 8. A decrease in the residual gain value appears to correlate with an increase in the antenna elevation. This is particularly evident during adverse weather conditions which degrade the input signal markedly. Under these circumstances the improvement to the residual gain is pronounced as the antenna dish tracks to higher elevations. The change in residual gain as a function of elevation may be primarily affected by the change in antenna gain as a function of elevation. The antenna gain vs elevation curves are included for the 64-meter antennas as Figs. 5, 7 and 9 for comparison.

Figure 10 illustrates the distribution of the residual gain data from all of the arrayed Deep Space Stations. The statistical mean of 0.22 dB falls within the theoretical accuracy range of 0.2 ±0.05 dB predicted for the Real-Time Combiner.

The residual gains are also averaged on a pass-by-pass basis. These data are plotted in Figs. 11 and 12. Figure 13 shows the distribution of the pass averages from the arrayed Deep Space Stations. The statistical mean of 0.205 dB again falls within the theoretical accuracy range as predicted.

V. Conclusion

The Real-Time Combiner has performed well during the Voyager Mission, as the data samples taken during the Saturn encounter indicate. The actual improvement in the signal-to-noise ratio of the combined signal is an average of 0.62 ±0.15 dB over the 64-meter signals alone. The Voyager Mission data have demonstrated that antenna arraying operates as designed, providing a clear improvement in telemetry performance.

On November 7, 1980, the Australian complex, under heavy cloud cover and falling snow, received the Saturn pictures depicted in Fig. 14. The clarity of the arrayed pictures compared to the unarrayed pictures is striking, particularly in the face of such adverse weather conditions. These pictures illustrate the performance extension achieved with array technology.

Bibliography

1. Layland, J. W., "Noisy Reference Effects on Multiple-Antenna Reception," in *The Deep Space Network Progress Report 42-25*, pp. 60-64, Jet Propulsion Laboratory, Pasadena, Calif., Feb. 15, 1975.
2. Wilck, H., "A Signal Combiner for Antenna Arraying," in *The Deep Space Network Progress Report 42-25*, pp. 111-117, Jet Propulsion Laboratory, Pasadena, Calif., Feb. 15, 1975.
3. Winkelstein, R. A., "Analysis of the Signal Combiner for Multiple Antenna Arraying," in *The Deep Space Network Progress Report 42-26*, pp. 102-118, Jet Propulsion Laboratory, Pasadena, Calif., April 15, 1975.

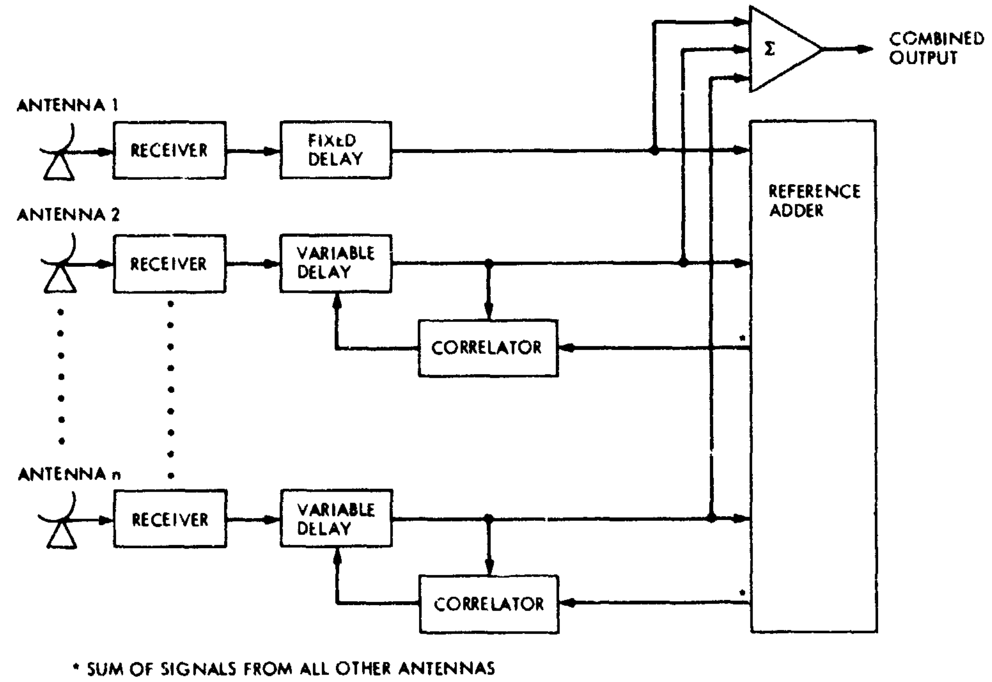

Fig. 1. Baseband signal combiner simplified block diagram

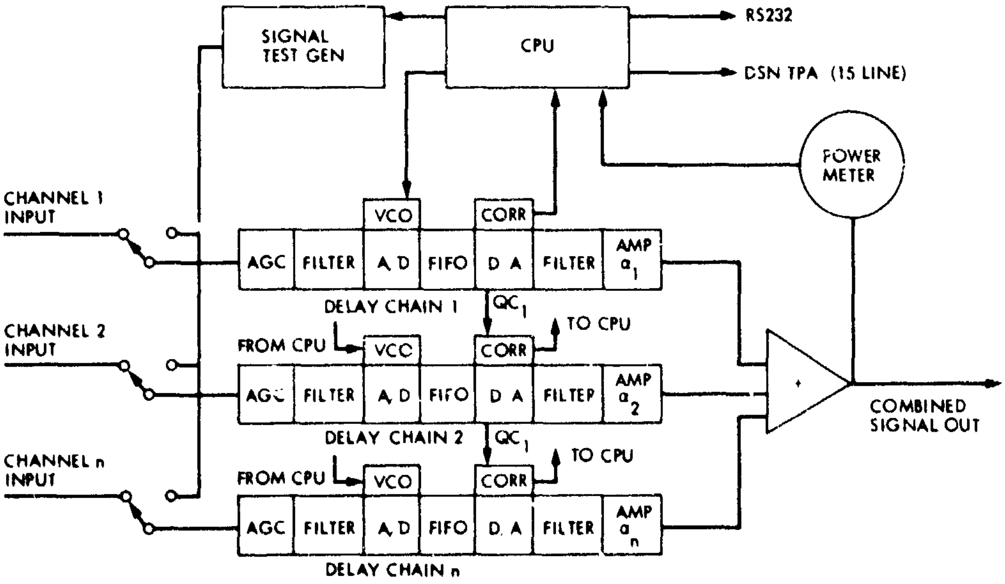

Fig. 2. RTA signal combiner block diagram

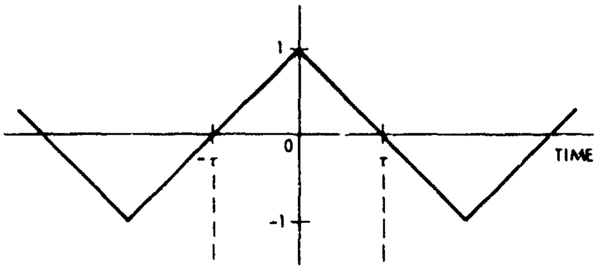

(a) SUBCARRIER IN PHASE WITH REFERENCE

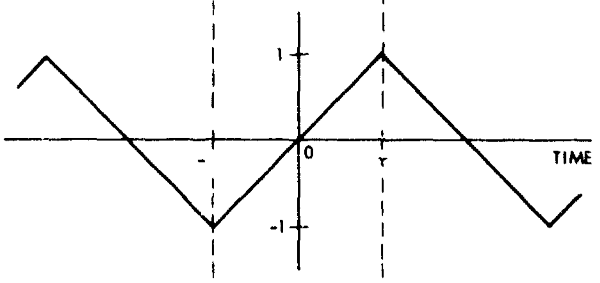

(b) SUBCARRIER ADVANCED BY 90 deg

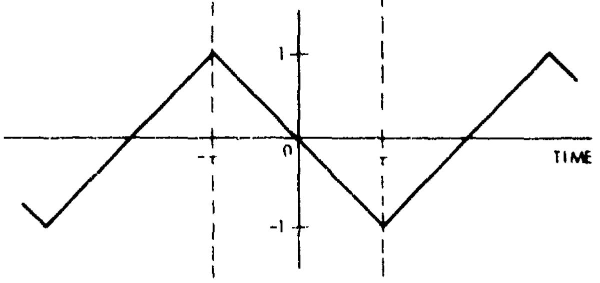

(c) SUBCARRIER RETARDED BY 90 deg

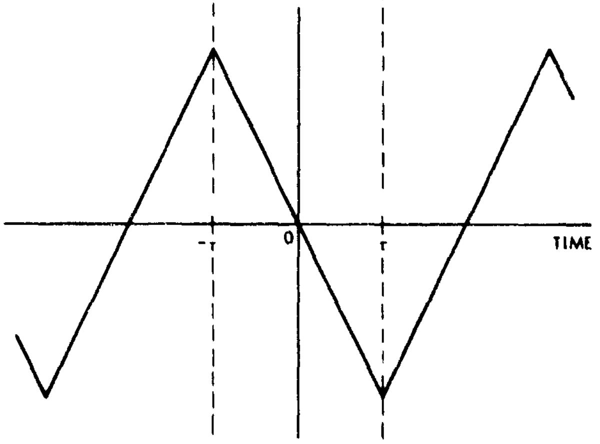

(d) QUADRATURE CORRELATION CURVE {(c) - (b)}

Fig. 3. Normalized correlation curves

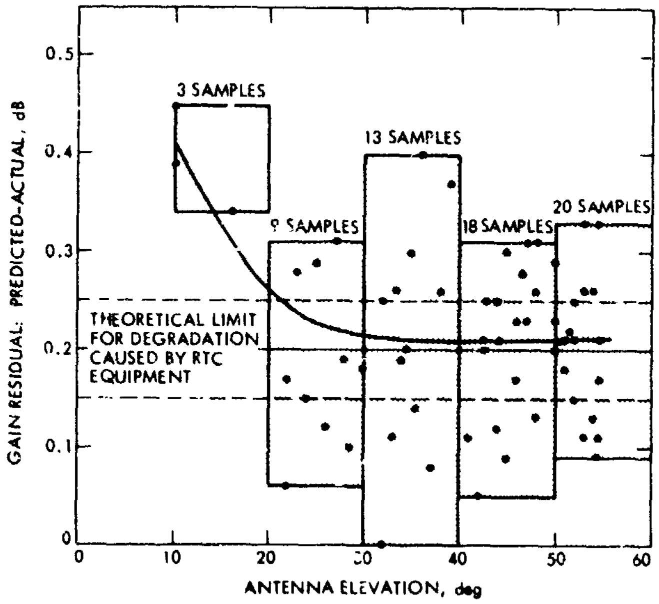

Fig. 4. Real-time combiner (44.8) hourly values, DSS 12/14 array, DOY 306-317

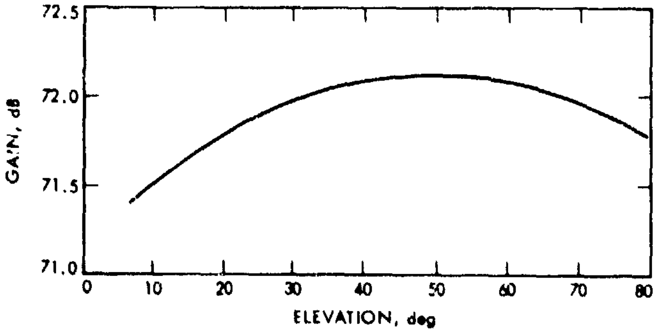

Fig. 5. Gain vs elevation, X-band, DSS 14

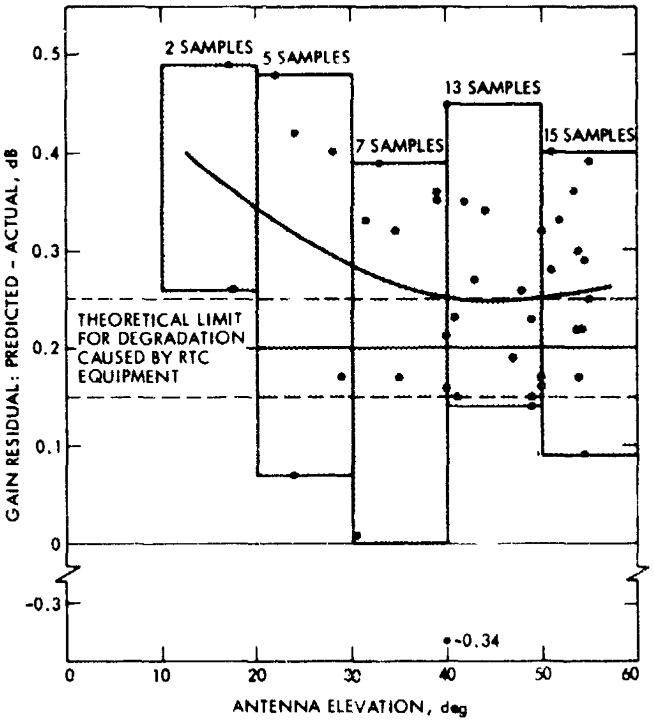

Fig. 6. Real-time combiner (44.8) hourly values, DSS 42/43 array, DOY 306–317

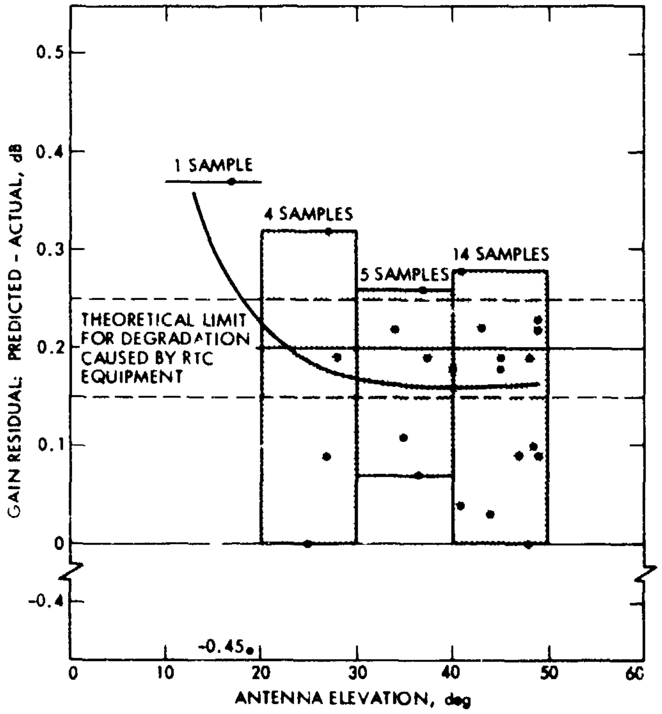

Fig. 8. Real-time combiner (44.8) hourly values, DSS 61/63 array, DOY 306–317

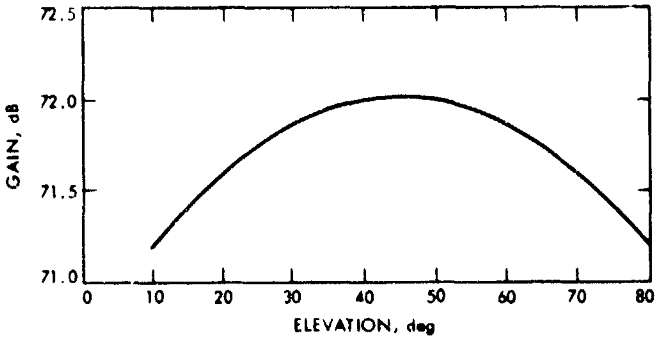

Fig. 7. Gain vs elevation, X-band, DSS 43

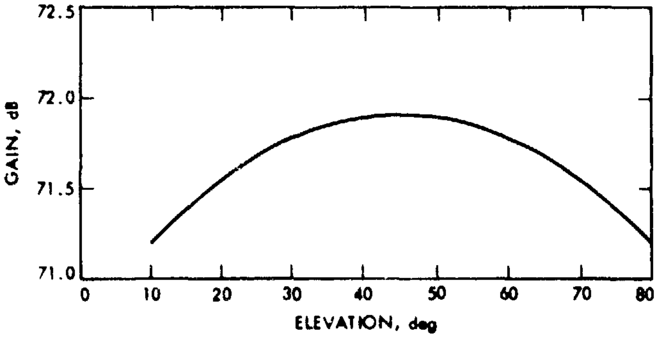

Fig. 9. Gain vs elevation, X-band, DSS 63

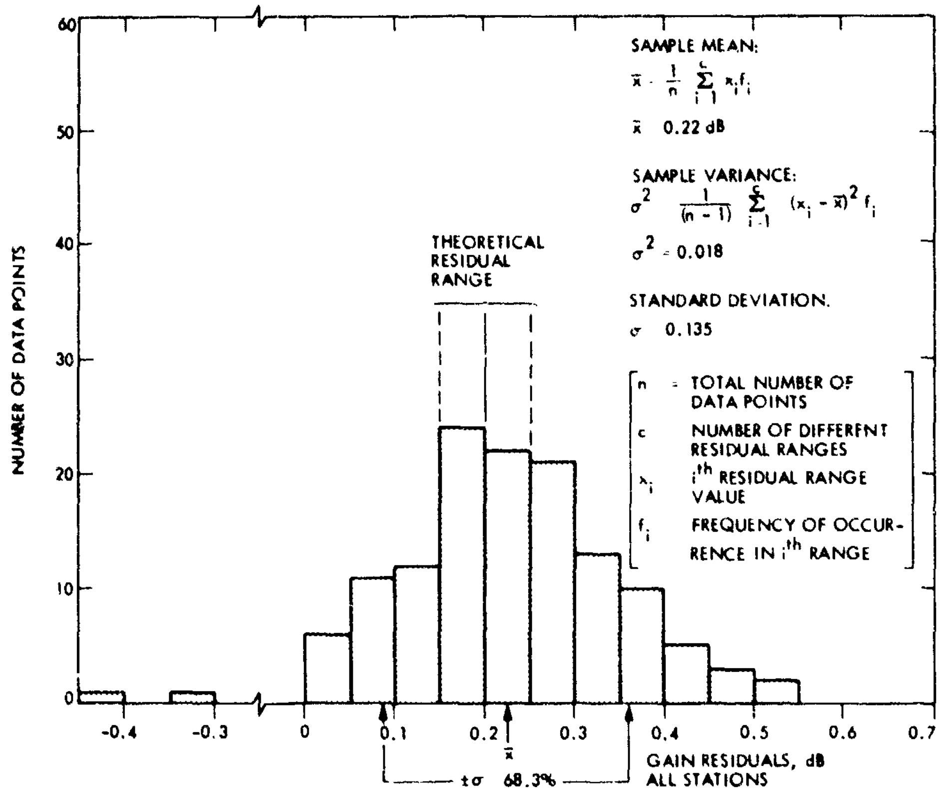

Fig. 10. Array data distribution

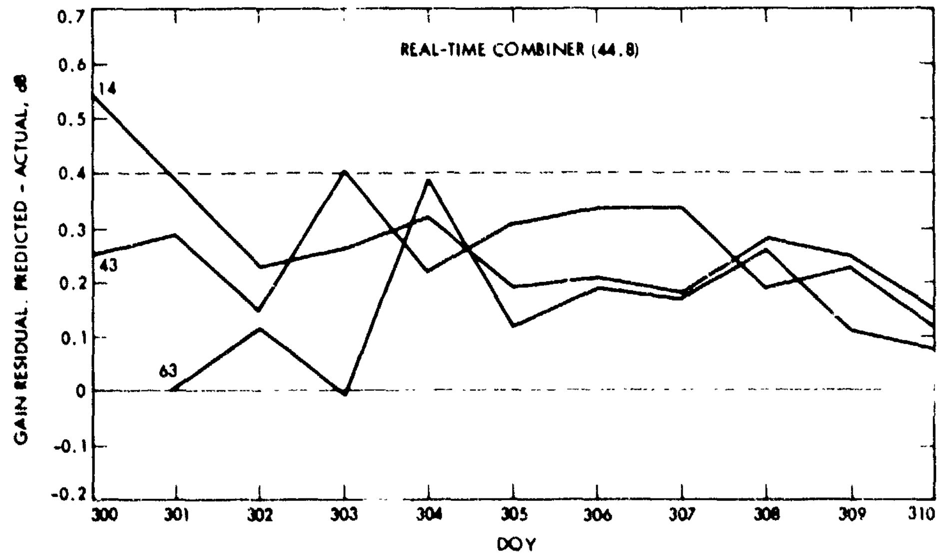

Fig. 11. Residual gain pass averages, DOY 300–310

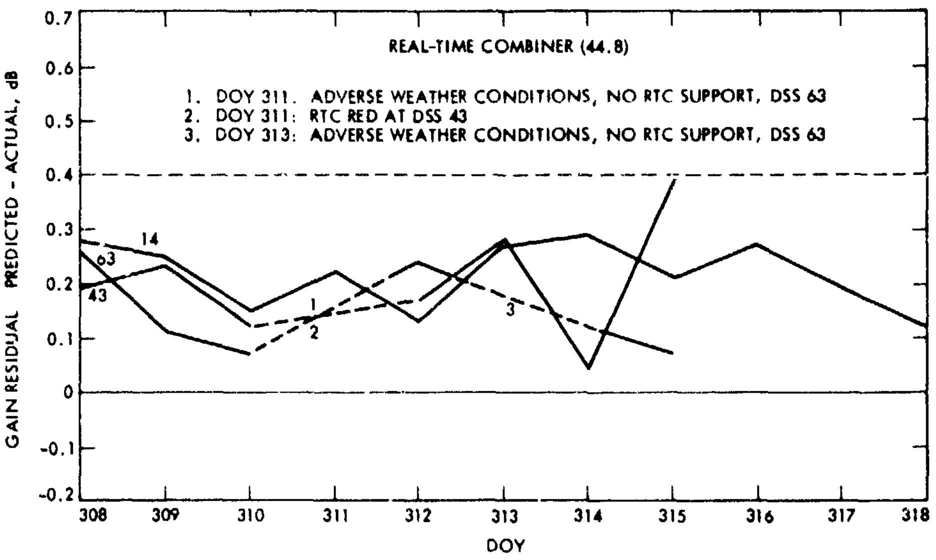

Fig. 12. Residual gain pass averages, DOY 308–318

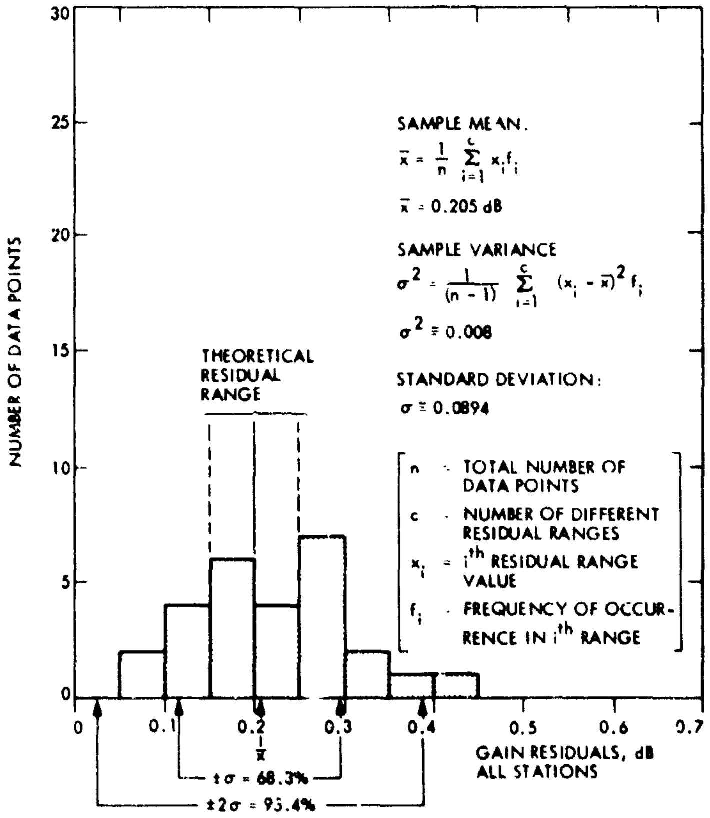

Fig. 13. Pass average data distribution

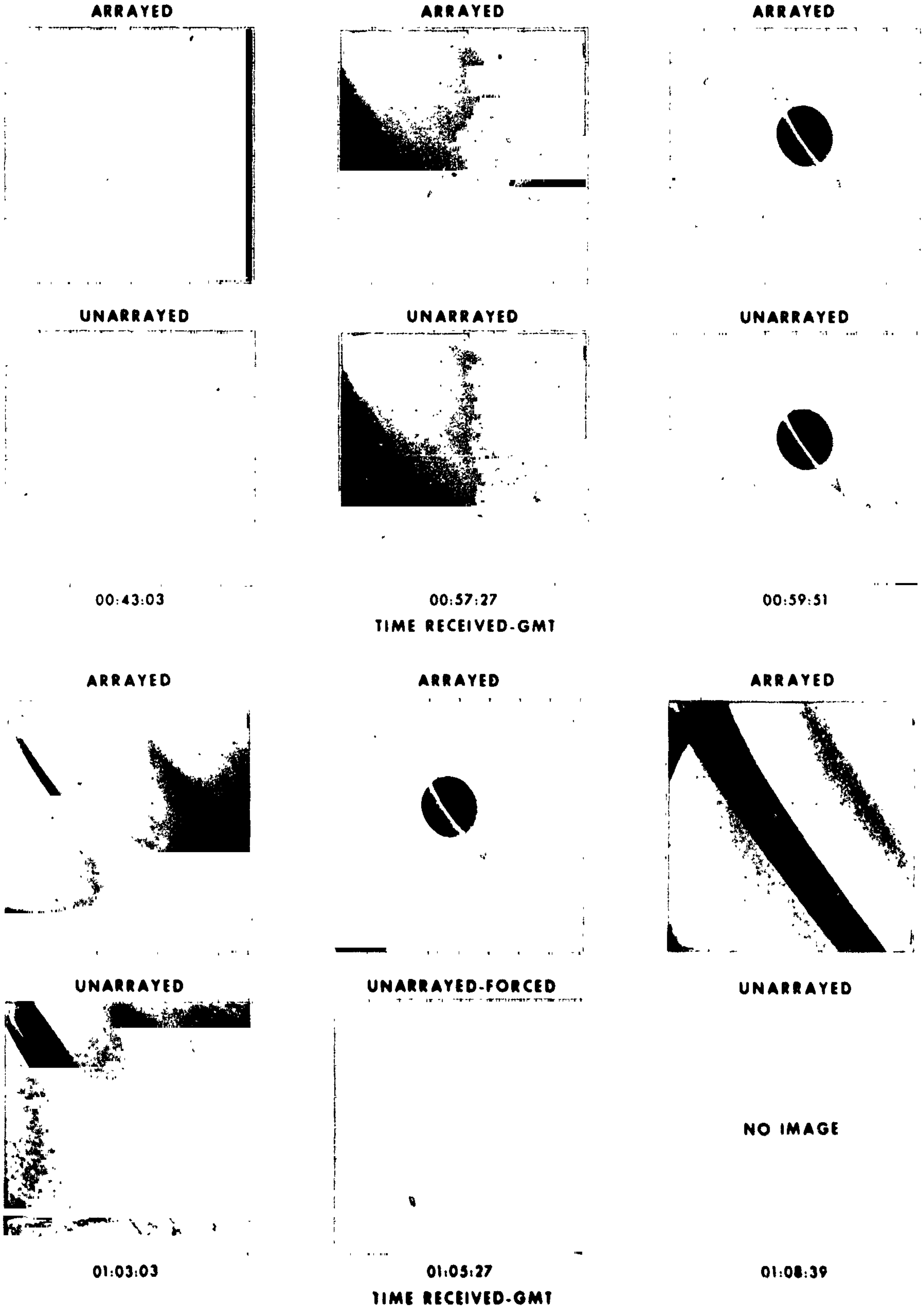

Fig. 14. Array performance—Voyager 1 Saturn encounter (Australian Complex, November 7, 1980)

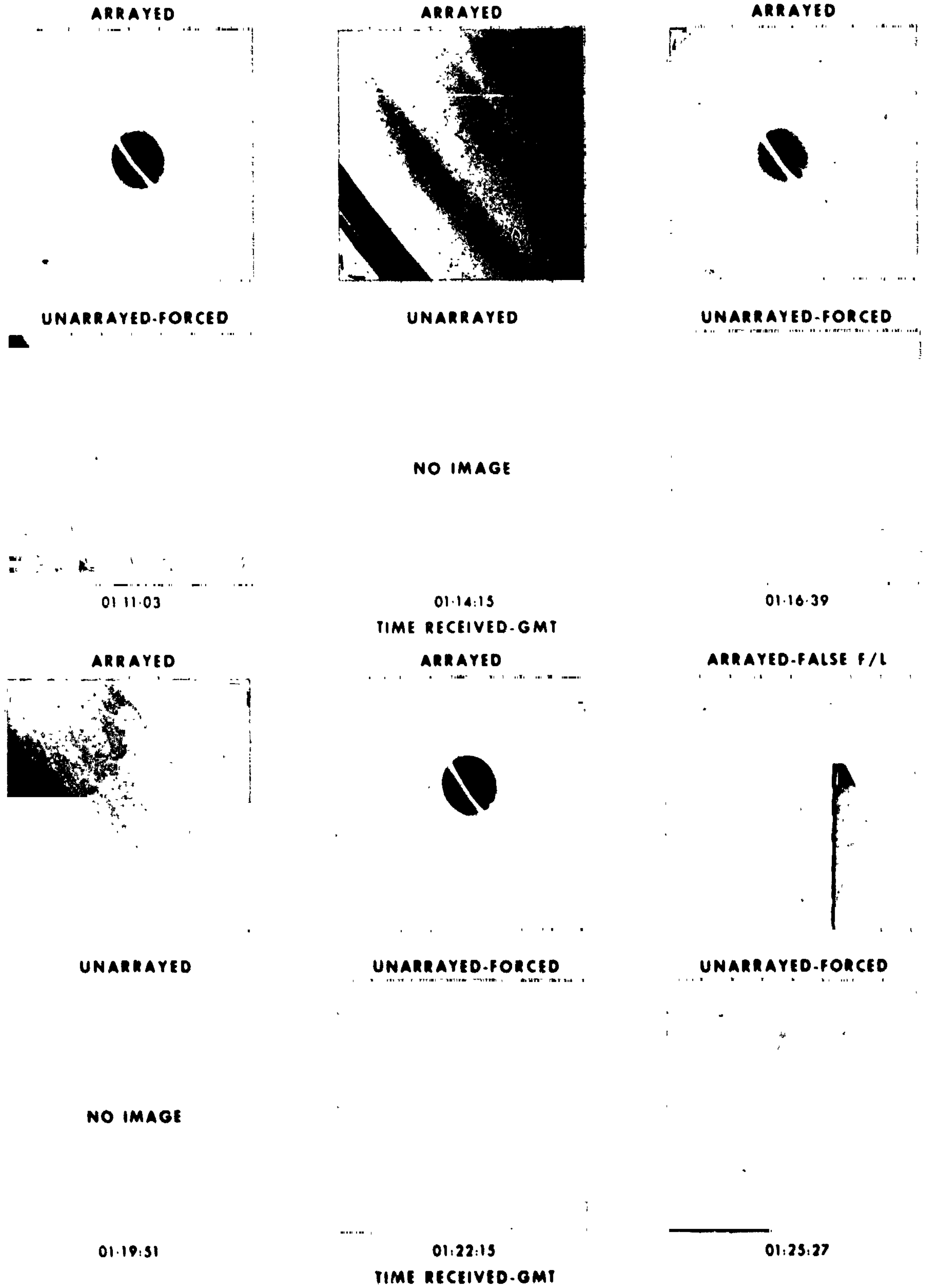
ARRAYED
ARRAYED
ARRAYED
UNARRAYED-FORCED
UNARRAYED
UNARRAYED-FORCED
NO IMAGE
01:11:03
01:14:15
01:16:39
TIME RECEIVED-GMT
ARRAYED
ARRAYED
ARRAYED-FALSE F/L
UNARRAYED
UNARRAYED-FORCED
UNARRAYED-FORCED
NO IMAGE
01:19:51
01:22:15
01:25:27
TIME RECEIVED-GMT

Fig. 14 (contd)

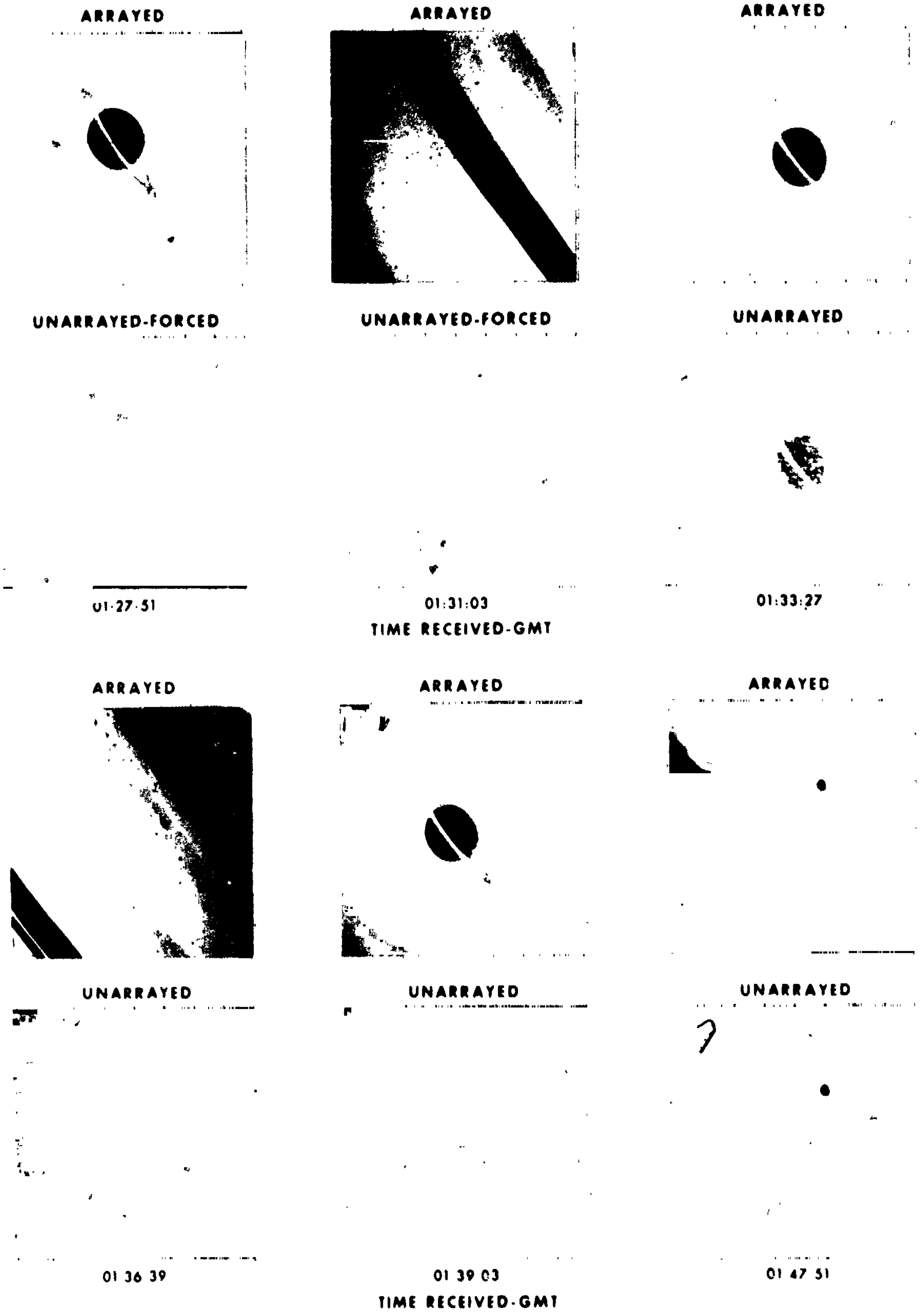
ARRAYED
UNARRAYED-FORCED
01:27:51
ARRAYED
UNARRAYED-FORCED
01:31:03
ARRAYED
UNARRAYED
01:33:27
TIME RECEIVED-GMT
ARRAYED
UNARRAYED
01 36 39
ARRAYED
UNARRAYED
01 39 03
ARRAYED
UNARRAYED
01 47 51
TIME RECEIVED-GMT

Fig. 14 (contd)

N81-27147 24

The Operational Performance of Hydrogen Masers in the Deep Space Network (The Performance of Laboratory Reference Frequency Standards in an Operational Environment)

S. C. Ward
Deep Space Network Support Section

Spacecraft navigation to the outer planets (Jupiter and beyond) places very stringent demands upon the performance of frequency and time (F&T) reference standards. The Deep Space Network (DSN) makes use of hydrogen masers as an aid in meeting the routine F&T operational requirements within the 64-m antenna network. Results as of October 1980 indicate the hydrogen masers are performing within the required specifications. However, two problem areas remain that affect operations performance: (1) there is insufficient control over the environment in which the reference standards reside and, (2) frequency drift makes it very difficult to maintain the 64-m-DSS-to-64-m-DSS synt over the 130-day period required by the flight project.

I. Introduction

The "laboratory standards" are three hydrogen masers (Smithsonian Astrophysical Observatory (SAO) Model VLG10B) and six cesium oscillators (Hewlett-Packard Model 5061A-004 option). The "operational environment" is an isolated temperature controlled room at each of three NASA/JPL Deep Space Network (DSN) complexes.

This Precision Time and Time Interval (PTTI) application is in support of refined spacecraft navigation to the outer planets (Jupiter and beyond) and to provide wideband (> 100 kilobits) telecommunications channels at S- and X-band. The Voyager project Navigation team guides the spacecraft to Jupiter, Saturn, Uranus, and perhaps Neptune. The Telemetry and Image Processing teams have brought us the beautiful full-color pictures of the planets and their satellites. Last, the Radio Science team uses spectral analysis to detect and measure the constituents of planetary atmospheres, orbital rings, and gravimetrics

II. Requirements and Specifications

Because the Voyager project requirements are currently the most stringent, they have been the dominant force in the design of the Frequency and Time System (FTS). The requirements are: (1) the fine-spectral performance of and long-term stability of the hydrogen maser, (2) the accuracy and reliability of the cesium oscillators, and (3) some means of synchronizing the intercontinental network of tracking stations.

The specifications relating to a typical frequency and timing system using hydrogen masers and cesium oscillators are listed in the Precision Time and Time Interval (PTTI) literature and manufacturers specifications, and will not be dealt with further in this article. I will instead address the very stringent requirements for syntonization and synchronization.

A. Syntonization Requirements

(1) The frequency offset between any pair of 64-m Deep Space Stations (DSS) shall be known to within less than $\pm 3 \times 10^{-13}$, such as DSS 63 (Madrid, Spain) vs DSS 43 (Canberra, Australia) = $< \pm 3 \times 10^{-13}$, or DSS 63 vs DSS 14 (Goldstone, California) = $< \pm 3 \times 10^{-13}$, or DSS 63 vs DSS 14 = $< \pm 3 \times 10^{-13}$.

(2) The frequency offset of the DSN master (DSS 14) shall be maintained within $\pm 3 \times 10^{-13}$ of Universal Time, Coordinated (UTC), kept by the National Bureau of Standards (NBS).

B. Synchronization Requirements

(1) The time offset between any pair of 64-m DSSs shall be known within ±20 μs.

(2) The time offset of any 64-m DSS from UTC shall be known within ±20 μs and, further, it shall actually be maintained to within < ±50 μs over the 130-day period August 4 through December 12, 1980.

III. Methodology

Both the synchronization (sync) and syntonization (synt) were established through use of a specially calibrated 5061A-001-004 portable unit.[1] For purposes of maintaining the individual DSS synchronization to UTC, the portable unit was carried to the host country frequency and time metrology agency. The sync/synt tool used by the San Fernando Observatory (SFO) in Spain is the Mediterranean chain LORAN-C. In Australia, the responsible agency is the Department of National Mapping and the frequency and time (F&T) maintenance resource is ABC television (see Fig. 1). In America, at Goldstone, California, regular 60-day traveling clock flights to NBS in Boulder, Colorado, and daily VLF transmissions from the NBS are used, in addition to LORAN-C and traveling clocks from other agencies (Goddard Space Flight Center and the U.S. Naval Observatory (USNO). The DSS-to-DSS synchronization and syntonization is being maintained through the use of Very Long Base Interferometry (VLBI). Some of the results are reported in Ref. 1. Figure 2 illustrates how the DSS-to-DSS and the DSN-to-UTC synchronization is maintained.

Each 64-m DSS has been delegated the responsibility of maintaining its own internal synchronization. Figure 3 illustrates the hardware configuration and data flow paths that achieve this. In addition, it is responsible for establishing and maintaining the synchronism of other DSSs within the complex (see the detail in the upper and lower right segments of Fig. 2).

IV. Test Results

A. Environmental Tests

Table 1 lists the results of environmental tests performed on five of the six 5061A cesium oscillators presently deployed within the DSN. These tests were performed at the Reference Standards Test Facility in Pasadena. Note that serial No. 1718 in its response to temperature variations differed from the others. When this unit was sent to the Goldstone Reference Standards Laboratory for zeeman calibration, it exhibited phase glitches. It was returned to Pasadena for further environmental testing.

Table 2 lists the results of environmental tests performed on the three hydrogen masers presently deployed within the DSN. Figure 4 illustrates the behavior of hydrogen-maser SAO serial No. 6 in a changing pressure environment. Note the improvement (8.2 dB) in its performance after being refurbished (Table 2, column 6).

Figure 5 illustrates the performance of SAO serial No. 7 in a changing magnetic environment. Having been given erroneous information on how far the 26-m antenna was from the planned site for the frequency standards room, it was decided that no further magnetic shielding would be required. SAO serial No. 6 failed in spring 1980 and was returned to the manufacturer for refurbishment. Table 2, column 5 indicates a 2.7-dB degradation to its performance in a changing magnetic environment.

Figure 6 illustrates the performance typical of a hydrogen maser in a high-temperature environment. The hydrogen maser is JPL serial No. 1 and the environment was an unventilated

---

[1] After allowing 24 hours for the portable 5061A to stabilize to its temperature and magnetic environment, the unit was degaussed and a measurement was made of the zeeman frequency vs frequency offset of the unit references to the DSN master. Using a digital frequency synthesizer and a differential voltmeter, the zeeman frequency readings were reproducible within 0.7 Hz. The portable unit was then carried to the remote DSS to be syntonized. Here again the unit was given 24 hours to stabilize, was degaussed and the zeeman frequency was measured. If the zeeman changed by more than 1.4 Hz it was reset. Otherwise a correction factor of 8.3×10^{-15}/Hz and 1×10^{-13}/°C was applied to the syntonization.

room in the cellar of DSS 43. The high temperatures caused the unit to fail in late summer (southern hemisphere). An air conditioner with 0.1°C temperature control was installed in early September 1980.

B. Stability Tests

Figure 7 illustrates the short-term stability (spectral performance) of a typical 5061A-004 cesium oscillator and a typical hydrogen maser. These measurements were made in Spain at DSS 63 where the Complex Maintenance Facility (CMF) was close enough to permit use of a coaxial cable from the hydrogen maser. Cesium oscillator serial No. 1511 was the portable unit and it was carried to the CMF facility.

Figures 8a and 8b (from Ref. 2) give the stability performance characteristics of the three hydrogen masers presently deployed. Figure 9 illustrates the stability characteristics of a recent series (serial Nos. 1718 and 1719) of 5061A-004 cesium oscillators.

V. Synchronization and Syntonization Data

A. Epoch Synchronization

Prior to departure for the trip to Spain, the portable clock designated RSL-2 was used to synchronize itself and the DSN master clock at DSS 14 to within 0.2 μs of the NBS and USNO epoch. It was then transported to DSS 63 at Robledo, Spain, then on to the SFO at San Fernando, Spain. One day prior to leaving Spain, the clock was transported to DSS 62 at Cebreros and the Madrid STDN station. Thus the three stations in the Madrid complex were synchronized to SFO and the DSN master to less than one μs.

Upon returning to America, the clock was immediately taken to Goldstone for closure against the DSN master. It then was taken to Australia where it was used to synchronize DSS 43 at Tidbinbilla, and then to the Department of National Mapping (DNM) installation in the Orroral Valley. On the day prior to leaving Australia, the portable clock was used to synchronize DSS 44 (Honeysuckle Creek) and Orroral (the STDN station) to the DNM, DSS 43, and the DSN.

The RSL-2 was then returned to America where closure was refined against both NBS and USNO. All the elements and agencies synchronized on these trips remain synchronized to within less than 1 μs, and are being maintained within 10 μs peak to peak.

B. Syntonization[2]

Each time the calibration process was performed, 24 hours was allowed for thermal stabilization and then 80 hours (ten 8-hour samples) of comparative phase data were collected. This was performed with instrumentation configured as that in Figure 3, except that a fourth phase comparator was added to permit the intercomparison of the hydrogen maser, cesium oscillator Nos. 1 and 2, and the portable cesium oscillator (RSL-2).

At DSS 63, after settling from the trauma of the trip and after thermal stabilization, the zeeman frequency of RSL-2 had shifted but 1.7 Hz. A C-field adjustment removed approximately one-half of the zeeman offset and the calibration process of the hydrogen maser began. At the end of the 88-hour calibration period, the hydrogen maser frequency offset from the DSN master was found to be zero $\pm 5 \times 10^{-14}$ instrumentation noise. It was thus unnecessary to make any adjustment to the hydrogen maser. It was, however, necessary to adjust both cesium oscillator Nos. 1 and 2. Data collected via LORAN-C indicate the frequency offset of the hydrogen maser and cesium oscillator No. 2 remain at zero $\pm 4.8 \times 10^{-13}$ as of November 8, 1980.

At DSS 43, the thermal stabilization period was extended to allow for the lack of good circulation (the air-handler installation was still in process). Also, the hydrogen maser had been installed just a few weeks and was still drifting. At the end of an 80-hour calibration period, the offset of the maser from the DSN master was 4.73×10^{-13}. Since this was beyond the Voyager specification, and since the drift was in a positive direction, the hydrogen maser synthesizer was reset to reduce its frequency by 6.345×10^{-13}. Frequency offset data of this maser vs UTC (Australia) (AUS) collected using simultaneous TV with the DNM indicate its drift has cancelled the value reset on September 30. Close examination of recent data indicate the second-order drift term has dropped from 4.6×10^{-14}/day to 2.1×10^{-14} to 0.7×10^{-14}/day.

All indications are that the frequency drift of SAO No. 5, the DSN master, has dropped well below its former value of 1×10^{-14}/day as observed between the departure for Spain and the return for closure. At present, SAO No. 5 vs UTC (NBS) = $-2.84 \times 10^{-13} \pm 0.3$ as verified by two closures against UTC(NBS) within a 21-day period. Figure 10 gives time offset data vs UTC(DSN) and associated frequency offset data for each of three 64-m DSSs. Figure 11 gives time offset data vs UTC(NBS and USNO) and the associated frequency offset data vs UTC(NBS) of the DSN master reference.

---

[2] Events occurring subsequent to the end of the Voyager 1 encounter period have provided additional performance data (see Appendix).

VI. Summary

(1) Hydrogen masers require 4 to 6 weeks of thermal stabilization before their long-term stability can be fully utilized.

(2) To use the full potential of present day hydrogen masers and cesium reference frequency standards, care must be exercised to provide a thermally stabilized and magnetically isolated environment.

(3) Syntonization to UTC can be accurately and economically maintained within a part in 10^{13} (after 1 week of daily observations) through use of the simultaneous reception of LORAN-C or TV transmissions by the DSS and the host country frequency and time metrology service agency.

References

1. Madrid, G. A., et al., "Short Turn-Around Intercontinental Clock Synchronization Using Very Long Baseline Interferometry - A Progress Report," in *Proceedings of the 12th Annual Precise Time and Time Interval Applications and Planning Meeting*, pp. 445-449. Goddard Spaceflight Center, Greenbelt, Md.
2. Kuhnle, P. F., "Hydrogen Maser Implementation in the Deep Space Network at the Jet Propulsion Laboratory," in *Proceedings of the 11th Annual Precise Time and Time Interval Applications and Planning Meeting*, November 27, 1979. Goddard Spaceflight Center, Greenbelt, Md.
3. U.S. Naval Observatory, *Report of Precise Time Measurement* 1/14/81 FTS 411 clock located DSSs 61 and 63, Madrid, Spain. Date and time of measurement: 1980 Dec. 11, 1450 UT, MJD 44584 measurement UTC(USNO MC)-UTC(FTS 411) = 0.8 ±0.2 μs.
4. U.S. Naval Observatory, *Report of Precise Time Measurement* 2/10/81 STA/HYM2 located DSSs 42 and 43, Tidbinbilla, Australia. Date and time of measurement: 1981 Jan. 6, 0026 UT, MJD 44610 measurement UTC(USNO MC)-UTC(STA HYM2) = 1.7 ± 0.2 μs.

Table 1. Cesium oscillator environmental parameters test data

Parameter	Hewlett-Packard 5061-A 004				
	No. 1694	No. 1695	No. 1717	No. 1718	No 1719
Temperature, $\frac{\Delta F}{F}$/°C	4.3×10^{-14}	6.25×10^{-14}	5.4×10^{-14}	1.2×10^{-13} to -2×10^{-13}	5.6×10^{-14}
Barometric pressure, $\frac{\Delta F}{F}$/in. Hg	1×10^{-13}	1×10^{-13}	1×10^{-13}	1×10^{-13}	1×10^{-13}
Magnetic field,[a] $\Delta F/F/10^4$ Wb/m^2	1×10^{-13}	1×10^{-13}	1×10^{-13}	1×10^{-13}	1×10^{-13}

[a] 1 gauss = 10^4 Wb/m^2

Table 2. Hydrogen-maser environmental parameters test data

Parameter	SAO 5	SAO 6	SAO 7	SAO 5	SAO 6
				(After refurbishment by mfr.)	
Temperature, $\frac{\Delta F}{F}$/°C	1.6×10^{-14}	1×10^{-13}	7.0×10^{-14}	-1.2×10^{-13}	7.2×10^{-14}
Barometric pressure, $\frac{\Delta F}{F}$/in. Hg	2.6×10^{-14}	-3.4×10^{-13}	2.3×10^{-14}	2.5×10^{-14}	-5.1×10^{-14}
Magnetic Field,[a] $\Delta F/F/10^4$ Wb/m^2	1.6×10^{-12}	5.0×10^{-12}	2.8×10^{-14}	3.0×10^{-12}	3.4×10^{-12}

[a] 1 gauss = 10^4 Wb/m^2

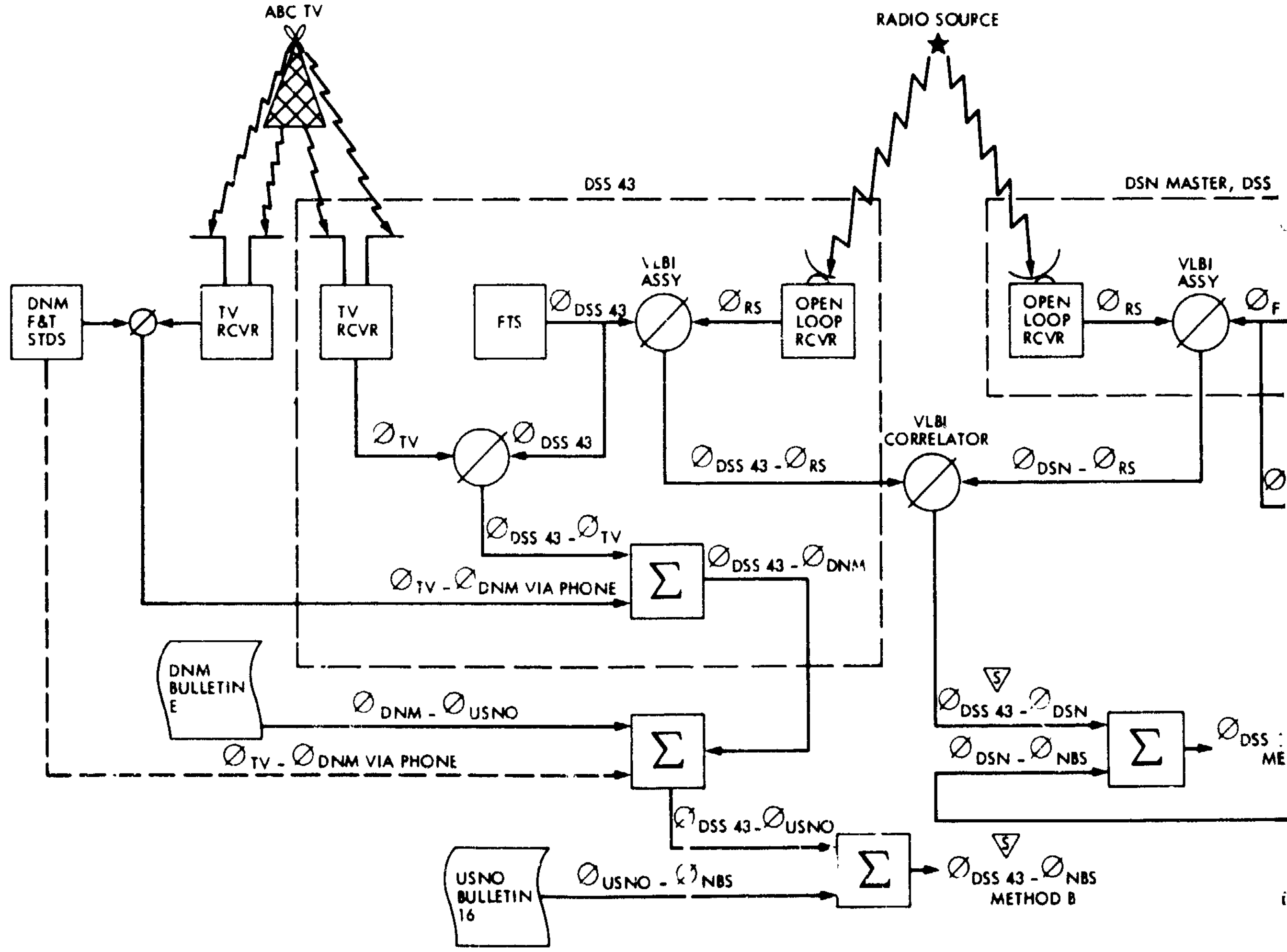

PRECEDING PAGE BLANK NOT FILMED

FOLDOUT FRAME 1

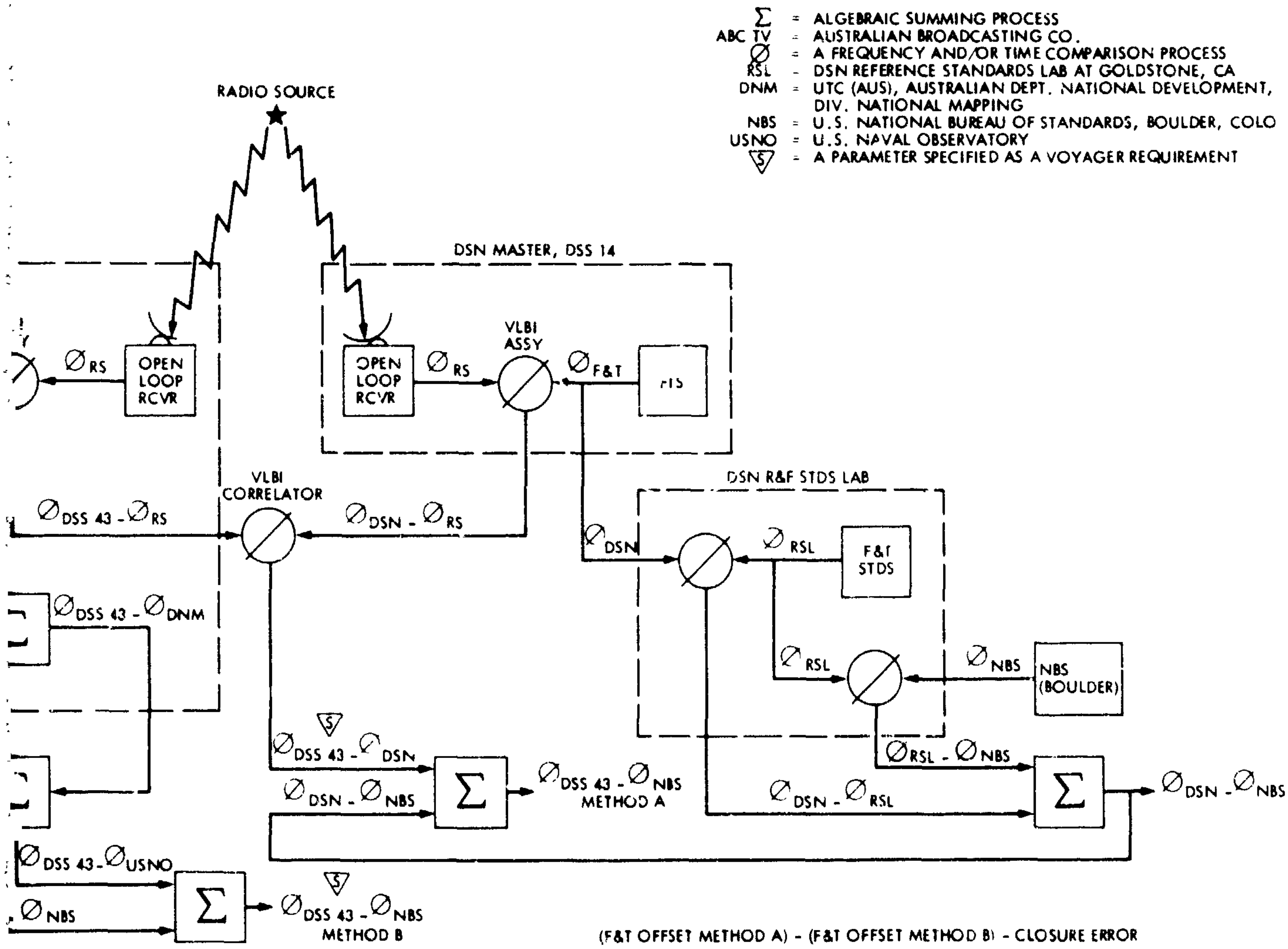

Σ = ALGEBRAIC SUMMING PROCESS
ABC TV = AUSTRALIAN BROADCASTING CO.
Ø = A FREQUENCY AND/OR TIME COMPARISON PROCESS
RSL - DSN REFERENCE STANDARDS LAB AT GOLDSTONE, CA
DNM = UTC (AUS), AUSTRALIAN DEPT. NATIONAL DEVELOPMENT, DIV. NATIONAL MAPPING
NBS = U.S. NATIONAL BUREAU OF STANDARDS, BOULDER, COLO
USNO = U.S. NAVAL OBSERVATORY
S = A PARAMETER SPECIFIED AS A VOYAGER REQUIREMENT

(F&T OFFSET METHOD A) - (F&T OFFSET METHOD B) - CLOSURE ERROR

Fig. 1. UTC (DSN) – UTC (NBS) vs UTC (DSN) – UTC (USNO) via UTC (Australia)

FOLDOUT FRAME 2

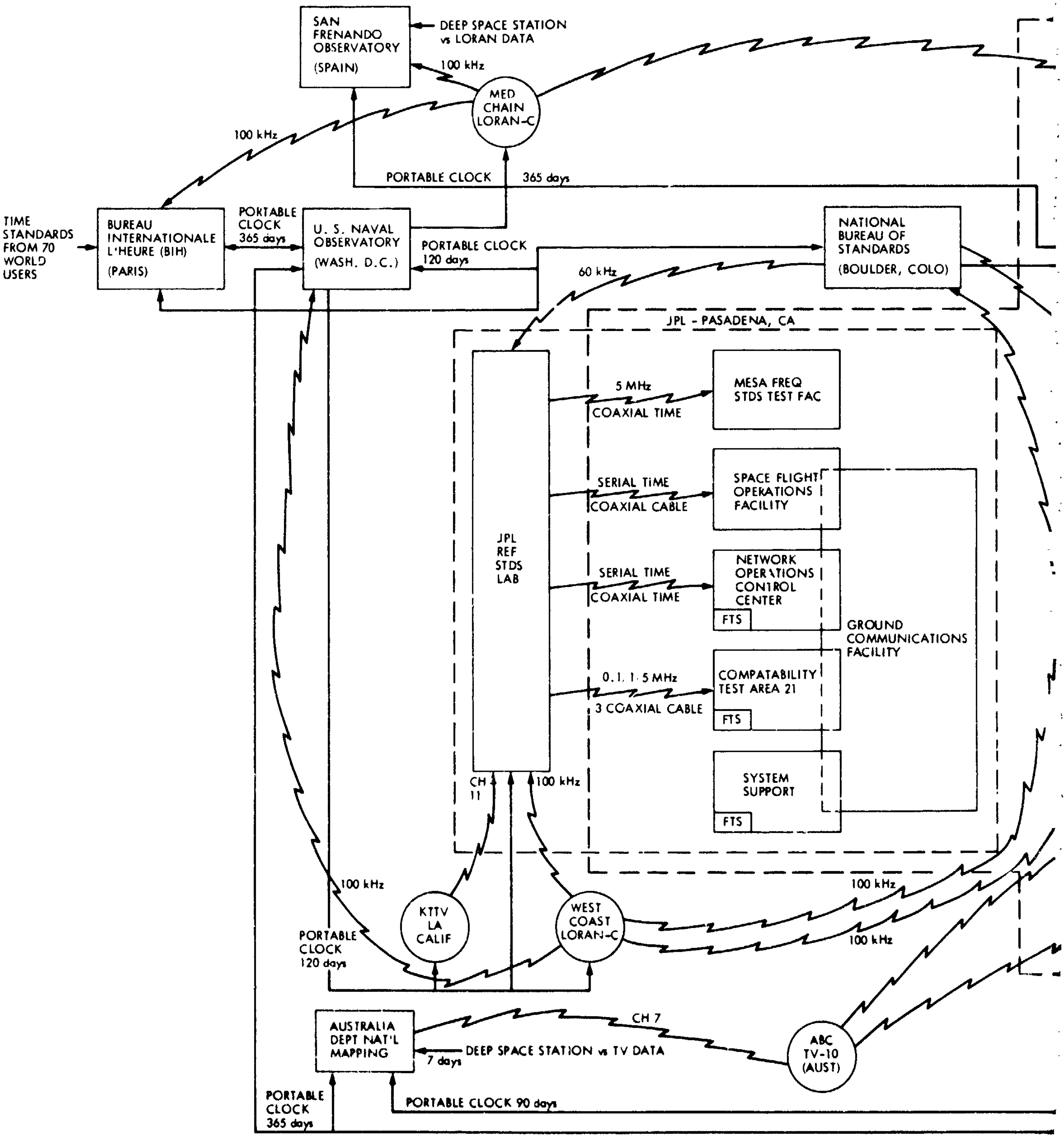

Fig. 2. NASA/JPL Intra/Extra DSN Frequency and Time Sync System

FOLDOUT FRAME 1

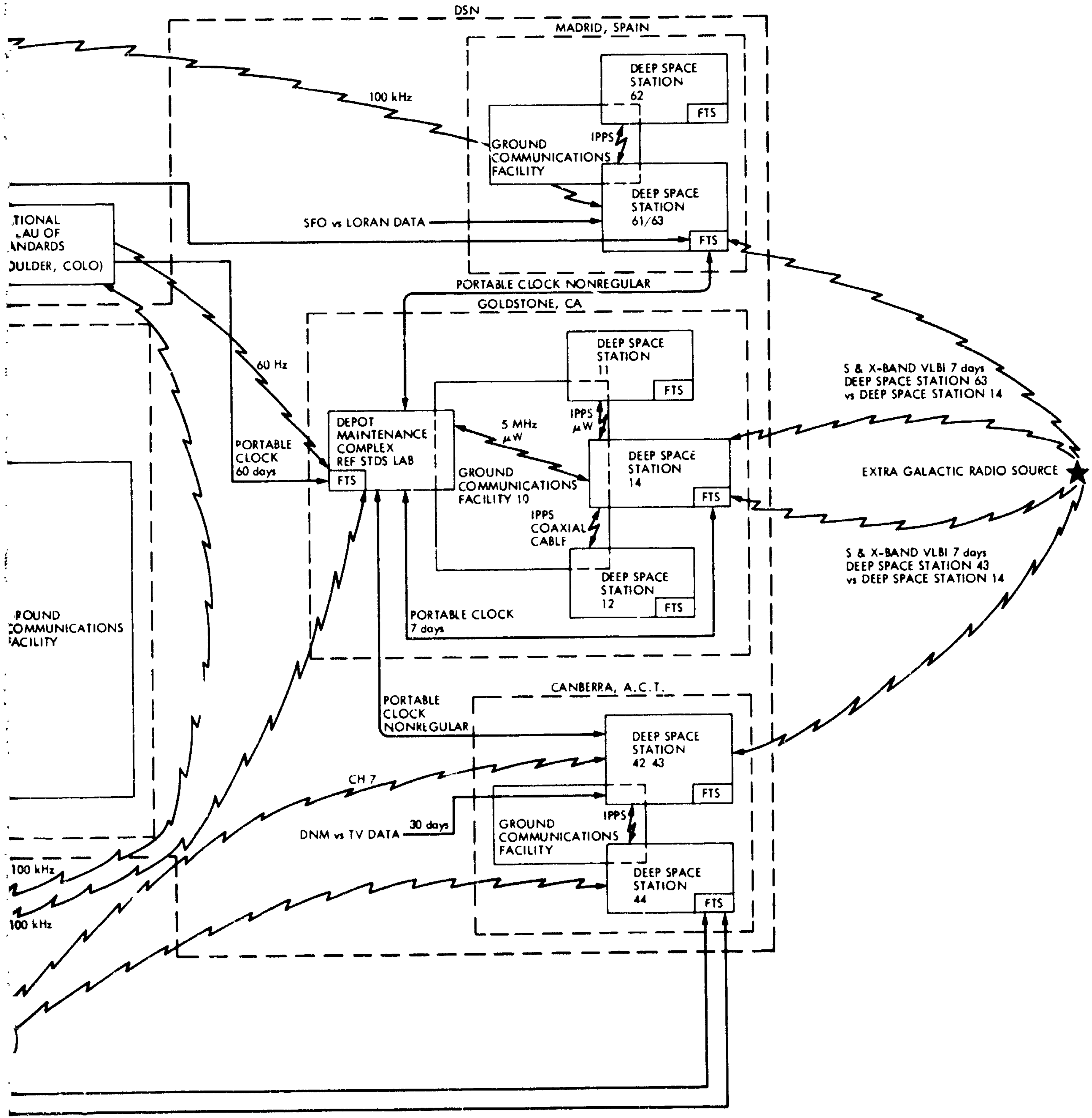
DSN
MADRID, SPAIN
100 kHz
DEEP SPACE STATION 62
FTS
IPPS
GROUND COMMUNICATIONS FACILITY
DEEP SPACE STATION 61/63
SFO vs LORAN DATA
FTS
TIONAL
AU OF
NDARDS
OULDER, COLO)
PORTABLE CLOCK NONREGULAR
GOLDSTONE, CA
60 Hz
DEEP SPACE STATION 11
FTS
IPPS μW
PORTABLE CLOCK 60 days
DEPOT MAINTENANCE COMPLEX REF STDS LAB
FTS
5 MHz μW
GROUND COMMUNICATIONS FACILITY 10
DEEP SPACE STATION 14
FTS
IPPS COAXIAL CABLE
DEEP SPACE STATION 12
FTS
PORTABLE CLOCK 7 days
S & X-BAND VLBI 7 days DEEP SPACE STATION 63 vs DEEP SPACE STATION 14
EXTRA GALACTIC RADIO SOURCE
S & X-BAND VLBI 7 days DEEP SPACE STATION 43 vs DEEP SPACE STATION 14
ROUND
OMMUNICATIONS
ACILITY
CANBERRA, A.C.T.
PORTABLE CLOCK NONREGULAR
DEEP SPACE STATION 42 43
FTS
CH 7
30 days
DNM vs TV DATA
IPPS
GROUND COMMUNICATIONS FACILITY
DEEP SPACE STATION 44
FTS
100 kHz
100 kHz

[illegible] 2

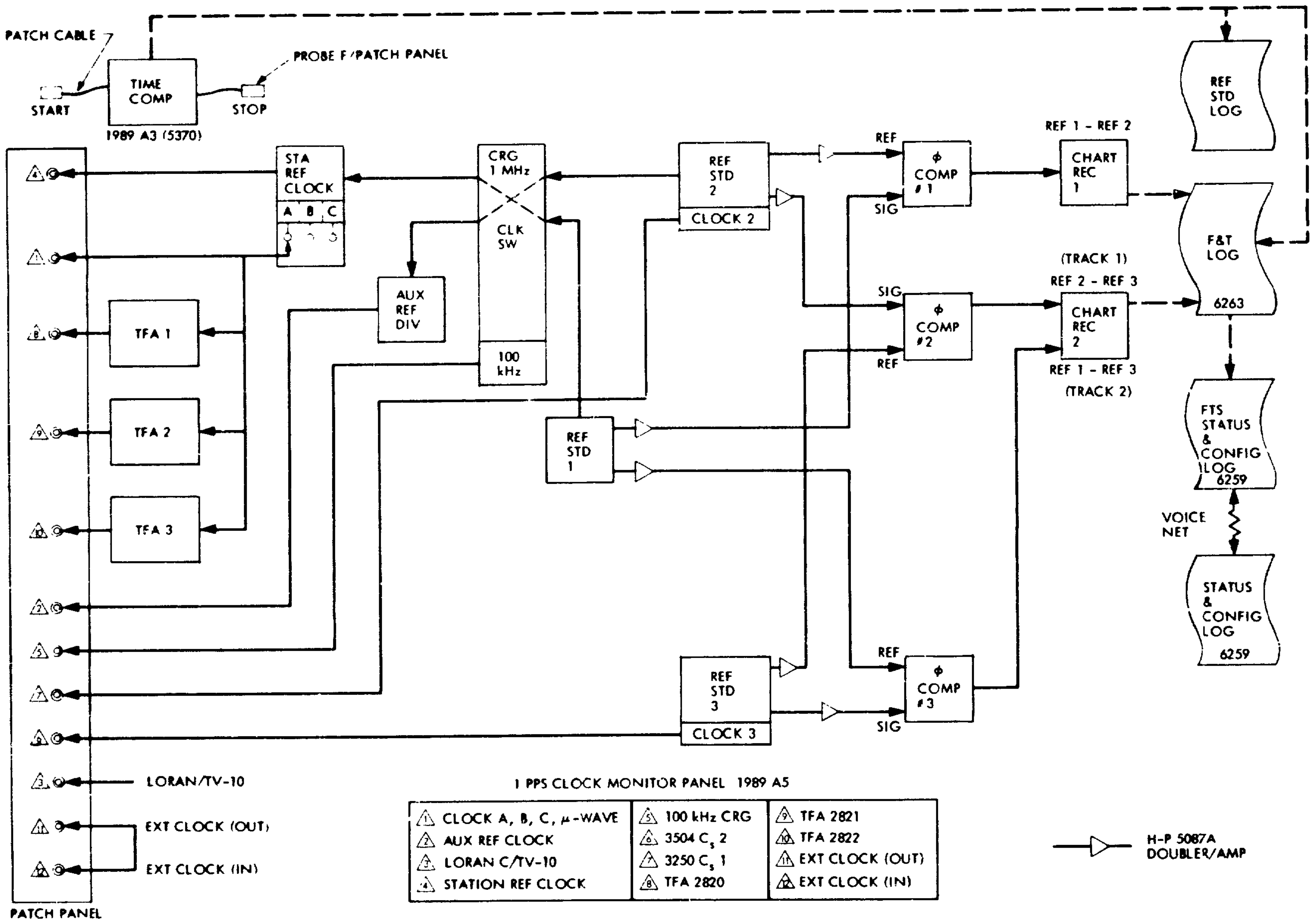

Fig. 3. Frequency and time monitoring at 64-meter DSS

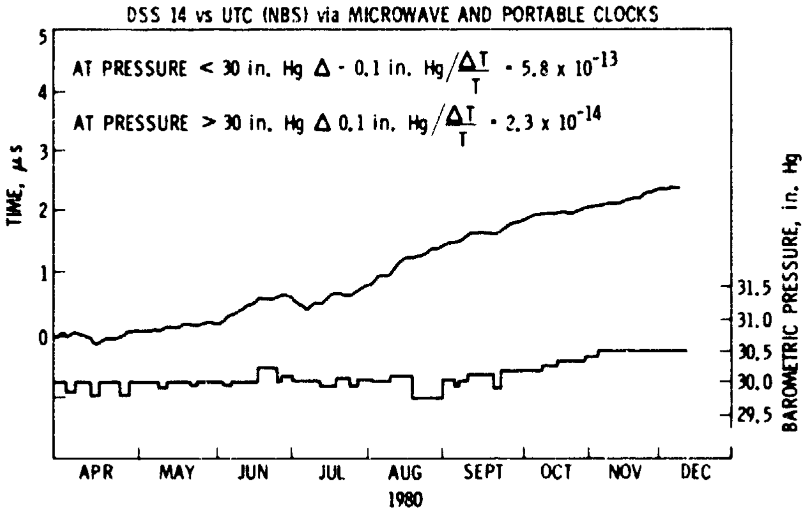

Fig. 4. Hydrogen-maser performance in a changing barometric pressure environment

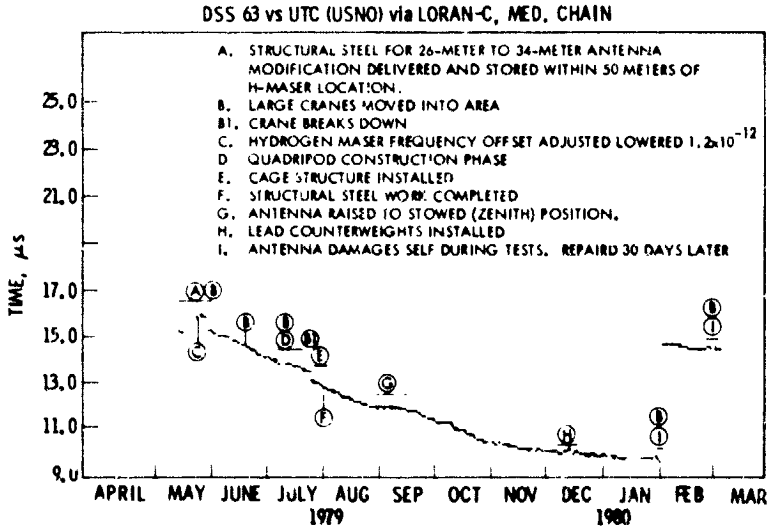

Fig. 5. Hydrogen-maser performance in a changing magnetic environment

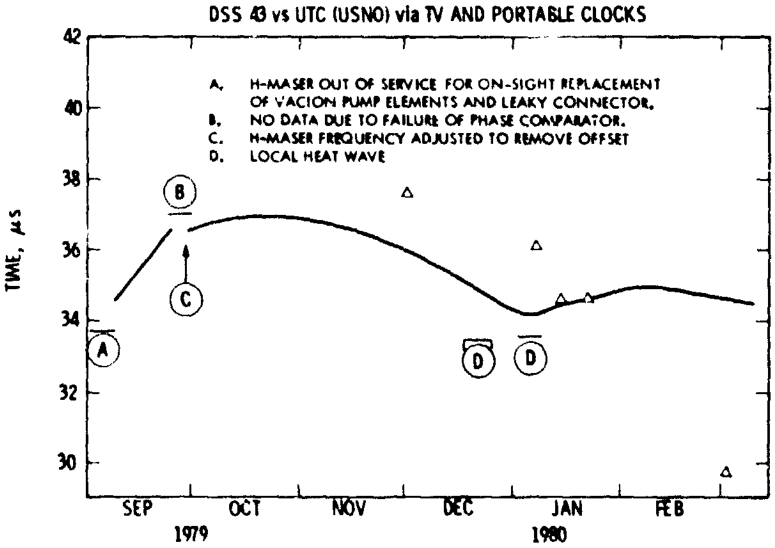

Fig. 6. Maser performance in a changing temperature environment

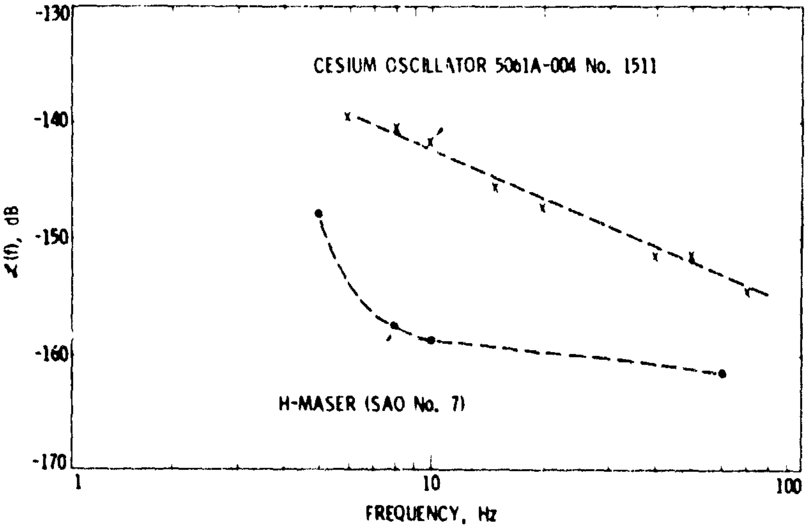

Fig. 7. Reference standards spectral performance (f) vs frequency

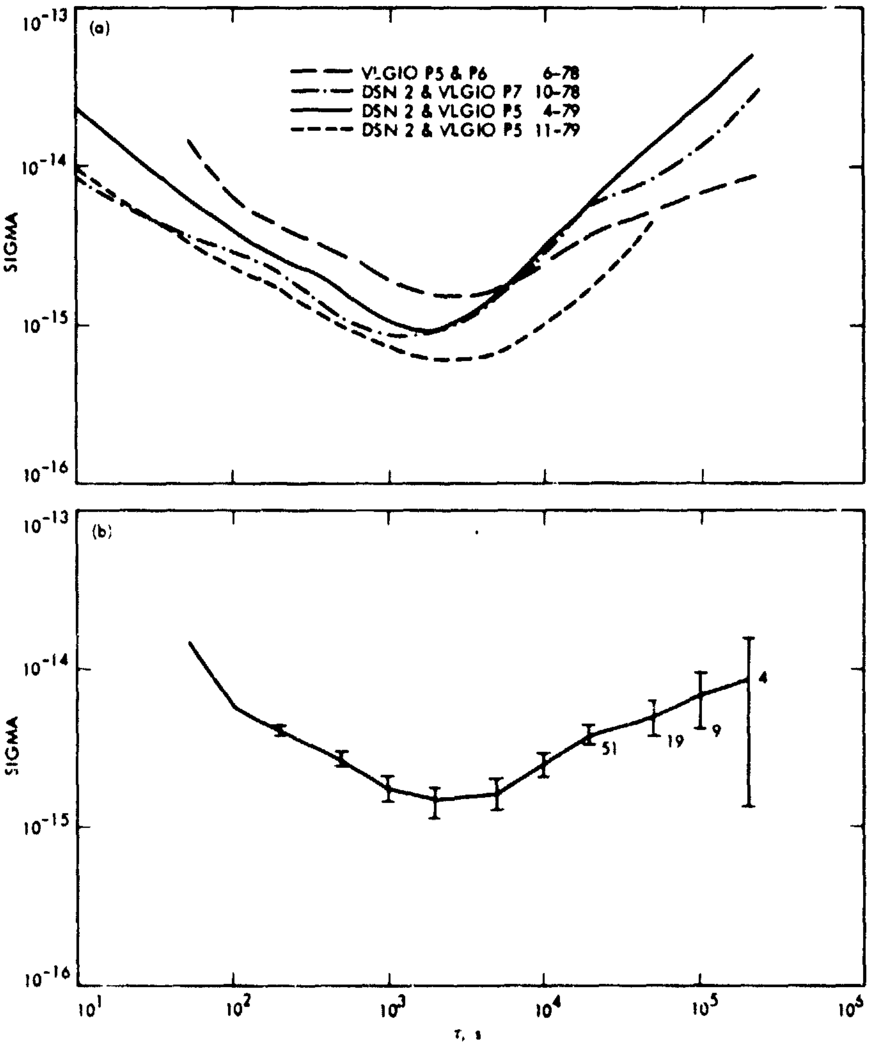

Fig. 8. Allan variance (a) vs sampling time, (b) vs sampling time with error bars

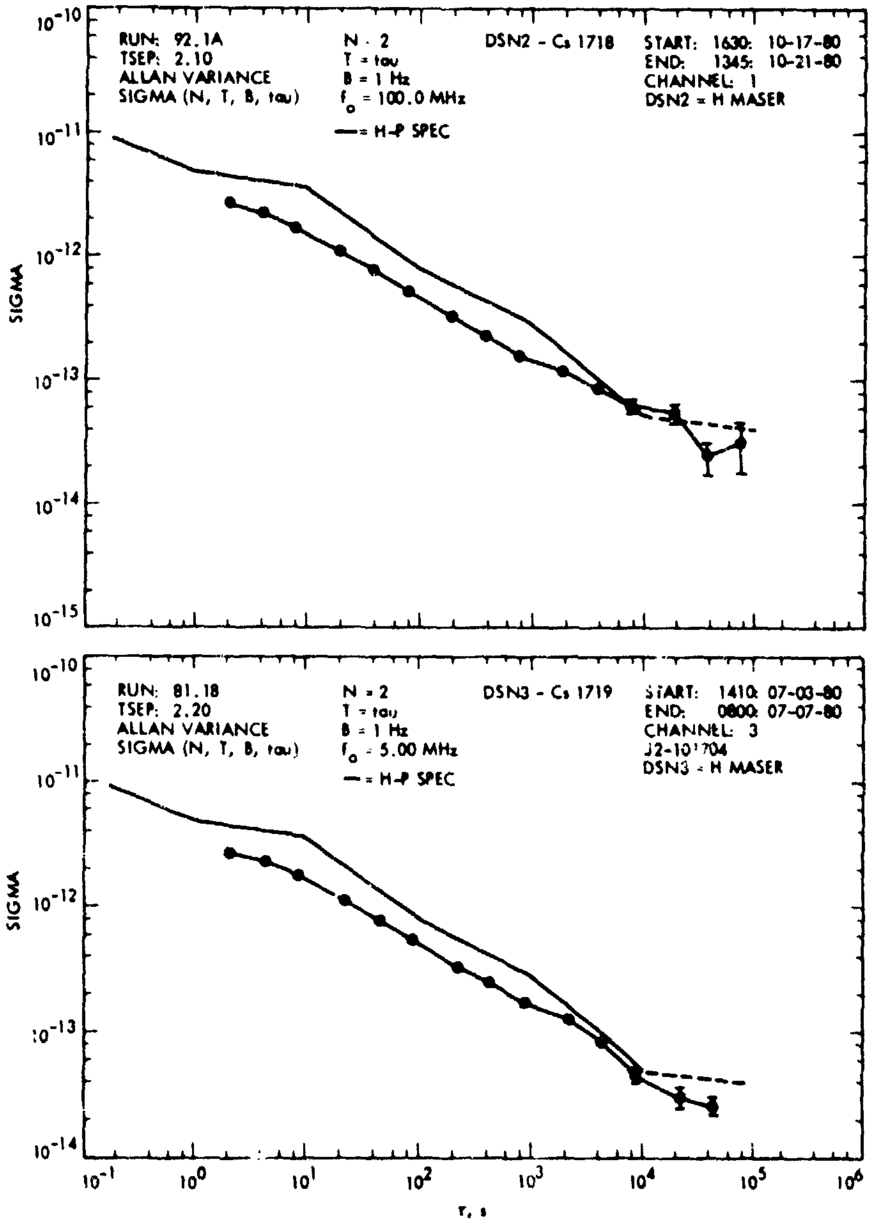

Fig. 9. Stability test data

FTS Quicklook Data

DOY	DSS-14 T.O. (μs)	DSS-14 Rel. Rate (μs/μs)	DSS-42/43 T.O. (μs)	DSS-42/43 Rel. Rate (μs/μs)	DSS-61/63 T.O. (μs)	DSS-61/63 Rel. Rate (μs/μs)
286	0.00	——	-2.70	——	2.3	——
287	0.00	0.0	-2.70	0.0	2.3	0.0
288	——	——	-2.67	3.47 (-13)	2.2	-1.16 (-12)
289	0.00	——	-2.63	4.63 (-13)	2.3	1.16 (-12)
290	0.80	9.26 (-12)	-2.60	3.47 (-13)	2.3	0.0
291	0.80	0.0	-2.56	4.63 (-13)	2.2	-1.16 (-12)
292	0.80	0.0	-2.52	4.63 (-13)	2.2	0.0
293	1.00	2.31 (-12)	-2.49	3.47 (-13)	2.3	1.16 (-12)
294	0.80	-2.31 (-12)	-2.44	5.79 (-13)	2.4	1.16 (-12)
295	1.20	4.62 (-12)	-2.41	3.47 (-13)	2.4	0.0
296	0.80	-4.62 (-12)	-2.38	3.47 (-13)	2.3	-1.16 (-12)
297	0.80	0.0	-2.34	4.63 (-13)	2.3	0.0
298	-0.30	-1.27 (-11)	-2.31	3.47 (-13)	2.4	1.16 (-12)
299	-0.30	0.0	-2.27	4.63 (-13)	2.4	0.0
300	-0.20	1.16 (-12)	-2.24	3.47 (-13)	2.5	1.16 (-12)
301	-0.30	1.16 (-12)	-2.20	4.63 (-13)	2.4	1.16 (-12)
302	-0.28	2.31 (-13)	-2.17	3.47 (-13)	2.4	0.0
303	-0.30	-2.31 (-13)	-2.13	4.63 (-13)	2.4	0.0
304	-0.30	0.0	-2.10	3.47 (-13)	2.3	1.16 (-12)
305	-0.35	-5.79 (-13)	-2.06	4.63 (-13)	2.3	0.0
306	-0.40	-5.79 (-13)	-2.03	3.47 (-13)	2.3	0.0
307	-0.30	1.16 (-12)	-2.00	3.47 (-13)	2.3	0.0

Considering weekly segments:

Over	$T_e - T_s$	Rel. Rate	$T_e - T_s$	Rel. Rate	$T_e - T_s$	Rel. Rate
286-293	1.00	1.45 (-12)	0.21	3.04 (-13)	0.0	0.0
293-300	-1.20	1.74 (-12)	0.25	3.62 (-13)	0.20	2.89 (-13)
300-307	-0.10	1.45 (-13)	0.24	3.47 (-13)	-0.20	-2.89 (-13)

Fig. 10. 64-meter DSS F & T offset report

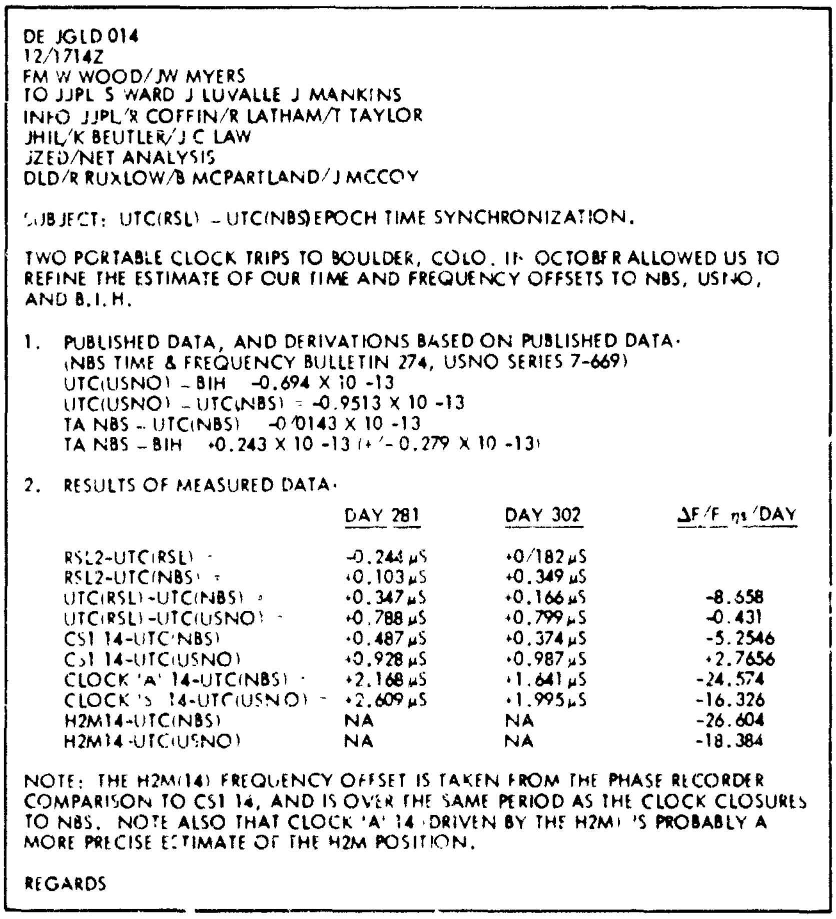

DE JGLD 014
12/1714Z
FM W WOOD/JW MYERS
TO JJPL S WARD J LUVALLE J MANKINS
INFO JJPL/R COFFIN/R LATHAM/T TAYLOR
JHIL/K BEUTLER/J C LAW
JZED/NET ANALYSIS
DLD/R RUXLOW/B MCPARTLAND/J MCCOY

SUBJECT: UTC(RSL) – UTC(NBS) EPOCH TIME SYNCHRONIZATION.

TWO PORTABLE CLOCK TRIPS TO BOULDER, COLO. IN OCTOBER ALLOWED US TO REFINE THE ESTIMATE OF OUR TIME AND FREQUENCY OFFSETS TO NBS, USNO, AND B.I.H.

1. PUBLISHED DATA, AND DERIVATIONS BASED ON PUBLISHED DATA:
   (NBS TIME & FREQUENCY BULLETIN 274, USNO SERIES 7-669)
   UTC(USNO) – BIH -0.694 X 10 -13
   UTC(USNO) – UTC(NBS) = -0.9513 X 10 -13
   TA NBS – UTC(NBS) -0.0143 X 10 -13
   TA NBS – BIH +0.243 X 10 -13 (+/- 0.279 X 10 -13)

2. RESULTS OF MEASURED DATA:

	DAY 281	DAY 302	ΔF/F ns/DAY
RSL2-UTC(RSL)	-0.244 µS	+0.182 µS	
RSL2-UTC(NBS)	+0.103 µS	+0.349 µS	
UTC(RSL)-UTC(NBS)	+0.347 µS	+0.166 µS	-8.658
UTC(RSL)-UTC(USNO)	+0.788 µS	+0.799 µS	-0.431
CS1 14-UTC(NBS)	+0.487 µS	+0.374 µS	-5.2546
CS1 14-UTC(USNO)	+0.928 µS	+0.987 µS	+2.7656
CLOCK 'A' 14-UTC(NBS)	+2.168 µS	+1.641 µS	-24.574
CLOCK 'A' 14-UTC(USNO)	+2.609 µS	+1.995 µS	-16.326
H2M14-UTC(NBS)	NA	NA	-26.604
H2M14-UTC(USNO)	NA	NA	-18.384

NOTE: THE H2M(14) FREQUENCY OFFSET IS TAKEN FROM THE PHASE RECORDER COMPARISON TO CS1 14, AND IS OVER THE SAME PERIOD AS THE CLOCK CLOSURES TO NBS. NOTE ALSO THAT CLOCK 'A' 14 (DRIVEN BY THE H2M) IS PROBABLY A MORE PRECISE ESTIMATE OF THE H2M POSITION.

REGARDS

Fig. 11. DSN master frequency and time report

Appendix

The following covers events relating to hydrogen maser performance history and the long-term stability performance of the two overseas units. The closure data resulting from the USNO traveling clock measurements (Refs. 3 and 4) provided the most accurate means of validating the frequency offset performance data.

(1) On day 319 (November 14, 1980), the hydrogen maser (H_2M), SAO-VLG-10 Serial No. 7, located at DSS 63 failed. This outage was caused by failure of the VACION pump assembly.

(2) On day 346 (December 11, 1980), a traveling clock, traceable to UTC (USNO), visit was made to DSS 63 Data from this Report of Precise Time Measurement (Ref. 3) has produced the following results:

(a) The DSS 63 on-line reference frequency standard was 5.9 X 10^{-13} (51 ns/day) faster than the UTC (USNO) rate over the 88-day period (September 15 through December 11, 1980). The uncertainty on this measurement was ±4 X 10^{-14} (±3.2 ns/day).

(b) Using daily time offset measurements referenced to Mediterranean Chain LORAN-C, DSS 63 personnel were able to maintain knowledge of the reference frequency standard's frequency offset to within ±4.1 X 10^{-13} of the UTC (USNO) rate. Noise on the LORAN-C receptions over this 88-day data span introduces an error > 90%.

(c) The drift in the output frequency of the H_2M SAO VLG-10 Serial No. 7 is less than 6.5 X 10^{-14} per day. This measurement, however, is seriously limited by instrumentation errors of >70%, and it includes the noise introduced by operator technique.

(3) On day 006, 1981, a traveling clock, traceable to UTC (USNO), visit was made to DSS 43. Data from this Report of Precise Time Measurement (Ref. 4) has produced the following results.

(a) The DSS 43 on-line reference frequency standard was 8.1 X 10^{-14} (7 ns/day) slower than the UTC (USNO) rate over the 100-day period (September 30, 1980, through January 6, 1981). The uncertainty on this measurement was ±3 X 10^{-14}.

(b) Using daily time offset measurements referenced to UTC (Australia) through the medium of public television broadcasts (Fig. 1, Method B), DSS 43 personnel were able to maintain knowledge of the reference standard's frequency offset to within ±2.3 X 10^{-14} of the UTC (USNO) rate. Noise on the TV receptions over this 100-day data span introduced an error of <10%.

(c) The drift in the output frequency of H_2M SAO VLG-10 Serial No. 6 is <5.7 X 10^{-14} per day. Again, the limitation on the accuracy of this measurement is instrumentation/technique errors (40%).

Summary: The performance of both the overseas hydrogen masers was within all Voyager Project specifications for Encounter No. 1. However, validation of this at DSS 63 was not possible without the second traveling clock visit, due to insufficient instrumentation precision.

D25

N81-27148

Electrical Load Management at the Goldstone DSN Complex

J. C. Rayburn,
Deep Space Network Support Section

The Southern California Edison Company issued a new time-of-day rate schedule for the Goldstone Complex which substantially increased the cost of commercial power during the daily high usage periods. Subsequently, a Power Load Management Plan was developed which would utilize the unique power generating capabilities of the stations to reduce the stress on the Edison Company's reserve capacity and reduce the cost of electrical power at the stations. The plan, which has now been implemented, has greatly reduced the cost of Goldstone electrical power by completely eliminating the use of commercial power during the Edison Company's high usage periods each day.

I. Introduction

In April 1979 the Southern California Edison (SCE) Company issued a new industrial rate schedule. Upon review of the new schedule it was apparent that the cost of purchased electrical power would sharply increase. SCE's time-of-day charging was designed to provide a substantial increase in the cost of power during high usage periods of the day. Figure 1 contains a 24-hour load profile which illustrates the new summer weekday rate schedule. Energy usage rates were established for "on", "mid", and "off" peak periods. The SCE rate structure also carried a severe penalty for every kilowatt of demand that occurred during the "On Peak" time period.

SCE's rate schedule referred to as No. TOU-8, General Service-Large, is outlined in Table 1. Key aspects of the new schedule include a $5.05 demand charge per kW for the maximum average kW used over a 15-minute period each month, and an energy charge (to be added to the demand charge) for the kWh used during each time-of-day period, i.e., the average kW load for each period multiplied by the hours of the period. The high "On Peak" charges are related to the amount of generating capacity which the power companies have in reserve. The fact that they are high is an indication that the utility has minimal reserve during the high usage "On Peak" periods.

II. Discussion

As anticipated, the cost of purchased electrical power jumped sharply when the new rate schedule became effective. The Deep Space Network Mission Support Operations Division in accordance with JPL Energy Conservation and Economic Policy initiated a three-phase effort. This effort was directed toward determining by load management whether or not we could alleviate, to some degree, the stress on the utility's minimum "On Peak" reserve capacity. Also, would this reduce the cost of electrical power at the Goldstone Tracking Station?

A. Phase I

This phase involved establishing what steps could be taken to reduce the "On Peak" loads and what benefit would be expected.

The Goldstone Complex has two electrical services which are metered separately:

(1) A 2400-volt service to Deep Space Station 14 (Mars).

(2) A 480-volt service to DSS 11, 12 and 13 (Goldstone).

The one-line power diagram in Fig. 2 indicates the metering for the two services as they enter the Goldstone Facility. DSS 11, 12, and 14 have their own powerhouses with diesel generators and an arrangement of circuit breakers to enable them to be synchronized and paralleled with the utility. This means that before the start of the "On Peak" power period the diesel generators could be started and paralleled with the utility and the station load transferred to the generators. The power equipment was capable of making this transfer without any interruption or disturbance to the electrical system. The DSS 14 station has a special dual bus arrangement that enables the high-power transmitter, an intermittent large load, to be connected to the diesel generators while the utility furnishes the balance of the station load.

Quite obviously, load management techniques should be economically rewarding. The penalty for using power during the "On Peak" periods was very high. The question that remained was, would it be cost-effective to generate all "On Peak" power, i.e., would the cost to generate electrical power over the "On Peak" period exceed the cost for utility power if purchased over the same period?

Parameters utilized in predicting the results that would be achieved if the stations were placed on generators during the "On Peak" period are listed in Table 2.

The following is a summary of the expected costs of generated vs commercial power at DSS 11, 12, and 14:

Diesel generation cost - peak periods per month

Fuel cost "On Peak" periods monthly	$ 9,640.00
Fuel cost "Mid Peak" periods	1,760.00
Maintenance cost	840.00
Total cost	$12,240.00

Commercial power costs – peak periods per month

Peak demand cost	$11,310.00
"On Peak"	6,550.00
"Mid Peak"	1,170.00
Total cost	$19,030.00

Predicted GDSCC savings

Commercial cost	$19,030.00
Diesel generator cost	$12,240.00
Monthly savings	$ 6,790.00

It is noted that additional savings could be expected since the analysis did not take into account the savings to be achieved by generating power required for the high-powered transmitter at DSS 14 during the "On Peak" periods.

B. Phase II

To verify the cost of generating power the "On Peak" power was generated at DSS 14 for one month. Complete records were kept and the fuel consumption of 12 kWh/gal was verified during the March billing period. 78,417 kWh of "On Peak" and 18,606 kWh of "Mid Peak" power were supplied by the generators. The following is a summary of the results obtained:

Projected Commercial "On Peak" demand charge	$5,654.00
Projected commercial "On Peak" energy charge	3,474.00
Projected commercial "Mid Peak" energy charge	799.00
Cost of commercial power	$9,927.00
Fuel cost for generated power	$6,145.00
Maintenance cost	279.00
Total cost	$6,424.00
Monthly savings	$3,503.00

However, if the utility's minimum demand charge of $1,252.00 is deducted, monthly savings for DSS 14 are $2,251.00. The minimum demand charge is 25% of the highest demand charge in the preceding 12 months. This charge would disappear after 12 months of "On Peak" power generation.

The estimated savings did not take into account the increased usages of the diesel generators that would eventually cause more maintenance work. However, maintenance does not increase directly proportionally to the number of hours of operation. In fact, by utilizing the engines we may be increasing their reliability. Certainly as far as the powerhouse operation and maintenance personnel are concerned, their level of competence would leap forward and would keep pace with the new demands. Synchronizing and paralleling with the utility would no longer be done only by a select set of personnel. All the electricians would become competent in doing this previously complicated procedure. In other words, extra practice would increase competence and the technical demands and activity would also give them a psychological boost as an added bonus.

C. Phase III

Having established the fact that power generation during "On Peak" periods was cost-effective, a load management plan was devised which would:

(1) Run generators when the high-power transmitter at DSS 14 is required during the "On Peak" periods, utilizing advanced notice from the station to minimize labor involvement.

(2) Run the generators at DSS 11, 12 and 14 to completely cover the "On Peak" station loads starting 30 minutes ahead and finishing 30 minutes after this critical period.

(3) Add at DSS 11, 12 and 14 automatic generator start and load takeover from the utility (stations on generators) at the push button command of the station operator. This would minimize powerplant operator involvement and also provide rapid changeover to generators in the event of storm warnings.

III. Implementation

These load management procedures were implemented during 1980. In March, DSS 14 started "On Peak" generation and even earlier had utilized generators for the high-power transmitter In August, DSS 11 and DSS 12 implemented "On Peak" generation. Profiles of "On Peak" station loading without load management provided bases for establishing the annual savings The savings are accurate since they were developed utilizing month-to-month tabulations of previous utility charges corrected to reflect the actual 1980 time-of-day periods. Table 3 lists the factors which determine the cost of generating power at the stations and compares the cost with the utility demand and energy charges. The savings of $120,000 per annum noted in Table 3 did not include the minimum demand charge for either the Mars feeder or the Goldstone feeder This minimum demand charge would exist for one full year after the "On Peak" demand was reduced to zero. Therefore, the annual savings would be approximately $15,000 less for the first 12 months of active load management. With the Goldstone feeder, it is not possible to reduce the demand to zero due to the power system configuration at DSS 13. This station's controls are not designed to permit paralleling with the utility. It therefore is not practical to use the diesel generators to supply the "On Peak" power since it would be necessary to interrupt the station power at the start and again at the finish of the "On Peak" demand period.

Results of the Load Management Program in eliminating or reducing the "On Peak" demands are reflected in the December 1980 electricity bill for the Goldstone feeder. This shows an "On Peak" demand of 240 kW (previous high demand was 1459 kW.) The "On Peak" demand kW would have reached at least 1140 kW if we had not been on generators during the "On Peak" period. The load management has consequently reduced this by 900 kW. The December 1980 electricity bill for the Mars feeder shows a zero "On Peak" demand as compared to the previous high demand, which was 992 kW.

Initially various objections were raised:

(1) It would require too much manpower from the technical plant services group

(2) It would increase the maintenance required on the engines and this would further tax the reduced manpower resources.

(3) Heavy workloads or oversight might delay starting the diesels, and just 15 minutes late would allow the "On Peak" demand to register to its full amount, thus aborting a whole month's activity and undermining the year's savings (to eliminate the minimum demand charge).

These objections were quite real and were systematically resolved. An automatic system was introduced first at DSS 14 and then at DSS 12 and DSS 11. This allowed the shift supervisor to press a button on the control console which started two engines and first paralleled them together and then paralleled them to the utility. Once paralleled, the utility was disconnected automatically and the diesel generators were supplying the station load. Thus, we could be assured that if the electricians were not available (say due to some plant emergency), then the station shift supervisors could put the generators on line automatically.

Further, it was decided that sufficient automatic generator plant safety devices existed so that the generator plant could operate satisfactorily and safely without personnel in attendance.

Maintenance was a problem that could not be resolved before the fact. However, experience from DSS 61/63 and DSS 42/43 had not shown any significant increase with increasing hours of operation, at least not until the engines reached the 50,000 to 60,000 hours running time; however, load management was only adding just over 2000 hours per year, and it would be 20 years before the 50,000-hour mark would be reached.

IV. Summary

Load Management techniques have been implemented at the Goldstone Complex to minimize the stress on SCE reserve capacity and lessen the cost of electrical power at the tracking stations. An average of 120,000 kWh per month is no longer required from the utility during high usage periods. The cost of electrical power at the complex has been reduced by a minimum of $10,000.00 each month. Factors such as changes in the cost of fuel and the Utility's fuel adjustment and energy charges affect the accuracy of projected future savings. JPL will continue to monitor these critical parameters to insure that the results obtained through judicial load management are consistent with the established objectives.

Table 1. Southern California Edison Company schedule no. TOU-8

Rates	Per meter per month
Customer Charge	$1,075.00
Demand Charge (to be added to Customer Charge)	
All kW of "On-Peak" billing demand per kW	$ 5.05
Plus all kW "Mid-Peak" billing demand, per kW	0.65
Plus all kW of "Off-Peak billing demand per kW	No Charge
Energy Charge (to be added to Demand Charge)	
All "On-Peak" kWh, per kWh	4.34¢*
Plus all "Mid-Peak" kWh, per kWh	4.19¢*
Plus all "Off-Peak" kWh, per kWh	4.04¢*

*Includes 3.81¢ Energy Cost Adjustment as of 3 February 1980

Minimum Charge

The monthly Demand Charge shall be not less than the charge for 25% of the maximum "On-Peak" demand established during the preceding 11 months

Daily time periods will be based on Pacific Standard Time and are defined as follows

"On-Peak"	12 00 noon to 6 00 p m summer weekdays except holidays
	5 00 p m. to 10.00 p.m winter weekdays except holidays
"Mid-Peak"	8 00 a m. to 12 00 noon and 6 00 p m. to 10 00 p m. summer weekdays except holidays
	8 00 a m. to 5 00 p m. winter weekdays except holidays
"Off-Peak"	All other hours

Table 2. Electrical power cost factors

Average load, kW	1290 kW avg[a]
Peak demand	2240 kW[a]
Peak periods per month, hr	
Summer 6 hr × 21.6 days	129.6 hr
Winter 5 hr × 21.6 days	108 hr
Average/month	118 hr
Edison charges[b]	
On peak demand	$5.05/kW
Energy charges Adjustment cost per kWh used	3.81¢/kWh
On peak energy charge ($3.81 + 0.53) =	4.34¢/kWh
Mid-peak energy charge ($3.81 + 0.38) =	4.19¢/kWh
Off-peak energy charge ($3.81 + 0.23) =	4.04¢/kWh
Diesel fuel cost	
Cost per gallon of fuel (Dec. 79)	$0.76
kWh per gallon of fuel (average)	12 kWh
Cost/kWh	6.33¢/kWh
Maintenance cost	
Material cost per diesel	$0.75/hr
Number of diesels on-line	8

[a] Values determined from August, September, and October SCE billings.

[b] Latest rate as of February 3, 1980.

Table 3. Cost of power—Goldstone Complex

	Mars feeder (DSS 14)		
Cost of generating	1,449,000 kWh		
Cost of fuel	$\frac{1449000}{12} \times 0.826$	=	$ 99,739
Average hours run	3350		
Cost of maintenance	(3350 × 0.75)		2,513
			102,252
Utility demand charge			112,110
Utility energy charge			68,103
			180,213
Less cost of generating power			102,252
			77,961
Savings	77,961		
	Goldstone feeder (DSS 11 and 12)		
Cost of generating	1,162,700 kWh		
Cost of fuel	$\frac{1162700}{12} \times 0.826$	=	80,033
Average hours run	3350		
Cost of maintenance	(3350 × 0.75)	=	2,513
			82,546
Utility demand charge			70,478
Utility energy charge			54,647
			125,125
Less cost of generating power			82,546
			42,579
Savings	42,579		
Total savings	120,540		

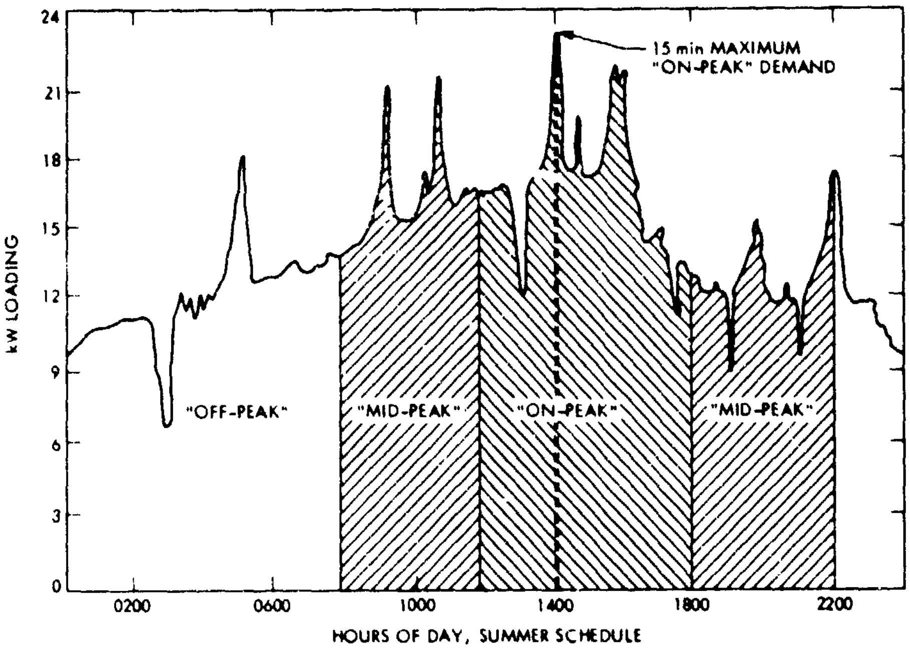

Fig. 1. 24-hour load profile SCE time-of-day schedule

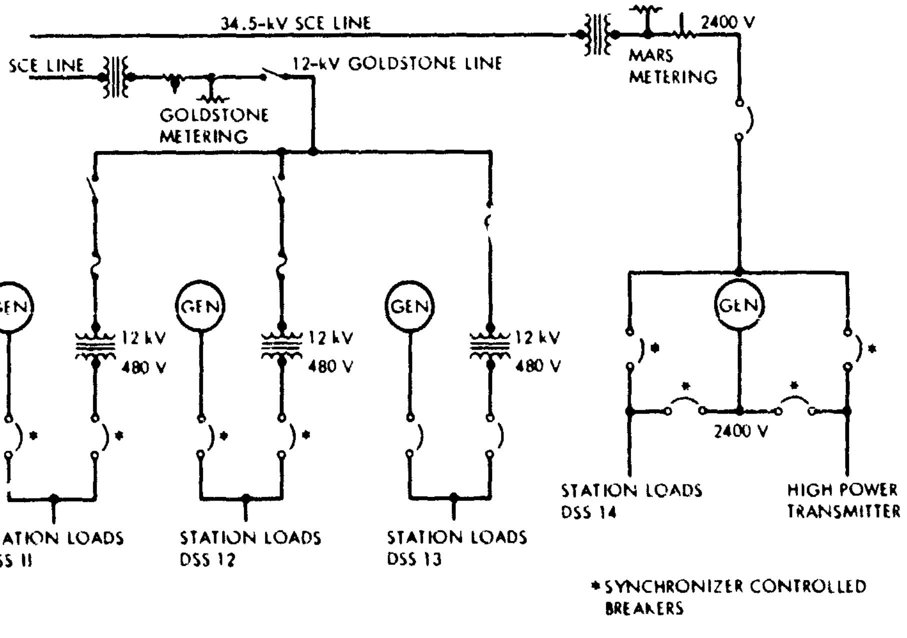

Fig. 2. Simplified power diagram, Goldstone Complex

D// N81-27149

Planetary Radar

R. D. Shaffer and P. R. Wolken
Control Center Operations Section

R. F. Jurgens
Communications Systems Research Section

This article reports on the radar astronomy activities supported by the Deep Space Network during the first quarter of 1981. The bodies observed include the asteroids Apollo and Toro, comet Bradfield, and the rings of Saturn.

The 64-meter Goldstone station utilizing S- and X-band high-power transmitters supported observations of the asteroids Apollo and Toro, comet Bradfield, and Saturn's rings during this period. Estimates of the amount of useable data acquired vs the total obtained reveal a preliminary success rate of approximately 50%.

The outstanding success has been the observation of the asteroid Apollo. Publication of these results is eagerly awaited. Continued observations of the asteroid Toro (see *TDA Progress Report 42-59, July-August 1980*) were not so successful, due to a lack of updates in the ephemeris used for predictions. Radar Astronomy also suffered equipment failures, notably in the X-band transmitter. The other disappointment to report is the spectra obtained of comet Bradfield. These appear to be contaminated by other spectra, but the investigation is continuing in an attempt to extract the comet data. Fair-to-marginal detection of Saturn's rings at X band was also achieved during this period. A particularly significant result of preliminary analyses is that the scattering function does not conform to any known theories or hypotheses and at this time remains undecipherable.

NASA-JPL-Coml. L.A. Calif.